CALIFORNIA INSTITUTE OF TECHNOLOGY

EARTHQUAKE ENGINEERING RESEARCH LABORATORY

SILENT BOUNDARY METHODS FOR TRANSIENT WAVE ANALYSIS

By

Martin Cohen

EERL 80-09

A Report on Research Conducted under Grants
from the National Science Foundation
and the Earthquake Research Affiliates
of the California Institute of Technology

Pasadena, California
September, 1980

SILENT BOUNDARY METHODS FOR TRANSIENT WAVE ANALYSIS

Thesis by

Martin Cohen

In Partial Fulfillment of the Requirements

for the Degree of

Doctor of Philosophy

California Institute of Technology

Pasadena, California

1981

(Submitted September 23, 1980)

ACKNOWLEDGMENTS

I would like to express gratitude to my advisor, Dr. P. C. Jennings, for his invaluable suggestions and guidance during the whole course of this investigation. I am also indebted to Dr. T.J.R. Hughes for his perspicacity and advice as how to proceed on several difficult problems.

Conversations with my fellow students, Paul Yoder, Shawn Hall, Chuck Krousgrill, Per Reinhall, and Wing Kam Liu, all proved to be extremely productive in my work, and I appreciate their generous giving of time to discuss my difficulties.

Gratitude is also extended to Ms. Sharon Vedrode and Ms. Gloria Jackson for their accomplished typing of the manuscript, and to the National Science Foundation for their funding of this project.

Lastly, and most importantly, I thank my wife, Mary, for her steadfast love and support through years of trying circumstances.

ABSTRACT

This thesis sets forth a dynamic model, designed to absorb infinitely radiating waves in a finite, computational grid. The analysis is primarily directed toward the problem of soil-structure interaction, where energy propagates from a region near a structure, outward toward the boundaries.

The proposed method, called the extended-paraxial boundary, is derived from one-directional, wave theories that have been propounded by other authors. In this thesis, the theory is presented from a more general viewpoint and is studied for its stability properties. This work suggests some modifications to the method as it was first presented. Innovations are also put forward in the boundary's implementation for finite element calculations. These alterations render the boundary an effective wave absorber.

The extended-paraxial boundary is then compared, both analytically and numerically, with two other transmitting (or silent) boundaries currently available -- the standard-viscous and unified-viscous methods. The analytical results indicate that the extended-paraxial boundary enjoys a distinct advantage in cancelling wave reflections; actual numerical tests revealed a small superiority over the viscous approaches.

Various issues are also discussed as they relate to the silent boundaries. These include Rayleigh waves, spherically symmetric and axially symmetric waves, nonlinear waves, anisotropic media, and numerical stability.

TABLE OF CONTENTS

TABLE OF CONTENTS (CONTINUED)

TABLE OF CONTENTS (CONTINUED)

CHAPTER 1

I. INTRODUCTION

The general motivation behind this thesis is to develop improved methods of analyzing problems in "soil-structure interaction." This term refers to how soil deformations affect the motions of buildings being subjected to a dynamic loading.[1] In this thesis, we address ourselves to one of the major difficulties posed by such an analysis -- the phenomenon of waves which are radiating outward from the vibrating structure, toward infinity. In numerical calculations, only a finite region of the foundation medium is analyzed. Unless something is done to prevent the outwardly radiating waves from reflecting from the region's boundaries, errors are introduced into the results. The present work concerns itself with the study of such effects, using the finite-element method, and an artificial, transmitting boundary at the edge of the computational grid. The reasons for studying infinitely-radiating waves, and for using this particular approach to a solution, have been documented. A background of the analysis of soil-structure interaction is included now in order to clarify the objective of this thesis.

Researchers have developed two major techniques for dealing with this phenomenon: 1) the continuum method,[3,7] and 2) the finite-element method.[82] The central feature of the continuum method is the

---

[1] For example, nuclear power plants, which are heavier and stiffer than most other structures, may "interact" with the relatively softer, underlying soil. In this case, we cannot assume that the building shakes on a rigid base; we must account for the flexibility of the soil.

assumption of a rigid foundation resting on an elastic medium. In perhaps the most common approach, one finds the relationship between $\underset{\sim}{F}_s$, the forces and moments which the foundation exerts on the ground; and $\underset{\sim}{u}_o$, the foundation displacements and rotations relative to the ground.[8] Therefore,

$$\underset{\sim}{F}_s = [\underset{\sim}{K}_s]\, \underset{\sim}{u}_o \quad , \tag{1}$$

where $[\underset{\sim}{K}_s]$ is called the impedance matrix. The second part of the analysis calculates $\underset{\sim}{F}_s^*$, the forces and moments caused by the seismic excitation. Hence,

$$\underset{\sim}{F}_s^* = [\underset{\sim}{K}_s]\, \underset{\sim}{u}_s^* \quad , \tag{2}$$

where $\underset{\sim}{u}_s^*$ contains the relative displacements and rotations caused by seismic waves. By superposition, the total displacement of the foundation is:

$$\underset{\sim}{u} = \underset{\sim}{u}_o + \underset{\sim}{u}_s^* \quad . \tag{3}$$

Once the generalized forces or displacements of the foundation have been computed, many different methods can be used to calculate the superstructure's response. For example, either a lumped mass model or the finite-element method could be employed to estimate the structure's motion.[2,5]

The principal advantages of the continuum approach are its accuracy and its relative simplicity and low cost. In performing this type of analysis, one probably gains more physical insight into the problem than results from doing a comparable amount of finite-element computations. The continuum method, however, is severely limited in that it can only treat linearly-elastic, or visco-elastic soils. The technique

is also restrictive in the range of foundation geometries it can analyze, being limited to simple shapes, such as circles and rectangles. This method also runs into complications when confronted by embedded structures.[4,6] For these reasons, we focus our attention on the finite-element method. Although the application of finite-element techniques to soil-structure interaction problems is burdened by its own considerable difficulties, as we discuss below, the continuous upgrading of computer technology, and the method's geometrical advantages, make it a promising approach.

The reader can refer to Zienkiewicz[82] for details of the finite-element method. Suffice it to say that it is conveniently able to handle geometrical irregularities and material nonlinearities. The method's major drawback, for soil-structure interaction problems, is that present computer hardware is unable to manage the enormous storage and computational requirements of a full-scale, three-dimensional transient calculation. Attempts to reduce the problem's scale can often produce large errors in the solution. For example, if the boundaries of the finite element mesh are situated too near a source of wave radiation, then spurious boundary reflections will significantly distort the solution. Likewise, making the element size too large filters the motions of the higher frequencies which participate in the response.

Researchers have proposed a number of ideas to reduce the computational demands. One of the most important has been the use of artificial boundaries, which allow radiating energy to exit from the system. Ideally, with the use of these mechanisms, one can obtain the same solution by employing a relatively small number of elements, as one

does when using a much larger mesh. The resulting economy in computational effort would then be considerable. Unfortunately, most of the boundary schemes with this aim suffer from significant drawbacks, or they are not applicable for this type of problem. Recent works on this subject are summarized in Section II.

Analysts have also attempted to utilize two-dimensional models in the solution of three-dimensional problems. Some work[25,62] indicates that this simplification causes an underestimation of the building response. Other errors in estimation may also result.

The substructuring[64] of the system is another method of reducing the problem's size. Here, the structure and the soil are analyzed separately, so that two smaller problems are solved instead of having to solve the original coupled system. This procedure may be viable when many analyses are to be performed.

Another problem is that the material properties of soils are both highly variable and highly nonlinear, and they have proved to be difficult to model correctly.[59] Often, crude approximations of soil behavior are used,[60,61] and it is not always clear how this oversimplification affects the system's general response.

At present, an ignorance of the variation of seismic motion with depth, and distance, impedes soil-structure interaction studies. The current dearth of underground seismic data prevents a truly accurate representation of the input to the system. Analysts must postulate seismic inputs[63] which will produce reasonable approximations of accelerograms obtained at a point on the surface of the ground.

In summary, we have reviewed several of the more important limitations to soil-structure interaction analysis. As is evident, much can be done to improve the state-of-the-art of these techniques. In this thesis, we focus our attention on one of these problems, the transmitting or silent boundary, and attempt to make additions to the current methodology.

II. REVIEW OF PAST WORK ON TRANSMITTING BOUNDARIES

Several different methods for the treatment of absorbing boundaries have been proposed and employed with varying success. We comment on several of them here, and list others. In all cases, the object of the work has been to make the artificial boundary behave, as nearly as possible, as if the mesh extended to infinity. In particular, since economy dictates that the boundary be near the central field of the mesh, the methods all try to avoid large, direct reflections of energy. The resulting techniques, or boundary elements, are variously known as transmitting boundaries, absorbing boundaries, or silent boundaries. These terms are used interchangeably in this thesis.

Lysmer and Kuhlemeyer[47] conceived of using viscous damping forces, which act along the boundary, as a means of absorbing, rather than reflecting, the radiated energy. The method, being directly analogous to the use of viscous dashpots, is relatively easy to implement, and it appears to treat both dilatational and shear waves with acceptable accuracy in many applications. The viscous forces, or dashpots, enjoy a third advantage, in that they do not depend upon the frequencies of the transmitted waves. This technique is thus suitable for transient analysis.

It is commonly believed ([11], [33], [34], [44], [47]) that one drawback to the viscous boundary is its inability to transmit Rayleigh waves as effectively as it does the body waves. A special viscous boundary was devised,[47] in which dashpots, which are suitable for the transmission of Rayleigh waves, have coefficients that depend upon the frequency of the waves. The accuracy of this Rayleigh-wave boundary is not well established. It has been noted[44] that in order to avoid inaccuracies, the computational mesh may have to be especially refined near the ground surface. This is because one of the dashpot's parameters, at a point somewhat below the surface, goes to infinity. In addition, there have been few comparisons between the standard- and Rayleigh-viscous boundaries, except for one axisymmetric problem which was discussed in [47]. The use of a standard-viscous boundary, for problems which involve Rayleigh waves, should not necessarily be ruled out. Unlike the Rayleigh boundary, it is independent of frequency and is much easier to implement. For example, Haupt,[15] using the standard-viscous boundary along with some of his own boundary innovations, achieved good, steady-state, Rayleigh-wave solution. Another Rayleigh-wave example is presented in Chapter 4.

White, Valliappan, and Lee[57] attempted to improve upon Lysmer and Kuhlemeyer's scheme, and also to broaden the theory to include anisotropic materials. To do this, they selected, and then minimized with respect to C_{ij}, a certain norm, I_{ij}, where

$$I_{ij} = \int_{\theta} (B_{ij} + C_{ij})^2 \cos^2 \theta \, d\theta \quad ; \qquad (4)$$

i = the number of stress components and j = the number of displacement components; θ is the angle of incidence of the wave. C_{ij} is the desired damping matrix that is used to cancel the stresses, $[\underset{\sim}{B}]\{\underset{\sim}{u}\}$, of the incoming waves. Therefore, I_{ij} is a measure of residual stress, or energy, that is not removed by the boundary terms, and will cause reflected waves.

After the minimization of I_{ij} to find C_{ij} is completed, this C_{ij} is used as a starting point to iterate for more "energy efficient" values of C_{ij}. This second minimization is performed on the energy ratio, $E_{reflected}/E_{incident}$, which is calculated by using harmonic wave forms and the previous values of C_{ij}.

The benefit to this approach is that anisotropic materials having infinite dimensions can be modeled. The authors have not clarified, however, just how efficient this boundary is for such materials. For the isotropic case, the method offers virtually no improvement upon the Lysmer/Kuhlemeyer boundary, and is more complicated to implement.

Claerbout[83] devised the idea of creating equations which transmit waves in only one direction. He derived these equations, termed paraxial approximations, for the two-dimensional, scalar-wave case. Clayton and Engquist[39] later expanded Claerbout's ideas to include elastic waves, and conceived the notion of applying it as an energy-absorbing boundary. In their approach, one takes the triple Fourier Transform (two spatial and one temporal) of the following two-dimensional, elasticity equations in plane strain.

$$\left.\begin{aligned} u_{tt} - c_d^2\, u_{xx} - (c_d^2 - c_s^2) w_{xz} - c_s^2\, u_{zz} &= 0 \quad , \\ w_{tt} - c_s^2\, w_{xx} - (c_d^2 - c_s^2) u_{xz} - c_d^2\, w_{zz} &= 0 \quad , \end{aligned}\right\} \qquad (5)$$

where c_d = the dilatational wave speed, c_s = the shear wave speed, and u and w are the respective horizontal and vertical displacements; x and z represent the spatial coordinates, and t = time.

The authors use the scalar-wave, paraxial equations "to provide a hint as to the general form of the paraxial approximation" for elasticity. They then take the Fourier transform of this general paraxial form, and "fit the coefficients by matching to the full, elastic wave equation." Using these derived coefficients, the general paraxial form becomes the governing equation for the boundary.

The authors implemented these equations using a finite-difference, numerical technique and, in the cases they presented, they obtained good body-wave transmission. The method, however, suffers from several difficulties. First, the technique, as formulated, does not lend itself to finite-element utilization. A straightforward, finite-element analysis divides the domain into two parts: the interior, where the regular equations of elasticity hold, and the boundary, where the paraxial equations are valid. The interface between the two discretized regions (elastic and paraxial) does not permit smooth wave transmission, and waves which do arrive in the paraxial area do not propagate correctly. A significant part of the wave energy is reflected into the elastic medium.

The effectiveness of the finite-element paraxial boundary, developed in this thesis, was notably improved by our utilization of some upwinding techniques suggested by Hughes,[73] and by our introduction of an interface element. The details of this approach are presented in Chapter 3, along with some comparisons between this boundary and others.

Another major difficulty with the earlier paraxial technique is that when Poisson's ratio is greater than 1/3, a negative stiffness term is introduced into the paraxial equations. This term clearly leads to instabilities; the boundary erroneously causes the displacements and stresses to grow in time. This problem is discussed in Chapter 2.

In a series of papers [Lysmer,[48] Lysmer and Waas,[49] and Lysmer and Drake[26]], a boundary was developed in order to transmit either Love waves or Rayleigh waves. The boundary was especially designed for a layered medium.

The method first assumes that a wave of a certain frequency is propagating in a certain layer. If another finite element having width h were present beyond the boundary, then its displacements would be e^{-ikh} (k equals the wave number) times those of the last element at the boundary. They then calculate the stiffness contribution of the supposed elements and put them into the equations of motion for the lumped masses at the boundary. Therefore,

$$\underset{\sim}{M}\ddot{u} + \underset{\sim}{K}u - k^2\underset{\sim}{K}^*u = 0 \quad . \tag{6}$$

If the frequency, ω, is known, and having set $\underset{\sim}{C} = \omega^2\underset{\sim}{M} + \underset{\sim}{K}$, equation (6) becomes

$$[\underset{\sim}{C} - k^2\underset{\sim}{K}^*]\underset{\sim}{u} = \underset{\sim}{0} \qquad (7)$$

k, the wave number, is different for each of the various layers, so the eigenvalue problem (7) must be solved. The impinging wave (shear or Rayleigh) causes stresses at the boundary. The idea is to apply oppositional forces to effectively nullify them. For the shear wave example, these stresses are proportional to both the displacements at the boundary and to the wave numbers (eigenvalues) solved in equation (7). This enables the authors to find the matrix, $\underset{\sim}{R}$, which relates the nullifying forces to be applied at the boundary to the displacements at the boundary. $\underset{\sim\sim}{Ru}$ serves as the boundary force contribution to the finite-element equations of the interior.

Although suitable for transmitting periodic, surface waves, this method is highly restrictive. First, the boundary terms are frequency dependent, meaning that one cannot generally perform a transient analysis in the time domain. If the governing equations of the interior region are <u>linear</u>, one can perform a transient analysis in the frequency domain. This approach, however, raises several questions. What are the costs of doing frequency-domain analysis, compared to doing an analysis in the time domain? Secondly, how effective can this approach be, if the interior equations are <u>nonlinear</u>? This technique is also restrictive in that only shear waves or Rayleigh waves can be transmitted. Other boundary methods are broader in scope. Finally, this transmitting boundary is more difficult to implement than are most other boundary schemes.

Smith[55] proposed the adding together of wave solutions having different boundary conditions, in order to eliminate reflections. In a

one-dimensional example, the reflection of a wave striking a free boundary cancels that of a wave striking a fixed boundary, when they are added to each other.

Two lubricated-rigid boundary conditions are imposed for two dimensions:

$$\left.\begin{aligned} u_1 &= 0 \\ \tau &= 0 \end{aligned}\right\} , \tag{8}$$

and

$$\left.\begin{aligned} u_2 &= 0 \\ \sigma &= 0 \end{aligned}\right\} . \tag{9}$$

u_1 and u_2 are the respective normal and tangential displacements at the boundary, and σ and τ are the respective normal and tangential stresses there. For the three-dimensional case, the plane of the boundary is either lubricated or fixed, and the normal displacement is conversely fixed or left free.

Smith demonstrates that this boundary method eliminates all reflections, regardless of frequency or angle of incidence. It also handles all types of waves, including body, Rayleigh or Love waves. The only drawback to this method, and it is an inescapable one, is that two solutions are required for each possible wave reflection. For example, if we have a two-dimensional corner, then two solutions for each boundary side are needed. The problem must be solved four times to cancel the wave reflections. Likewise, if there is enough time for a wave to reflect from one boundary, strike another, and then return, then the number of calculations must be doubled. Therefore, 2^n is equal to the

number of complete solutions, where n is the number of possible reflections. If one performs the calculations over a long period of time, the number of required solutions increases very rapidly. This method does not appear as attractive as other approaches, except for one-dimensional problems and problems with very short, characteristic times.

Cundall, et al.,[40] have recently introduced a cost-saving scheme that attempts to retain the advantages of the Smith boundary. Their idea is to set up a small boundary region, in which equations are formed and solved for each of the above-mentioned boundary conditions. Smith's idea of adding the two solutions is implemented at every fourth time step. Thus, the boundary area, which is four elements deep, requires two solutions at each step, while the interior region needs only one solution.

The authors encountered some practical difficulties with this incremental approach. They solved them by using two pairs of constant stress and constant velocity conditions at the boundary, instead of the fixed and free conditions that Smith presented. Wave-reflection theory clearly shows how the reflections are eliminated in the Smith model by adding the "fixed" and "free" solutions. With constant velocity, and stress boundary conditions, it is not obvious as to how the reflections are controlled. The authors, however, have observed that these conditions perform well and reduce the "numerical shocks" that are caused by the adding of the fixed and free boundary solutions.

The main question about this incremental ("superposition") approach is its practicability. It effectively adds a layer of eight elements, which have to be formed and calculated at each step. In addition, the

constant velocity, and constant stress conditions, at the boundary must be stored for all times. It would be cheaper, and less cumbersome, to simply add a layer of eight elastic elements and to employ either the viscous, or paraxial, boundary conditions. However, the comparative accuracy of the superposition method and the latter schemes is unknown.

Tseng and Robinson[54] and Robinson[51] investigated wave propagation using another transmitting boundary proposal. This method relies on the separation of S and P waves by the potentials, ϕ and ψ. First, the transmitting condition for two-dimensional, plane waves is obtained. For example,

$$\phi_t + c_d \phi_x = 0 \quad . \tag{10}$$

Then a correction is added for cylindrical waves. Although equations (10) are written in terms of potentials, they appear to be similar to the equations of the first paraxial approximation[42,83] shown below.

$$u_t + c_d u_x = 0 \quad . \tag{11}$$

Equations (10) and (11) are derived for waves oriented in the positive-x direction.

The authors demonstrate the method's superior transmission of cylindrical waves but, so far, the benefit does not appear to be significant enough to clearly justify this boundary's use over other techniques.

Still another idea was proposed by Isenberg[17] and later by Zhen-peng, Pai-puo, and Yi-fan.[58] At the n^{th} time step, they use the known displacements of all points on or near the boundary to predict

the boundary's motion at the (n+1) step. The rest of the displacements in the interior are then solved.

In order to develop a predictor for the boundary, one needs the frequency and wave number of the impinging wave. In this way, this method could be effective for steady-state problems. One would probably have to resort to Fourier analysis to model the transient waves.

Isenberg[45] suggested an alternative, frequency-independent, predictor method. In this proposal, the preliminary step would be to apply unit forces at the nodes adjacent to the boundary, and to calculate the boundary's reaction to each of these loads. This information would be stored for use during the main calculation. The effects of the various nodal loadings are scaled and then superimposed on each other, in order to predict the boundary's response for the next time step.

No one has, as yet, implemented this idea, so its feasibility and accuracy are unknown. It has only recently come to attention and would seem to deserve an investigation. Apparently, a significant effort to set up such a boundary is required, but the concept may have the potential to solve infinite-domain problems.

Researchers[41,56] have also investigated the boundary integral method, where the interior displacements of a region are found by evaluating integrals along the region's boundary. The boundary is discretized into segments, and the integrations are performed numerically. As yet, the technique has not been completely satisfactory. Not only does taking integrals along the boundary depend upon the linearity of the interior equations, it also leads to nonsymmetric matrices. For large problems, it could be computationally expensive.

In still another attempt to simulate the effects of wave radiation, analysts[25] have incorporated material damping into their models. Alternately, one could employ numerical damping[70] to account for the transmitted energy. While these damping procedures are conceivable, how one could practically implement them is not clear. Just how much damping should be put into the system, and where should it be applied? Can this damping discriminate the effects of wave radiation from the actual physical dissipation taking place within the model?

A systematic approach to the usage of damping in various systems is not available. Luco, et al.,[25] demonstrated some of the pitfalls of this method. They compared analytical solutions of wave propagation to the calculations of a finite element model which used some plausible damping estimates. In general, the material damping did a poor job of duplicating the radiation effect. At this stage, the proper application of damping to account for radiation effects seems to be more of an art than a science.

Another relatively simple idea, which was proposed by Haupt,[15] can be applied for repetitive analyses of certain systems which can be split into interior and exterior parts. The interior is altered for each analysis (e.g., each interior geometry or load history could be different), but the exterior region remains constant. One initially sets up an extensive mesh of the entire system, but then he condenses those degrees-of-freedom that are in the outlying region. Each successive problem could be solved by utilizing just the small interior mesh and the force contribution from the condensed equations. This substructuring method reduces the computational expense for these special cases.

Finally, investigators[9,12,19] have experimented with extensive meshes, and have determined where the boundary should be placed in order to produce acceptably small reflections. Day[12] found that by successively increasing the size of outlying elements by a factor of 1.1, he could prevent undesirable reflections. This growth factor of 1.1 provides some help in reducing the number of required elements, but the computational costs remain prohibitive, especially for three-dimensional calculations.

In review, each of the proposed transmitting boundary schemes has been shown to be effective for selected wave problems. The basic criticism of all of these methods is that, to one degree or another, none has been extensively verified. For example, there are available few comparisons between the results of using a truncated mesh having a transmitting boundary and of calculations with an extended mesh. Some of these ideas, such as the viscous damping mechanism, have been incorporated into programs for other purposes.[11,27,30,34] This has generated a degree of qualitative confidence in their use, but their accuracy is not well known.

III. ORGANIZATION

The object of this study is to develop a transmitting boundary which can be applied to transient analysis in the time domain. It is also desirable that this boundary be applicable to as many situations where nonlinear behavior is important, as possible.

In Chapter 2, theories of some absorbing boundaries are outlined. Since the boundaries are supposed to remove energy from the system, we discuss several of the forms which these mechanisms might take. Next,

assorted, transmitting boundary ideas are analyzed. The basic paraxial idea[83] is studied in a different light, and is developed and modified to improve its energy-absorbing character. The viscous-boundary proposals are also presented. Through the equilibrium equations, their underlying precepts are shown to be equivalent to those of the paraxial boundary. The unified- ("optimized-") version of the viscous boundary is also set forth. The various boundary methods are then compared, using standard, wave-reflection analysis. We also discuss the boundaries' ability to transmit Rayleigh waves and suggest some special, frequency-independent, Rayleigh-wave boundaries. Lastly, the extension of silent boundaries to spherical and cylindrical coordinates is considered.

Chapter 3 primarily deals with the numerical implementation of the boundary schemes discussed in Chapter 2. In Sections I and II, we point out some of the practical considerations of implementing a silent boundary. The boundary methods should be designed so that the practical limitations, such as the time-step size, are no greater than are those which other considerations impose.

We then propose some procedures which facilitate the paraxial method's practicality for finite elements. These include the "upwinding" of certain paraxial terms and a nodal assembling procedure to eliminate a finite-element "interfacing" effect. In the next section, numerical stability limits are determined for the various boundaries. Lastly, the numerical procedures are verified with a singular-loading problem, Lamb's problem.

Chapter 4 contains most of the extensive results and comparisons of the boundary methods. These examples include a radial-dilatational pulse, horizontal- and vertical-pulse loadings, and a Rayleigh-wave excitation. The working of these problems illustrates the primary strengths and drawbacks of the various methods and leads to some improvements, such as the application of numerical damping.

In the final chapter, we present our conclusions and proffer recommendations in the use of the silent boundaries.

CHAPTER 2

I. INTRODUCTION

In these next Chapters, 2, 3, and 4, we investigate, implement, and compare several silent-boundary methods. As noted in Chapter 1, we are seeking a suitable boundary for nonlinear, transient, finite-element analysis. This rules out most of the transmitting boundary ideas previously discussed. The exceptions are the paraxial, superposition, and viscous boundary proposals.

The parameters of the transmitting boundary should be not only independent of frequency, they also should employ only information from nearby regions of the mesh. These requirements allow the interior mesh equations to be nonlinear; only the outer-region equations (those near the silent boundary) need remain linear. In addition, it is desirable to have the method be easily implemented and understood. We would also hope to establish a stability criterion and a measure of the boundary's accuracy. Lastly, the boundary should be capable of handling all types of incoming waves, and of proving its reliability over a wide range of different conditions. For example, it should place no significant restriction on the material properties which are being modeled. All of these issues are explored in this chapter.

In Section II, we consider basic energy requirements and some general forms which transmitting boundaries might take. We then move on to a few specific proposed boundaries. In Sections III, IV, and V, their fundamental precepts are stated and analyzed. Some tentative

comparisons are established among the different boundaries, and in the next chapters, we investigate their performance numerically.

II. ENERGY FORMS

In constructing an absorbing boundary, the absorbing mechanism must be made dissipative. In other words, the change of total energy in the system with respect to time (excluding the effect of work done on the system) must be negative.

$$\frac{d}{dt}\,(\text{energy}) \;<\; 0 \quad . \tag{1}$$

One can meet this energy condition in many different ways. Here, we present some general energy forms for the wave equation and the equations of elasticity.

In the simplest example, one adds a boundary contribution term, $h(x,t)$, to the one-dimensional wave equation; thus

$$\left.\begin{aligned} \rho u_{tt} - \rho c^2 u_{xx} + h(x,t) &= 0 \quad , \\ h(x,t) &= 0 \quad \text{when} \quad x_1 \le x < x_b \quad , \\ h(x,t) &\neq 0 \quad \text{when} \quad x_b \le x \le x_2 \quad ; \end{aligned}\right\} \tag{2}$$

c = the wavespeed, ρ = density, x = the spatial variable, and t = time. This one-dimensional system is depicted in Figure 1, using the elastic bar as an example. If we multiply equation (2) by u_t, integrate over the interval x_1 to x_2, and integrate the second term by parts, then

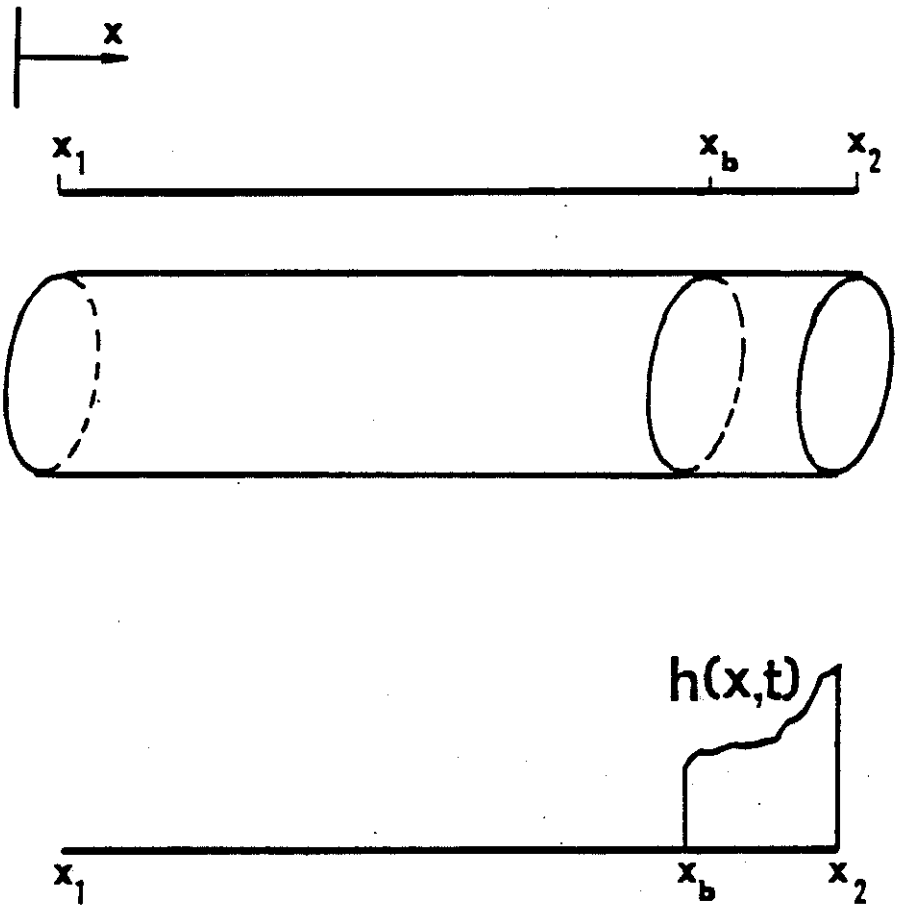

Figure 1. Simple absorbing boundary for one-dimensional wave propagation.

$$\frac{\partial}{\partial t}\left[\frac{1}{2}\int_{x_1}^{x_2}\rho u_t^2\,dx + \frac{1}{2}\int_{x_1}^{x_2}\rho c^2(u_x)^2 dx\right] =$$

$$\rho c^2(u_t u_x)\Big|_{x_1}^{x_2} - \int_{x_b}^{x_2} h(x,t)u_t\,dx \quad , \tag{3a}$$

or

$$\frac{\partial}{\partial t}[KE + PE] = (c^2\rho u_t u_x)\Big|_{x_1}^{x_2} - \int_{x_b}^{x_2} h(x,t)u_t\,dx \quad . \tag{3b}$$

KE = kinetic energy, PE = potential energy.

In equation (3), either the displacements, u, or the stresses, u_x, are prescribed at the boundaries. If no external forces do work at the boundaries ($x = x_1$ or $x = x_2$), then either u or u_x must equal zero. Having u be equal to zero for all time implies that the velocities, u_t, also equal zero for all time. With no work being done on the system, $u_t = 0$, or $u_x = 0$ at all times. Thus, the first term on the right equals zero. The second term on the right determines whether the total energy is decreasing with time. The energy requirement dictates that

$$\int_{x_b}^{x_2} h(x,t)u_t\,dx > 0 \quad . \tag{4}$$

Letting h be proportional to u_t in the boundary region is an obvious choice for satisfying equation (4), but some alternatives exist. For example, if h is proportional to $-u_{txx}$, then having

$$\int_{x_1}^{x_2} -u_{txx}u_t dx = -(u_{tx}u_t)\Big|_{x_1}^{x_2} + \int_{x_2}^{x_b} u_{tx}u_{tx}\, dx > 0 \qquad (5a)$$

also satisfies equation (4). The integrated term involving $u_{tx}u_t$ vanishes for reasons noted above. Similarly, by letting h be proportional to u_{tx},

$$\left.\begin{aligned} &\int_{x_b}^{x_2} u_{tx}u_t\, dx = \frac{1}{2}\, u_t^2\Big|_{x_b}^{x_2} > 0 \\ &\text{if} \\ &\qquad |u_t(x_2)| > |u_t(x_b)| \quad . \end{aligned}\right\} \qquad (5b)$$

In this case, h becomes a convective term, which passes energy in the positive-x direction and eventually out of the system. These choices have physical interpretation. The taking of h as proportional to u_t, or u_{txx}, corresponds to absolute damping and strain rate damping, respectively.

Analyzing the boundary problem from this energy standpoint exposes many possible avenues of attack. It does not indicate, however, whether these boundary terms are removing all of the energy as it impinges on the boundary. For this, we make a detailed examination of the paraxial and viscous models.

III. THEORY OF PARAXIAL BOUNDARIES

In this section, we present the paraxial boundary from a different viewpoint than did Clayton and Engquist,[39] who originally applied the

paraxial equations to a silent boundary. We believe that our alternate approach gives better insight as to how and why the paraxial method may work. Also, a stability analysis which was performed indicates that the paraxial equations must be modified from their original form.

In the derivation herein, the paraxial boundary idea is best introduced by means of the one-dimensional wave equation,

$$u_{tt} - c^2 u_{xx} = 0 \quad , \quad \begin{pmatrix} -\infty < x < \infty \\ 0 \leq t < \infty \end{pmatrix} \quad . \tag{6}$$

It has the solution

$$u = p(x - ct) + q(x + ct) \quad , \tag{7}$$

in which $u = u(x,t)$, and x, t, and c are the same as they are in equation (2); $p(x - ct)$ represents an arbitrarily-shaped wave moving in the positive-x direction, q is another arbitrarily-shaped wave moving in the negative-x direction. To change the equation into that of a paraxial boundary, we seek a similar, partial differential equation whose solution only allows waves to travel in the positive-x direction. This equation will then govern a boundary region which only transmits waves in the positive-x direction.

Several partial differential equations produce this solution, $u = p(x - ct)$. One of these was presented by Clayton and Engquist:[39]

$$\left.\begin{aligned} u_t + cu_x &= 0 \quad , \qquad \begin{pmatrix} -\infty < x < \infty \\ 0 \le t < \infty \end{pmatrix} \quad , \\ u(x,0) &= u_0(x) \quad , \end{aligned}\right\} \tag{8}$$

$$\text{solution:} \quad u = u_0(x - ct) \quad .$$

However, we choose to analyze another, related equation with this same solution:

$$\left.\begin{aligned} u_{tt} + cu_{tx} &= 0 \quad , \qquad \begin{pmatrix} -\infty < x < \infty \\ 0 \le t < \infty \end{pmatrix} \quad , \\ u(x,0) &= u_0(x) \quad , \\ u_t(x,0) &= v_0(x) \quad , \end{aligned}\right\} \tag{9}$$

$$\text{solution:} \quad u = \int_0^t v(x - c\xi)\, d\xi + u_0(x) \quad .$$

Waves, $p(x - ct)$, which impinge on a medium governed by equations (8) or (9), continue to propagate through the medium. This is established by setting $u_0(x) = p(x)$ and $v_0(x) = -cp'(x)$. Unlike equation (8), equation (9) is dimensionally consistent with the original wave equation. It also more closely resembles the paraxial equations that we intend to use for two- and three-dimensional problems. In these more complicated cases, we study equation (9) for the purpose of developing the numerical technique.

For the one-dimensional example, we have all of the solutions to the differential equation, so we can select the correct paraxial equation. Multi-dimensional equations, however, often do not have known solutions. This necessitates a different approach, whereby the equations of the boundary regions are constructed to accommodate one-directional, plane, harmonic waves. For the purposes of simplicity, this different method is illustrated with the one-dimensional example.

For most practical problems, the boundary conditions to equation (6) are such that solutions are of the form:

$$u = A \exp [i(k_x x - \omega t)] \quad , \tag{10}$$

in which k_x = the wave number (2π/wavelength) and ω = the frequency of the wave. One example of such a boundary condition is the requirement that u be finite, as x goes to infinity. This precludes either hyperbolic or linearly increasing solutions ($u = Ax + B$) for equation (6).

If we substitute equation (10) into equation (6), then

$$(-\omega^2 + k_x{}^2 c^2) = 0 \quad ,$$

or

$$\frac{k_x}{\omega} = \pm \frac{1}{c} \quad . \tag{11}$$

In equation (10), if k_x/ω is positive, then u represents only positive-x-traveling waves. We now seek a differential equation which, upon substitution of the desired solution represented by equation (10), produces

$$\frac{k_x}{\omega} = + \frac{1}{c} \quad .$$

It happens that both equations (8) and (9) meet this condition. They each possess the harmonic solution (9) and have the positive k_x/ω requirement. For applications to higher dimensions, we now utilize this procedure in the development of other differential equations which have only positive-x-traveling wave solutions.

IV. TWO-DIMENSIONAL SCALAR WAVE EQUATION

In this section, as an introduction to the development of a silent boundary for the equations of elasticity, we present an analysis of the two-dimensional, scalar-wave equation. Having just one unknown, it is:

$$\left.\begin{aligned} u_{tt} - c^2(u_{xx} + u_{zz}) &= 0 \quad , \qquad \begin{pmatrix} -\infty < x < \infty \\ -\infty < z < \infty \end{pmatrix} \quad , \\ u &= f(x,z) \quad \text{at} \quad t = 0 \quad , \\ u_t &= g(x,z) \quad \text{at} \quad t = 0 \quad . \end{aligned}\right\} \qquad (0 \le t < \infty) \quad , \qquad (12)$$

Once again, the goal is to find a differential equation which allows only positively moving waves. To this end, Claerbout[83] developed a "paraxial" method. If the solution of equation (12) has the form,

$$u = A \exp\left[i(k_x x + k_z z - \omega t)\right] \quad , \qquad (13)$$

then (12) becomes

$$\omega^2 - c^2 k_x^{\,2} - c^2 k_z^{\,2} = 0 \quad . \qquad (14)$$

Factoring equation (14),

$$\left[ck_x - \omega\sqrt{1 - \left(\frac{ck_z}{\omega}\right)^2}\right]\left[ck_x + \omega\sqrt{1 - \left(\frac{ck_z}{\omega}\right)^2}\right] = 0 \quad . \qquad (15)$$

Equation (15) furnishes the two "roots" of ck_x/ω in equation (14); $(ck_x/\omega)_1$ is positive, $(ck_x/\omega)_2$ is negative (with $ck_z/\omega < 1$). If we substitute the positive ck_x/ω root into equation (13), then this equation represents waves traveling in the positive-x direction. Conversely, a negative ck_x/ω signifies negatively traveling waves.

We consider the positive-ck_x/ω relation,

$$\frac{ck_x}{\omega} - \sqrt{1 - \left(\frac{ck_z}{\omega}\right)^2} = 0 \quad . \tag{16}$$

Expanding the square root term, equation (16) becomes

$$\frac{ck_x}{\omega} - \left[1 - \frac{1}{2}\left(\frac{ck_z}{\omega}\right)^2 + 0\left(\frac{ck_z}{\omega}\right)^4\right] = 0 \quad . \tag{17}$$

We can determine the differential equation which corresponds to the first three terms of equation (17) by inspection of equation (13) and its derivatives:

$$u_{tt} + cu_{tx} - \frac{c^2}{2} u_{zz} = 0 \quad . \tag{18}$$

Equation (18) has a solution in the form of equation (13), but with ck_x/ω defined by the first three terms of equation (17). Further expansions of equation (17) to higher orders in (ck_z/ω) have been carried out by Clayton and Engquist.[39]

Equation (18) represents an approximation of an equation which would only transmit positive-x-directed waves. The nature of this approximation is shown with the help of Figure 2. The plane harmonic

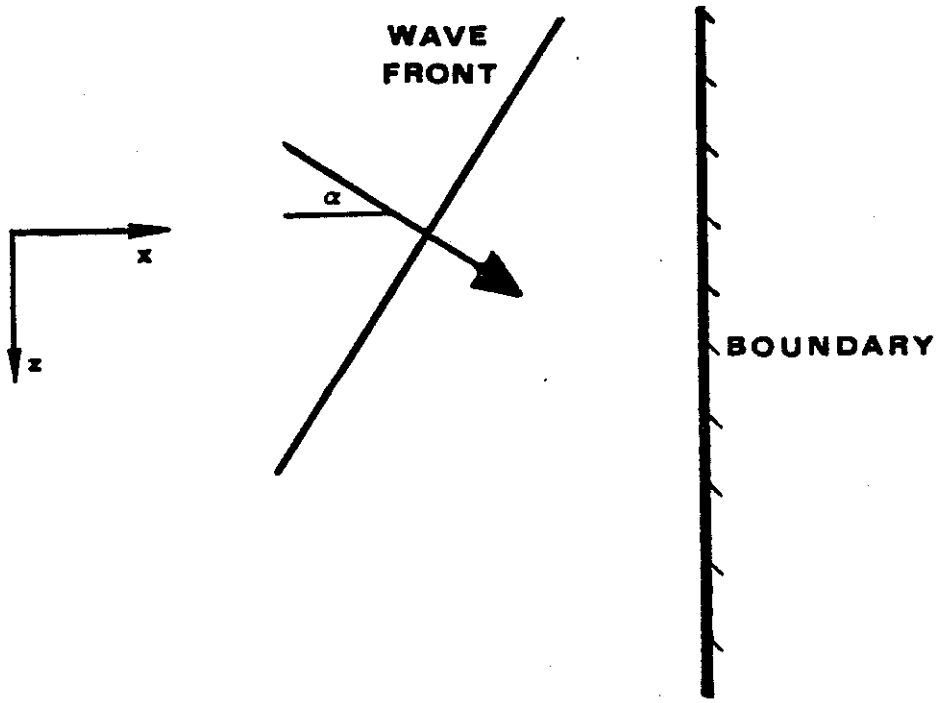

Figure 2. Orientation of wave used in the scalar-wave, and elasticity analysis.

wave illustrated in this figure has the form:

$$u = A \exp\left[i\left(\frac{\omega}{c}\cos\alpha\ x + \frac{\omega}{c}\sin\alpha\ z - \omega t\right)\right] \quad .$$

In this case, $ck_z/\omega = \sin\alpha$, where α is the angle of incidence. The first three terms of equation (17) best approximate equation (16) when ck_z/ω is small. Hence, we expect the differential equation (18) to perform best with small values of α, that is, with waves which are nearly normal to the boundary. As α grows larger, the paraxial approximation is less effective in transmitting positively traveling waves.

V. BOUNDARY APPROXIMATIONS FOR TWO-DIMENSIONAL, LINEAR ELASTICITY

The analysis using the elasticity equations follows along lines similar to the previous cases. We are determining here the appropriate, paraxial-boundary equations for the following equation of elasticity for plane strain, which is illustrated in Figure 3.

$$\underset{\sim}{u}_{tt} - \underset{\sim}{E}_{11}c^2\underset{\sim}{u}_{xx} - \underset{\sim}{E}_{12}c^2\underset{\sim}{u}_{xz} - \underset{\sim}{E}_{22}c^2\underset{\sim}{u}_{zz} = \underset{\sim}{0} \quad , \tag{19}$$

where

$$\underset{\sim}{u} = \begin{Bmatrix} u \\ w \end{Bmatrix} \quad , \qquad \underset{\sim}{E}_{11} = \frac{1}{c^2}\begin{bmatrix} c_d^2 & 0 \\ 0 & c_s^2 \end{bmatrix} \quad ,$$

$$\underset{\sim}{E}_{12} = \frac{1}{c^2}(c_d^2 - c_s^2)\begin{bmatrix} 0 & 1 \\ 1 & 0 \end{bmatrix} \quad , \qquad \underset{\sim}{E}_{22} = \frac{1}{c^2}\begin{bmatrix} c_s^2 & 0 \\ 0 & c_d^2 \end{bmatrix} \quad ;$$

u and w are the two-dimensional displacements which act in the respective x and z coordinate directions shown in Figure 3; c_d = the dilatational velocity and c_s = the shear velocity; c, which has the dimensions of a wave speed, is included in equation (19) in order to render several quantities as dimensionless. The equations and their solutions are <u>independent</u> of c, as is seen in the way equation (19) is formed; t represents the time derivative.

Solutions to (19) are assumed to be of the form:

$$\left.\begin{aligned} u &= U \exp\left[i(k_x x + k_z z - \omega t)\right] \quad , \\ w &= W \exp\left[i(k_x x + k_z z - \omega t)\right] \quad . \end{aligned}\right\} \tag{20}$$

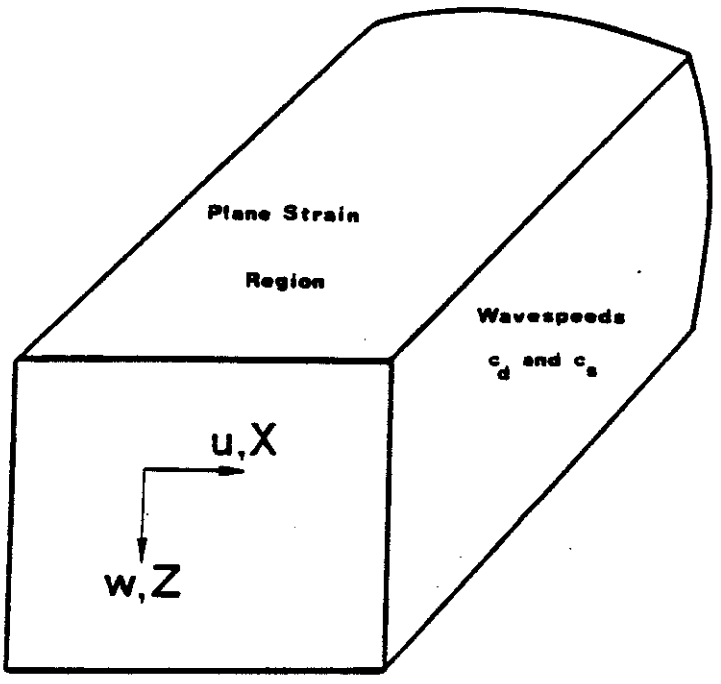

Figure 3. Displacements and coordinate axes utilized in the plane-strain, elastic problems.

After substituting equation (20) into (19), we find that

$$[\underset{\sim}{I}\omega^2 - \underset{\sim}{E}_{11}k_x^2c^2 - \underset{\sim}{E}_{12}k_xk_zc^2 - \underset{\sim}{E}_{22}k_z^2c^2]\begin{Bmatrix} U \\ W \end{Bmatrix} = 0 \quad . \qquad (21)$$

Equations (20) and (21) describe plane waves propagating in the elastic medium under consideration. In the first of three analogies with the scalar-wave example, we examine the "roots" of ck_x/ω, which are obtained by the approximate factoring of equation (21).

$$\left[\underset{\sim}{I}\,\frac{k_x c}{\omega} - \underset{\sim}{B}_1 - \underset{\sim}{B}_2\,\frac{k_z c}{\omega} - \underset{\sim}{B}_3\left(\frac{k_z c}{\omega}\right)^2\right] \cdot$$

$$\left[\underset{\sim}{I}\,\frac{k_x c}{\omega} - \underset{\sim}{B}_4 - \underset{\sim}{B}_5\,\frac{k_z c}{\omega} - \underset{\sim}{B}_6\left(\frac{k_z c}{\omega}\right)^2\right]\begin{Bmatrix} U \\ W \end{Bmatrix} = \underset{\sim}{0} \quad . \tag{22}$$

We are solving for the matrices $\underset{\sim}{B}_j$. In equation (22), either of the two roots, ck_x/ω, satisfies equation (21). If we substitute the first root,

$$\underset{\sim}{I}\left(\frac{k_x c}{\omega}\right) = \underset{\sim}{B}_1 + \underset{\sim}{B}_2\,\frac{k_z c}{\omega} + \underset{\sim}{B}_3\left(\frac{k_z c}{\omega}\right)^2 \quad , \tag{23}$$

into equation (21), we obtain:

$$\left[\underset{\sim}{I} - \underset{\sim}{E}_{11}\underset{\sim}{B}_1^{\,2}\right]\left(\frac{ck_z}{\omega}\right)^0 + \left[-\underset{\sim}{E}_{12}\underset{\sim}{B}_1 - \underset{\sim}{E}_{11}\underset{\sim}{B}_1\underset{\sim}{B}_2 - \underset{\sim}{E}_{11}\underset{\sim}{B}_2\underset{\sim}{B}_1\right]\left(\frac{ck_z}{\omega}\right)^1$$

$$+ \left[-\underset{\sim}{E}_{22} + \underset{\sim}{E}_{11}\underset{\sim}{B}_2 - \underset{\sim}{E}_{11}\underset{\sim}{B}_1\underset{\sim}{B}_3 - \underset{\sim}{E}_{11}\underset{\sim}{B}_3\underset{\sim}{B}_1 - \underset{\sim}{E}_{11}\underset{\sim}{B}_2^{\,2}\right]\left(\frac{ck_z}{\omega}\right)^2 \tag{24}$$

$$+ \left[-\underset{\sim}{E}_{12}\underset{\sim}{B}_3 - \underset{\sim}{E}_{11}\underset{\sim}{B}_2\underset{\sim}{B}_3 - \underset{\sim}{E}_{11}\underset{\sim}{B}_3\underset{\sim}{B}_2\right]\left(\frac{ck_z}{\omega}\right)^3 + \left[-\underset{\sim}{E}_{11}\underset{\sim}{B}_3^{\,2}\right]\left(\frac{ck_z}{\omega}\right)^4 = 0 \quad .$$

Setting the coefficients of $(ck_z/\omega)^0$ equal to zero,

$$\underset{\sim}{B}_1 = \pm\begin{bmatrix} \frac{1}{c_d} & 0 \\ 0 & \frac{1}{c_s} \end{bmatrix} c \quad . \tag{25}$$

A second analogy to the scalar-wave case is that the positive root of $\underset{\sim}{B}_1$ leads to a positive-x-direction, paraxial boundary. Now setting the $(ck_z/\omega)^1$ and $(ck_z/\omega)^2$ coefficients equal to zero,

$$\underset{\sim}{B}_2 = -(c_d - c_s)\begin{bmatrix} 0 & \frac{1}{c_d} \\ \frac{1}{c_s} & 0 \end{bmatrix} , \tag{26}$$

$$\underset{\sim}{B}_3 = -\begin{bmatrix} c_s - \frac{c_d}{2} & 0 \\ 0 & c_d - \frac{c_s}{2} \end{bmatrix}\frac{1}{c} . \tag{27}$$

The substitution [from equation (22)] of the second root of (ck_z/ω) into equation (21) produces

$$\underset{\sim}{B}_4 = -\underset{\sim}{B}_1 , \quad \underset{\sim}{B}_5 = \underset{\sim}{B}_2 , \quad \text{and} \quad \underset{\sim}{B}_6 = -\underset{\sim}{B}_3 . \tag{28}$$

If one puts these $\underset{\sim}{B}$ matrices into equation (22) and multiplies the terms, equation (21) and some third and fourth order terms of (ck_z/ω) result. The approximate factoring given by equation (22) is most accurate for small values of ck_z/ω. (Recall that $ck_z/\omega = \sin \alpha$, where α = the angle of wave incidence.) From this analysis, it can also be seen that $\underset{\sim}{B}_1$ is the zeroth order term and, therefore, is the most important part of the paraxial approximation. The inclusion of $\underset{\sim}{B}_2$ and $\underset{\sim}{B}_3$ renders closer agreement between the elasticity equations (21) and the factored paraxial equations (22).

If we use equation (23) with the calculated $\underset{\sim}{B}$ matrices, then rearrange all of the terms, we find that:

$$\left[-\begin{bmatrix} 1 & 0 \\ 0 & 1 \end{bmatrix} \omega^2 + \begin{bmatrix} c_d & 0 \\ 0 & c_s \end{bmatrix} k_x \omega + (c_d - c_s) \begin{bmatrix} 0 & 1 \\ 1 & 0 \end{bmatrix} k_z \omega \right.$$

$$\left. + \begin{bmatrix} c_d \left(c_s - \frac{c_d}{2} \right) & 0 \\ 0 & c_s \left(c_d - \frac{c_s}{2} \right) \end{bmatrix} k_z^2 \right] \begin{Bmatrix} U \\ W \end{Bmatrix} = \underset{\sim}{0} \quad . \qquad (29)$$

The third analogy to the scalar-wave case is that the paraxial differential equations can now be derived. If the harmonic solution (20) is substituted into the desired differential equation, then equation (29) is the product. By this inverse logic, the desired equation is:

$$\begin{bmatrix} 1 & 0 \\ 0 & 1 \end{bmatrix} \underset{\sim}{u}_{tt} + \begin{bmatrix} c_d & 0 \\ 0 & c_s \end{bmatrix} \underset{\sim}{u}_{tx} + (c_d - c_s) \begin{bmatrix} 0 & 1 \\ 1 & 0 \end{bmatrix} \underset{\sim}{u}_{tz}$$

$$- \begin{bmatrix} c_d \left(c_s - \frac{c_d}{2} \right) & 0 \\ 0 & c_s \left(c_d - \frac{c_s}{2} \right) \end{bmatrix} \underset{\sim}{u}_{zz} = 0 \quad . \qquad (30)$$

Equation (30) produces approximately the same harmonic wave solution in the positive-x direction as the elasticity equations (19) do. If one employs equation (28), the paraxial equations for the negative-x direction are:

$$\begin{bmatrix} 1 & 0 \\ 0 & 1 \end{bmatrix} \underset{\sim}{u}_{tt} - \begin{bmatrix} c_d & 0 \\ 0 & c_s \end{bmatrix} \underset{\sim}{u}_{tx} - (c_d - c_s) \begin{bmatrix} 0 & 1 \\ 1 & 0 \end{bmatrix} \underset{\sim}{u}_{tz}$$

$$- \begin{bmatrix} c_d \left(c_s - \frac{c_d}{2} \right) & 0 \\ 0 & c_s \left(c_d - \frac{c_s}{2} \right) \end{bmatrix} \underset{\sim}{u}_{zz} = 0 \quad . \qquad (31)$$

Clayton and Engquist[39] derived equations which were the same as those above, except for a change of sign in their $\underset{\sim}{B}_2$ and $\underset{\sim}{B}_4$ matrices. They did this through a method based on Fourier analysis. It was not clear how Fourier analysis would lead to one-directional equations. It seems more logical to derive the paraxial boundary equations on the basis of transmitting harmonic waves. The two analyses, however, are parallel and lead to nearly the same results.

We can immediately identify some characteristics of equations (30) and (31). These equations have the same mass term as the original elasticity equations. The other paraxial terms, however, bear little resemblance to those of their parent equations. $\underset{\sim}{u}_{tx}$ and $\underset{\sim}{u}_{tz}$ are ostensibly damping-like terms, but an energy analysis reveals that these terms are not necessarily dissipative. The $\underset{\sim}{u}_{zz}$ term constitutes a transverse stiffness which can be negative if

$$c_s < \frac{c_d}{2} \quad . \tag{32}$$

Because this derivation is based on the kinematics of the desired solution, it is difficult to understand what makes the paraxial equations represent a boundary that absorbs energy. This is with the exceptions of the $\underset{\sim}{u}_{tx}$ and $\underset{\sim}{u}_{tt}$ terms, which were also found in the paraxial equations for the one- and two-dimensional scalar-wave cases and were shown to be dissipative (under certain conditions) in Section II. In fact, the negative-stiffness term raises the question of whether the paraxial equations are stable.

In three dimensions, the paraxial equations are derived by the same method. The three-dimensional elasticity equations are:

$$\underset{\sim}{u}_{tt} - \underset{\sim}{E}_{11}c^2\underset{\sim}{u}_{xx} - \underset{\sim}{E}_{22}c^2\underset{\sim}{u}_{yy} - \underset{\sim}{E}_{33}c^2\underset{\sim}{u}_{zz} - \underset{\sim}{E}_{12}c^2\underset{\sim}{u}_{xy}$$

$$- \underset{\sim}{E}_{13}c^2\underset{\sim}{u}_{xz} - \underset{\sim}{E}_{23}c^2\underset{\sim}{u}_{yz} = \underset{\sim}{0} \quad , \tag{33}$$

where

$$\underset{\sim}{E}_{11} = \frac{1}{c^2}\begin{bmatrix} c_d^2 & 0 & 0 \\ 0 & c_s^2 & 0 \\ 0 & 0 & c_s^2 \end{bmatrix} \quad , \quad \underset{\sim}{E}_{22} = \frac{1}{c^2}\begin{bmatrix} c_s^2 & 0 & 0 \\ 0 & c_d^2 & 0 \\ 0 & 0 & c_s^2 \end{bmatrix} \quad ,$$

$$\underset{\sim}{E}_{33} = \frac{1}{c^2}\begin{bmatrix} c_s^2 & 0 & 0 \\ 0 & c_s^2 & 0 \\ 0 & 0 & c_d^2 \end{bmatrix} \quad , \quad \underset{\sim}{E}_{12} = \frac{\left(c_d^2 - c_s^2\right)}{c^2}\begin{bmatrix} 0 & 1 & 0 \\ 1 & 0 & 0 \\ 0 & 0 & 0 \end{bmatrix} \quad ,$$

$$\underset{\sim}{E}_{13} = \frac{c_d^2 - c_s^2}{c^2}\begin{bmatrix} 0 & 0 & 1 \\ 0 & 0 & 0 \\ 1 & 0 & 0 \end{bmatrix} \quad , \quad \underset{\sim}{E}_{23} = \frac{\left(c_d^2 - c_s^2\right)}{c^2}\begin{bmatrix} 0 & 0 & 0 \\ 0 & 0 & 1 \\ 0 & 1 & 0 \end{bmatrix} \quad .$$

When, as before, we assume an harmonic solution:

$$\begin{aligned} u &= A \exp\left[i(k_x x + k_y y + k_z z - \omega t)\right] \quad , \\ v &= B \exp\left[i(k_x x + k_y y + k_z z - \omega t)\right] \quad , \\ w &= C \exp\left[i(k_x x + k_y y + k_z z = \omega t)\right] \quad . \end{aligned} \tag{34}$$

Then, by substituting it into equation (33) and solving for the roots of ck_x/ω, we find

$$\begin{bmatrix} 1 & 0 & 0 \\ 0 & 1 & 0 \\ 0 & 0 & 1 \end{bmatrix} \underset{\sim}{u}_{tt} + \begin{bmatrix} c_d & 0 & 0 \\ 0 & c_s & 0 \\ 0 & 0 & c_s \end{bmatrix} \underset{\sim}{u}_{tx} + (c_d - c_s) \begin{bmatrix} 0 & 0 & 1 \\ 0 & 0 & 0 \\ 1 & 0 & 0 \end{bmatrix} \underset{\sim}{u}_{tz}$$

$$+ (c_d - c_s) \begin{bmatrix} 0 & 1 & 0 \\ 1 & 0 & 0 \\ 0 & 0 & 0 \end{bmatrix} \underset{\sim}{u}_{ty} - (c_d - c_s) \begin{bmatrix} 0 & 0 & 0 \\ 0 & 0 & 1 \\ 0 & 1 & 0 \end{bmatrix} \underset{\sim}{u}_{yz}$$

$$- \begin{bmatrix} c_d \left(c_s - \frac{c_d}{2} \right) & 0 & 0 \\ 0 & c_s \left(c_d - \frac{c_s}{2} \right) & 0 \\ 0 & 0 & \frac{c_s}{2} \end{bmatrix} \underset{\sim}{u}_{yy}$$

$$- \begin{bmatrix} c_d \left(c_s - \frac{c_d}{2} \right) & 0 & 0 \\ 0 & \frac{c_s}{2} & 0 \\ 0 & 0 & c_s \left(c_d - \frac{c_s}{2} \right) \end{bmatrix} \underset{\sim}{u}_{zz} = 0 \quad . \tag{35}$$

Equations (35) govern a medium which transmits waves only in the positive-x direction. A rotational transformation on the finite-element boundary terms is all that is required for orienting the boundary in other directions.

The overall behavior of equations (35) would appear to be the same as that of the two-dimensional paraxial equations. If

$$c_s < \frac{c_d}{2} \quad ,$$

then $\underset{\sim}{u}_{yy}$ and $\underset{\sim}{u}_{zz}$ have terms indicating negative stiffnesses. The other paraxial terms in the three-dimensional version are also similar to their two-dimensional counterparts: $\underset{\sim}{u}_{tx}$ represents the zeroth-order term; $\underset{\sim}{u}_{ty}$ and $\underset{\sim}{u}_{tz}$ are the first-order terms; and $\underset{\sim}{u}_{yz}$, $\underset{\sim}{u}_{yy}$, and $\underset{\sim}{u}_{zz}$ are the higher-order contributions. The order of the terms refers to the powers of k_y/ω or k_z/ω that result, when equation (34) is substituted into equation (33).

The above technique for deriving one-directional equations also seems to be applicable to anisotropic materials. Equations (33) would be somewhat altered due to the anisotropy, but one would assume that the harmonic-wave forms (34) are still valid. Equations (34) would then be substituted into the governing, anisotropic equations, and the factoring, and solving, for ck_x/ω would be performed as before.

VI. STABILITY ANALYSIS

The stability characteristics of the paraxial equations can be identified through an energy analysis. A paraxial region, which is designed to transmit rightward-traveling waves, is illustrated in Figure 4.

If we put equation (30) into matrix form, premultiply it by $\underset{\sim}{u}_t^T$, and integrate it over the boundary region Ω_b, then:

$$\int_{\Omega_b} \left[\frac{1}{2} \frac{\partial}{\partial t} \left[\underset{\sim}{u}_t^T \underset{\sim}{M}_b \underset{\sim}{u}_t \right] + \frac{1}{2} \frac{\partial}{\partial x} \left[\underset{\sim}{u}_t^T \underset{\sim}{C}_x \underset{\sim}{u}_t \right] \right.$$

$$\left. + \frac{1}{2} \frac{\partial}{\partial z} \left[\underset{\sim}{u}_t \underset{\sim}{C}_z \underset{\sim}{u}_t \right] + \underset{\sim}{u}_t^T \underset{\sim}{K}_b \underset{\sim}{u}_{zz} \right] d\Omega_b = 0 \quad , \qquad (36)$$

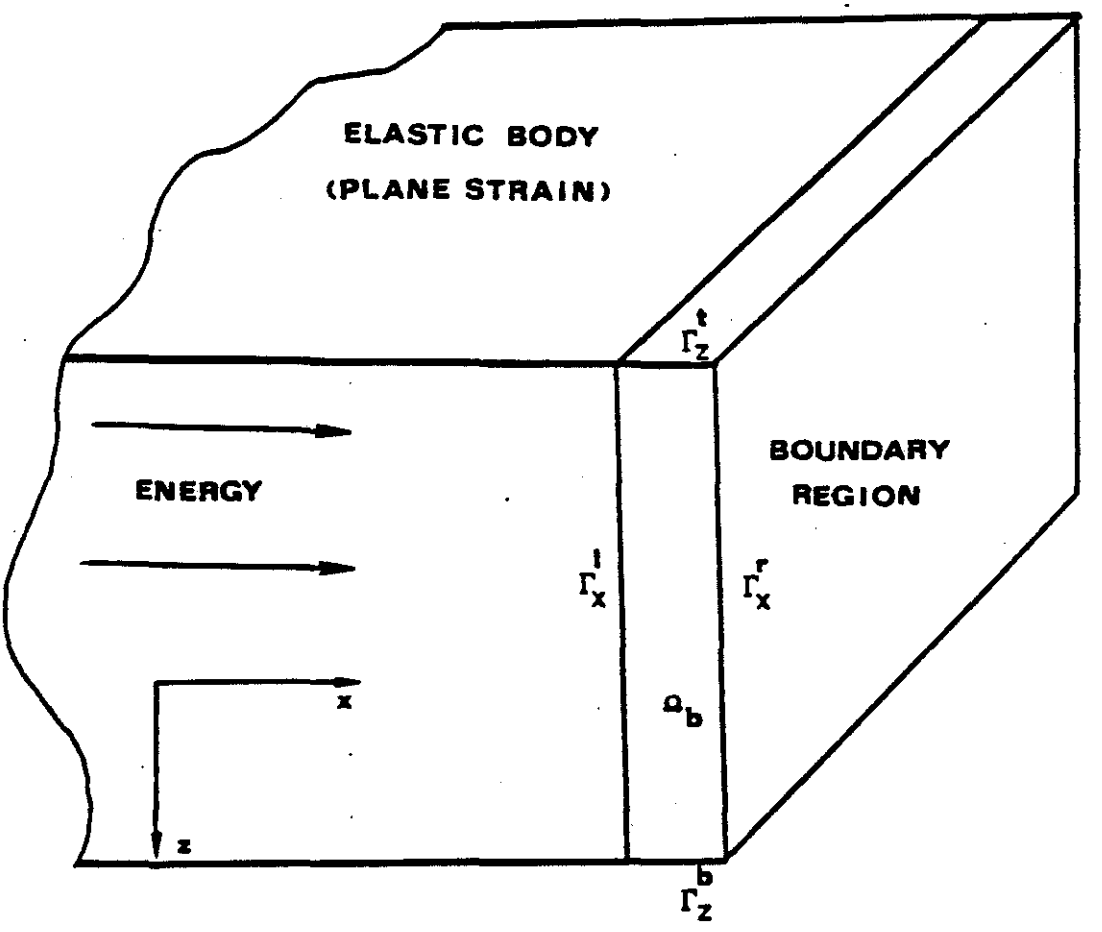

Figure 4. Schematic representation of a paraxial boundary for plane strain.

where

$$\left.\begin{aligned} \underset{\sim}{M}^b &= \begin{bmatrix} 1 & 0 \\ 0 & 1 \end{bmatrix} \quad , \qquad \underset{\sim}{C}^x = \begin{bmatrix} c_d & 0 \\ 0 & c_s \end{bmatrix} \quad , \\ \underset{\sim}{C}^z &= (c_d - c_s)\begin{bmatrix} 0 & 1 \\ 1 & 0 \end{bmatrix} \quad , \\ \underset{\sim}{K}^b &= \begin{bmatrix} c_d\left(c_s - \frac{c_d}{2}\right) & 0 \\ 0 & c_s\left(c_d - \frac{c_s}{2}\right) \end{bmatrix} . \end{aligned}\right\} \tag{37}$$

The paraxial domain, Ω_b, and its boundaries, Γ_x^l, Γ_x^r, Γ_z^t, and Γ_z^b, are depicted in Figure 4.

We modify equation (36) and set either $\underset{\sim}{u} = 0$, or $\underset{\sim}{u}_z = 0$, at the boundaries, Γ_z^t and Γ_z^b.

$$\left.\begin{aligned} &\frac{1}{2}\int_{\Omega_b} \frac{\partial}{\partial t}\left[\underset{\sim}{u}_t^T \underset{\sim}{M}^b \underset{\sim}{u}_t + \underset{\sim}{u}_z^T \underset{\sim}{K}^b \underset{\sim}{u}_z\right] d\Omega_b = \\ &\quad + \frac{1}{2}\int_{\Gamma_x^l} \left[\underset{\sim}{u}_t^T \underset{\sim}{C}^x \underset{\sim}{u}_t\right] d\Gamma_x - \frac{1}{2}\int_{\Gamma_x^r} \left[\underset{\sim}{u}_t^T \underset{\sim}{C}^x \underset{\sim}{u}_t\right] d\Gamma_x \\ &\quad + \frac{1}{2}\int_{\Gamma_z^b} \left[\underset{\sim}{u}_t^T \underset{\sim}{C}^z \underset{\sim}{u}_t\right] d\Gamma_z - \frac{1}{2}\int_{\Gamma_z^t} \left[\underset{\sim}{u}_t^T \underset{\sim}{C}^z \underset{\sim}{u}_t\right] d\Gamma_z \quad , \end{aligned}\right\} \tag{38a}$$

or

$$\left.\begin{aligned} &\frac{1}{2}\int_{\Omega_b}\frac{\partial}{\partial t}\left[\underset{\sim}{u}_t^T\underset{\sim}{M}^b\underset{\sim}{u}_t+\underset{\sim}{u}_z^T\underset{\sim}{K}^b\underset{\sim}{u}_z\right]d\Omega_b \;=\\ &\text{Energy Flux (x-direction) + Energy Flux (z-direction)} \quad . \end{aligned}\right\} \tag{38b}$$

For most problems, the orientation of the boundaries is such that the flux is mainly perpendicular to the long axis of the boundary region. Therefore, the accumulated energy within the system is represented primarily by the energy flux in the x-direction. If no energy is flowing into the boundary region via Γ_x^l, then the Γ_x^r integral dominates the right-hand side.[1] C^x is diagonal, with positive elements, so

$$-\int_{\Gamma_x^r}\underset{\sim}{u}_t\underset{\sim}{C}^x\underset{\sim}{u}_t d\Gamma_x \;\le\; 0 \quad .$$

Therefore, we conclude from equation (38) that if $\underset{\sim}{M}^b$ and $\underset{\sim}{K}^b$ are positive-definite matrices, then $|\underset{\sim}{u}|$ is bounded. $\underset{\sim}{M}^b$ is always positive-definite, but $\underset{\sim}{K}^b$ is only positive-definite for the range of shear velocities, $c_s > c_d/2$. For $c_s < c_d/2$ (i.e., Poisson's ratio greater than 1/3), instabilities may result in the use of the paraxial equations.

Another, more specific way to evaluate the paraxial instability is to assume that an harmonic wave is impinging on the paraxial boundary.

---

[1] If the energy flux in the z-direction is integrated by parts, it becomes $(c_d - c_s)\int u_t w_t d\Gamma_z$. This energy term is neither positive- nor negative definite, but it is assumed to be small because Γ_z is small and because the primary direction of the flux is in the x-direction.

(Refer to Figure 2.) The wave is represented by equations (39):

$$\begin{aligned} u &= U \exp [i \kappa (\cos\alpha\, x + \sin\alpha\, z - ct)] \quad , \\ w &= W \exp [i \kappa (\cos\alpha\, x + \sin\alpha\, z - ct)] \quad , \end{aligned} \tag{39}$$

where α = the angle of incidence and κ = the wave number, which is assumed to be real. We wish to determine the value of c in equation (39). If it has a negative, imaginary component, then u and w are growing exponentially in time, and therefore are unstable. The substitution of equations (39) into the paraxial equations (30) gives:

$$\begin{bmatrix} c^2 - c(c_d \cos\alpha) + c_d\left(\frac{c_d}{2} - c_s\right)\sin^2\alpha & -c(c_d - c_s)\sin\alpha \\ -c(c_d - c_s)\sin\alpha & c^2 - c(c_s\cos\alpha) + c_s\left(\frac{c_s}{2} - c_d\right)\sin^2\alpha \end{bmatrix} \begin{Bmatrix} U \\ W \end{Bmatrix} = 0 \quad , \tag{40a}$$

or

$$\underset{\sim}{\overline{D}}\, \underline{U} = \underline{0} \quad . \tag{40b}$$

For a nontrivial solution of equations (40), the determinant of the matrix, $\underset{\sim}{\overline{D}}$, must vanish.

$$|\underset{\sim}{\overline{D}}| = \underline{0} \quad . \tag{41}$$

The taking of the determinant of $\underset{\sim}{\overline{D}}$ results in a quartic equation for c. The computed soutions of this quartic, for various angles of incidence and Poisson's ratios, are plotted in Figure 5.

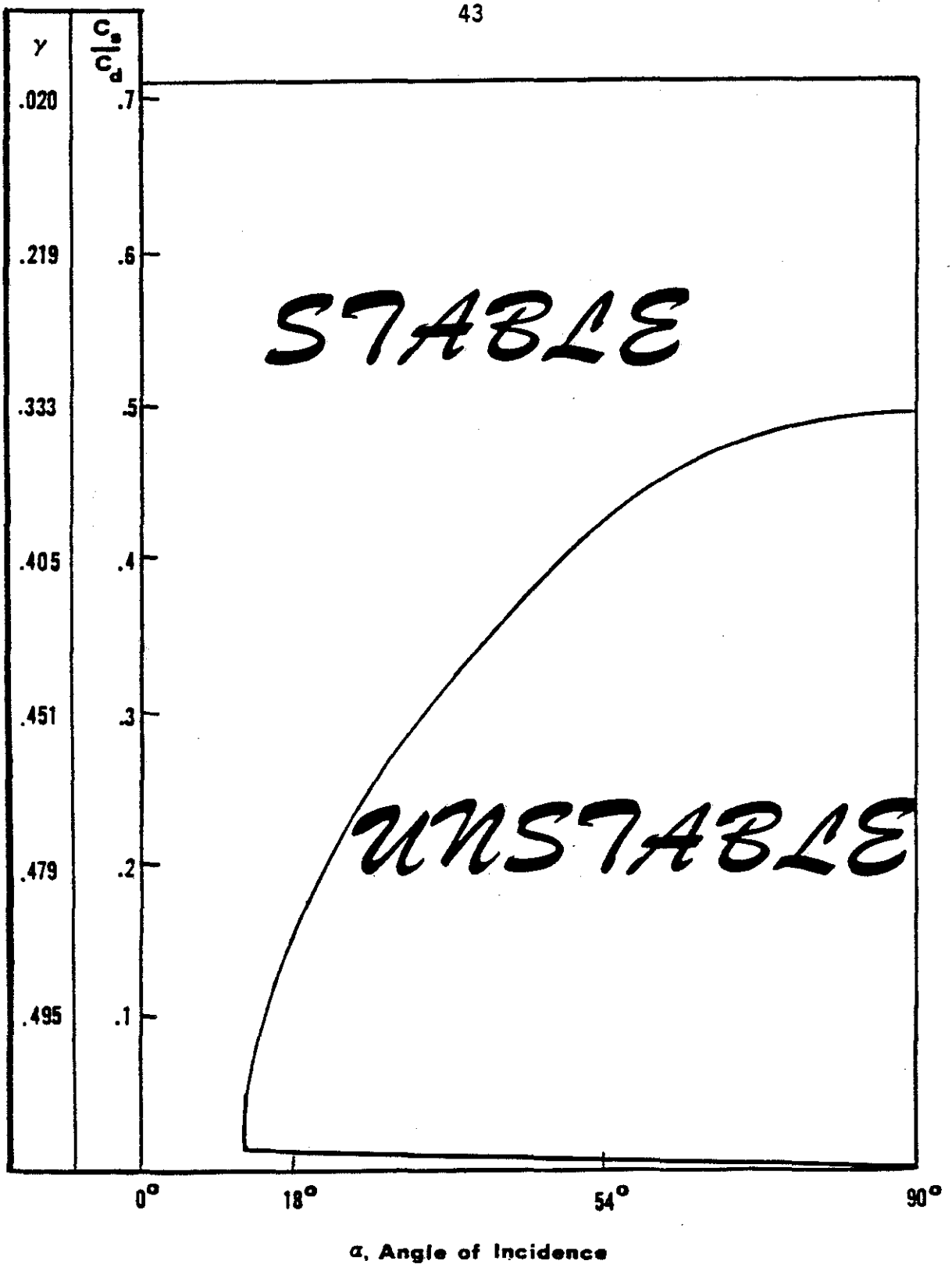

Figure 5. Stability regions for the paraxial equations, for different material properties and angles of incidence. (ν = Poisson's ratio.)

One can see that for Poisson's ratios of less than 1/3 ($c_s/c_d < .5$), the paraxial equations are always stable. They are also stable for waves which impinge almost normally on the boundary. There exists, however, a large unstable zone for Poisson's ratios of greater than 1/3. We conducted several numerical tests using points inside the unstable region, and our results confirmed the existence of the instability. In transient and nonlinear problems, we cannot guarantee that the waves striking the boundary will always be normal to it. Guided by the approximate nature of the paraxial equations, our practical solution to this problem is to set the negative stiffness term, $c_d(c_s - c_d/2)$, equal to zero, if Poisson's ratio is greater than 1/3. The justification for this simple solution is that the stiffness terms are the least important element of the paraxial approximation, as was noted in the derivation of the paraxial equations. A similar stability analysis of the revised paraxial equations revealed no instabilities.

The set of equations, then, which we shall use for all future work with paraxial boundaries is:

$$\left.\begin{array}{l} \left.\begin{array}{l} \rho\left[u_{tt} + c_d u_{tx} + (c_d - c_s)w_{tz} - c_d\left(c_s - \frac{c_d}{2}\right)u_{zz} = 0\right] \\ \rho\left[w_{tt} + c_s w_{tx} + (c_d - c_s)u_{tz} - c_s\left(c_d - \frac{c_s}{2}\right)w_{zz} = 0\right] \end{array}\right\} \quad \text{for } \nu \le 1/3 \\ \left.\begin{array}{l} \rho\left[u_{tt} + c_d u_{tx} + (c_d - c_s)w_{tz} = 0\right] \\ \rho\left[w_{tt} + c_s w_{tx} + (c_d - c_s)u_{tz} - c_s\left(c_d - \frac{c_s}{2}\right)w_{zz} = 0\right] \end{array}\right\} \quad \text{for } \nu > 1/3 \end{array}\right\} \tag{42}$$

The second set of equations (42) could serve for all Poisson's ratios, but when $\nu < 1/3$, the first set of (42) would be slightly more accurate.

VII. THEORETICAL COMPARISONS OF PARAXIAL TO VISCOUS BOUNDARIES

VII.A. The Viscous Boundary

The basic idea of a viscous boundary was proposed by Lysmer and Kuhlemeyer,[47] and is illustrated in Figure 6 for plane strain. One applies boundary stresses, σ and τ, to an otherwise free boundary. These stresses cancel the stresses which are produced at the boundary by incoming waves, or

$$\left.\begin{aligned} \sigma_{in} + \sigma_{bd} &\cong 0 \quad , \\ \tau_{in} + \tau_{bd} &\cong 0 \quad , \end{aligned}\right\} \tag{43a}$$

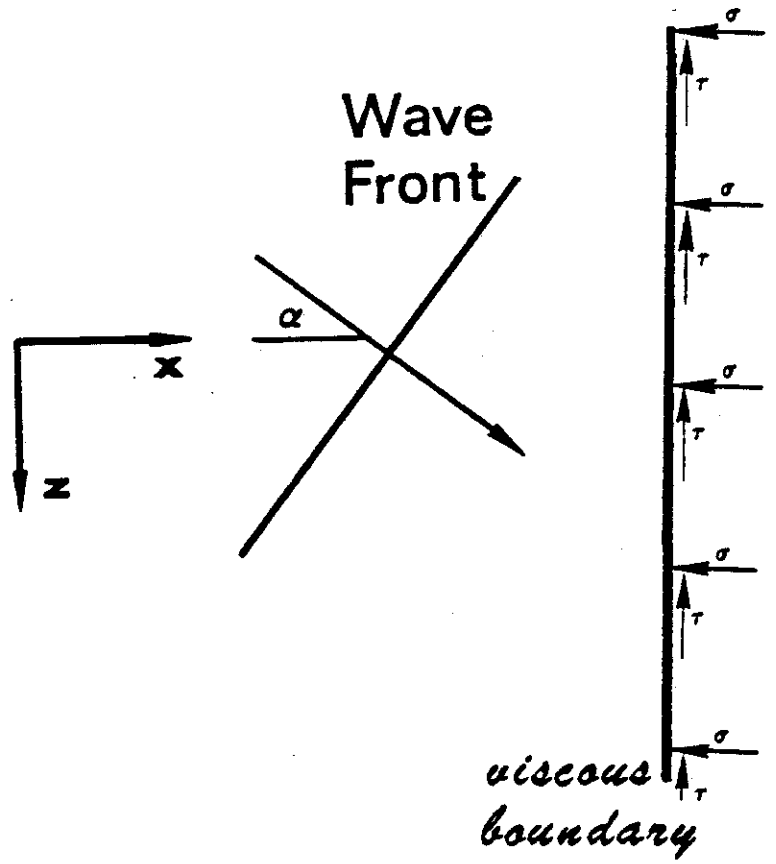

Figure 6. Schematic representation of a viscous boundary.

in which σ_{in} and τ_{in} are the incident stresses, and σ_{bd} and τ_{bd} are the applied boundary stresses. Thus, the zero-traction condition at this free boundary,

$$\left.\begin{aligned}(\sigma_{in} + \sigma_{bd}) + \sigma_{rf} &= 0 \quad , \\ (\tau_{in} + \tau_{bd}) + \tau_{rf} &= 0 \quad ,\end{aligned}\right\} \tag{43b}$$

causes σ_{rf} and τ_{rf} to be zero, where σ_{rf} and τ_{rf} are stresses caused by reflected waves.

One set of applied boundary stresses is defined by equations (44):

$$\left.\begin{aligned}\sigma_{xx} &= -\rho c_d \, u_t \quad , \\ \tau_{xz} &= -\rho c_s \, w_t \quad ,\end{aligned}\right\} \tag{44}$$

as was proposed by Lysmer and Kuhlemeyer.[47] These applied stresses are clearly dissipative. Their taking of energy from the system is illustrated in Section II of this chapter.

White, Valliappan, and Lee[57] proposed a "unified" viscous boundary, where

$$\left.\begin{aligned}\sigma_{xx} &= -a \, \rho \, c_d \, u_t \quad , \\ \tau_{xz} &= -b \, \rho \, c_s \, w_t \quad .\end{aligned}\right\} \tag{45}$$

The parameters, a and b, vary according to the material properties of the medium. The authors performed two minimization processes in order to obtain the optimum values of a and b. We compare, in Chapter 4, the

wave-absorbing characteristics of this boundary to those of the original viscous boundary.

VII.B. Relationship Between Paraxial and Viscous Boundaries

Although the concepts of the paraxial and viscous boundaries seem to be completely different, they can be related through the equilibrium equations using the following, heuristic analysis. In Figure 7, an element is shown, which contains mass density, ρ, and stresses, σ and τ. If the element in Figure 7 were elastic, then the stresses would be proportional to the strains, and we would arrive at the usual elasticity equations. However, if the element is such that

$$\left.\begin{aligned} \sigma_{xx} &= -\rho\, c_d\, u_t \quad , \\ \tau_{xz} &= -\rho\, c_s\, w_t \quad , \end{aligned}\right\} \tag{46}$$

and τ_{zx} and σ_{zz} are constant through the element in the z-direction, then the equilibrium equations in the x and z directions, respectively, are:[2]

$$\left.\begin{aligned} \rho u_{tt} - \frac{\partial \sigma_{xx}}{\partial x} &= \rho u_{tt} + \rho c_d u_{tx} = 0 \quad , \\ \text{and} \qquad \rho w_{tt} - \frac{\partial \tau_{xz}}{\partial x} &= \rho w_{tt} + \rho c_s w_{tx} = 0 \quad . \end{aligned}\right\} \tag{47}$$

Equations (47) happen to be the zeroth-order, paraxial equations for a medium which transmits waves in the positive-x direction. [See equations (42).]

---

[2]The equations of rotational equilibrium are not considered in this approximate comparison.

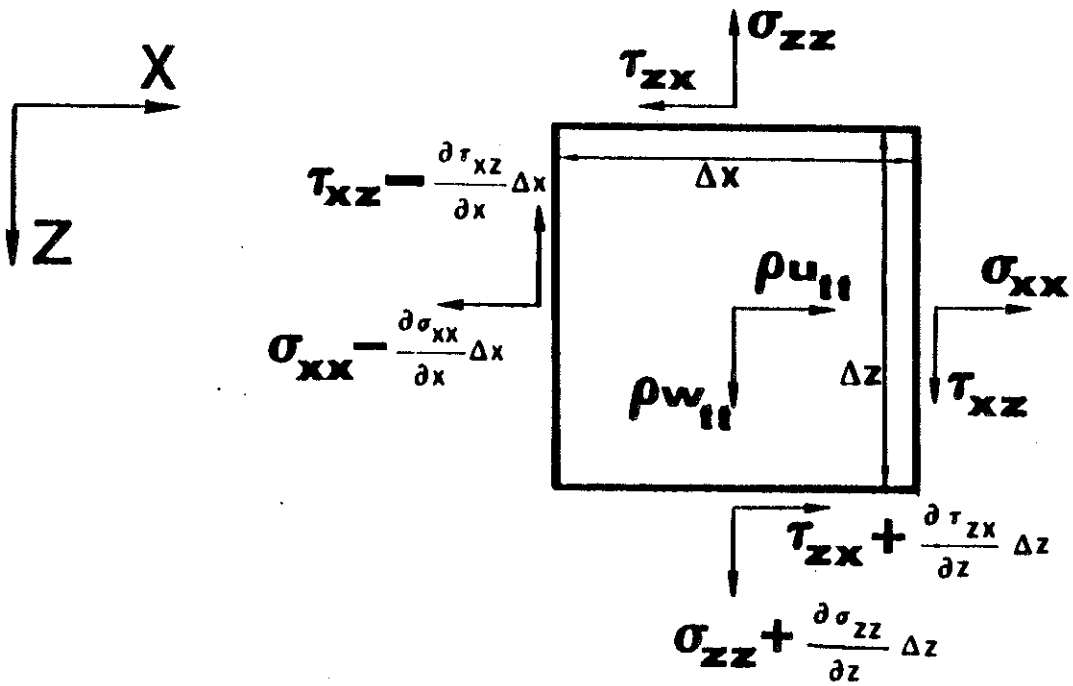

Figure 7. Stresses acting on a two-dimensional body in equilibrium.

The similarity between the paraxial and viscous approaches can be seen with the help of these equations and of Figure 7. The stresses, which are developed in the paraxial element, are proportional to the product of the element thickness, Δx, and the x-direction gradients of the velocities, u_t and w_t. The viscous boundary directly applies the u_t and w_t values to the left side of the element. In other words, the paraxial method applies dashpots across the width of an element, while the viscous technique attaches dashpots from the boundary nodes to a rigid base. Since both of the boundaries utilize the nodal velocities in a similar manner, it appears that they are performing essentially the same function. It is not a coincidence that the viscous coefficients, ρc_d and ρc_s, are also found in the paraxial equations (47).

Thus, the paraxial technique is seen to be one way to extend the viscous-boundary idea. This generalization, with the help of Figure 7, helps link the physical idea of using viscous dashpots for absorbing energy to the paraxial method of fitting solution forms. The paraxial technique, with its introduction of the higher-order terms, $\underset{\sim}{u}_{tz}$ and $\underset{\sim}{u}_{zz}$, potentially could lead to a more efficient, energy-absorbing boundary.

VII.C. Theoretical Comparison of the Paraxial and the Viscous Boundaries

In this section we perform a standard analysis of wave-reflection coefficients. For more details on this procedure, see Miklowitz.[86]

We assume that plane-harmonic, elastic waves are impinging upon a boundary strip, as is shown in Figure 8. The problem is again that of plane strain.

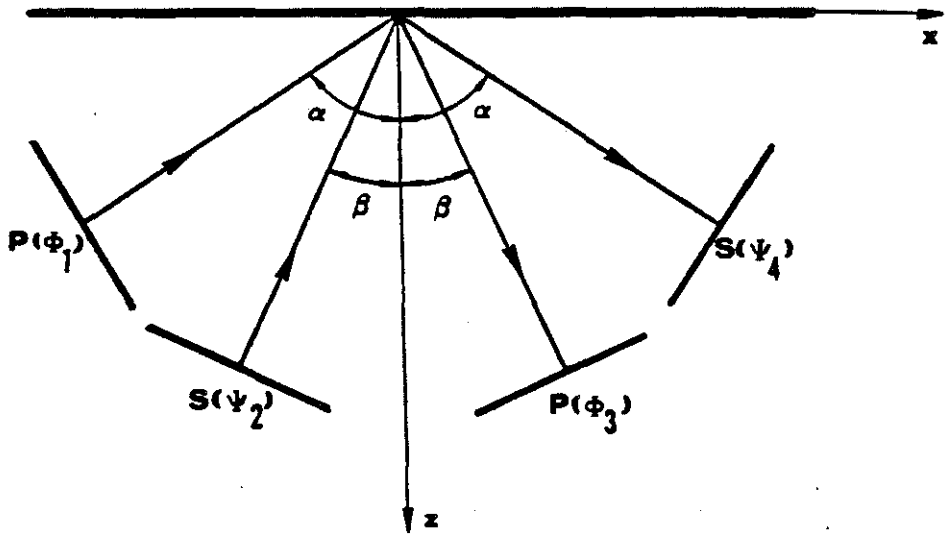

Figure 8. Schematic illustration of dilatational and shear waves reflecting from a boundary.

The wave potentials, which satisfy the governing equations of motion, are:

$$\left.\begin{aligned}
\phi_1 &= \exp\left[i\frac{\omega}{c_d}(\sin\alpha x - \cos\alpha z - c_d t)\right], \\
\phi_2 &= \exp\left[i\frac{\omega}{c_d}(\sin\alpha x + \cos\alpha z - c_d t)\right], \\
\Psi_3 &= \exp\left[i\frac{\omega}{c_s}(\sin\beta x - \cos\beta z - c_s t)\right], \\
\Psi_4 &= \exp\left[i\frac{\omega}{c_s}(\sin\beta x + \cos\beta z - c_s t)\right], \\
\phi &= I_p\phi_1 + A_p\phi_2, \\
\Psi &= I_s\Psi_3 + A_s\Psi_4,
\end{aligned}\right\} \qquad (48)$$

where c_d = the dilatational wave speed, c_s = the shear wave speed, I_p = 1 for an incident P-wave, I_s = 1 for an incident S-wave, A_p = the amplitude of the reflected P-wave, and A_s = the amplitude of the reflected S-wave.

We can now calculate the reflection coefficients for the paraxial boundary. For an incident P-wave, I_s is set equal to zero. The elastic wave is described by Lamé's solution,

$$\begin{aligned} u &= \frac{\partial \phi}{\partial x} - \frac{\partial \Psi}{\partial z} \quad , \\ w &= \frac{\partial \phi}{\partial z} + \frac{\partial \Psi}{\partial x} \quad . \end{aligned} \tag{49}$$

The substitution of the potentials in equations (48) into equations (49) produces the elastic displacements which propagate in the elastic region. This wave strikes the paraxial-boundary region, which is governed by equations (42). After substituting the elastic-displacement solution into equations (42), we have two equations for the solution of the reflected-wave amplitudes, A_p and A_s. These reflected waves also exist in the elastic medium.

The viscous-boundary scheme applies a stress condition to the boundary. Instead of setting the stresses equal to zero, as would be done at a free boundary, they are set equal to the viscous stresses. Again, we assume that we have potential solutions which lead to:

$$\left.\begin{aligned} \sigma_{zz} &= \frac{\lambda}{c_d^2}\phi_{tt} + 2\mu(\phi_{zz} + \Psi_{xz}) = -a\rho c_d w_t \quad , \\ \tau_{zx} &= \mu\left[\Psi_{tt}/c_s^2 + 2(\phi_{xz} - \Psi_{zz})\right] = -b\rho c_s u_t \quad , \end{aligned}\right\} \tag{50}$$

in which λ and μ are Lamé's elastic parameters. The velocities, u_t and w_t, are determined by using Lamé's solution, (equation (49)). The constants, a and b, are positive in equations (50). In the standard viscous boundary,

$$a = b = 1 \quad . \tag{51}$$

For the unified viscous boundary, however, a and b are set equal to the "optimized" values, which were set forth by White, Valliappan, and Lee.[57] The wave-reflection amplitudes, A_p and A_s, which may be complex, are computed for the various angles of incidence. The absolute values of the amplitudes, for different values of Poisson's ratio, are plotted in figures 9 through 16. The three different silent boundaries are labeled as follows:

Standard-Viscous Boundary	- V
Unified-("Optimized") Viscous Boundary	- O
Modified-Paraxial Boundary	- P.

There are four sets of curves:

1) P-reflections from an incident P-wave
2) S-reflections from an incident P-wave
3) P-reflections from an incident S-wave
4) S-reflections from an incident S-wave.

We should note a few points before interpreting the wave-reflection figures. First, the reflection amplitudes for low angles of incidence are more important than are those for high angles of incidence. Waves which strike a silent boundary at high angles will usually hit one or more boundaries before returning to the interior. In addition, one usually knows in advance the source of wave radiations, and consequently

can orient the silent boundaries toward that source. Therefore, the fact that most of the incoming energy is reflected, when incident angles are nearly equal to 90°, does not necessarily reduce the boundary's efficiency by a significant amount.

Secondly, the assumptions which govern the wave-reflection calculations are not strictly the same as are those that , by necessity, govern our finite-element representation of the boundary. The finite-element method spatially discretizes the boundary equations, and the boundary contributions are calculated for the outermost set of nodes. In contrast, the above theoretical analysis employs an infinitesimal boundary strip, from which the boundary effects are calculated.

When we consider the first set of curves, the reflected P-wave amplitudes caused by incident P-waves, (figures 9 and 10), we can see that all of the boundaries are nearly equal in their reflection amplitudes. Near-to-perfect absorption is attained for those incident waves which are almost normal to the boundary. Conversely, total reflection occurs for the waves which impinge at 90° angles. As Poisson's ratio decreases, the absorption characteristics of all three silent boundaries improve. The one exception to this trend is the optimized-viscous boundary where Poisson's ratio is nearly equal to zero. It performs less effectively for this condition.

The viscous-boundary curves dip near 60° for $c_s/c_d \geq .55$. These abrupt interruptions in slope are due to changes in the reflected amplitudes' signs. The reflected, paraxial amplitudes retain the same sign for all angles of incidence, and therefore display no dips.

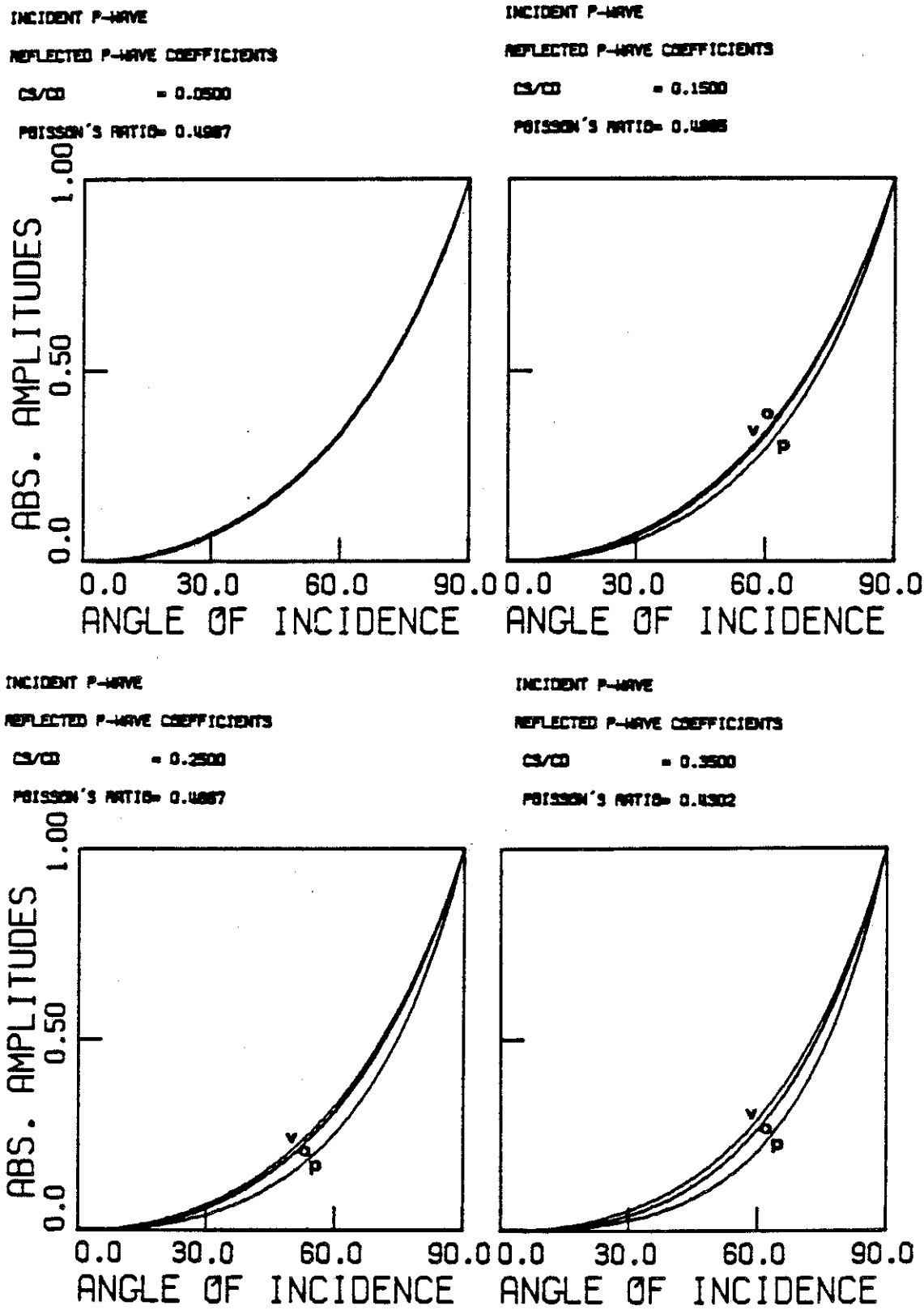

Figure 9. Absolute amplitudes of reflected waves for various angles of incidence (plane strain).

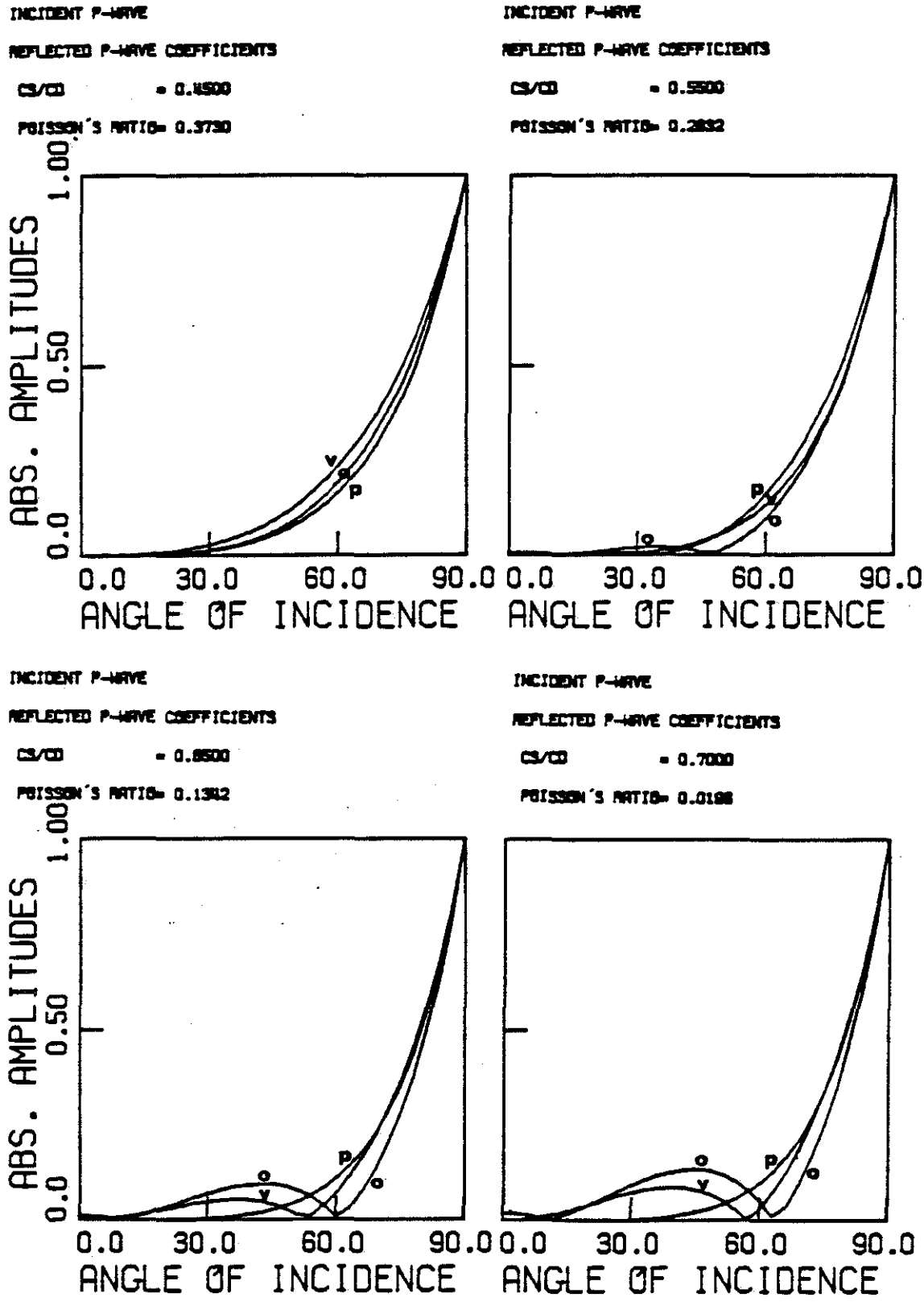

Figure 10. Absolute amplitudes of reflected waves for various angles of incidence (plane strain).

The reflected S-wave amplitudes, caused by incident P-waves, are shown in Figures 11 and 12. All three boundary methods show negligible reflections when Poisson's ratio is near to one half. The modified-paraxial magnitudes are so small that they all are nearly zero. In addition, the quiet boundaries are almost as effective for materials with lower Poisson's ratios, as they are for higher ones.

The illustrations of those reflected, S-wave magnitudes arising from incident S-waves, Figures 13 and 14, depict larger differences among the three boundary schemes than do the previous figures. In this test, the modified-paraxial boundary clearly outperforms its competitors. For all Poisson's ratios, the optimized-viscous boundary produces 10-15 percent reflections of normally-incident waves. It should also be noted, however, that with high Poisson's ratios, the incident S-wave curves are somewhat misleading. In this case, the shear-wave propagation speed is only a small fraction of the dilatational speed. The S-wave reflections will be traveling slowly, and therefore, may not significantly influence the response in the interior region. Again, the dips or kinks, which are evident particularly for the optimized viscous boundary, are caused by changes in the amplitudes' signs.

The last set of comparisons, (figures 15 and 16), describes P-wave reflections due to incident S-waves. These curves are influenced by the critical-angle phenomenon. If the incident, shear-wave angle is larger than a certain angle called the critical angle, then the reflected, dilatational wave becomes a surface wave which travels along the boundary. In each of the plots in Figures 15 and 16, one can detect the critical angles by the abrupt changes in the slopes of the

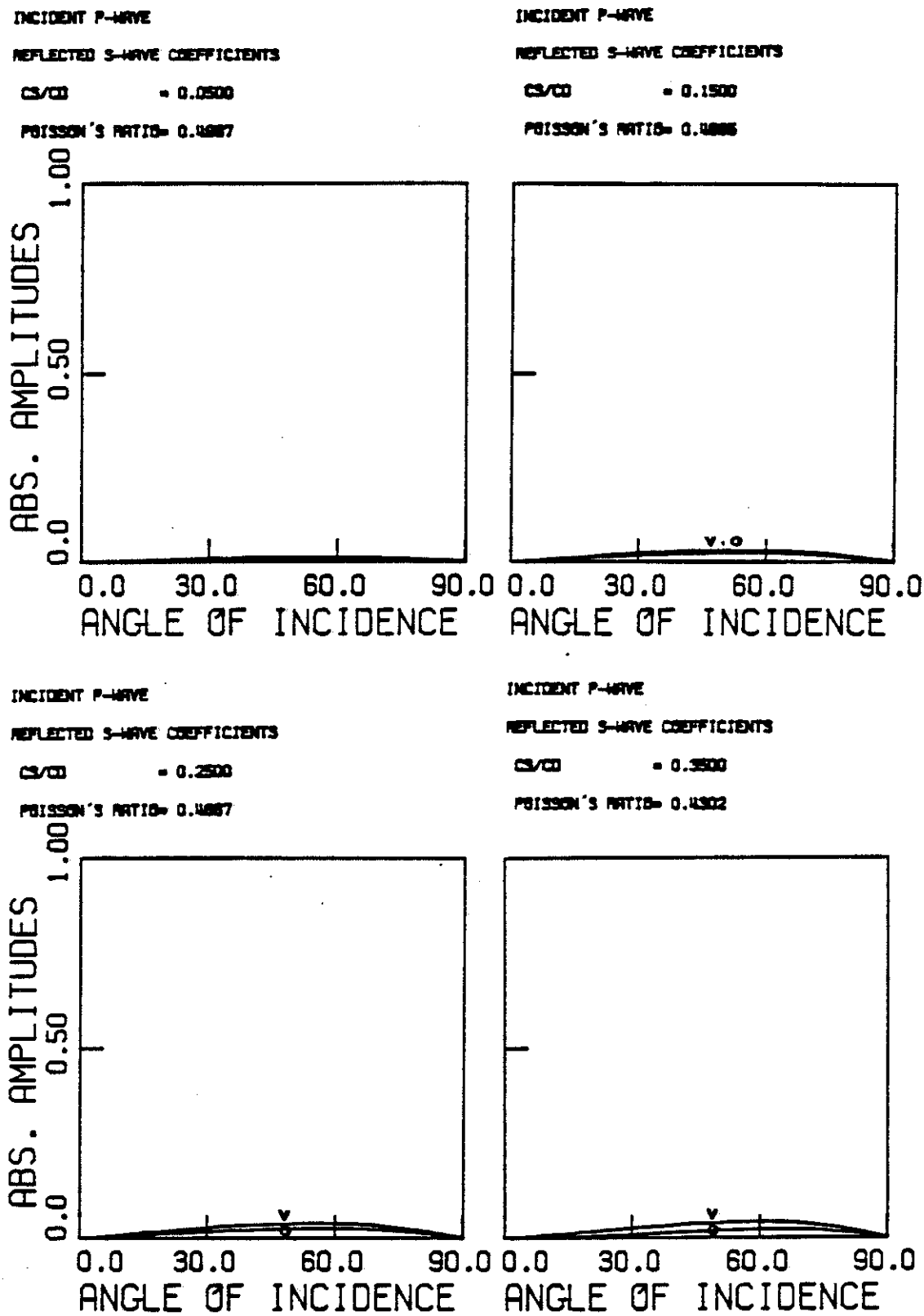

Figure 11. Absolute amplitudes of reflected waves for various angles of incidence (plane strain).

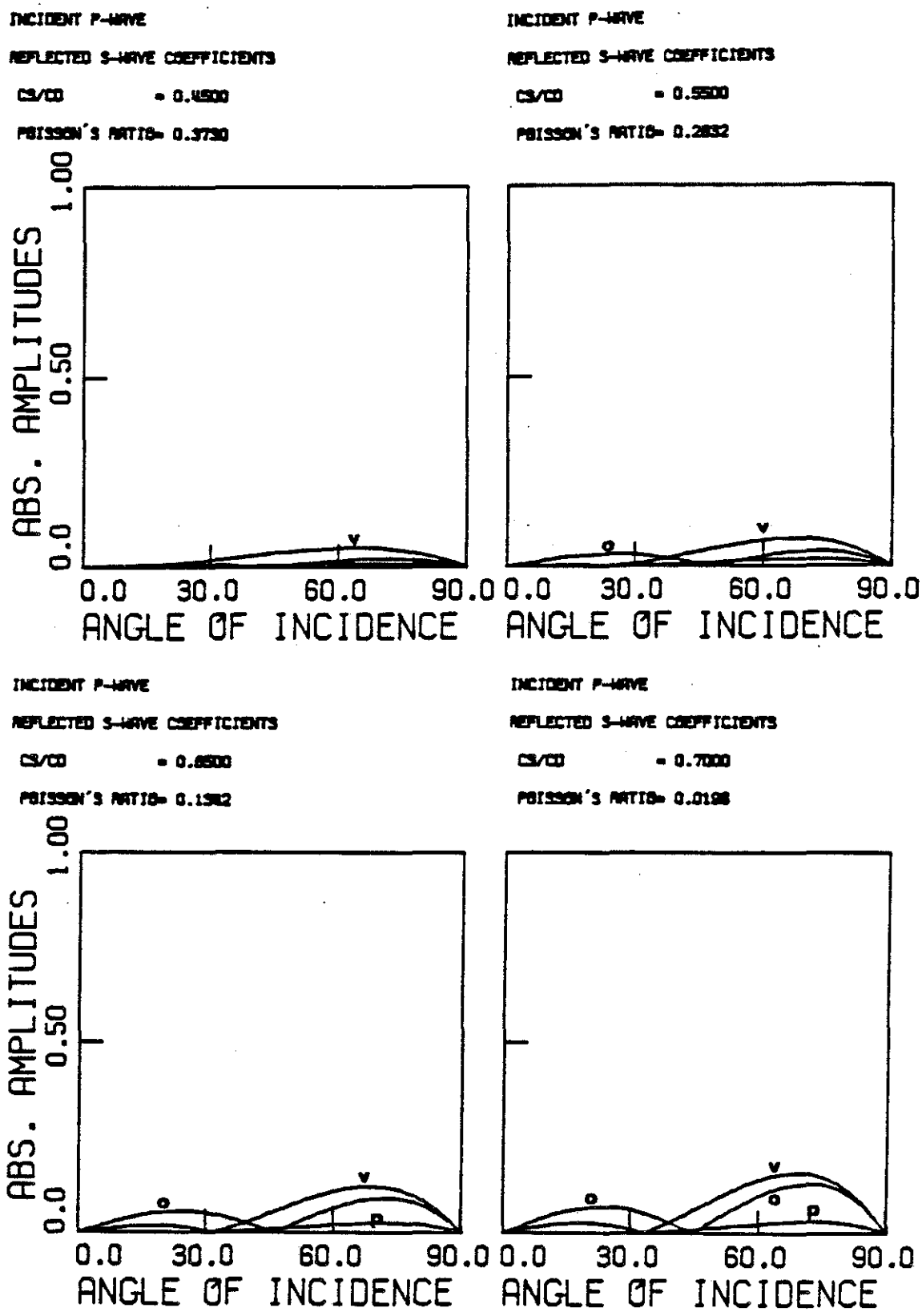

Figure 12. Absolute amplitudes of reflected waves for various angles of incidence (plane strain).

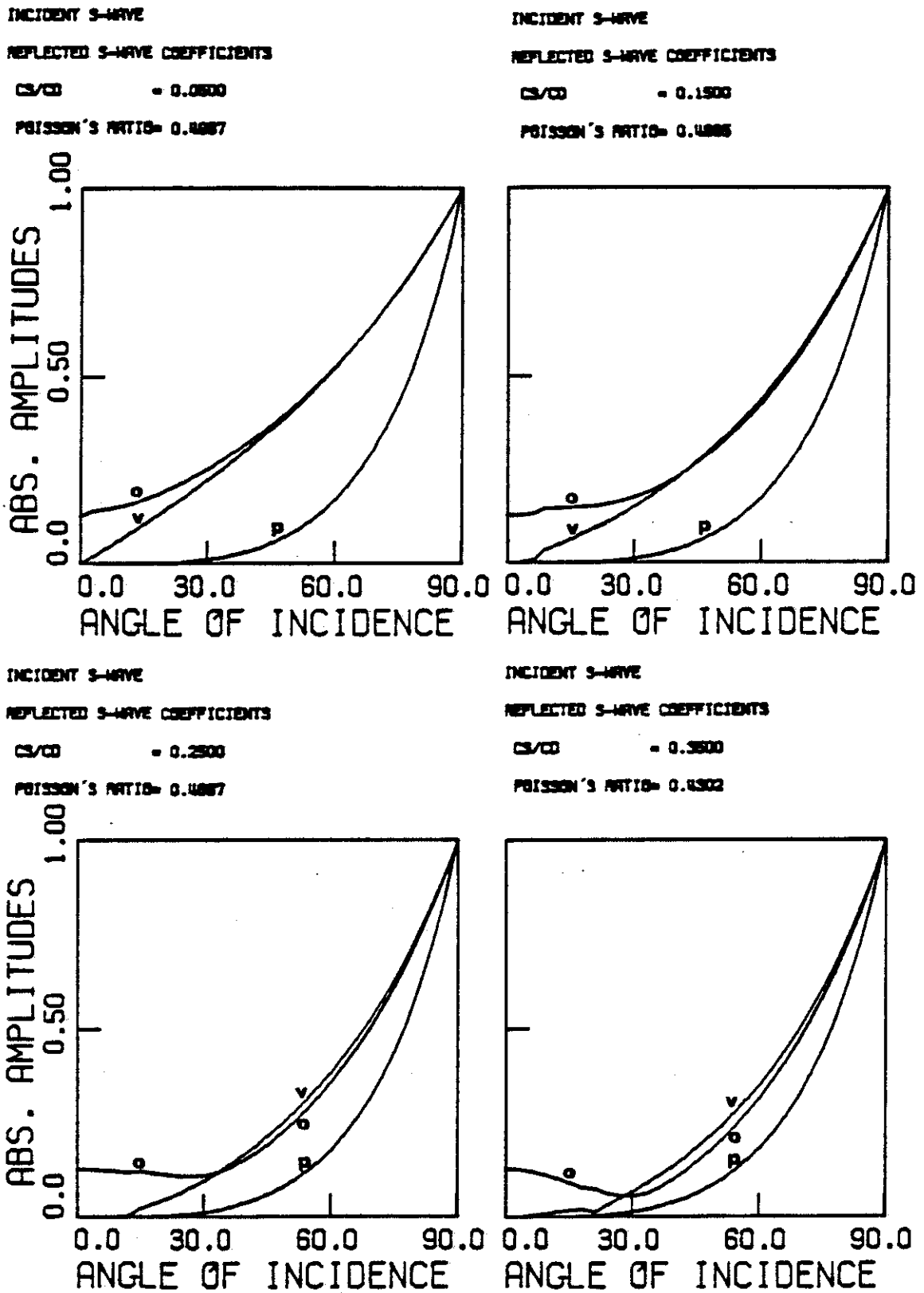

Figure 13. Absolute amplitudes of reflected waves for various angles of incidence (plane strain).

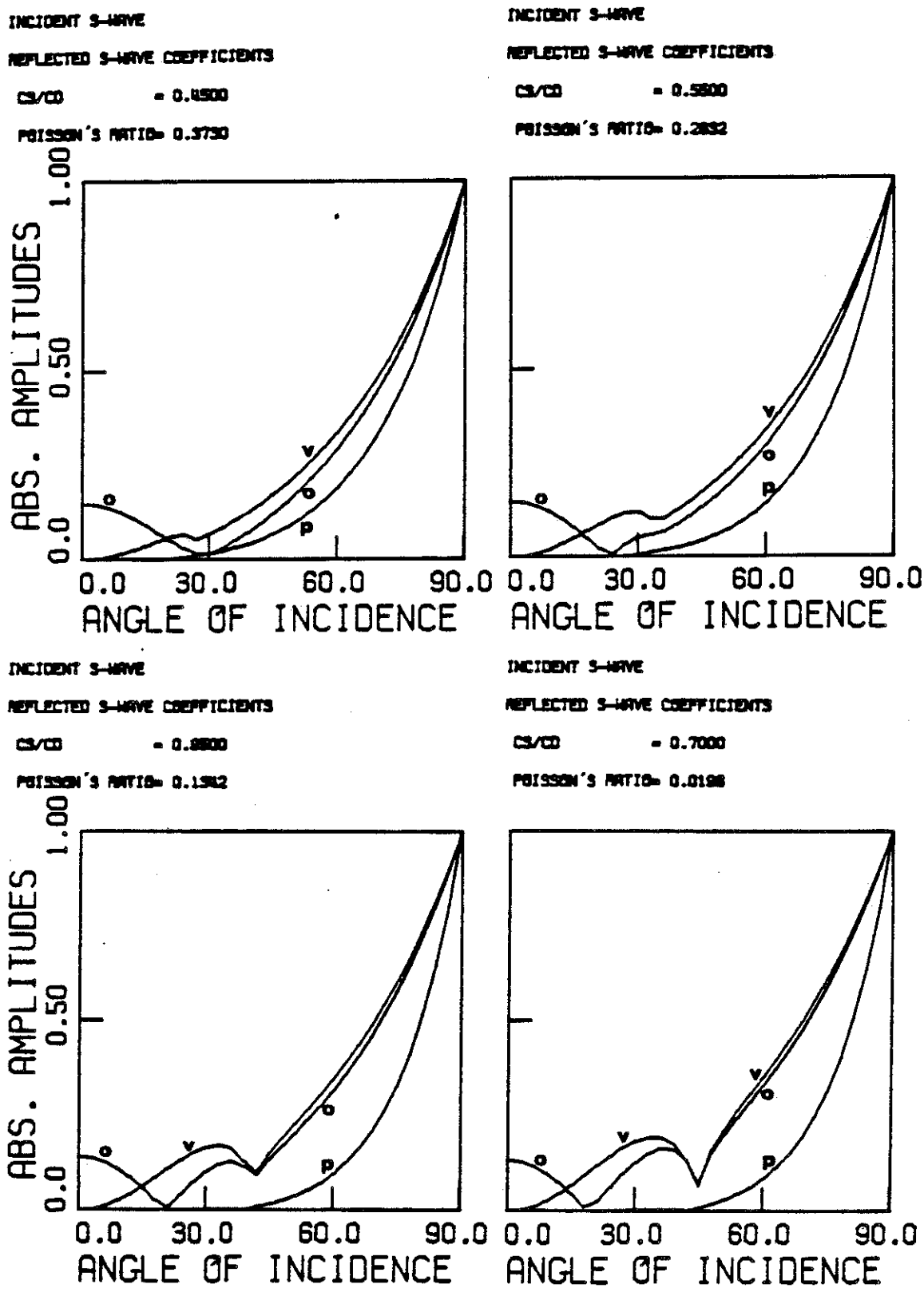

Figure 14. Absolute amplitudes of reflected waves for various angles of incidence (plane strain).

reflection curves. This occurs in the region of from 0° to 45°, depending on Poisson's ratio. As the shear-wave speed decreases, (thus Poisson's ratio increases), so does the critical angle decrease.

In this analysis, we are dealing with an incident, plane, harmonic wave which extends infinitely in the x-z plane. (See Figure 2.) Hence, it contains infinite energy. Likewise, the reflected body waves extend infinitely in x-z space. The reflected surfave wave, however, which is created when the shear-wave angle is greater than the critical angle, is confined to a region near the boundary. Theoretically, this surface wave contains only a finite amount of energy. Therefore, in Figures 15 and 16, the fact that P-wave amplitudes are large for those incidence angles which are greater than the critical angle, is probably not seriously detrimental. In fact, previous authors[47,57] eliminated these amplitudes from comparison when they multiplied them by the wave speed times cos α (α = angle of incidence.) This new quantity measured the energy flux at the boundary; energy propagating along the boundary was assumed to be confined there.

In general, by considering all of the wave-reflection curves, we conclude that each of the boundary schemes produces acceptable results. All of them generally perform well when the incident angles are less than 40 degrees. With high Poisson's ratios, however, shear waves may cause some difficulties, particularly for the viscous boundaries.

The modified-paraxial boundary appears to be generally superior to the viscous schemes. It outperforms the others on every curve shown, and it demonstrates significant improvement for those reflected, shear-wave amplitudes which are produced by incident shear waves.

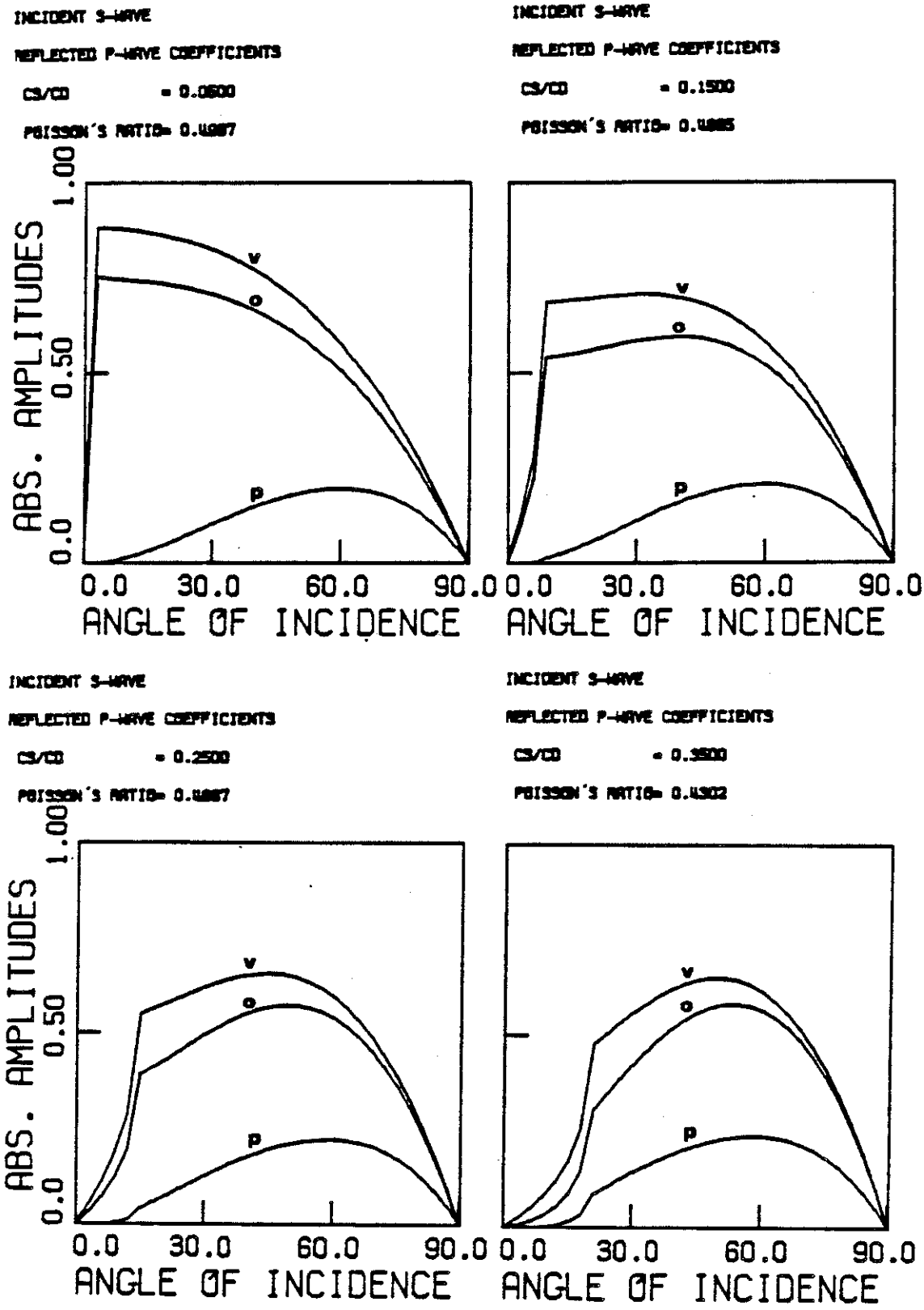

Figure 15. Absolute amplitudes of reflected waves for various angles of incidence (plane strain).

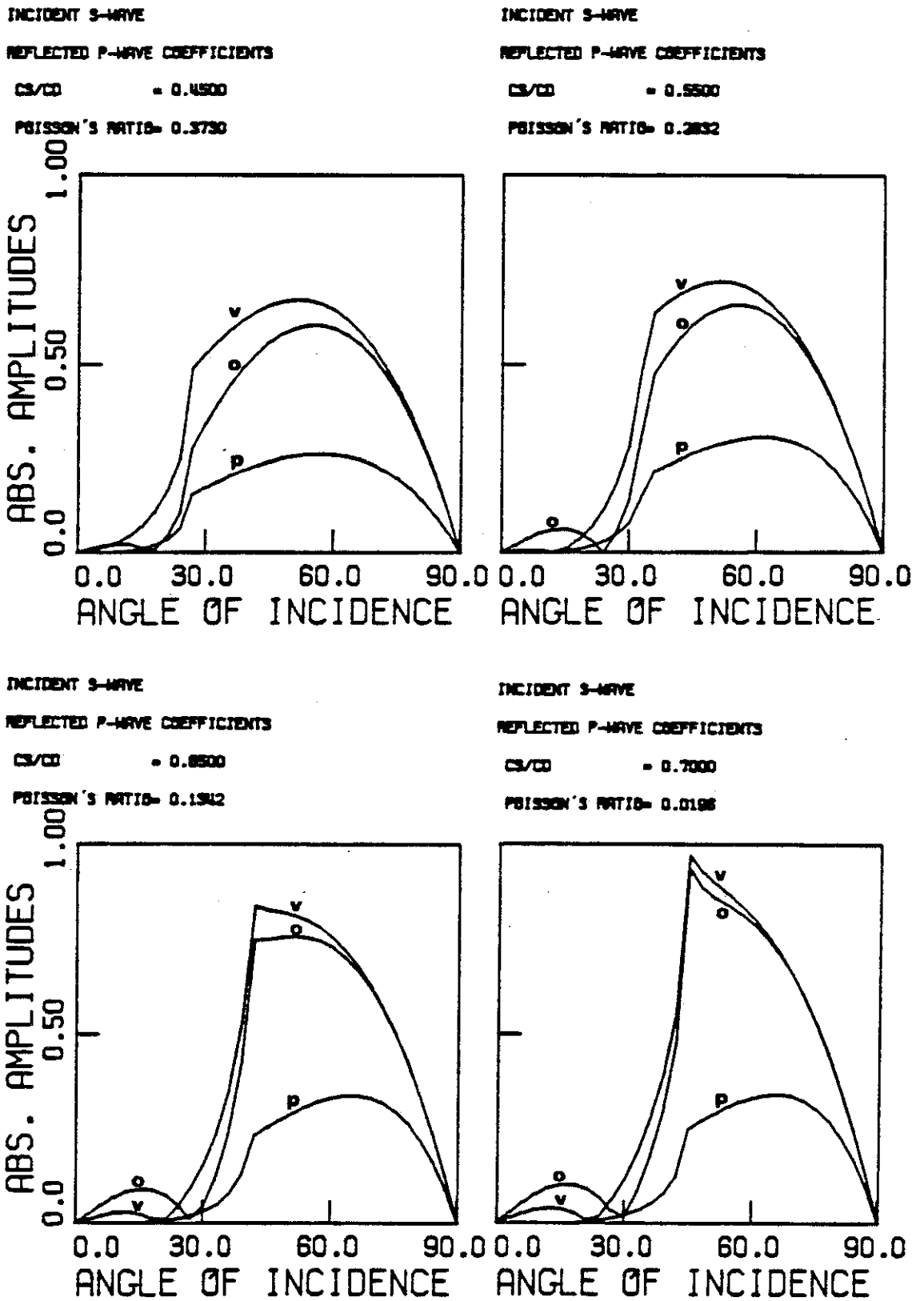

Figure 16. Absolute amplitudes of reflected waves for various angles of incidence (plane strain).

As it was first formulated,[39] the paraxial boundary (the one that includes the potentially negative stiffness terms) causes reflection amplitudes to be greater than one, when Poisson's ratios are greater than 1/3. These are illustrated in Figure 17. For an incident shear wave, the reflected-shear and reflected-dilatational amplitudes become increasingly large as Poisson's ratio approaches 1/2. These curves highlight the instability caused by the negative, paraxial stiffness term.

VIII. RAYLEIGH WAVES

In the soil-structure interaction problem, all types of waves may be generated. In a typical case, the energy radiating toward the boundaries could be simultaneously composed of Rayleigh, Love, and body waves. In many instances, such as for the Rayleigh-wave case, the waves have not completely formed. The energy would then be in a transition state, and it could be propagating at different speeds. Therefore, it is desirable to install a transmitting boundary which can handle all of the different wave motions.

The previous, wave-reflection analysis, however, is not valid in the case of Rayleigh waves.[2] Therefore, it is difficult to assess the various boundaries' effectiveness in transmitting these waves.

---

[2] Viktorov[88] presents some experimental data for Rayleigh waves striking a free boundary (in effect, a corner). These results show that about 40% of the incoming energy is transmitted around the corner as Rayleigh waves, 35% is reflected as Rayleigh waves to the interior and the remainder is converted to body waves, which propagate radially from the corner.

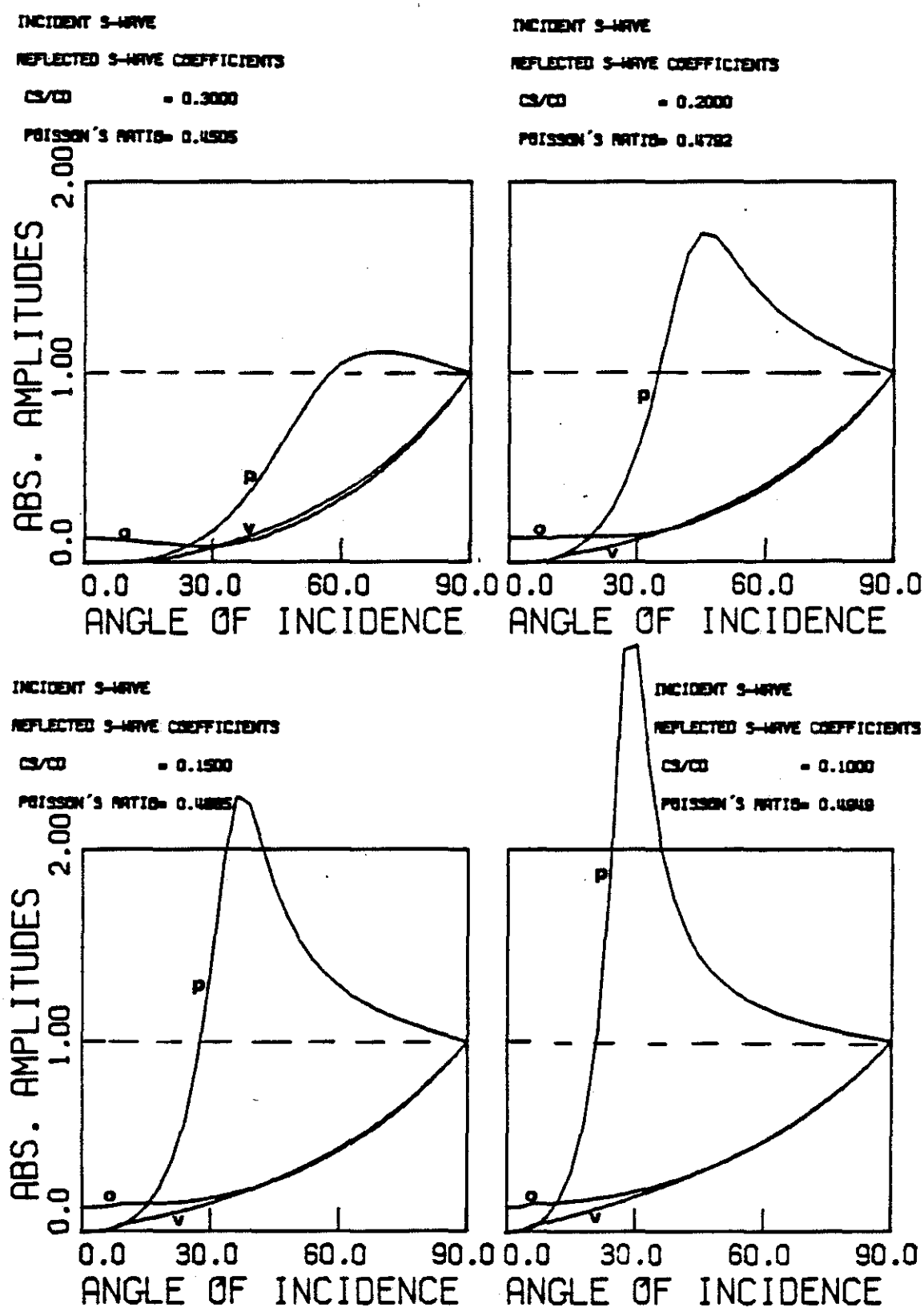

Figure 17. Absolute amplitudes of reflected waves for various angles of incidence (plane strain); 'p' represents the paraxial boundary containing all stiffness terms.

In the paraxial approach, special equations are constructed in order to satisfy a particular harmonic solution. For positively-directed Rayleigh waves, shown in Figure 18, these solutions are:

$$\left.\begin{aligned} \phi &= A \exp(-\kappa r z) \exp[i\kappa(x-c_R t)] \quad , \\ \Psi &= B \exp(-\kappa s z) \exp[i\kappa(x-c_R t)] \quad . \end{aligned}\right\} \tag{52}$$

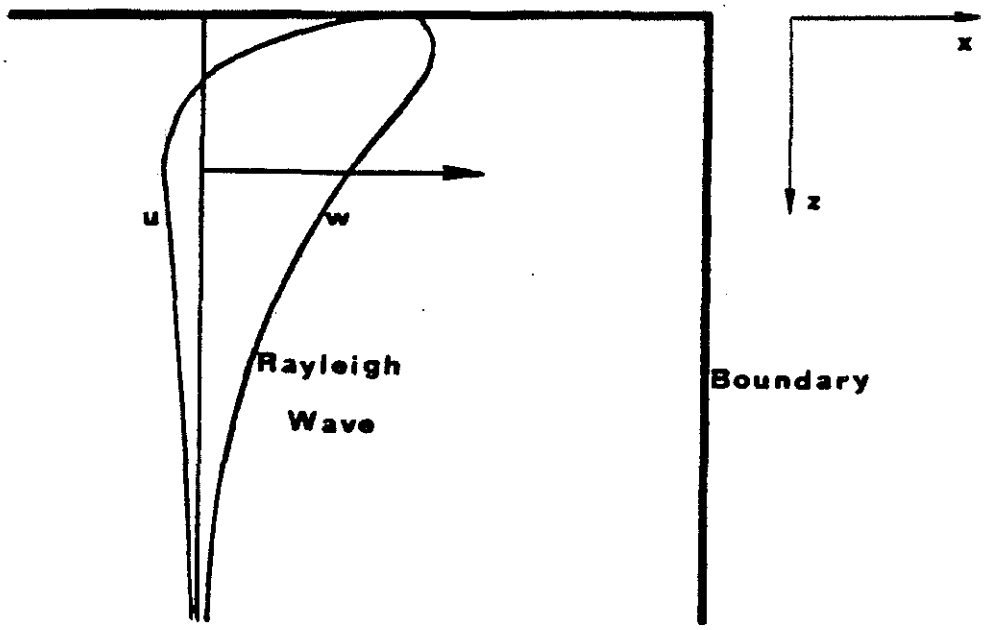

Figure 18. Schematic diagram of a Rayleigh wave approaching a boundary.

c_R = the Rayleigh wave speed, c_d = the dilatational wave speed, c_s = the shear wave speed, ω = the frequency of the wave, κ = the wave number = ω/c_R, $r = \sqrt{1-(c_R/c_d)^2}$, and $s = \sqrt{1-(c_R/c_s)^2}$. The displacements are given by equations (49):

$$u = \frac{\partial \phi}{\partial x} - \frac{\partial \Psi}{\partial z} \quad ,$$

$$w = \frac{\partial \phi}{\partial z} + \frac{\partial \Psi}{\partial x} \quad ,$$

or,

$$\left.\begin{aligned} u &= Ai\kappa \exp[-\kappa r z] \exp[i\kappa(x-c_R t)] \\ &\quad + B\kappa s \exp[-\kappa s z] \exp[i\kappa(x-c_R t)] \quad , \\ w &= -A\kappa r \exp[-\kappa r z] \exp[i\kappa(x-c_R t)] \\ &\quad + Bi\kappa \exp[-\kappa s z] \exp[i\kappa(x-c_R t)] \quad . \end{aligned}\right\} \tag{53}$$

A and B are related to each other through one of the free boundary conditions at z = 0. c_R is calculated by using the other free boundary condition. Miklowitz[86] discusses these solutions in more depth.

One set of paraxial equations which has equations (53) as a solution can be determined:

$$\left.\begin{aligned} u_{tt} + c_R u_{tx} &= 0 \quad , \\ w_{tt} + c_R w_{tx} &= 0 \quad . \end{aligned}\right\} \tag{54}$$

A boundary region governed by equations (54) is theoretically capable of transmitting these Rayleigh waves. However, it cannot absorb body waves as effectively as does the paraxial region using

equations (42). Therefore, we wish to assess the ability of the "body wave" paraxial equations to absorb Rayleigh-wave motion.

One way to do this is to determine the degree of modification required to change the paraxial equations into absorbers of Rayleigh waves. Beginning with equations (42), the paraxial equation for Rayleigh waves can be written as:

$$\underset{\sim}{M}_b \underset{\sim}{u}_{tt} + \underset{\sim}{C}_x \underset{\sim}{u}_{tx} + \underset{\sim}{C}_z \underset{\sim}{u}_{tz} + \underset{\sim}{K}_b \underset{\sim}{u}_{zz} + \underset{\sim}{L}(\underset{\sim}{u}) = 0 \quad . \tag{55}$$

$\underset{\sim}{M}_b$, $\underset{\sim}{C}_x$, $\underset{\sim}{C}_z$, and $\underset{\sim}{K}_b$ are the constant-coefficient matrices as defined by equations (37). $\underset{\sim}{L}$ is an added linear operator which allows equations (55) to be satisfied in the case of Rayleigh waves.

If one substitutes the solution (53) into equations (55), he can determine the magnitudes of the respective terms in (55).

$$\left.\begin{aligned} &(R^{tt1} + R^{xt1} + R^{zt1} + R^{zz1} + R^{L1}) \exp(-\kappa r z) \\ &+ (S^{tt1} + S^{xt1} + S^{zt1} + S^{zz1} + R^{L1}) \exp(-\kappa s z) = 0 \quad , \\ &(R^{tt2} + R^{xt2} + R^{zt2} + R^{zz2} + R^{L2}) \exp(-\kappa r z) \\ &+ (S^{tt2} + S^{xt2} + S^{zt2} + S^{zz2} + S^{L2}) \exp(-\kappa s z) = 0 \quad , \end{aligned}\right\} \tag{56}$$

where R^{tt}, R^{xt}, R^{zt}, R^{zz}; and S^{tt}, S^{xt}, S^{zt}, S^{zz} are the normalized coefficients of $\underset{\sim}{u}_{tt}$, $\underset{\sim}{u}_{tx}$, $\underset{\sim}{u}_{tz}$, and $\underset{\sim}{u}_{zz}$ respectively. R^L and S^L are the coefficients necessary to make equation (56) valid. These terms are produced by the operator, $\underset{\sim}{L}$. The numerical values of the resulting coefficients for $\nu = 0$ and $\nu = .45$ are listed in Tables 1 and 2.

	$\underset{\sim}{u}_{tt}$	$\underset{\sim}{u}_{tx}$	$\underset{\sim}{u}_{tz}$	$\underset{\sim}{u}_{zz}$	$\underset{\sim}{L}$
R_1	-.619	1	-.181	-.206	.006
S_1	-.380	.614	-.180	-.048	-.006
R_2	.486	-.555	-.230	.357	-.058
S_2	-.789	.901	.087	-.219	.020

Table 1 - $\nu = 0$

	$\underset{\sim}{u}_{tt}$	$\underset{\sim}{u}_{tx}$	$\underset{\sim}{u}_{tz}$	$\underset{\sim}{u}_{zz}$	$\underset{\sim}{L}$
R_1	-.287	1	-.642	-	-.071
S_1	-.156	.545	-.381	-	-.008
R_2	.275	-.289	-.669	.785	-.102
S_2	-.501	.526	.119	-.152	+.008

Table 2 - $\nu = .45$

The values of the coefficients for other Poisson's ratios are in the same range as those presented in Tables 1 and 2.

In order to render the modified-paraxial equations (55) into perfect Rayleigh-wave absorbers, we would need to determine the operator, $\underset{\sim}{L}$. However, it is clear from Tables 1 and 2 that $\underset{\sim}{L}$ makes only a small contribution to equations (55). The other terms in these equations account for almost all of the Rayleigh-wave behavior suggesting that it is permissible to neglect the second-order effects of $\underset{\sim}{L}$. This is not a proof that the modified-paraxial boundary can transmit

positively-directed Rayleigh waves. It does indicate, however, that the boundary can absorb these waves just as it largely absorbs body waves. An example of Rayleigh-wave transmission is presented in Chapter 4.

The efficacy of the standard viscous boundary in the transmission of Rayleigh waves is largely untested. Lysmer and Kuhlmeyer[47] pointed out that because of the waves' exponential decay in the z direction, the formerly constant parameters, a and b, should also be functions of z. The authors' plots of the required coefficients, as a function of the normalized depth, κz, are reproduced in Figure 19.

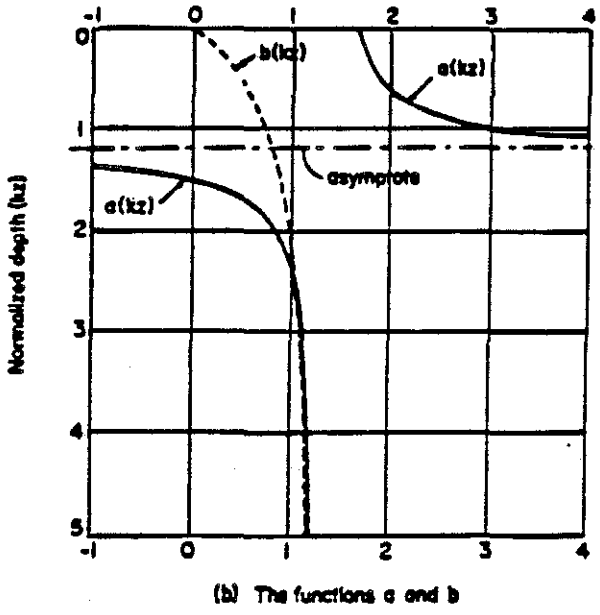

Figure 19. The functions $a(\kappa z)$ and $b(\kappa z)$ used for Rayleigh waves, as proposed by Lysmer and Kuhlemeyer.[47]

As can be seen from Figure 19, these viscous coefficients vary with κ, and therefore, they are frequency dependent. One must know in advance the frequency of the incoming waves and implement the correct values for $a(\kappa z)$ and $b(\kappa z)$ accordingly. Thus, the boundary may be applied for steady-state problems, but it is not suitable for transient analysis. The frequency-dependent coefficients are also more cumbersome to apply than are the constant coefficients designed for body waves.

In a practical sense, it is not clear that the use of the variable coefficients would improve the absorption of Rayleigh waves. It would be extremely difficult, by employing a finite element mesh, to approximate the variation in $a(\kappa z)$ from $-\infty$ to $+\infty$ (which is illustrated in Figure 19). Further, as will be pointed out in Chapter 4, the behavior of the viscous boundaries is relatively insensitive to changes in a and b.

Another set of boundary stresses, which cancel exactly the stresses induced by Rayleigh waves are:

$$\left.\begin{aligned} \sigma_{xx} &= \frac{-\rho c_d^2}{c_R} u_t + \lambda w_z \quad , \\ \tau_{xz} &= \mu u_z - \frac{\rho c_s^2}{c_R} w_t \quad , \end{aligned}\right\} \tag{57}$$

in which μ and λ are Lamé's elastic parameters. Equations (57) were derived by first substituting the wave potentials, equations (52) into the stress equations (50), and then cancelling these terms with the addition of u_t, w_t, u_z, and w_z terms.

The advantage of using the boundary equations (57) is that their effectiveness, in theory, is independent of frequency just as the standard-viscous boundary is independent of frequency. Upon implementing them, we found, however that certain numerical procedures have to be modified in order to render the scheme workable. The boundary causes a significant reduction in the critical time step for the explicit part of the solution algorithm (which is described in Chapter 3). For the implicit part, the u_z and w_z terms lead to nonsymmetrical matrices, hence, a nonsymmetrical equation solver is required. These particular restrictions violate the silent-boundary criteria that we shall set forth in Section II.A of Chapter 3. For this reason, the Rayleigh-wave boundary (57) was not pursued. However, if the above considerations are relatively less important, then the boundary stresses (57) may be useful for Rayleigh-wave applications.

IX. OTHER SILENT-BOUNDARY APPLICATIONS

IX.A. Spherically Symmetric Case

The paraxial, and viscous boundaries, can be easily derived for this one-dimensional system. The spherically symmetric equation of elasticity is:

$$u_{rr} + \frac{2u_r}{r} - \frac{2u}{r^2} = \frac{u_{tt}}{c_d^2} \quad , \tag{58}$$

wherein u is the radial displacement, and r is the radial coordinate. The solution to equation (58), expressed in terms of a potential ϕ, is:(86)

$$\phi = \frac{1}{r} f(r - c_d t) + \frac{1}{r} g(r + c_d t) \quad , \tag{59}$$

$$u = \frac{\partial \phi}{\partial r} \quad . \tag{60}$$

If we consider only outwardly radiating waves,

$$\left.\begin{aligned} \phi &= \frac{1}{r} f(r - c_d t) \quad , \\ u &= -\frac{1}{r^2} f(r - c_d t) + \frac{1}{r} f'(r - c_d t) \quad . \end{aligned}\right\} \tag{61}$$

One, partial differential equation which has equations (61) as its approximate solution is:

$$u_{tt} + c_d u_{tr} + \frac{c_d}{r} u_t = 0 \quad . \tag{62}$$

The substitution of equations (61) into (62) produces a residual term, $\frac{-f'(r-c_d)\ c_d^{\,2}}{r^3}$, which grows smaller as r increases (assuming that $f'(r-c_d t)$ is bounded for large r). Equation (62) appears to be a suitable paraxial approximation for outwardly (positive-r) radiating waves, and it may be useful for spherically symmetric problems.

The corresponding viscous boundary employs the boundary stress,

$$\sigma_{rr} = -\rho c_d u_t \quad . \tag{63}$$

Castellani[38] discusses this version of the viscous boundary. He offers a method for evaluating its effectiveness, which we believe can be adapted to the paraxial equation (62). It compares stresses not

canceled by the viscous boundary to those stresses created by the incident wave. The author begins with the assumption that

$$u = \frac{1}{r} f(r - c_d t) \quad , \tag{64}$$

but a broader spectrum of problems is covered by equations (61), after which we may apply his analysis. It turns out that both the paraxial, and viscous boundaries are frequency dependent. Using a given r, they behave more capably for high frequency motion.

IX.B. Axially Symmetric Waves

We present a preliminary investigation of the viscous boundary's effectiveness for the axially symmetric case. The derivation and implementation of the paraxial boundary, though not pursued here, follows from this analysis and the procedures outlined earlier in this chapter.

The displacements, which are axially symmetric about the z-axis, are represented by:

$$\left.\begin{aligned} u &= u(r,z,t) \quad , \qquad w = w(r,z,t) \quad , \\ v &= 0 \quad , \qquad \text{and} \qquad \frac{\partial}{\partial \theta} = 0 \quad , \end{aligned}\right\} \tag{65}$$

in which u = the radial displacement, w = the displacement in the z direction, and v = the displacement in the θ direction.

Using equation (65), the elastic, displacement-potential relations are [see Miklowitz,[86] pg. 220]:

$$\left.\begin{aligned} u &= \phi_r + \eta_{rz} \\ w &= \phi_z - \frac{\eta_r}{r} - \eta_{rr} \end{aligned}\right. \tag{66}$$

and

$$\left.\begin{aligned} \phi &= A^{*} J_0(\eta_d r) \exp\,[i\kappa(z-ct)] \quad , \\ \eta &= B^{*} J_0(\eta_s r) \exp\,[i\kappa(z-ct)] \quad , \end{aligned}\right\} \tag{67}$$

where J_0 is the zeroth-order Bessel function, $\eta_d = \frac{\omega}{c_d} \cos\alpha$, $\eta_s = \frac{\omega}{c_s} \cos\beta$, α and β are the angles of incidence, κ = the wave number = $2\pi/L$, L = the wavelength, and $L_d = \frac{c_d}{c} L$.

If $\eta_d r$ and $\eta_s r$ are "large", then the potentials (67) become:

$$\left.\begin{aligned} \phi &= \frac{A}{r^{1/2}} \exp\left[i\omega \left(\pm \frac{\cos\alpha}{c_d} r + \frac{\sin\alpha}{c_d} z - t \right) \right] \quad , \\ \eta &= \frac{B}{r^{1/2}} \exp\left[i\omega \left(\pm \frac{\cos\beta}{c_s} r + \frac{\sin\beta}{c_s} z - t \right) \right] \quad , \end{aligned}\right\} \tag{68}$$

with

$$\left.\begin{aligned} A &= \frac{A^{*}(1 \mp i)}{2(\eta_d \pi)^{1/2}} \quad , \\ B &= \frac{B^{*}(1 \mp i)}{2(\eta_s \pi)^{1/2}} \quad . \end{aligned}\right\} \tag{69}$$

The Bessel function, $J_0(x)$, along with the function,

$$f(x) = \frac{1}{(\pi x)^{1/2}} [\cos x + \sin x] \quad , \tag{70}$$

is plotted in Figure 20. The two functions are nearly equivalent for $x \geq 1$, but they part company near the origin. In the range, $1 \leq x \leq 5$, the approximation (70) is equal to $J_0(x)$ up to 1 or 2 decimal places; for $5 \leq x \leq 20$, equation (70) gradually approaches 3 place accuracy. When cos x and sin x in equation (70) are replaced with e^{ix} and e^{-ix},

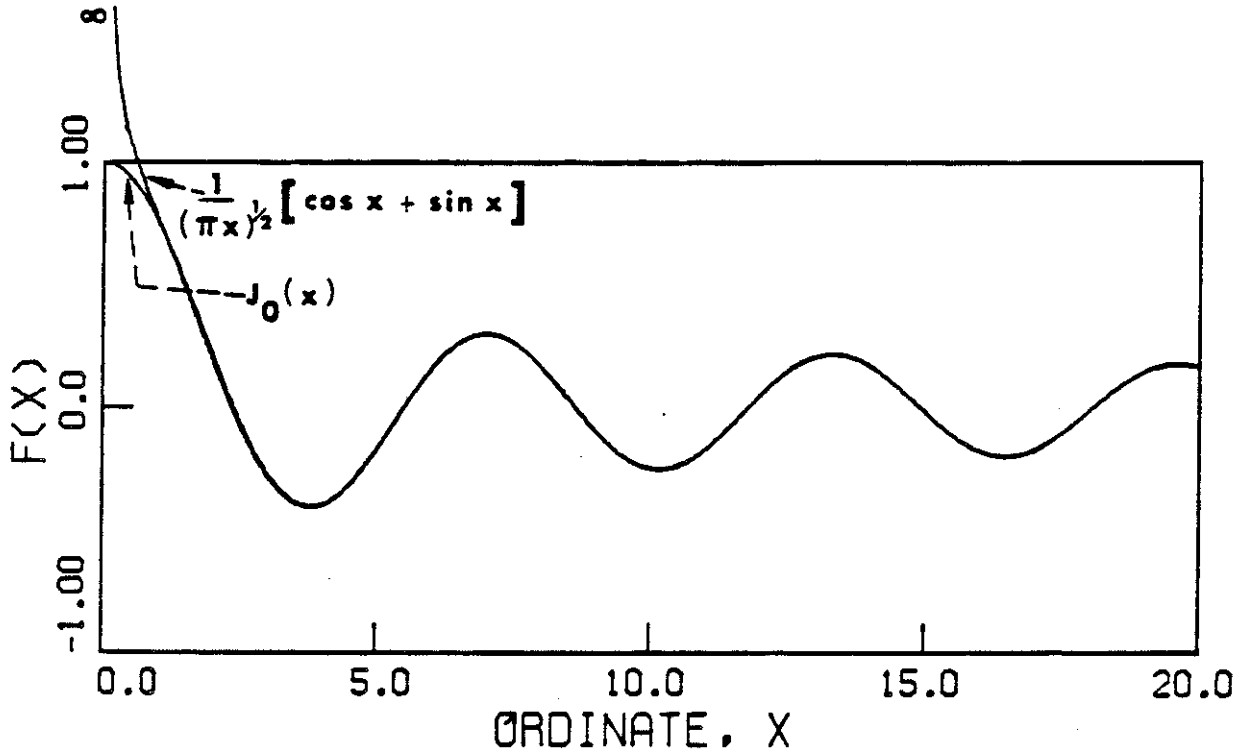

Figure 20. Comparison of the Bessel function, $J_0(x)$, to the function, $\frac{1}{(\pi x)^{1/2}}$ (cos x + sin x).

the outwardly (+x), and inwardly moving waves can be distinguished. Thus, the potentials (68) result from the approximation of the potentials (67).

If we assume that the approximation (68) holds, then the potentials for incident and reflected waves, shown in Figure 21, are:

$$\begin{aligned}
\phi_I &= I_p r^{-1/2} \exp\left[i\omega\left(\frac{\cos\alpha}{c_d} r + \frac{\sin\alpha}{c_d} z - t\right)\right] \quad , \\
\phi_R &= A_p r^{-1/2} \exp\left[i\omega\left(-\frac{\cos\alpha}{c_d} r + \frac{\sin\alpha}{c_d} z - t\right)\right] \quad , \\
\eta_I &= I_s r^{-1/2} \exp\left[i\omega\left(\frac{\cos\beta}{c_s} r + \frac{\sin\beta}{c_s} z - t\right)\right] \quad , \\
\eta_R &= A_s r^{-1/2} \exp\left[i\omega\left(-\frac{\cos\beta}{c_s} r + \frac{\sin\beta}{c_s} z - t\right)\right] \quad ,
\end{aligned} \tag{71}$$

and

$$\left.\begin{aligned}
\phi &= \phi_I + \phi_R \quad , \\
\eta &= \eta_I + \eta_R \quad .
\end{aligned}\right\} \tag{72}$$

I_p and A_p are labeled as "P" wave coefficients: I_s and A_s are called "S" wave amplitudes. This is analogous to the wave-reflection analysis in Section 7.

The elastic stresses at the boundary shown in Figure 21 are:

$$\begin{aligned}
\sigma_{rr} &= \frac{\lambda}{c_d^2} \phi_{tt} + 2\mu(\phi_{rr} + \eta_{rrz}) \quad , \\
\sigma_{rz} &= 2\mu\phi_{rz} + \mu\eta_{rzz} + \mu\left(\frac{\eta_r}{r^2} - \frac{\eta_{rr}}{r} - \eta_{rrr}\right) \quad .
\end{aligned} \tag{73}$$

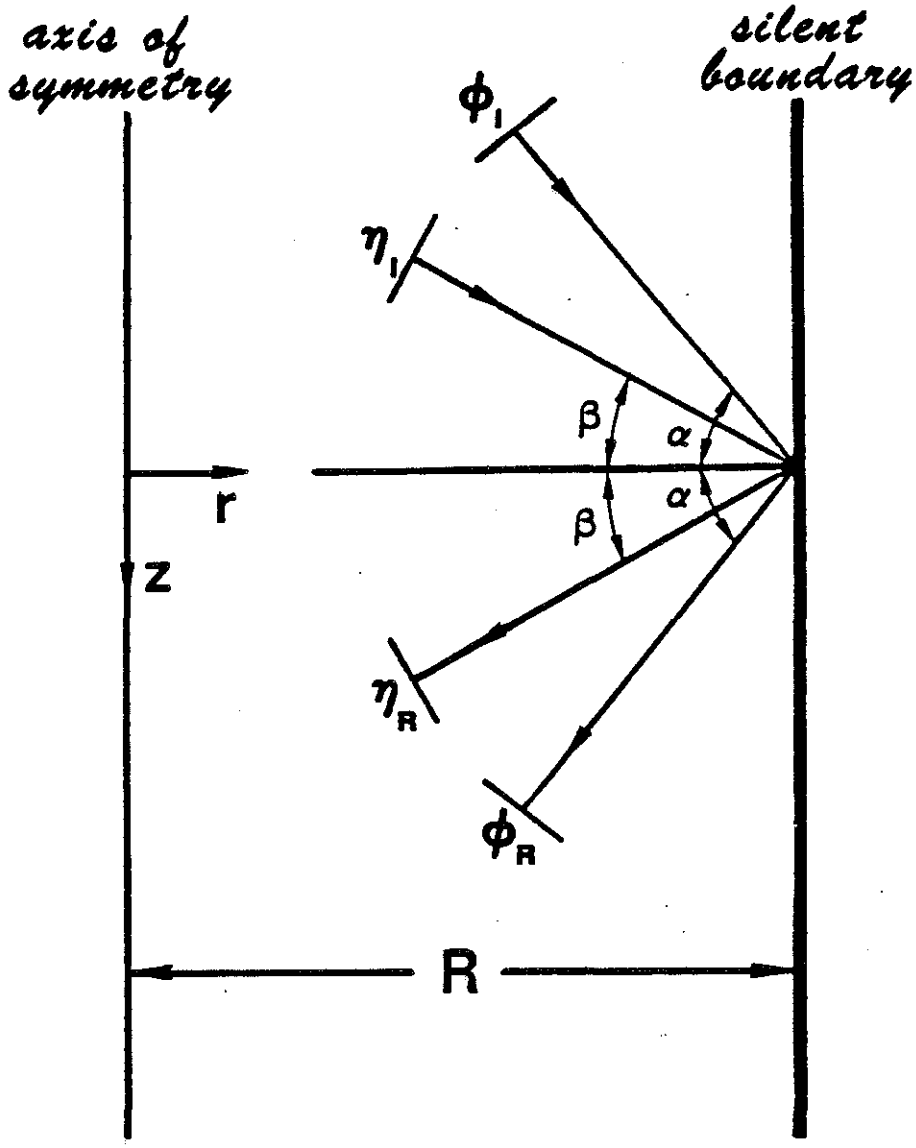

Figure 21. Illustration of waves reflecting from an axially symmetric boundary.

If one would employ a free boundary, these stresses would be set equal to zero. For the standard-viscous boundary, however, the boundary stresses are defined as:

$$\begin{aligned} \sigma_{rr} &= -\rho c_d u_t \quad , \\ \sigma_{rz} &= -\rho c_s w_t \quad . \end{aligned} \tag{74}$$

The substitution of the displacement-potential relations (66) into the viscous stresses (74) produces:

$$\begin{aligned} \sigma_{rr} &= -\rho c_d \phi_{rt} - \rho c_d \eta_{rzt} \quad , \\ \sigma_{rz} &= -\rho c_s \phi_{zt} + \rho c_s \eta_{rt} + \rho c_s \eta_{rrt} \quad . \end{aligned} \tag{75}$$

The stresses (73) are set equal to those in equations (75). If one now substitutes the potentials (69) and (72) into equations (73) and (75), he obtains two equations for the solutions of the two unknowns, A_p and A_s.

For purposes of comparison to the plane-strain case, we can determine the amplitudes of the potential, ψ, used in the analysis in Section VII. The vector potential, $\underset{\sim}{\psi}$, is related to η by equation (76),

$$\underset{\sim}{\psi} = \nabla \times \eta \underset{\sim}{z} \quad , \tag{76}$$

in which $\nabla \times$ is the symbol for the curl of a vector, and $\underset{\sim}{z}$ is the unit vector in the z direction. In our case,

$$\psi = -\eta_r \quad . \tag{77}$$

When

$$\psi = A_\psi r^{-1/2} \exp\left[i\omega \left(-\frac{\cos\beta}{c_s} r + \frac{\sin\beta}{c_s} z - \omega t \right) \right] \quad , \tag{78}$$

then

$$A_\psi = \left[\frac{1}{2} + \frac{i\omega}{c_s} c_d \left(\frac{R}{L_d} \right) \cos\beta \right] \left(\frac{A_s}{r} \right) \quad . \tag{79}$$

The results for an incident "P" wave ($I_1 = 1$, $I_s = 0$) are illustrated

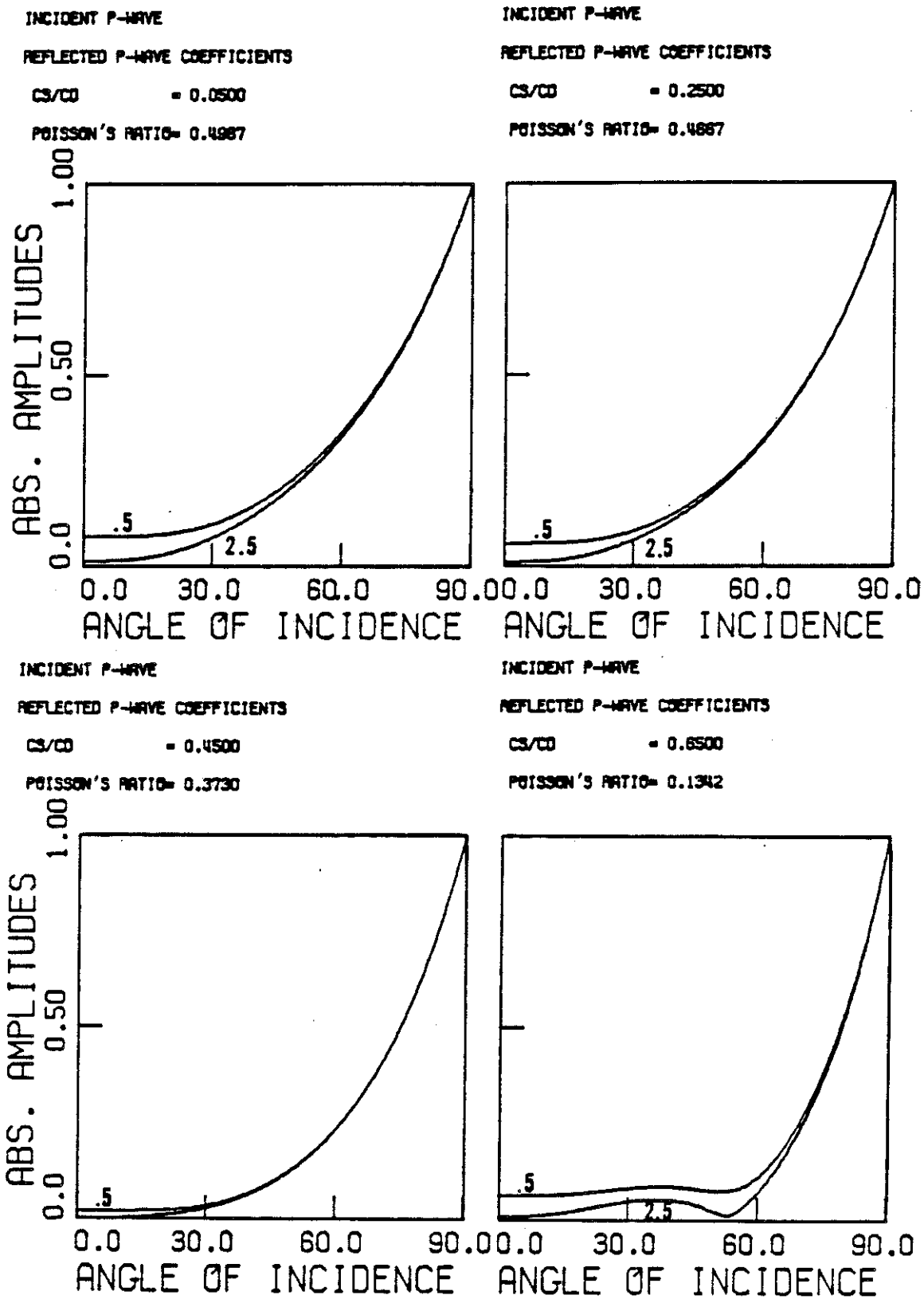

Figure 22. Absolute amplitudes of reflected waves for various angles of incidence (axial symmetry).

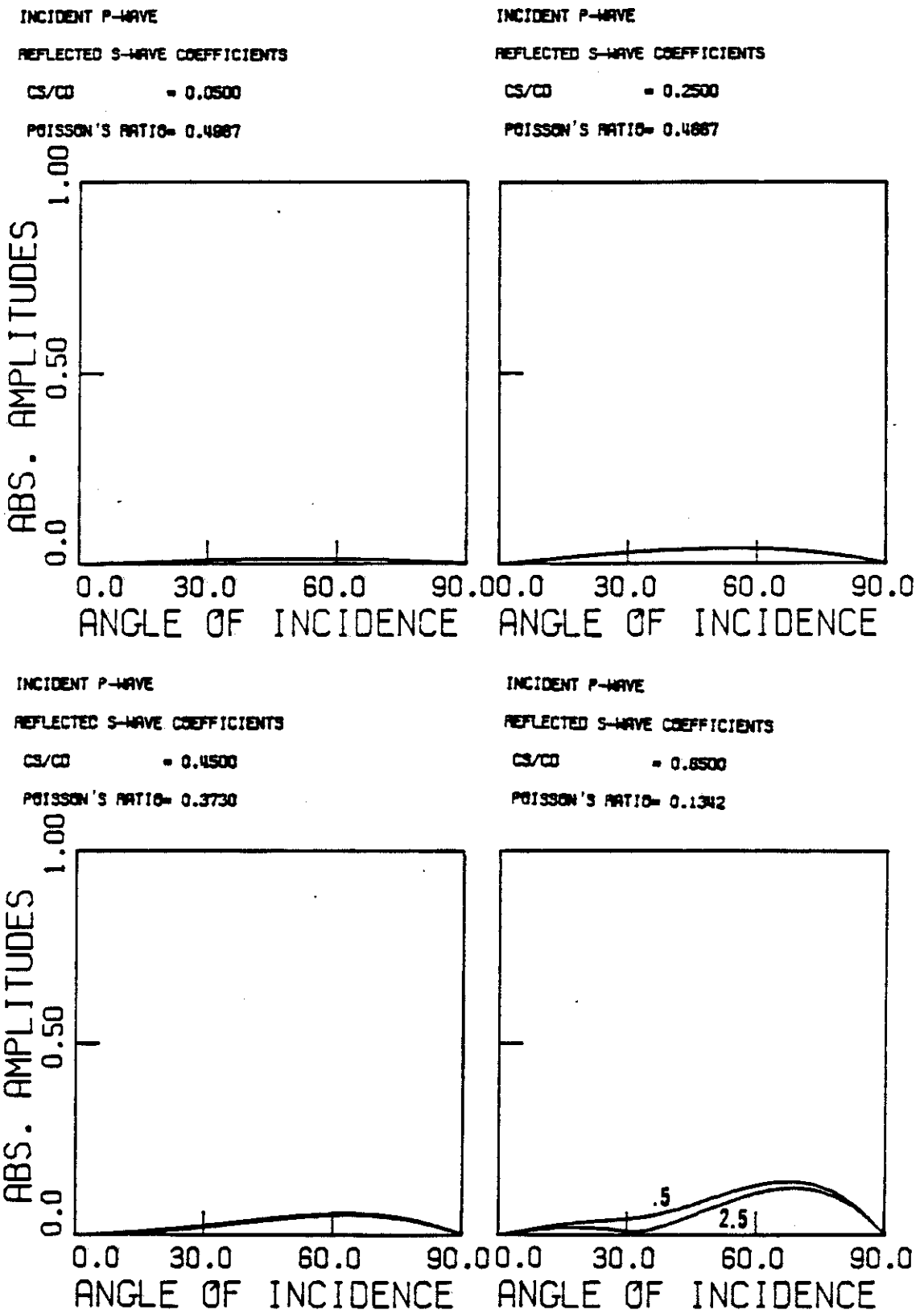

Figure 23. Absolute amplitudes of reflected waves for various angles of incidence (axial symmetry).

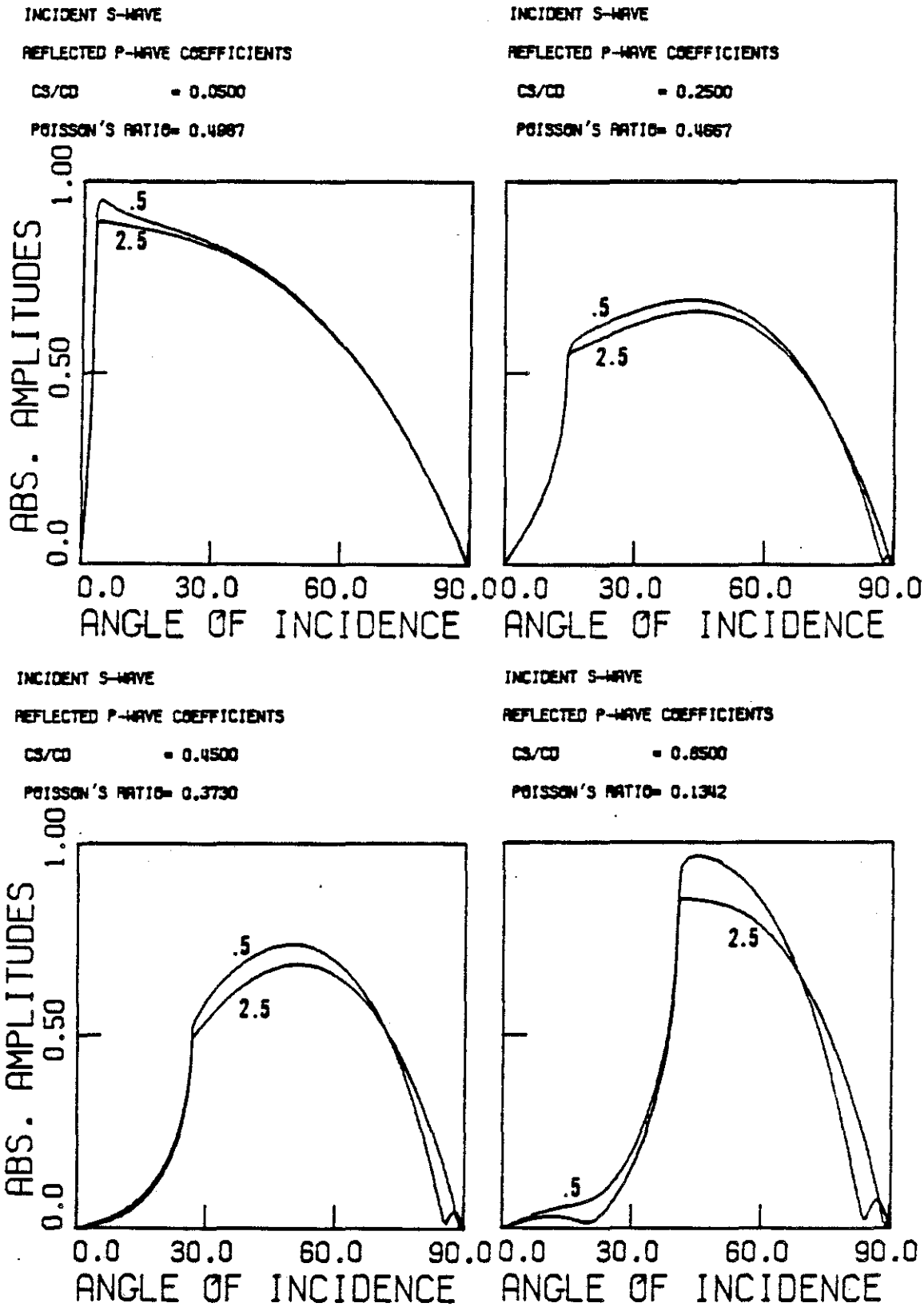

Figure 24. Absolute amplitudes of reflected waves for various angles of incidence (axial symmetry).

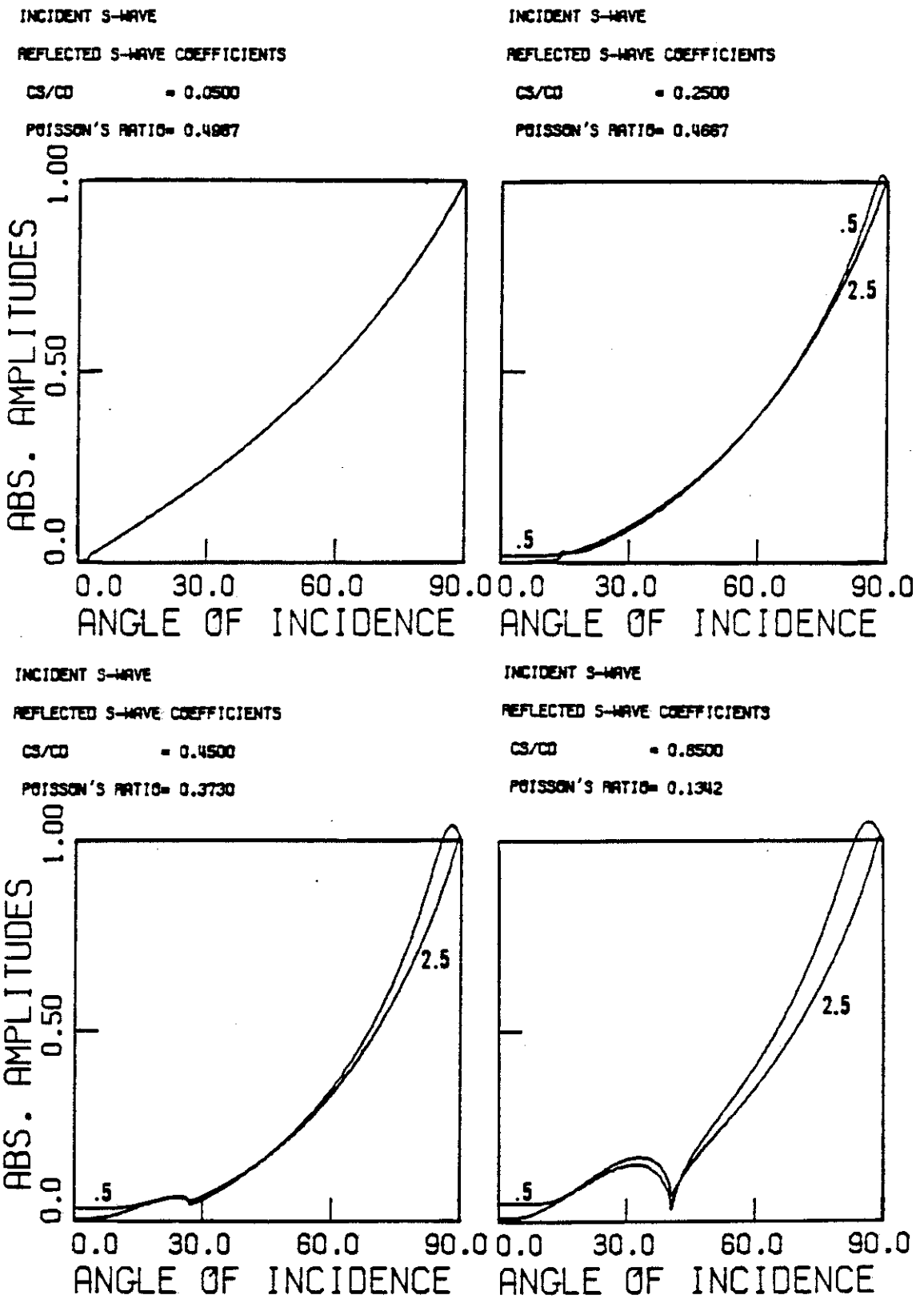

Figure 25. Absolute amplitudes of reflected waves for various angles of incidence (axial symmetry).

in Figures 22 and 23; the "S" wave reflections are shown in Figures 24 and 25. The numerals '.5' and '2.5' in the figures denote the reflection coefficients calculated with $R/L_d = .5$, and $R/L_d = 2.5$, respectively. R is the distance from the axis of symmetry to the viscous boundary.

Several preliminary conclusions can be gathered from the results in the figures. Unlike the plane-strain case, the axially symmetric, viscous boundary depends on R/L_d, and is therefore frequency dependent. Although the boundary's accuracy is greater for higher frequency waves, it does not significantly downgrade in the range of R/L_d shown. This result would seem to be corroborated in [57].

One may also notice that the axially symmetric amplitudes, with $R/L_d = 2.5$, are nearly identical to the corresponding, plane-strain results in Section VII.[3] As R/L_d is decreased, the differences become perceptible. The curves with $R/L_d = .5$ intimate a trend of increased reflections for smaller ratios of R/L_d. One must be aware, however, that at certain values of R/L_d and α, the argument in the Bessel function (67), $2\pi \cos\alpha\ R/L_d$, becomes too small for the approximation (68) to adequately represent the elastic-wave solutions. This error is manifested in Figure 25. Here, the fact that some reflection amplitudes exceed one, when α is close to 90^o, is a consequence of using the simplification (68).

Some authors have implemented the viscous boundary for axially symmetric waves and have attained mixed results. Lysmer and Kuhlemeyer,[47] having discovered the energy-absorbing potential of

---

[3] We review the characteristics of the plane-strain curves in Section VII. That discussion explains the large reflections observed in Figure 23, and the kinks in the curves of Figures 21, 22, and 24.

the standard-viscous boundary for plane waves, proceeded to apply the boundary to axially symmetric problems. The boundary was situated at $R/L_R = .75$ and $R/L_R = 1.50$, which correspond to $R/L_d = .35$ and $R/L_d = .69$, respectively. (L_R = the Rayleigh wavelength, Poisson's ratio = 1/3.) The authors' results indicate good agreement with analytical solutions when $R/L_d = .69$, but the boundary with $R/L_d = .35$ acquits itself only fairly. These test results appear to be consistent with the reflection curves in Figures 22-25.

Baladi[37] also scrutinized the standard-viscous boundary in an axially symmetric setting. His boundary was aligned parallel to the r axis, so that it absorbed waves travelling in the z-direction. (The transmission of waves in the r direction was analyzed above.) The author found generally satisfactory agreement between the silent-boundary results and those produced with an extended mesh.

In summary, it appears that the standard-viscous boundary is suitable for axially symmetric waves. What limited data are available in the literature tend to confirm this suposition.

CHAPTER 3

I. INTRODUCTION

The analyses of Chapter 2 suggest that the previously-discussed boundary schemes could reproduce most of the effects of an infinite domain. There are, however, a number of practical limitations to their usage which one must consider. For example, we need to appraise the boundary's numerical stability. If a silent boundary demands a smaller critical time step than does the interior region, it may engender larger computer costs. Also, problems in accuracy may arise in the numerical treatment of the boundary terms.

Our chosen numerical algorithm is described in this chapter. We discuss the problems of employing a paraxial boundary, and then the implementation of the two viscous boundaries. After this, the numerical stability of the boundaries is evaluated. Finally, in the last section, we compare some numerical solutions to analytical ones. This is done in order to validate our numerical procedures and their implementation.

II. FINITE-ELEMENT PROCEDURES

II.A. Implicit-Explicit Algorithm

Our time-domain solution method, which was developed by Hughes and Liu,[76] is called the Implicit-Explicit method. The basic procedure is outlined in Appendix B and more of its properties are discussed in references [77] and [78].

The algorithm enjoys considerable versatility in coping with transient problems. One can effectively divide the domain of analysis into "implicit" and "explicit" regions, thus capitalizing on the

advantages of each scheme. For example, a nonlinear region could be treated explicitly in order to save factorization costs. On the other hand, implicit elements have superior, numerical-stability properties, and would function well for relatively stiff elements.

II.B. Finite-Element Implementation of the Paraxial Boundary

II.B.1 General Considerations

We recall the one-dimensional, paraxial equation -- equation (9) of Chapter 2.

$$u_{tt} + cu_{tx} = 0 \quad . \tag{1}$$

Appendix (A) briefly shows how the application of finite-element procedures to the u_{tx} term leads to a nonsymmetrical matrix. The equation of motion, including both interior and boundary contributions, is:

$$\underset{\sim}{M}\underset{\sim}{d}_{tt} + \underset{\sim}{C}\underset{\sim}{d}_{t} + \underset{\sim}{K}\underset{\sim}{d} + \underset{\sim}{N}(\underset{\sim}{d}) = \underset{\sim}{F} \quad . \tag{2a}$$

$\underset{\sim}{C}$ is the matrix which is derived from the boundary term, u_{tx}; $\underset{\sim}{N}$ is a nonlinear operator in the interior. Equation (2a) may be solved with a variety of numerical algorithms, all of which lead to

$$K^{*(j)}{}_{d_{n+1}}{}^{(j+1)} = F^{*(j)} \quad , \tag{2b}$$

in one form or another. 'n' denotes the time step number, and 'j' is an iteration counter. $\underset{\sim}{K}^{*}$ may include components derived from $\underset{\sim}{M}$, $\underset{\sim}{C}$, $\underset{\sim}{K}$, or $\underset{\sim}{N}$.

If the contributions from $\underset{\sim}{M}$, $\underset{\sim}{K}$, and $\underset{\sim}{N}$ are symmetrical matrices, then the use of a nonsymmetrical boundary matrix, $\underset{\sim}{C}$, would require a doubling of the storage on the left-hand side. It would also demand a

nonsymmetrical equation solver, which needs twice the time to reduce a given matrix than does a symmetrical solver. An explicit, paraxial-boundary scheme does not suffer from the above difficulties and is therefore chosen. The explicit algorithm, however, does limit the allowable time step (see Section IV of this chapter for a discussion of numerical stability).

II.B.2 Upwinding

As was noted above, the finite-element treatment of the u_{tx} term leads to a nonsymmetrical matrix, $\underset{\sim}{C}$. In other problems which generate nonsymmetrical matrices, it has been observed that spurious oscillations can occur in, for example, a large range of fluid-dynamics problems. In many respects, the paraxial equations are similar to the equations of fluid mechanics. In our case, u_{tx} serves as a convective mechanism for transporting energy across a domain.

We can evaluate the behavior of the extended-paraxial equations, for a one-dimensional mesh which is drawn in figure 1.

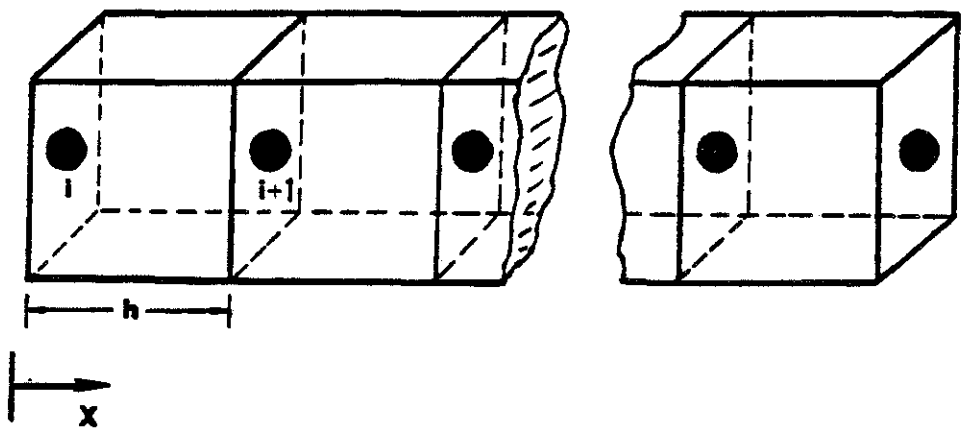

Figure 1. Schematic diagram of an elastic bar which is discretized into a one-dimensional mesh.

From Appendix A:

$$\underset{\sim}{m} = \frac{h}{2}\begin{bmatrix} 1 & 0 \\ 0 & 1 \end{bmatrix} , \tag{3}$$

$$c_{ab} = c\int_{-1}^{1} N_a N_{b,x}\,dx = 2cN_a(\xi_\ell)N_{b,\xi}(\xi_\ell) \quad ,$$

$$\underset{\sim}{c} = \frac{c}{2}\begin{bmatrix} -(1-\xi_\ell) & (1-\xi_\ell) \\ -(1+\xi_\ell) & (1+\xi_\ell) \end{bmatrix} . \tag{4}$$

ξ_ℓ is the location of the integration point in ξ-space, as is shown in figure 2.

If we rewrite the Implicit-Explicit algorithm (Appendix B) in terms of an explicit calculation for the velocity, $\underset{\sim}{v}_{n+1}$, we find that

$$\frac{1}{\Delta t\gamma}\underset{\sim}{M}\,\underset{\sim}{v}_{n+1} = \frac{1}{\Delta t\gamma}\underset{\sim}{M}\,\tilde{\underset{\sim}{v}}_{n+1} - \underset{\sim}{C}\,\tilde{\underset{\sim}{v}}_{n+1} . \tag{5}$$

At a given time step, with the help of equations (3), (4), and (5), the equations for the paraxial nodes, i and i+1, are assembled.

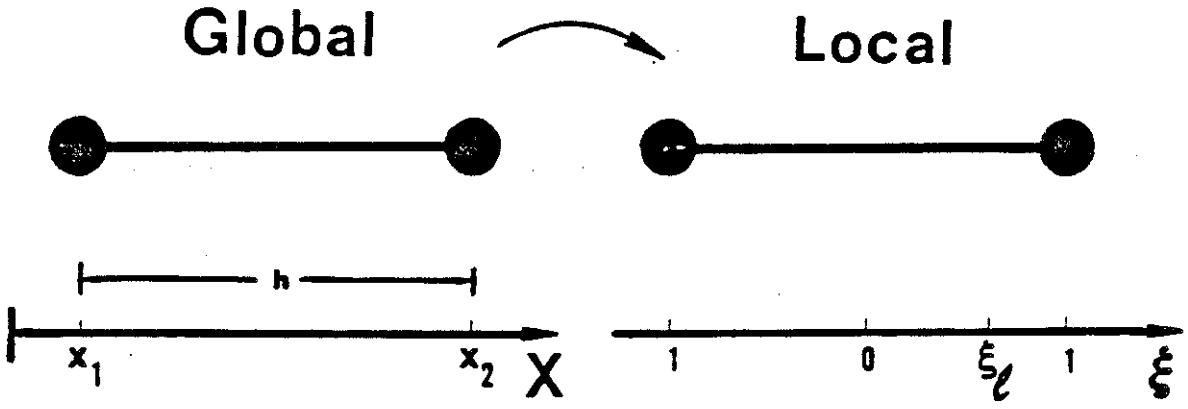

Figure 2. A one-dimensional, finite element shown in global and local coordinates.

$$\frac{h}{\gamma\Delta t}\begin{bmatrix}\frac{1}{2} & 0\\ 0 & 1\end{bmatrix}\begin{Bmatrix}v^i\\ v^{i+1}\end{Bmatrix} =$$

$$\begin{bmatrix}\left(\frac{h}{\Delta t\gamma 2}+c\xi_\ell\right) & -\frac{(1-\xi_\ell)c}{2}\\ c\,\frac{(1+\xi_\ell)}{2} & \frac{h}{\Delta t\gamma}-\frac{(1+\xi_\ell)c}{2}\end{bmatrix}\begin{Bmatrix}\tilde{v}^i\\ \tilde{v}^{i+1}\end{Bmatrix} = \underset{\sim}{0} \quad . \qquad (6)$$

The above algorithm performs optimally for the parameter $\gamma = 1/2$, and for the critical time step,

$$\Delta t = \frac{h}{c} \quad . \qquad (7)$$

For these particular values, we have

$$\begin{bmatrix}1 & 0\\ 0 & 2\end{bmatrix}\begin{Bmatrix}v^i\\ v^{i+1}\end{Bmatrix} = \begin{bmatrix}(1-\xi_\ell) & -\left(\frac{1-\xi_\ell}{2}\right)\\ \frac{(1+\xi_\ell)}{2} & \left(\frac{3}{2}-\frac{\xi_\ell}{2}\right)\end{bmatrix}\begin{Bmatrix}\tilde{v}^i\\ \tilde{v}^{i+1}\end{Bmatrix} = \underset{\sim}{0} \quad . \qquad (8)$$

$\tilde{\underset{\sim}{v}}$ represents the predicted velocities at this time step, and they are calculated from the velocities and accelerations of the previous step. In our case, for a velocity pulse traveling in an elastic material.

$$\left.\begin{aligned} v^i &= 1 \quad , & a^i &= 2 \quad ,\\ v^{i+1} &= 0 \quad , & a^{i+1} &= 0 \quad , \end{aligned}\right\} \ (n-1)^{th} \text{ step} \quad , \qquad (9)$$

in which a^i and a^{i+1} are accelerations for nodes i and i+1. One finds the n^{th} step predictors using the algorithm equations in Appendix B:

$$\left.\begin{aligned} \tilde{v}^i &= v^i + \Delta t(1-\gamma)a^i = 2 \quad , \\ \tilde{v}^{i+1} &= 0 \quad . \end{aligned}\right\} \; n^{th} \text{ step} \quad . \qquad (10)$$

Equations (9) and (10) result when the critical parameters of equation (7) are employed. Here, we assume that this wave has somehow entered the paraxial region at node i. For the chosen values of h, c, and Δt, the wave (9) should arrive at the next node, i+1. Hence, if the material were elastic, the correct solution for the n^{th} step is:

$$\left.\begin{aligned} v^i &= 0 \\ v^{i+1} &= 1 \end{aligned}\right\} \quad . \qquad (11)$$

The solution of the paraxial equations (8) is:

$$\left.\begin{aligned} v^i &= (1-\xi_\ell)\tilde{v}^i - \left(\frac{1-\xi_\ell}{2}\right)\tilde{v}^{i+1} \\ v^{i+1} &= \frac{1}{2}\left(\frac{1+\xi_\ell}{2}\right)\tilde{v}^i + \left(\frac{3}{2} - \frac{\xi_\ell}{2}\right)\tilde{v}^{i+1} \quad . \end{aligned}\right\} \qquad (12)$$

For this optimal case, the choosing of $\xi_\ell = 1$, in equation (12), produces the desired solution, (11). As ξ_ℓ is moved to the left, less and less of the wave is transmitted to the right. The location of ξ_ℓ, therefore, determines the character of the solution.

Hughes[73] demonstrates how this same quadrature idea applies to the steady, advection-diffusion equation in one-dimension.

$$\mu \frac{\partial u_t}{\partial x} = \frac{\partial}{\partial x}\left[k(x) \frac{\partial u_t}{\partial x}\right] \qquad (13)$$

The paraxial equation is a transient version of equation (13) [that is,

u_{tt} is added to equation (13), but k, the diffusivity coefficient in (13), equals zero.] Hughes[73] established that the integration point's location, ξ_ℓ, goes to one as k approaches zero.

The above examples illustrate the effect of quadrature upwinding. This technique is one way of "weighting" the finite element integration in the direction of the flow. Other "upwind" methods include the Petrov-Galerkin approach[67,68] and streamline upwinding.[74]

The Petrov-Galerkin method employs specially weighted functions, $\tilde{v}$, in the finite-element discretization. For example, in [66],

$$\left.\begin{aligned} \int_\Omega u_{tt}\,\tilde{v}\,dx + c\int_\Omega u_{tx}\,\tilde{v}\,dx &= \int_\Omega f\,\tilde{v}\,dx \quad , \\ \tilde{v} &= v + \frac{\tilde{k}\,u\,v_x}{u^2} \quad , \end{aligned}\right\} \tag{14}$$

where v is the weighting function of Appendix A, and $\tilde{k}$ is the numerical diffusivity coefficient. Brooks and Hughes[66] used it for an equation which is similar to the paraxial equation and obtained very good results. One reason we did not attempt to implement the boundary in this form is because it leads to a nonsymmetrical mass matrix. This not only leads to a more complicated elasticity/paraxial interface, it also rules out our preferred explicit boundary form.

Streamline upwinding[74] adds a numerical, diffusion term to the paraxial equations. It turns out that for this case, streamline and quadrature upwinding are identical. The latter technique is a little easier to implement.

In two- and three-dimensional cases, the paraxial equations are designed to be one-directional in the following sense. The $\underset{\sim}{u}_{tx}$ term was created in order to transmit energy in the general flow direction, as is shown in Figure 3, whereas $\underset{\sim}{u}_{tz}$ and $\underset{\sim}{u}_{zz}$ are the lower-order corrections for the angle of incidence. Hence, the quadrature points for $\underset{\sim}{u}_{tx}$ are located where shown in Figure 3.

There exist, for other two- and three-dimensional problems, upwind procedures which more accurately account for flows at different angles of incidence. The Petrov-Galerkin approach and streamline upwinding,

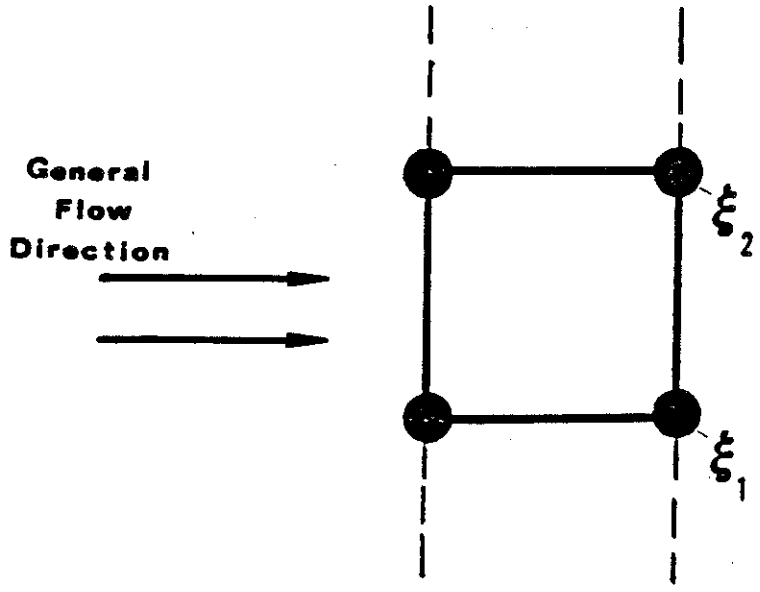

Figure 3. Location of the integration points, ξ_1 and ξ_2, with respect to the general flow direction.

both described above, are two such proposed methods. Which of all is the best technique is not clear, and research [66] is continuing in this area. In the above silent-boundary problem, however, this angle-of-incidence error is already "built-in" to the paraxial theory. Energy propagating at angles inclined to the boundary will be partially reflected regardless of the upwinding scheme. Therefore, an attempt to correct the flow errors that are caused by the discretization and integrating procedures may not render the boundary more efficient. We did experiment with adding artificial diffusion terms, but they did not have a significant effect on our results.

The $\underset{\sim}{u}_{tz}$ term is also integrated at the points shown in Figure 3. Because this quadrature scheme is symmetrical in the z direction, it does not upwind $\underset{\sim}{u}_{tz}$. This term could be integrated with the standard 2x2, or 1x1, Gaussian quadrature. The two-point integration method, however, seems to provide slightly better accuracy. The paraxial stiffness term, $\underset{\sim}{u}_{zz}$, was integrated using standard 2x2 quadrature. The quadrature method used for $\underset{\sim}{u}_{tz}$ and $\underset{\sim}{u}_{zz}$, however, does not significantly affect the boundary's efficacy because they are the lower-order, paraxial terms.

II.B.3 Assembling Procedure

The algorithm we employed in our transient calculations (see Appendix B for details) performs well for waves in either the elastic medium or the paraxial medium. We found, however, that an interfacing effect inhibits elastic waves from smoothly proceeding into the paraxial area. The method developed to circumvent this problem, an element-assembly procedure, is portrayed in Figure 4.

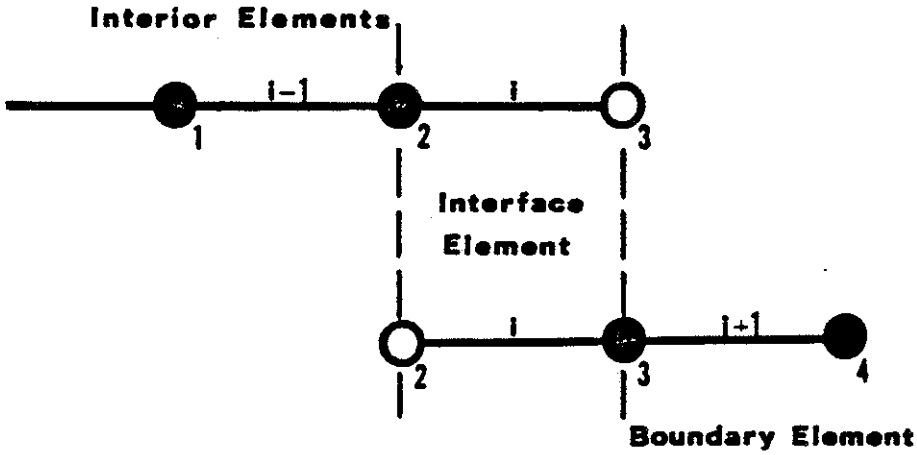

Figure 4. Schematic diagram of the interface elements. The top row of nodes are elastic while the bottom row are in the paraxial region.

The finite-element equations for node 2 are written as if there are interior elements present on each side of it, while the equations for node 3 are formulated as if it were bracketed by boundary elements. In other words, the i^{th} element, shown in the picture, contributes regular-wave terms to node 2 and boundary terms to node 3. The mass matrix is unaffected because it remains uniform for all of the elements.

The reason for adopting this procedure is due to the apparent success of the finite difference solution, used by Clayton and Engquist.[39] The finite-element method of assembling contributions on an element basis simply did not work at the interface. Therefore, we

attempted to "finite difference" these interface nodes. The latter procedure allows the respective elastic and paraxial nodal equations to be assembled independently of each other. In the former approach, elastic and paraxial contributions were being added together in the same set of nodal equations. This led to the difficulty.

In two and three dimensions, the interface nodes are assembled in the same manner as is described above and shown in Figure 4.

We experimented with other ideas, such as employing a different algorithm for each of the two regions, or multiplying the paraxial equations by a factor which minimized the wave impedance. Although these methods were also successful, the above-described assembly procedure seemed to erase the interface effect most completely.

II.C. Numerical Implementation of the Viscous Boundary

The viscous stresses are applied continuously along the boundary, as is depicted in Chapter 2, Figure 6. Their contributions are assembled at the nodes through the use of one-dimensional, finite-element, shape functions (as shown in Figure 5, wherein linear shape functions are employed).

$$N_1 = N_4 = 0 \quad , \tag{15}$$

$$\left.\begin{aligned} N_2 &= \tfrac{1}{2}(1-\zeta) \quad , \\ N_3 &= \tfrac{1}{2}(1+\zeta) \quad , \end{aligned}\right\} \tag{16}$$

where ζ is the natural coordinate ($-1 \le \zeta \le 1$), and $\dot{u}_2$ and $\dot{u}_3$ are the nodal velocities.

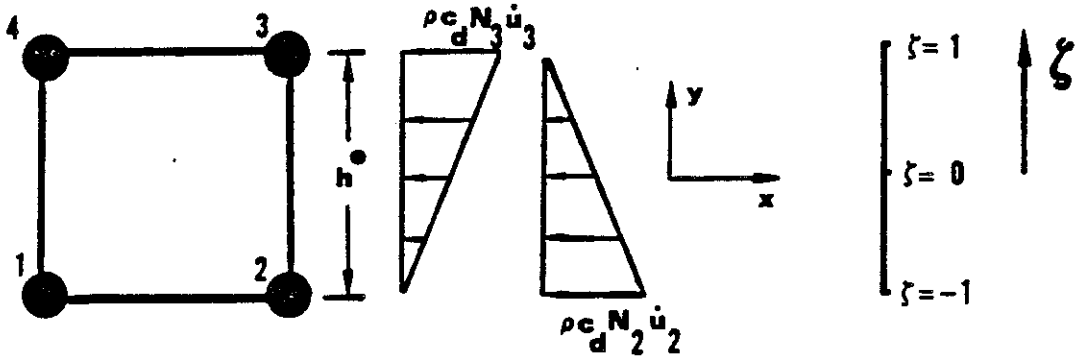

Figure 5. Distribution of the viscous stresses applied to a boundary element.

The boundary force, F_a, acting at node a is defined as:

$$F_a = \int_{y_2}^{y_3} N_a \sigma(y) dy$$

$$= \int_{-1}^{1} -N_a \rho c_d (N_2 \dot{u}_2 + N_3 \dot{u}_3) \frac{dy}{d\zeta} d\zeta \quad , \qquad \text{where a = 2,3.} \qquad (17)$$

If we substitute into equation (17) both $\frac{dy}{d\zeta} = \frac{h^e}{2}$ and the above defined shape-function equations, N_a, we find that:

$$\begin{Bmatrix} F_2 \\ F_3 \end{Bmatrix} = \frac{-\rho c_d h^e}{6} \begin{bmatrix} 2 & 1 \\ 1 & 2 \end{bmatrix} \begin{Bmatrix} \dot{u}_2 \\ \dot{u}_3 \end{Bmatrix} = -\underset{\sim}{C}\, \underset{\sim}{\dot{u}} \quad . \qquad (18)$$

Though we chose not to, it appears that one could "lump" the $\underset{\sim}{C}$ matrix in the same way that mass matrices are lumped. That is,

$$\underset{\sim}{C}_{\ell} = \frac{\rho c_d h^e}{2} \begin{bmatrix} 1 & 0 \\ 0 & 1 \end{bmatrix} \quad . \tag{19}$$

The boundary shear stresses are applied in the same manner as are the normal stresses. When the boundary parameters, a and b, are optimized, they multiply the appropriate terms in equation (18).

One advantage of the viscous boundary is that equations (18) and (19) are symmetric. Thus, one can convert this boundary to fit either an implicit, or an explicit algorithm without any difficulty. For an implicit algorithm, the symmetrical $\underset{\sim}{C}$ matrix enables us to easily determine the boundary's numerical stability. The boundary's simplicity is another major advantage. The $\underset{\sim}{C}$ matrix is explicitly defined by equations (18) and (19), so there is little additional cost in making these contributions to the boundary elements.

III. NUMERICAL STABILITY OF THE EXTENDED-PARAXIAL AND VISCOUS BOUNDARIES

III.A. One-Dimensional Analysis (Paraxial Boundary)

We first consider the one-dimensional equation,

$$u_{tt} + c\, u_{tx} = 0 \quad . \tag{20}$$

The element mass and stiffness matrices, both derived from equation (20), are:

$$\left.\begin{aligned} \underset{\sim}{M} &= \frac{h}{2}\begin{bmatrix} 1 & 0 \\ 0 & 1 \end{bmatrix} , \\ \underset{\sim}{C} &= c\begin{bmatrix} 0 & 0 \\ -1 & 1 \end{bmatrix} . \end{aligned}\right\} \tag{21}$$

(See Appendix A.) Next, the global matrices are assembled for the discretized, paraxial region shown in Figure 6. Energy, propagating from the elastic region into the paraxial region, is considered to be external to the system, for the purpose of analyzing the stability. The assembled matrices are:

$$\left.\begin{aligned} \underset{\sim}{M} &= h\begin{bmatrix} 1 & & & & \\ & 1 & & \underset{\sim}{0} & \\ & & \ddots & & \\ & \underset{\sim}{0} & & 1 & \\ & & & & \frac{1}{2} \end{bmatrix} , \\ \underset{\sim}{C} &= c\begin{bmatrix} 1 & 0 & & & & \\ -1 & 1 & 0 & & \underset{\sim}{0} & \\ 0 & -1 & 1 & 0 & & \\ & & & \ddots & \ddots & \\ & \underset{\sim}{0} & & & 1 & 0 \\ & & & & -1 & 1 \end{bmatrix} , \end{aligned}\right\} \tag{22}$$

and

$$\underset{\sim}{K} = \underset{\sim}{0} \quad .$$

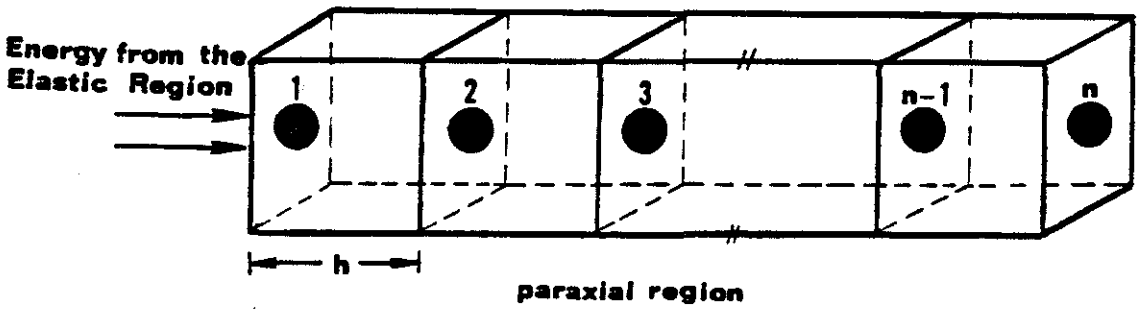

Figure 6. One-dimensional, discretized paraxial region being analyzed for numerical stability.

Hughes and Liu[76] write the algorithm equations, and the equations of motion, in terms of energy:

$$\underset{\sim}{a}_{n+1}^T \overline{\underset{\sim}{A}}\, \underset{\sim}{a}_{n+1} + \underset{\sim}{v}_{n+1}^T \underset{\sim}{K}\, \underset{\sim}{v}_{n+1}$$

$$= \underset{\sim}{a}_n^T \overline{\underset{\sim}{A}}\, \underset{\sim}{a}_n + \underset{\sim}{v}_n^T \underset{\sim}{K}\, \underset{\sim}{v}_n - (2\gamma-1)[\underset{\sim}{a}_n]^T \overline{\underset{\sim}{B}}[\underset{\sim}{a}_n] - 2\Delta t \langle \underset{\sim}{a}_n \rangle^T \underset{\sim}{C} \langle \underset{\sim}{a}_n \rangle \quad , \quad (23)$$

$$\left.\begin{aligned} \overline{\underset{\sim}{B}} &= \underset{\sim}{M} - \frac{\Delta t}{2}\underset{\sim}{C} - \frac{\Delta t^2}{2}\gamma \underset{\sim}{K} \quad , \\ \overline{\underset{\sim}{A}} &= \overline{\underset{\sim}{B}} + \Delta t\left(\gamma - \frac{1}{2}\right)\underset{\sim}{C} \quad . \end{aligned}\right\} \quad (24)$$

$$\left.\begin{aligned} [\underset{\sim}{a}_n] &= \underset{\sim}{a}_{n+1} - \underset{\sim}{a}_n \quad , \\ \langle \underset{\sim}{a}_n \rangle &= \frac{1}{2}\,(\underset{\sim}{a}_{n+1} + \underset{\sim}{a}_n) \quad . \end{aligned}\right\} \tag{25}$$

According to the stability theorem presented in [76], if $\gamma \geq 1/2$, $\overline{\underset{\sim}{B}}$ is positive definite, and $\underset{\sim}{C}$ is positive semi-definite, then $\underset{\sim}{a}_n$ and $\underset{\sim}{v}_n$ are uniformly bounded.

Clearly, $\underset{\sim}{C}$ is diagonally dominant, and so by Gershgorin's Theorem (Noble, p. 446), it is positive semi-definite. $\overline{\underset{\sim}{B}}$ takes the form:

$$\overline{\underset{\sim}{B}} = \begin{bmatrix} (h - \frac{c\Delta t}{2}) & 0 & & & \\ \frac{c\Delta t}{2} & (h - \frac{c\Delta t}{2}) & & \underset{\sim}{0} & \\ & \ddots & \ddots & & \\ \underset{\sim}{0} & & \frac{c\Delta t}{2} & (h - \frac{c\Delta t}{2}) & 0 \\ & & 0 & \frac{c\Delta t}{2} & (\frac{h}{2} - \frac{c\Delta t}{2}) \end{bmatrix} \quad . \tag{26}$$

If we expand the quadratic form of $\overline{B}$, then,

$$\underset{\sim}{X}^T\ \overline{\underset{\sim}{B}}\ \underset{\sim}{X} = (x_1, x_2, \ldots, x_n)\ \overline{\underset{\sim}{B}} \begin{Bmatrix} x_1 \\ \vdots \\ x_n \end{Bmatrix} =$$

$$\left(h - \frac{c\Delta t}{2}\right) x_1^2 + \frac{c\Delta t}{2}\, x_1 x_2 + \left(h - \frac{c\Delta t}{2}\right) x_2^2 + \ldots +$$

$$\left(h - \frac{c\Delta t}{2}\right) x_{n-1}^2 + \frac{c\Delta t}{2}\, x_{n-1} x_n + \left(\frac{h}{2} - \frac{c\Delta t}{2}\right) x_n^2 \tag{27}$$

$$= \frac{1}{2}\left(h - \frac{c\Delta t}{2}\right)x_1^2 + \left[\frac{1}{2}\left(h - \frac{c\Delta t}{2}\right)x_1^2 + \frac{c\Delta t}{2}x_1x_2 + \frac{1}{2}\left(h - \frac{c\Delta t}{2}\right)^2 x_2^2\right]$$

$$+ \left[\frac{1}{2}\left(h - \frac{c\Delta t}{2}\right)x_2^2 + \frac{c\Delta t}{2}x_2x_3 + \frac{1}{2}\left(h - \frac{c\Delta t}{2}\right)x_3^2\right] + \ldots +$$

$$+ \left[\frac{1}{2}\left(h - \frac{c\Delta t}{2}\right)x_{n-1}^2 + \frac{c\Delta t}{2}x_{n-1}x_n + \left(\frac{h}{2} - \frac{c\Delta t}{2}\right)x_n^2\right] \quad , \tag{28}$$

where $\underset{\sim}{x}$ is an arbitrary vector composed of real components. Each set of terms (excluding the last set) is greater than, or equal to, zero if

$$h - \frac{c\Delta t}{2} \geq \frac{c\Delta t}{2} \quad ,$$

or

$$\Delta t \leq \frac{h}{c} \quad . \tag{29}$$

For the last group, however,

$$\frac{1}{2}\left(h - \frac{c\Delta t}{2}\right)x_{n-1}^2 + \frac{c\Delta t}{2}x_{n-1}x_n + \frac{1}{2}(h - c\Delta t)x_n^2 \geq 0 \quad ,$$

if

$$h - c\Delta t \geq \frac{c\Delta t}{2} \quad ,$$

or

$$\Delta t \leq \frac{2h}{3c} \quad . \tag{30}$$

Therefore, the algorithm is stable if $\gamma \geq 1/2$, and if

$$\left.\begin{aligned} \Delta t &\leq \frac{h}{c} \quad \text{(last node fixed)} \quad , \\ \Delta t &\leq \frac{2h}{3c} \quad \text{(last node free)} \quad . \end{aligned}\right\} \tag{31}$$

A stability analysis for the one-dimensional wave equation produces the stability condition, $\Delta t \leq h/c$. Therefore, if the last (or n^{th}) paraxial node is fixed, as it is in the calculations of this study, the explicit-paraxial boundary imposes no added time-step restrictions.

III.B. Two-Dimensional Analysis and Its Extension to Three Dimensions

The two-dimensional, modified-paraxial equation is:

$$\begin{bmatrix} 1 & 0 \\ 0 & 1 \end{bmatrix} \underset{\sim}{u}_{tt} + \begin{bmatrix} c_d & 0 \\ 0 & c_s \end{bmatrix} \underset{\sim}{u}_{tx} + (c_d - c_s) \begin{bmatrix} 0 & 1 \\ 1 & 0 \end{bmatrix} \underset{\sim}{u}_{tz} + \underset{\sim}{K}\, \underset{\sim}{u}_{zz} = \underset{\sim}{0} \quad . \quad (32)$$

The element matrices are found analogously to those in Appendix A.

$$m_{ab} = \int_{-1}^{1} \int_{-1}^{1} N_a N_b \, J \, d\xi \, d\zeta \quad , \quad (33)$$

$$c^x_{ab} = \underset{\sim}{D} \int_{-1}^{1} \int_{-1}^{1} N_a N_{b,x} \, J \, d\xi \, d\zeta \quad , \quad (34)$$

$$c^z_{ab} = (c_d - c_s) \int_{-1}^{1} \int_{-1}^{1} N_a N_{b,z} \, J \, d\xi \, d\zeta \quad . \quad (35)$$

$J = \det \begin{vmatrix} x_{,\xi} & x_{,\zeta} \\ y_{,\xi} & y_{,\zeta} \end{vmatrix}$, and $\underset{\sim}{D}$ is a matrix composed of the constants, c_d and c_s. ξ and ζ are the local coordinates, $\underset{\sim}{C}^x$ is the matrix formed from the $\underset{\sim}{u}_{tx}$ term, and $\underset{\sim}{C}^z$ is formed from $\underset{\sim}{u}_{tz}$. If we evaluate equations (33) and (34), for the typical element depicted in Figure 7, we find that:

$$\underset{\sim}{m} = \frac{\rho h^x h^z}{4} \begin{bmatrix} 1 & & & & & & & \\ & 1 & & & & & \underset{\sim}{0} & \\ & & 1 & & & & & \\ & & & 1 & & & & \\ & & & & 1 & & & \\ & & & & & 1 & & \\ & \underset{\sim}{0} & & & & & 1 & \\ & & & & & & & 1 \end{bmatrix} , \tag{36}$$

$$\underset{\sim}{c}^x = \frac{\rho h^z}{2} \begin{bmatrix} 0 & 0 & 0 & 0 & 0 & 0 & 0 & 0 \\ 0 & 0 & 0 & 0 & 0 & 0 & 0 & 0 \\ -c_d & 0 & c_d & 0 & 0 & 0 & 0 & 0 \\ 0 & -c_s & 0 & c_s & 0 & 0 & 0 & 0 \\ 0 & 0 & 0 & 0 & 0 & 0 & 0 & 0 \\ 0 & 0 & 0 & 0 & 0 & 0 & 0 & 0 \\ 0 & 0 & 0 & 0 & -c_d & 0 & c_d & 0 \\ 0 & 0 & 0 & 0 & 0 & -c_s & 0 & c_s \end{bmatrix} . \tag{37}$$

At this point, if we use only the zeroth-order paraxial approximation [that is, if we ignore the second two terms in equation (32)], then the stability limits can be explicitly obtained as follows. In this case, nodes 1 and 2 are related in the same way as they would be in one dimension. Thus, if we consider just the x degree-of-freedom for a string of nodes in the x direction, as in Figure 8,

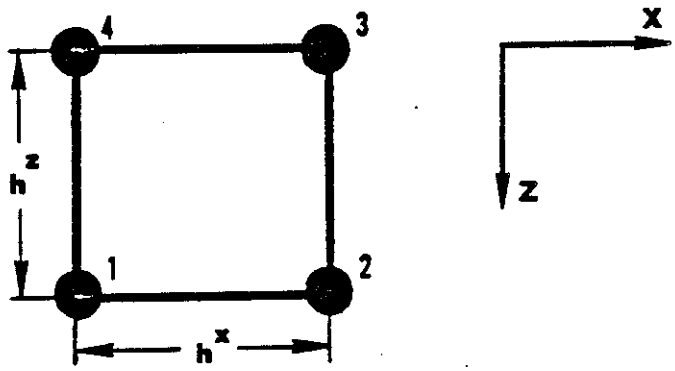

Figure 7. Two-dimensional, four-noded element used for deriving the mass, and paraxial damping matrices.

$$\underset{\sim}{M} = \rho h^x h^z \begin{bmatrix} 1 & & & \underset{\sim}{0} \\ & 1 & & \\ & & \ddots & \\ & & & 1 \\ \underset{\sim}{0} & & & \frac{1}{2} \end{bmatrix} , \tag{38}$$

$$\underset{\sim}{C} = \rho h^z c_d \begin{bmatrix} 1 & 0 & & & \underset{\sim}{0} \\ -1 & 1 & \ddots & & \\ & \ddots & \ddots & \ddots & \\ & & & 1 & 0 \\ \underset{\sim}{0} & & & -1 & 1 \end{bmatrix} . \tag{39}$$

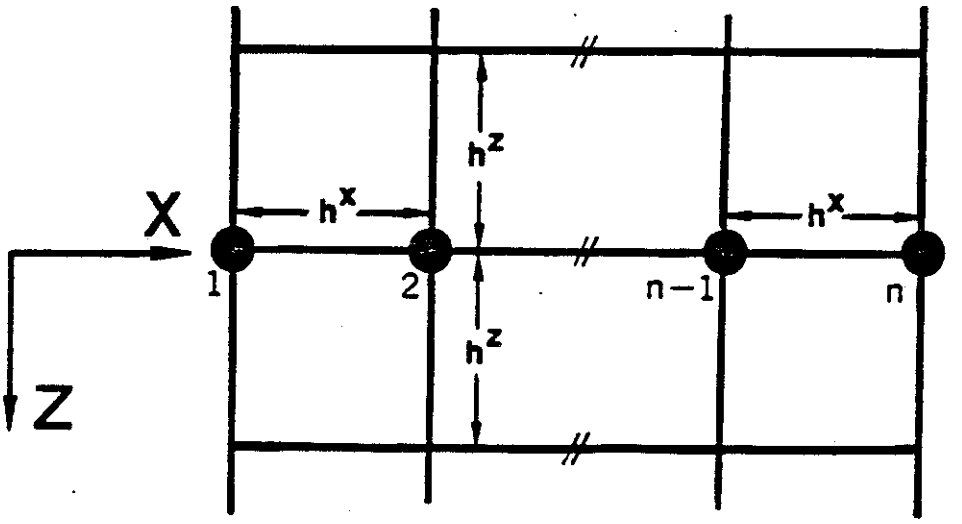

Figure 8. Row of paraxial nodes in a two-dimensional mesh used for the purposes of numerical stability.

These are the same matrices that arise in the one-dimensional case. Hence,

$$\left.\begin{aligned} \Delta t &\leq \frac{h^x}{c_d} \qquad \text{(last row fixed)} \quad , \\ \Delta t &\leq \frac{2h^x}{3c_d} \qquad \text{(last row free)} \quad . \end{aligned}\right\} \tag{40}$$

Likewise, by considering the z degree-of-freedom, for a string of nodes in the x direction,

$$\left.\begin{aligned} \Delta t &\leq \frac{h^x}{c_s} \qquad \text{(last row fixed)} \\ \Delta t &\leq \frac{2h^x}{3c_s} \qquad \text{(last row free)} \quad . \end{aligned}\right\} \tag{41}$$

This is a less stringent condition than is equation (40). Thus, for two dimensions, the matrix derived from the $\underset{\sim}{u}_{tx}$ term has the same stability properties as does its counterpart in one dimension. The analysis clearly extends to three dimensions.

Now, if we consider the higher-order, paraxial approximations, that is, if we include the last two terms in equations (32), then the stability becomes somewhat more involved. Due to the assembly procedure which is used in the interface region, the $\underset{\sim}{u}_{tz}$ and $\underset{\sim}{u}_{zz}$ terms lead to nonsymmetrical matrices, which are not accounted for in the theorem [76] used in the previous analysis. In the numerical calculations that we have performed, these terms have not caused any difficulties. (The $\underset{\sim}{C}^z$ matrix is, in fact, almost entirely antisymmetrical.) If problems of numerical stability were encountered in other applications, one could use only the zeroth-order, paraxial approximation, wherein the stability limits are clearly defined.

III.C. Numerical Stability of the Viscous Boundary

The stability characteristics of the viscous boundary also proceed from the stability theorem in [76]. An implicit, viscous boundary is unconditionally stable, if $\gamma \geq 1/2$ and $\beta \geq \gamma/2$. The numerical stability limits for the explicit, viscous boundary stem from equations (23) and (24). If $\overline{\underset{\sim}{B}}$, in equation (24), is positive definite, and if $\gamma \geq 1/2$, then $\underset{\sim}{a}_n$ and $\underset{\sim}{v}_n$ are uniformly bounded. $\overline{\underset{\sim}{B}}$ is a symmetric matrix, and its

eigenvalues can be easily determined after γ, Δt and $\underset{\sim}{K}$ have been selected. Thus, the stability properties of the explicit, viscous boundary can be defined for each specific case. The implicit, viscous boundary is more convenient for our purposes, because of its unconditional stability properties. However, this may not be true in other applications, and it is useful to have the explicit option.

IV. VALIDATION OF NUMERICAL PROCEDURES

We verified our implementation by comparing our program results to several static, and dynamic, analytical solutions. In all of these problems, and in the test examples of Chapter IV, the silent boundaries were implemented as they are shown in Figure 9. As the symbol for a silent boundary, we employed a thick black strip, which is illustrated on the left side of Figure 9. In the case of the viscous boundary, the black strip denotes a set of applied stresses, σ_{xx} and τ_{xz}, which are applied to the boundary. For a paraxial boundary, it indicates a row of paraxial nodes which are adjacent to the interior region.

The solution for one simple problem, a one-dimensional bar, is shown in Figures 10 and 11. A load is applied in the interior of the bar during the first time step and is then removed. The wave pulses are denoted by circles, whose diameters represent the magnitude and direction of the particle velocities. "Superconvergence"[77] is attained by utilizing the explicit algorithm and the following parameters: c_d = wave speed = 1 element/second, γ = .5, β = .25, Δt = 1 second, and Poisson's ratio = 0.

The circles, which remain at the paraxial boundary after step number 9, do so because of the fixing of the boundary nodes on the

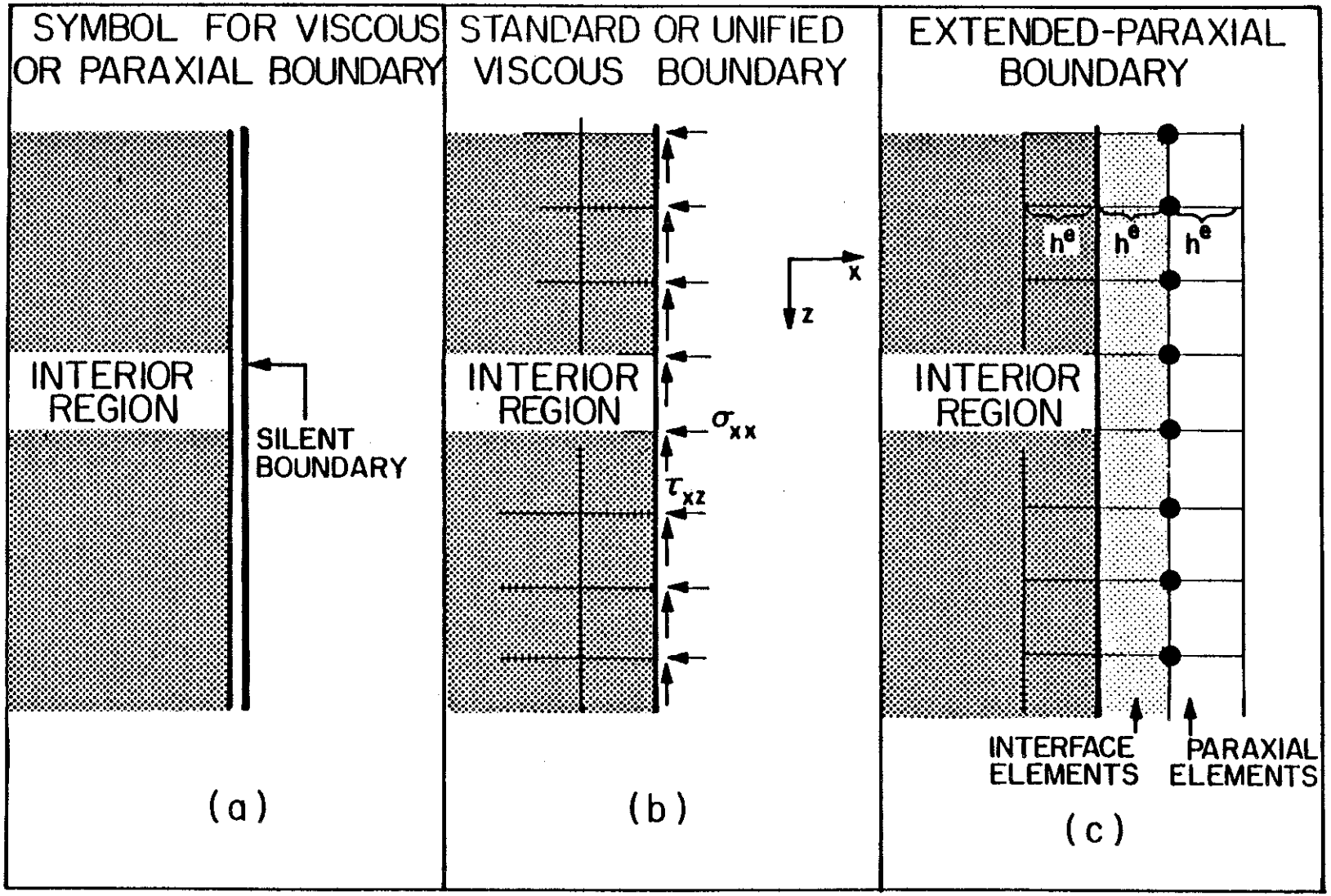

Figure 9. Schematic drawings of the silent boundaries: a) thick black strip which symbolizes a silent boundary; b) the standard-, or unified-viscous boundary, as applied in all of our examples; c) the extended-paraxial boundary.

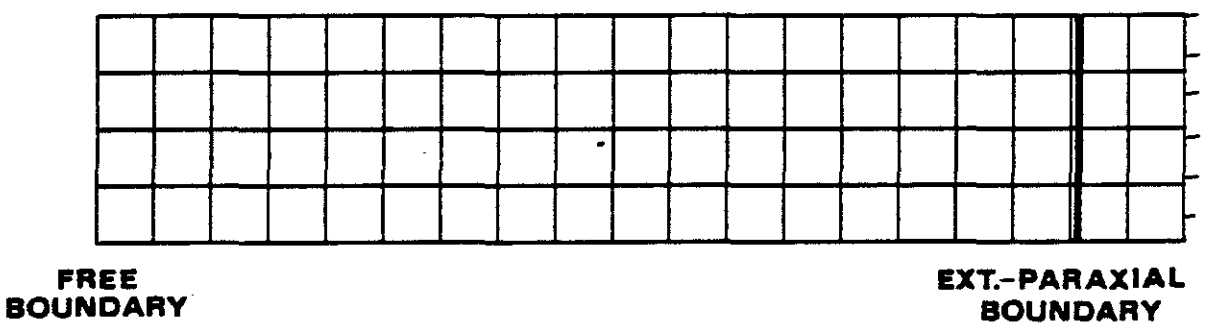

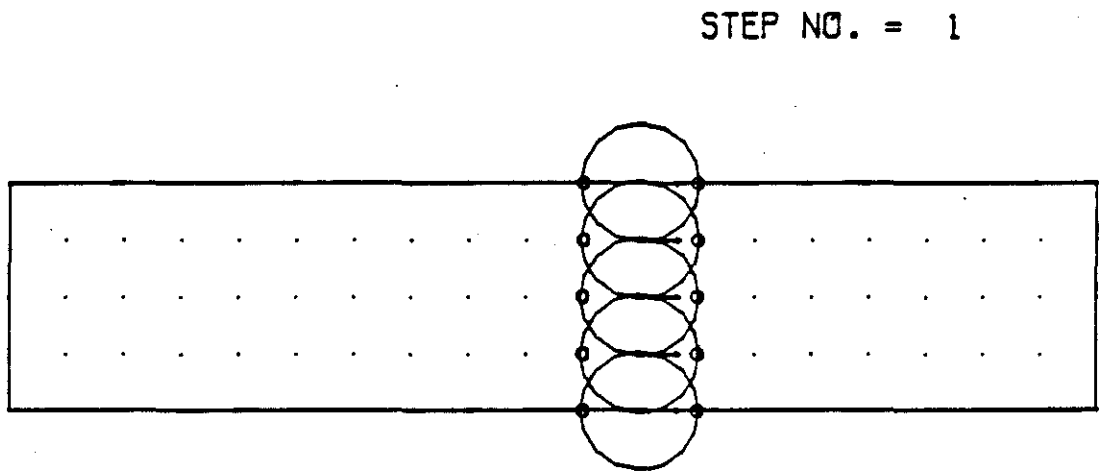

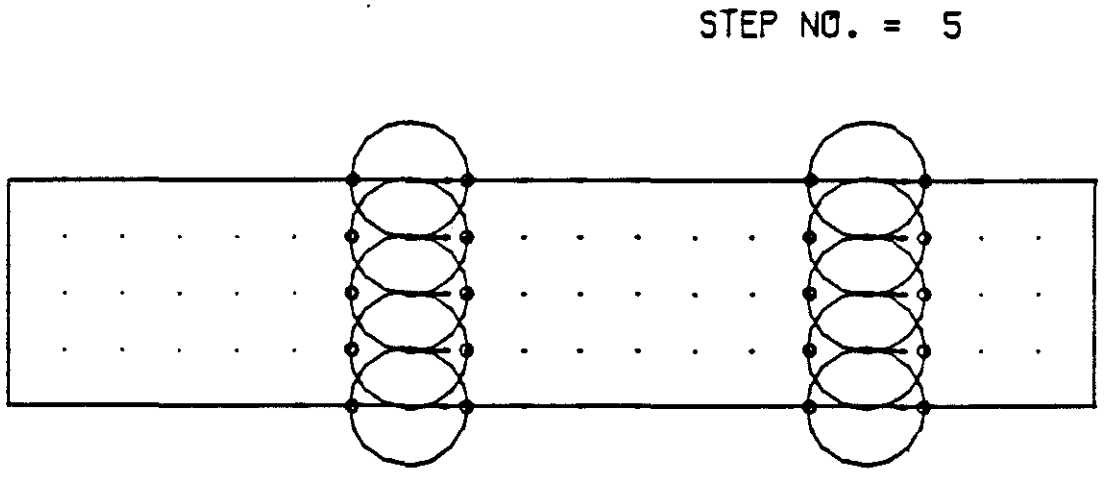

Figure 10. Top: Mesh used for a one-dimensional wave;
Middle: Energy and velocity plots at t = 5 seconds;
Bottom: Energy and velocity plots at t = 9 seconds.

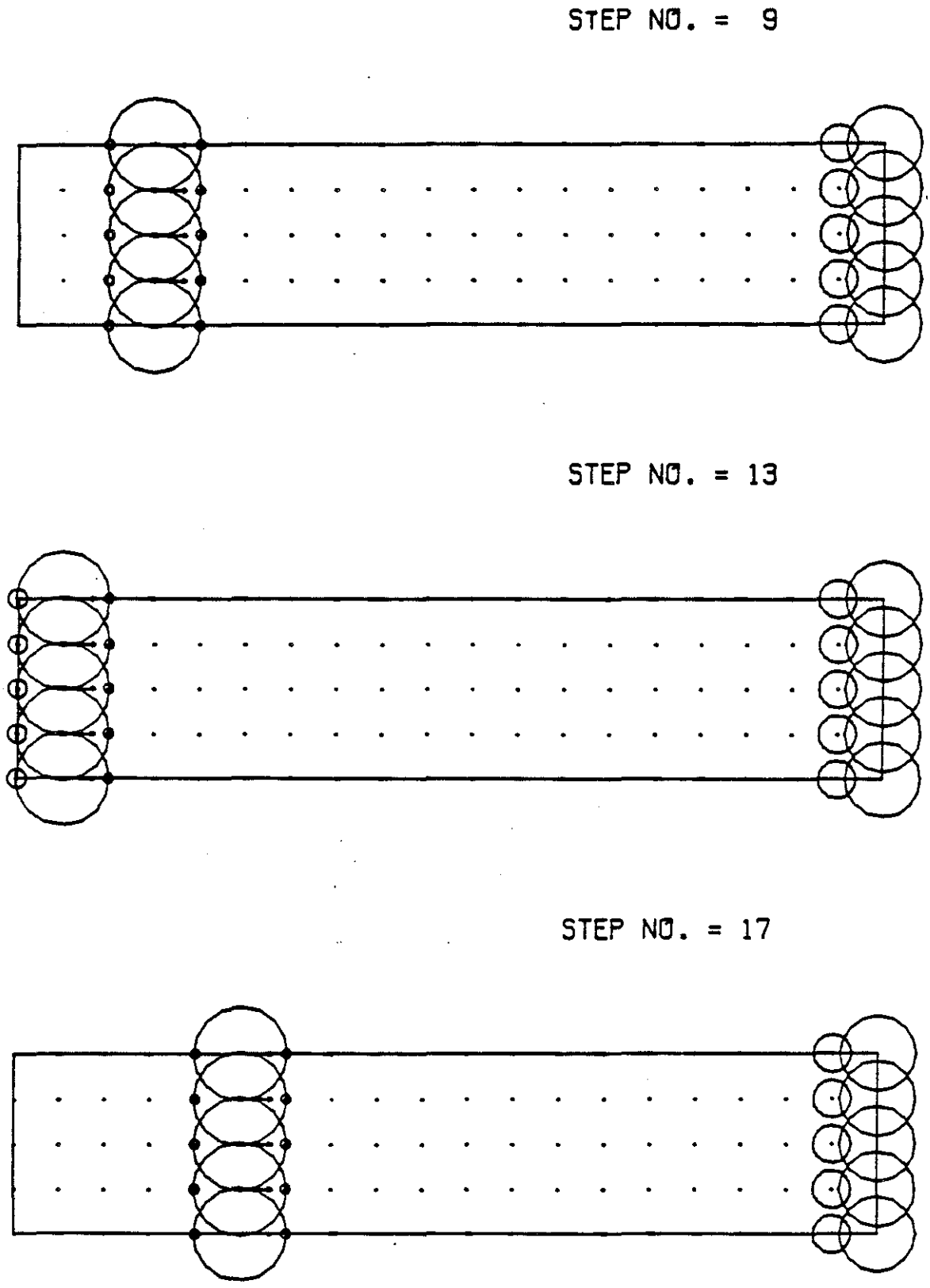

Figure 11. Energy and velocity plots at t = 9, 13, and 17 seconds, respectively.

right. All of the free nodes experience a certain displacement as the wave passes by them, but the right-sided nodes remain stationary. Therefore, these circles on the right indicate the displacement of the free nodes. In a global sense, the paraxial region acts as a dashpot -- it brakes the motion of the elastic bar, but in doing so, the bar undergoes some permanent displacement to the right.

Having checked the code with several simple, smooth analytical solutions, we test its ability to model discontinuous waves, generated by a delta-function load in both time and space. Our aim with this calculation is to help validate our implementation, and to test the limits of the finite-element discretization. A by-product from this example is that the results indicate the effectiveness of the silent-boundary methods.

The example, called Lamb's problem in plane strain, is illustrated in Figure 12. It represents a particularly difficult case for finite-element analysis. Miklowitz[86] presents a derivation, based on the Cagniard-DeHoop method, of Lamb's analytical solutions and plots them along the x and z axes. We compare these results to those produced by a mesh which is coarse in relation to the wave front. This mesh is depicted in Figure 13. Symmetrical boundary conditions are imposed on the left face of the region under consideration.

In the following diagrams, the length of 4 elements = 1 "unit", c_d = 1 unit/second, c_s = .57735 units/second, ρ = density = 1 (Poisson's ratio = .25), DT = .25 seconds, γ = .51, and β = .255. Two different loadings, labeled Case 1 and Case 2, are sketched in Figure 14. Case 2 more closely resembles the delta-function loading in the analytical

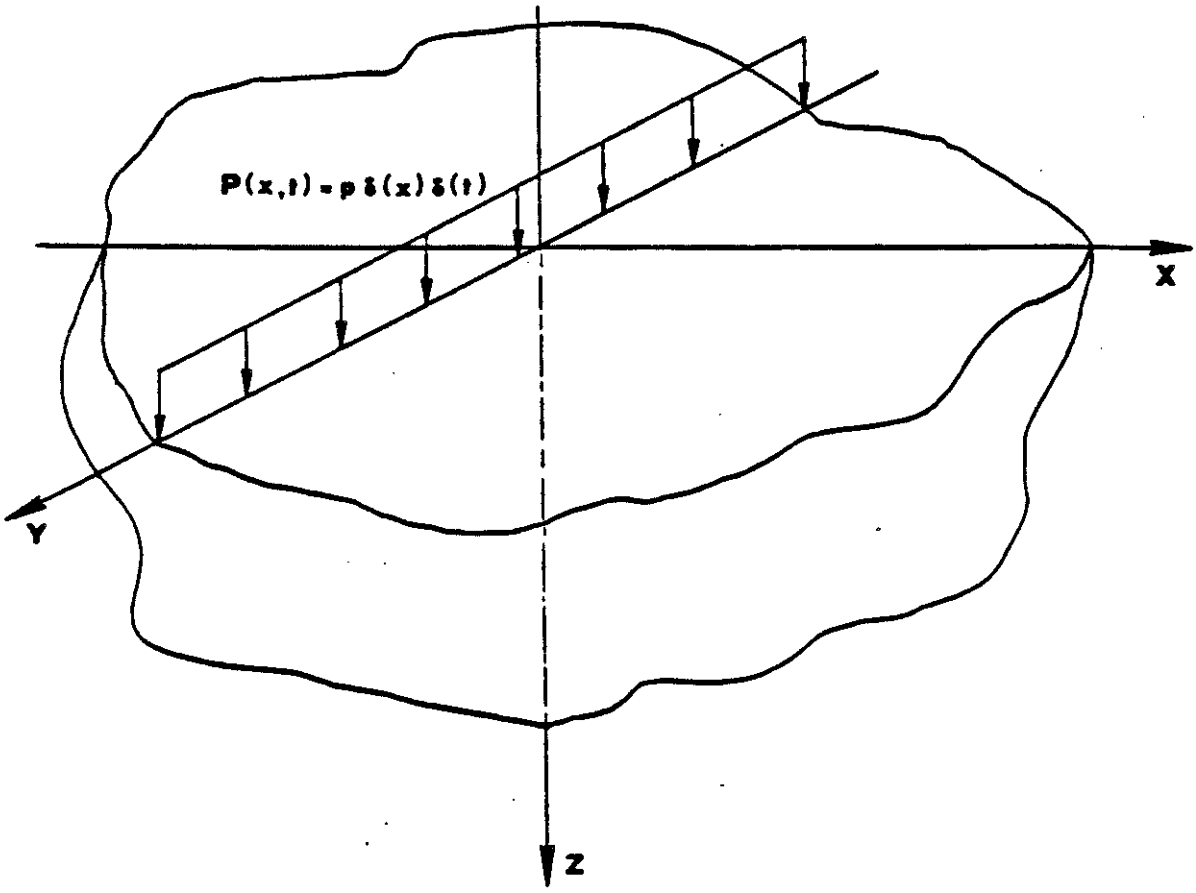

Figure 12. Schematic diagram of the problem posed by Lamb [85] in 1904.

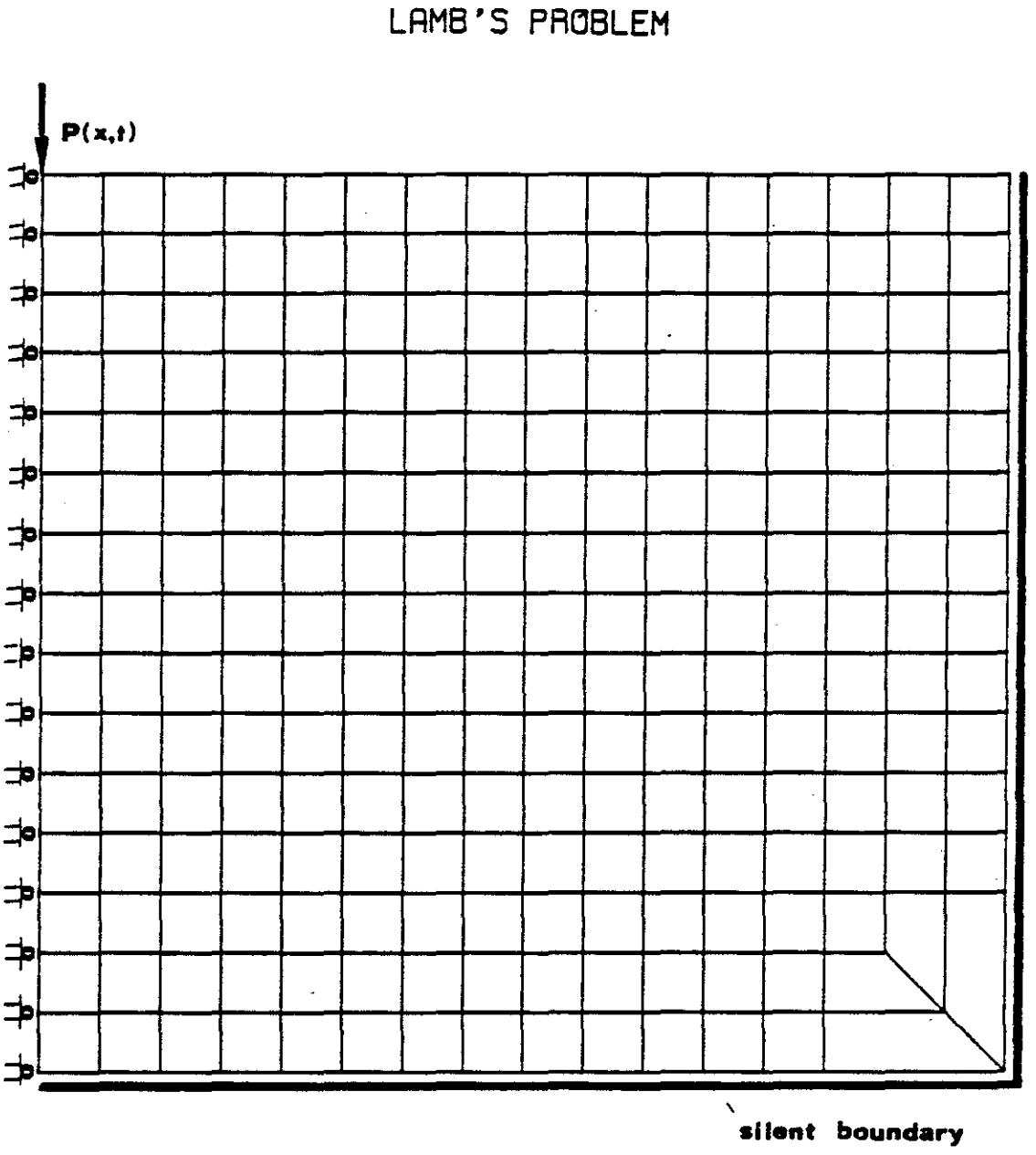

Figure 13. Two-dimensional mesh and boundary conditions employed for Lamb's problem.

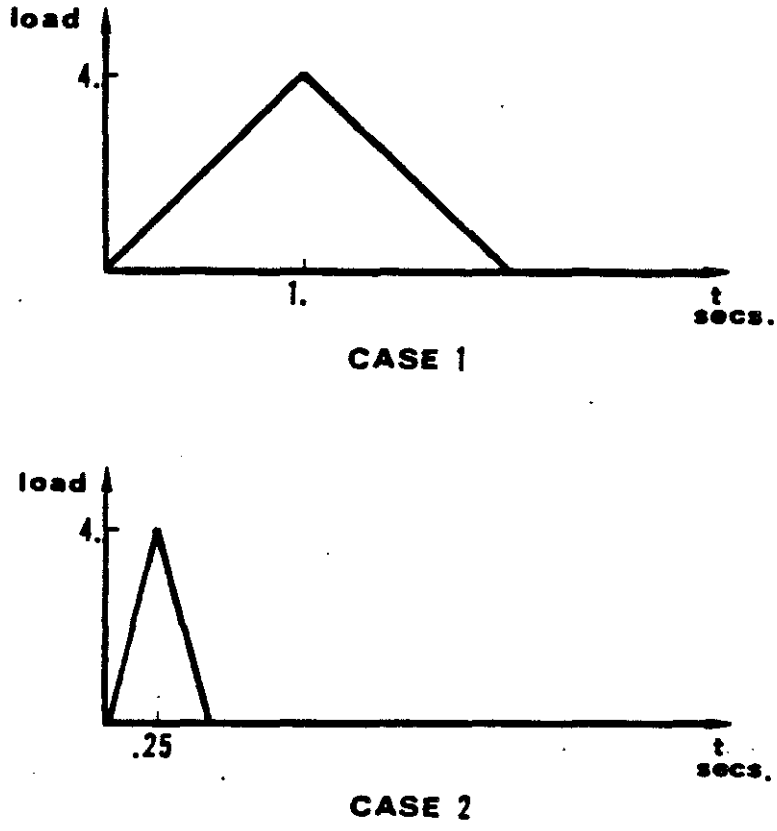

Figure 14. Discretized approximations to the delta-function load.

solution. We used both the extended-paraxial and the standard-viscous boundaries in this problem. They each produced nearly the same results, but for the final calculations, we employed the viscous boundary. The comparisons between the analytical solutions,and finite-element solutions using the implicit algorithm, are presented in Figures 15 and 16.

Figure 15 illustrates, for Cases 1 and 2, the vertical displacements at the surface, x = 1.25 and z = 0.0. The analytical result depicts a Rayleigh singularity, where a negative infinite displacement changes instantaneously into a positive infinite displacement. The finite element method, with its bilinear basis functions, cannot possibly duplicate such behavior, so it "smooths" the singularity. It does manage to capture the long-term displacement. The Case 2 loading introduces slight numerical noise into the system.

When we compare the analytical and finite element solutions in the interior (x = 0.0, z = 2.75), we obtain better agreement between the methods. The solution is less singular there, as is illustrated in Figure 16. The width of the initial wave pulse is still narrower than one element, but its magnitude is finite, unlike the displacement along the surface. Here, the loading of Case 2 leads to a more accurate peak amplitude than that which is produced by the smooth loading. On the other hand, the sharp loading causes significant numerical noise.

The explicit algorithm was also used to solve Lamb's problem. It leads to slightly improved accuracy in the interior, but it adds spurious noise at the surface.

In summary, Lamb's highly-singular solution tests the limits of the spatialy and temporal discretizations which are employed. The

LAMB'S PROBLEM

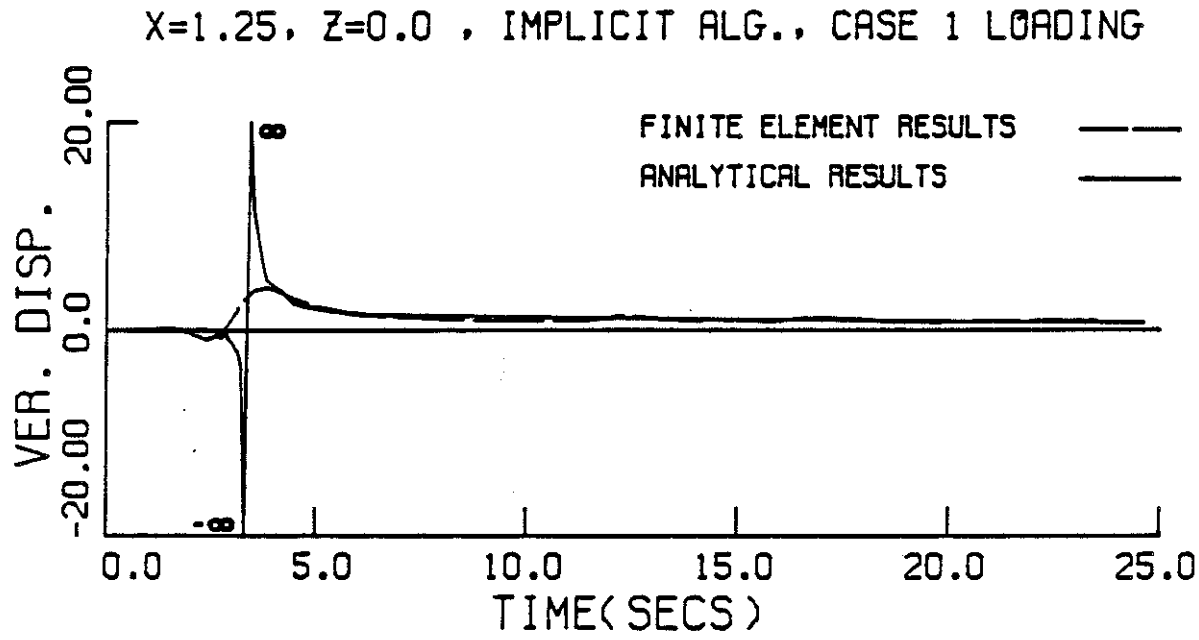

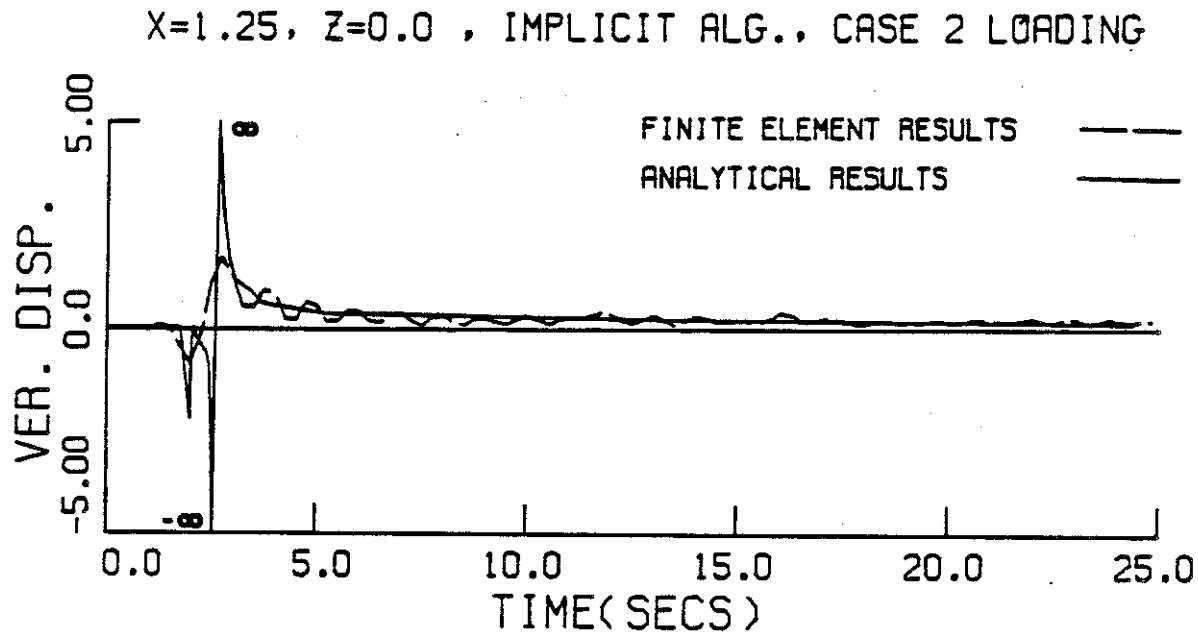

Figure 15. Vertical displacements at the surface as a function of time.

LAMB'S PROBLEM

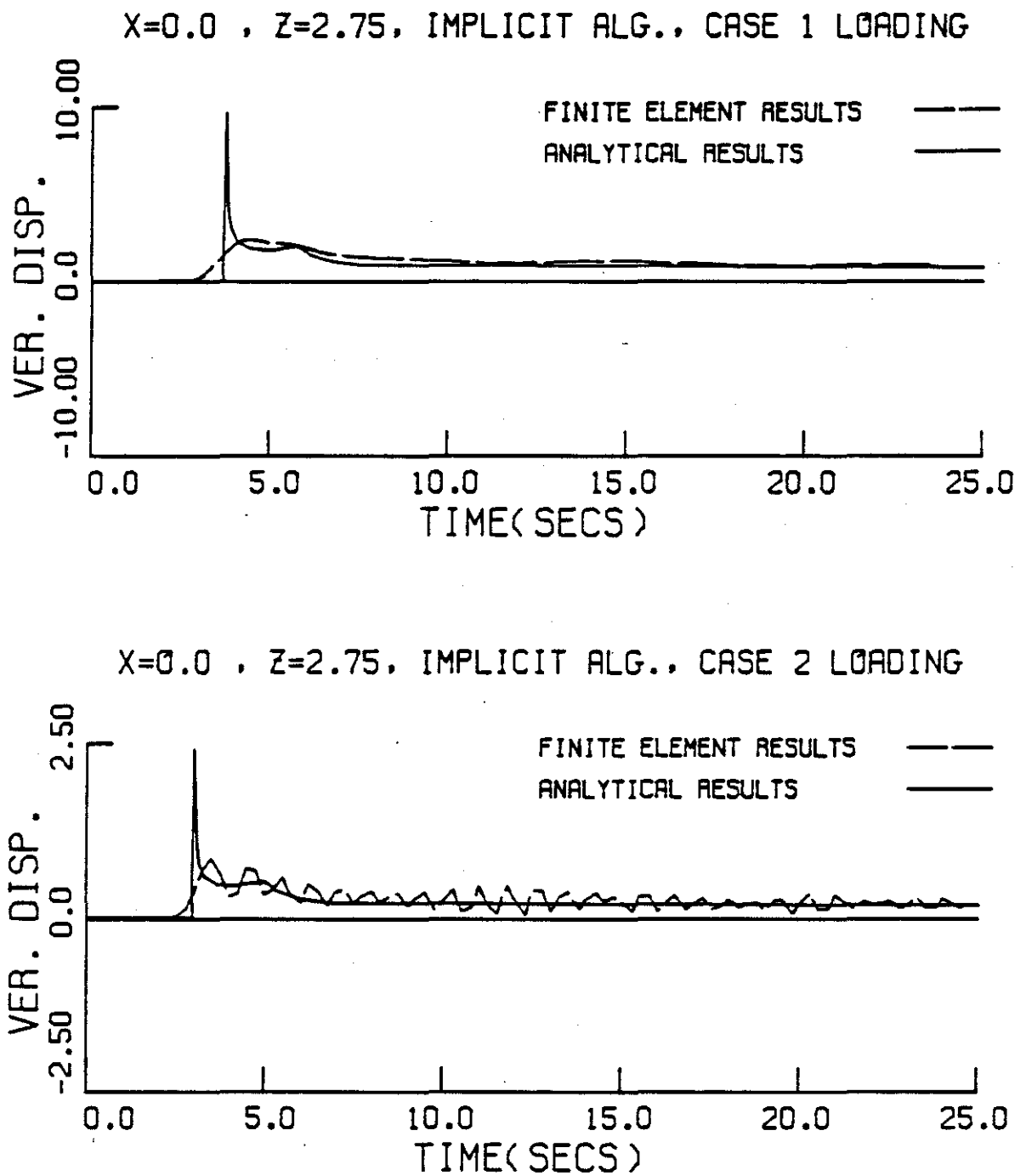

Figure 16. Vertical displacements in the interior as a function of time.

method does reproduce the smooth part of the solution, and it duplicates, to varying degrees, the sharp wave fronts, depending on the idealization of the loading pulse and the coarseness of the mesh. The smooth loading of Case 1 eliminates most of the numerical noise which arises from the delta-like, Case 2 loading.

CHAPTER 4

I. INTRODUCTION

I.A. General Aim

In order to assess the relative merits of the extended-paraxial, the standard-viscous, and the unified- (optimized-) viscous boundaries, we present in this chapter summaries of our numerical investigations. The main thrust of the work was aimed along the following lines:

1. to evaluate and compare the boundaries' effectiveness in handling high-frequency waves ("high-frequency" refers to wavelengths which consist of only a few element lengths);
2. to determine if the boundaries' efficiency is affected by material properties, particularly as Poisson's ratio approaches 1/2;
3. to evaluate the boundaries' ability to transmit certain types of nonlinear waves;
4. to test the boundaries' effectiveness in transmitting Rayleigh waves.

While conducting these numerical investigations, a voluminous amount of information was generated for examination and comparison. We cannot reproduce all of it here, so representative graphs are selected. These illustrate what we consider to be the major characteristics of the various methods.

I.B. Description of the Numerical Procedure

All of the examples in this chapter were solved by using the silent boundaries described in Chapter 3. Both the elastic and the boundary regions were discretized with four-noded elements which employ bilinear, isoparametric shape functions. The elastic stiffness is decomposed into a shear (μ) part, and a lambda (λ) component, where μ and λ are Lamé's constants. This separation is useful because each set of terms can be integrated with different, numerical-quadrature rules. The elastic-shearing stiffness is integrated with the standard 2x2 Gaussian quadrature, while the lambda terms are evaluated by a 1-point quadrature at the element's center. This selective integration procedure is valid because the μ and λ stiffness terms are each invariant with respect to coordinate transformations. (See Hughes, Cohen and Haroun,[75] Section 3.3.) We selected this integration rule because it avoids the "lockup" difficulties[72] which are experienced when Poisson's ratio goes to 1/2 (that is, when lambda goes to infinity.)

The captions to the figures in this chapter specify whether the "interior" region is solved implicitly, or explicitly. The algorithm parameters, γ and β, and the time step, DT, are also defined in the figure captions. The viscous-boundary areas are always analyzed as implicit regions, in order to utilize the implicit algorithm's unconditional stability. The explicit method, however, is employed in the

extended-paraxial domain, for the reasons mentioned in Chapter 3. The mass matrices are lumped, regardless of the chosen algorithm.[1]

I.C. Selection of Wave Problems

The meshes used in this chapter are significantly coarser than those which one would normally use for practical engineering problems. In fact, most of the loadings of the following systems are applied over one or two elements and for only one time step. This input, similar to a delta function, generates much high-frequency motion in the solutions. We selected this approach because it subjects the silent boundaries to relatively severe test conditions. Since the boundaries are designed to absorb smooth, wave-like pulses, this transient, high-frequency excitation should challenge the limits of their capabilities.

The purpose of these tests, then, is to evaluate and compare the silent boundaries using the above-described input. Because of the deliberate selection of coarse meshes, the resulting motion may not duplicate the correct solution in all of its details, but that is not really the concern here. The accuracy of the finite-element method, and its dependence upon the fineness of the mesh, is well understood. For our purposes, the "correct" response is that which is produced by a mesh extensive enough to prevent the boundary reflections from reaching the "interior" zone.

---

[1] This lumping of the mass matrix was done in order to facilitate the calculations of energy. Krieg and Key [79] and Mullen and Belytchsko [81] discuss some of the beneficial and deleterious effects of using lumped mass matrices in conjunction with either implicit or explicit algorithms.

II. DIRECT INCIDENCE OF DILATATIONAL WAVES

Figure 1 illustrates the case of direct incidence, where the wave strikes the boundary at an incidence angle of zero degrees. The basic problem is that of an axially symmetric, pulse loading of an infinite material in plane strain. It is, for example, a two-dimensional, idealized version of a bomb exploding underground. The symmetry of the loading allows one to reduce the problem to that of a conveniently solved, quarter-plane. Symmetrical boundary conditions were installed at the sides, and a dilatational pressure was applied for one time step and then removed. c_d = 1 unit/second, c_s = .5345 units/second, one "unit" = the distance that one element extends in the radial direction, DT = the time step = .9 seconds, and ρ = density = 1. The silent boundaries are denoted by a thick black strip on the outer radial edge of the mesh. This symbol, and its meaning, are expressed in Figure 9 of Chapter 3.

The circles on the graphs symbolize the total energy at a given node, and the arrows within the circles express the magnitude, and the direction, of the particle velocities.

Figure 2 delineates the progress of the dilatational pulse through an elastic region and an extended-paraxial boundary. The pulse first strikes the boundary at the 12th time step; it is reflected and then it returns to its origin at the 23rd step. As is seen in Figure 2, these reflections appear to be negligible.

The same problem is depicted in Figure 3 but for a standard-viscous boundary. This boundary absorbs almost all of the radiated energy, except for a small reflection that appears on the inner boundary, at

RADIAL, DILATATIONAL PULSE

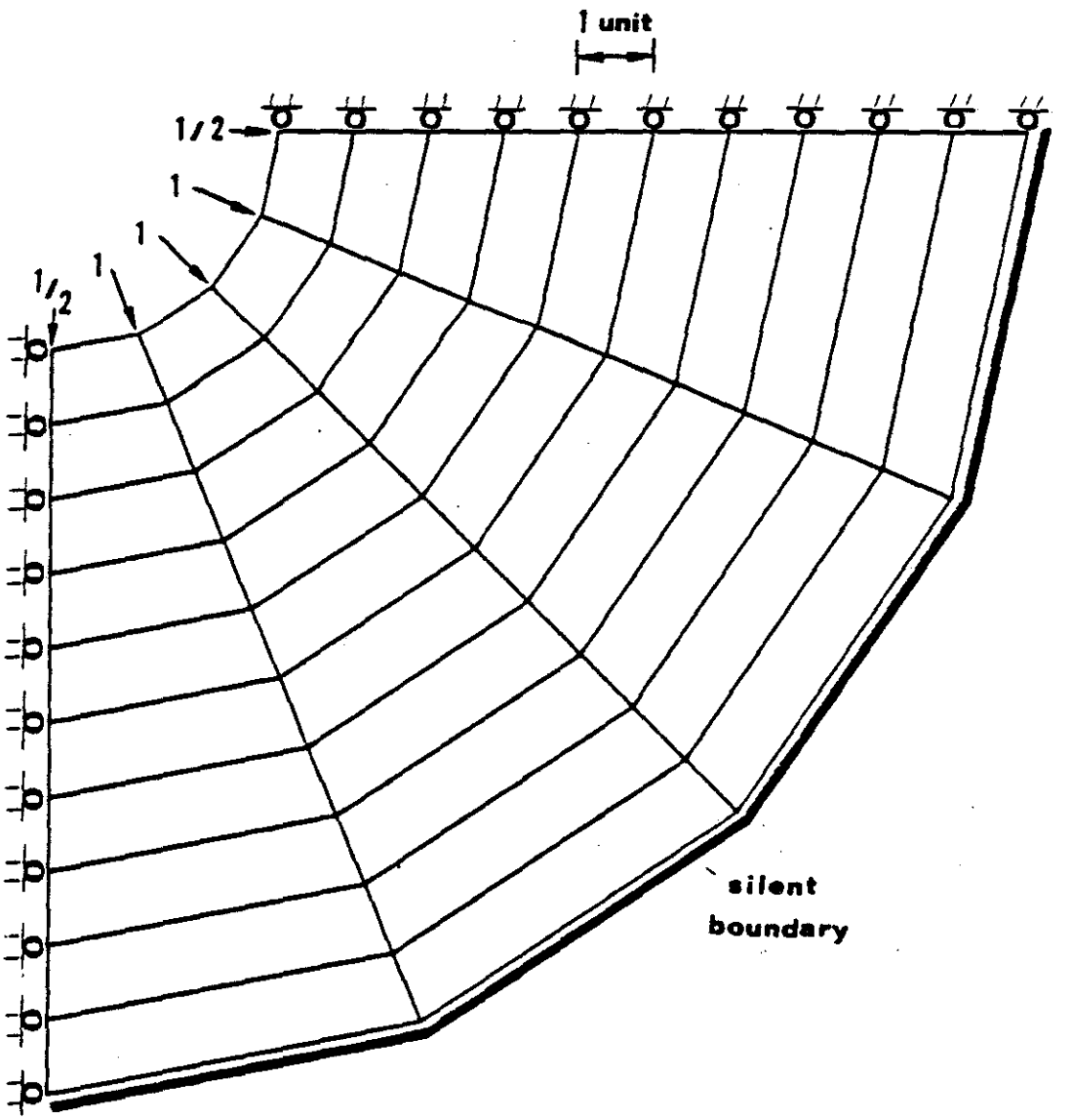

Figure 1. Finite-element mesh used for radially propagating, dilatational waves.

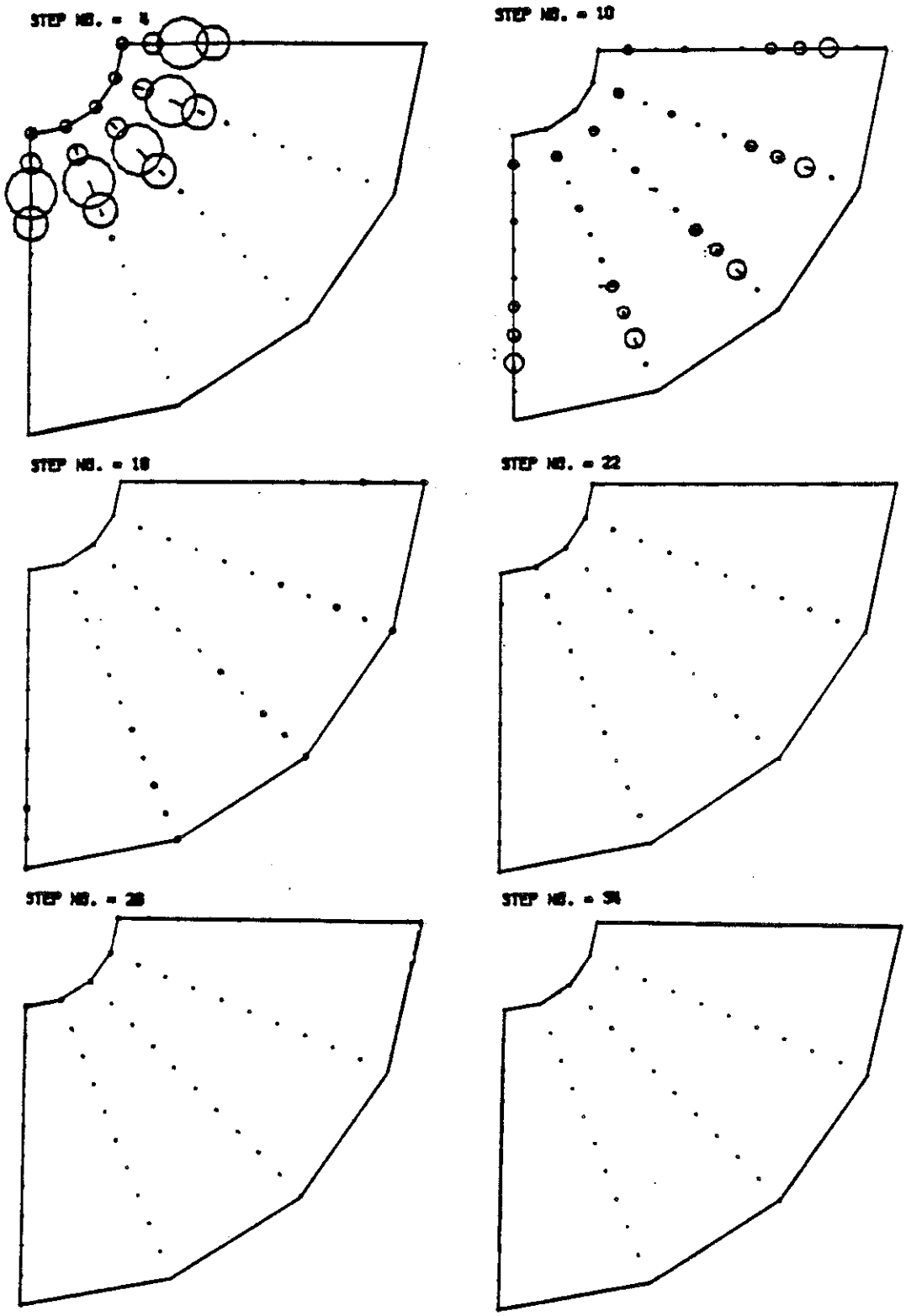

Figure 2. Illustration of energy and velocity at various times in the mesh.

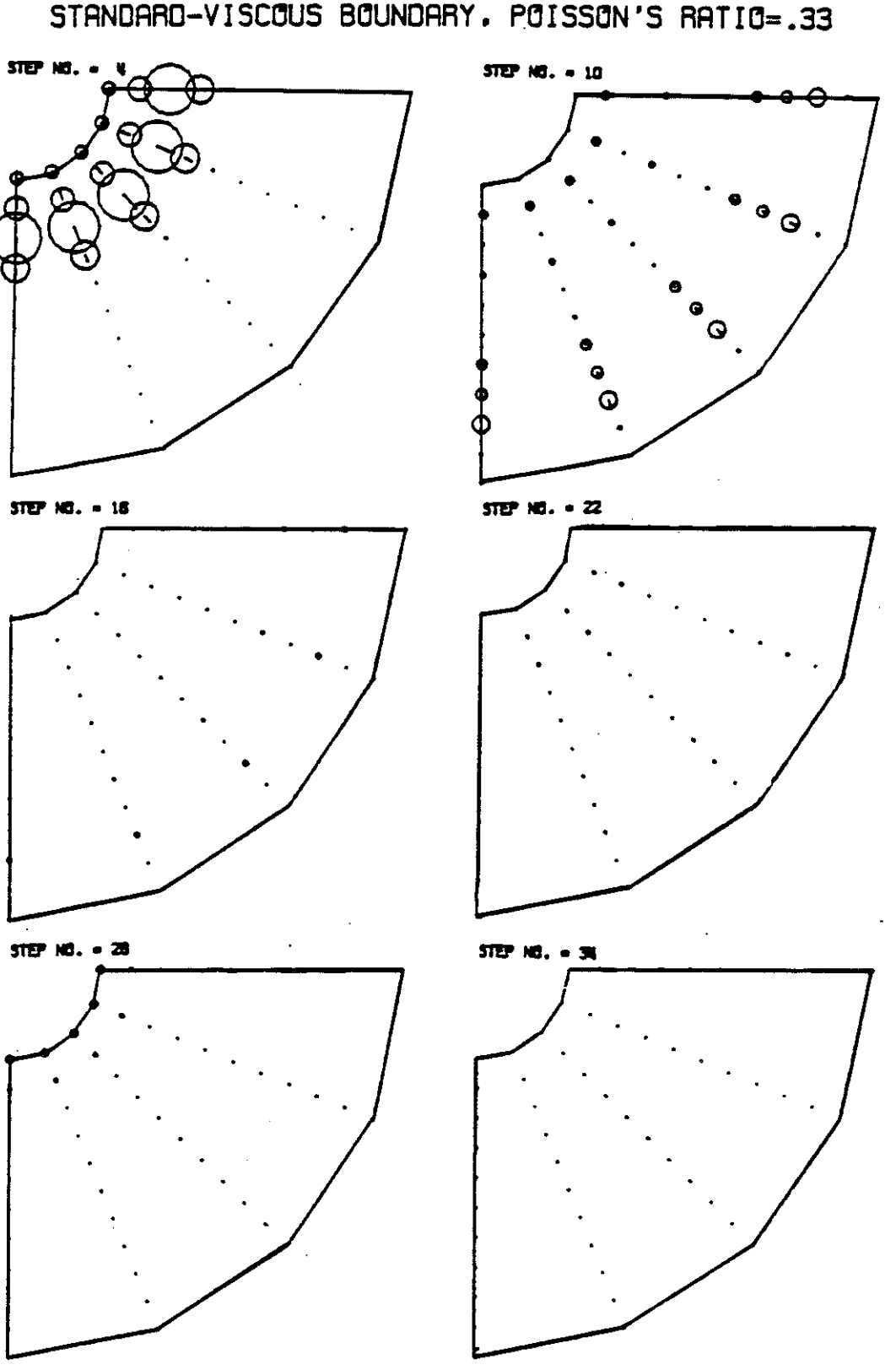

Figure 3. Illustration of energy and velocity at various times in the mesh.

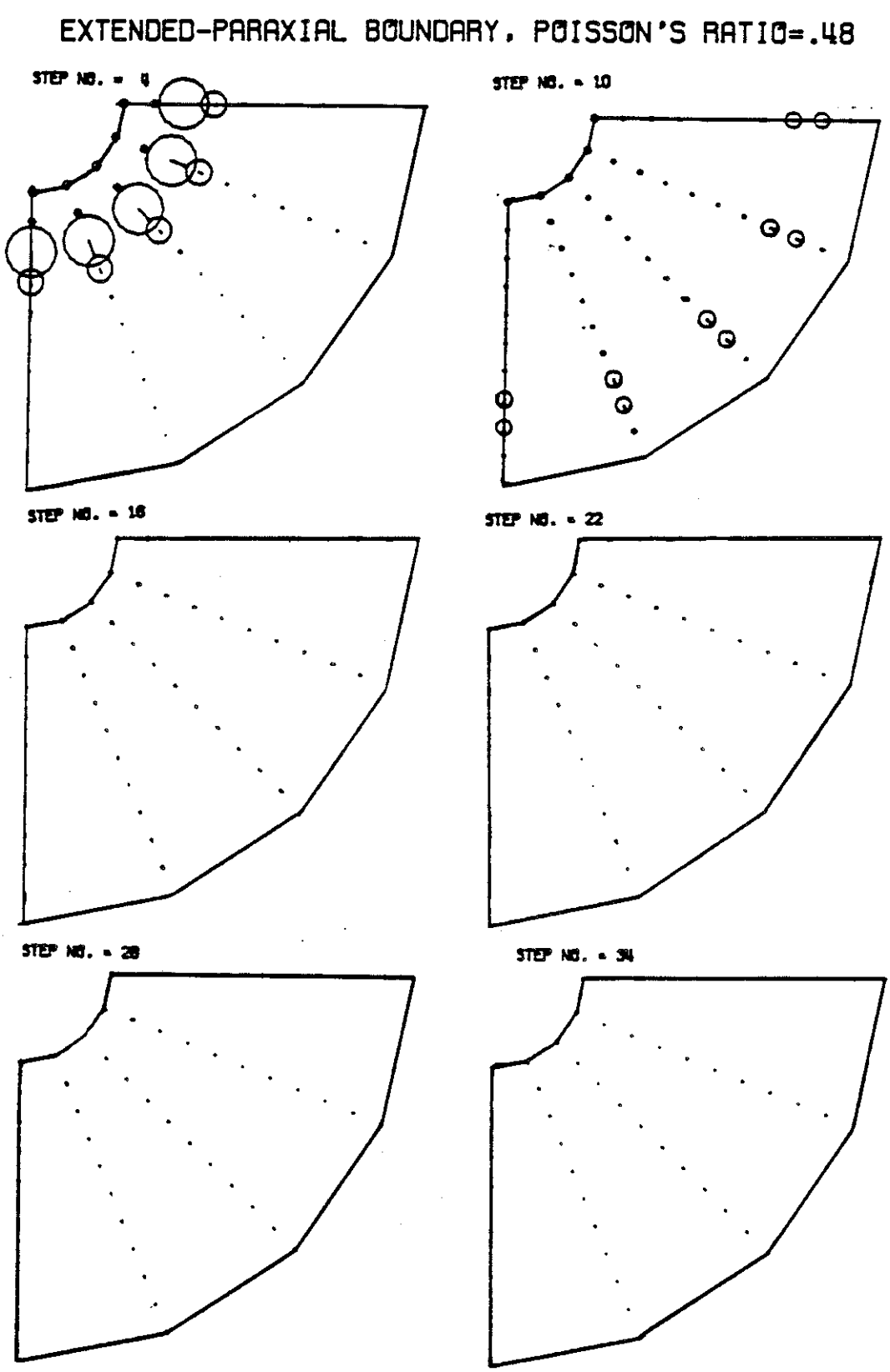

Figure 4. Illustration of energy and velocity at various times in the mesh.

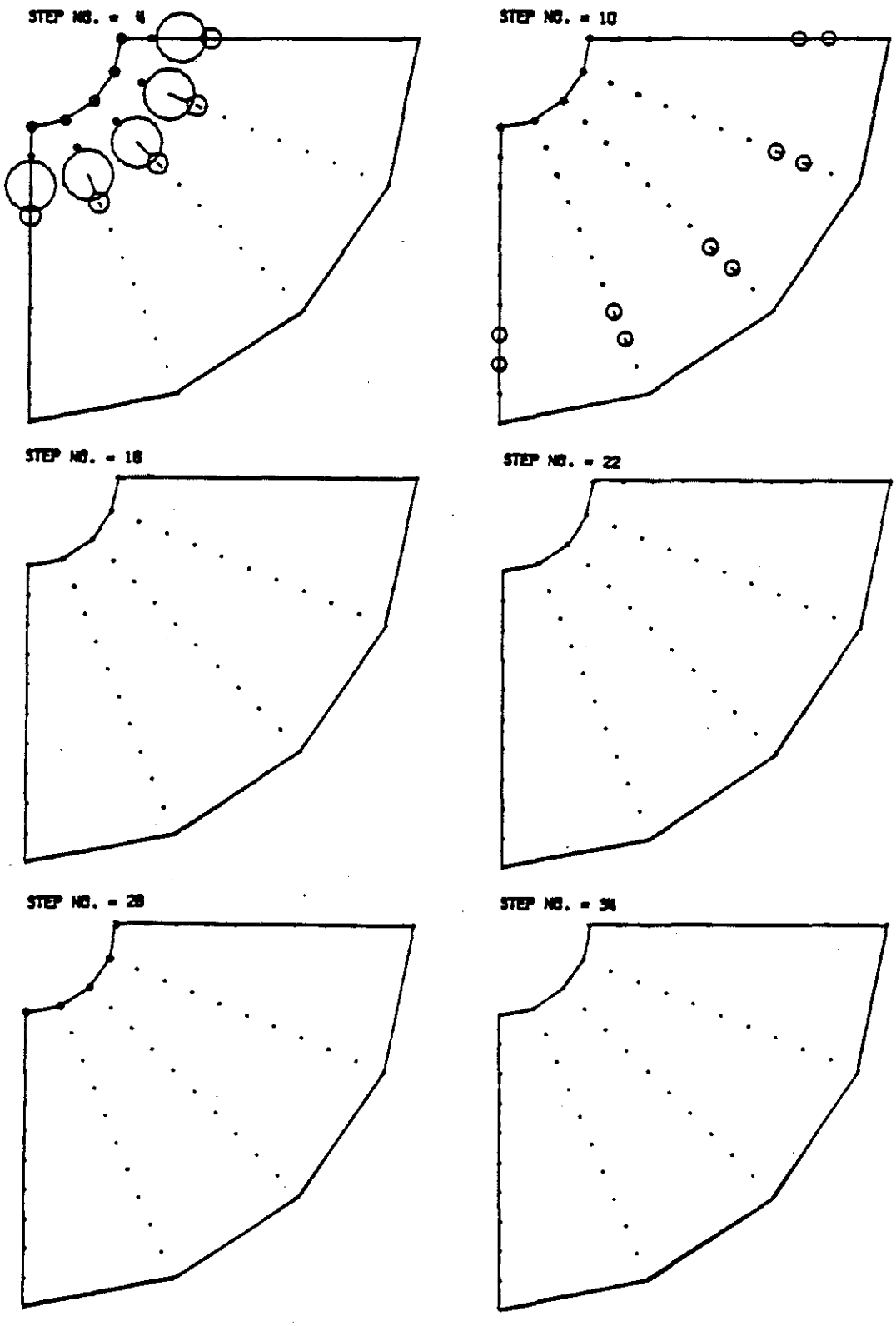

Figure 5. Illustration of energy and velocity at various times in the mesh.

the 28th time step. We also tested the unified-viscous boundary and obtained results identical to those in Figure 3.

Figures 4 and 5 depict the same wave in a material having c_s = .2 units/second. The pictures of waves striking a unified-viscous boundary again duplicated those of the standard-viscous boundary. Our conclusion for this particular test is the differences in material properties do not seem to alter the efficiency of the respective boundaries. All three perform well and are nearly equal in effectiveness.

Each of the above examples examines dilatational waves striking at a normal angle of incidence. In the next section, we will present other examples which indicate the absorption of shear waves.

III. PULSE LOADINGS - GENERAL DISCUSSION

With the following examples of pulse loadings, we compare the results produced by a small mesh having absorbing boundaries to those generated by an extended mesh. The respective, two-dimensional meshes are drawn in Figure 6. Time histories of the response are recorded at three points, labeled A, B, or C, in each of the meshes in Figure 6.

The two excitations which are considered are a vertical pulse that mainly generates dilatational waves, and a traction pulse that primarily generates shear waves. These are applied to the top surface near point A (see Figure 7). These loadings were selected because of their simplicity and their relevance to the vertical and horizontal loadings that occur in soil-structure interaction problems. In the vertical-pulse loading, the x degree-of-freedom is fixed along the left face of the mesh. These are the "symmetrical" boundary conditions which allow us to analyze a half space with a quarter mesh. Nodal forces at two nodes

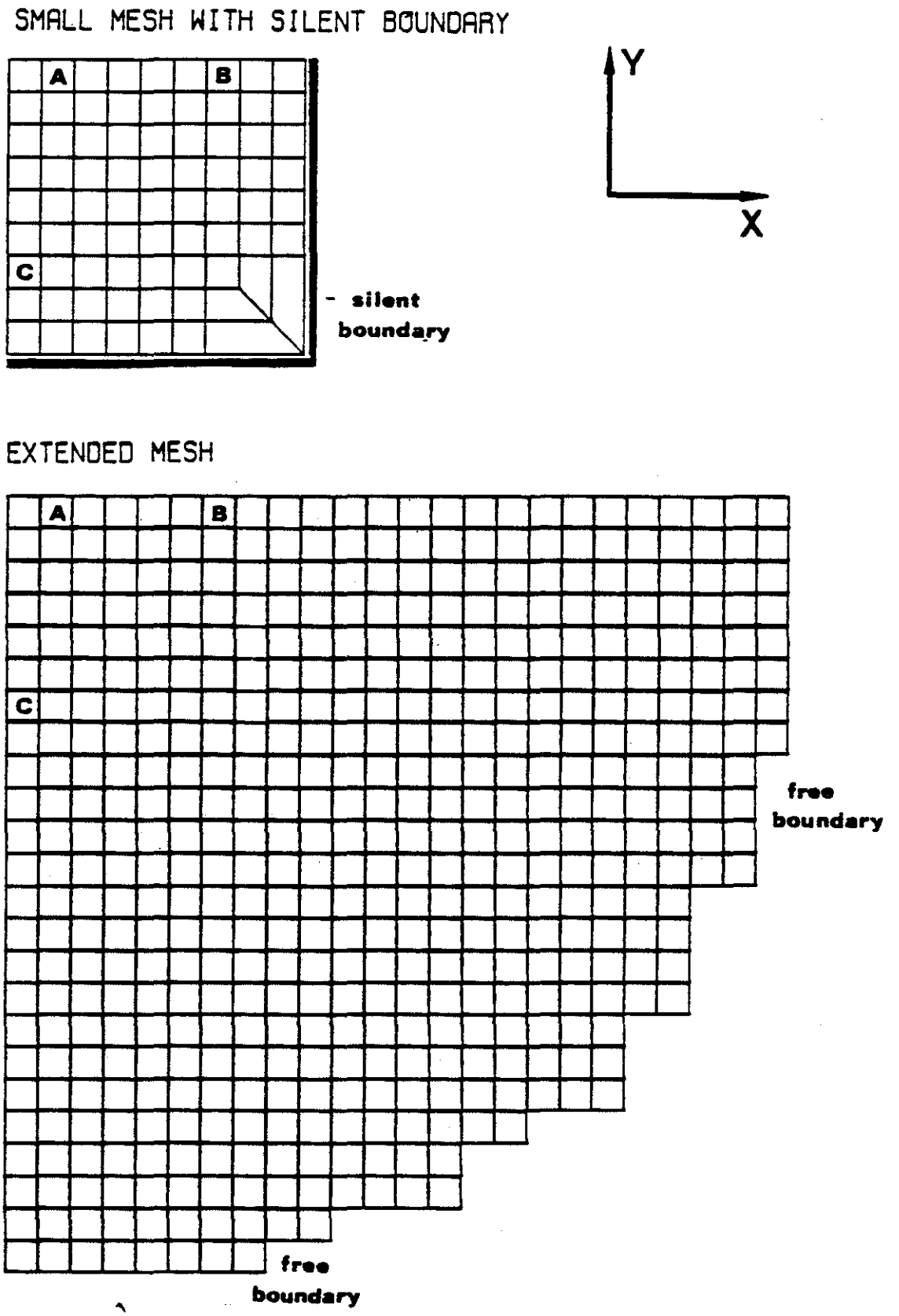

Figure 6. Finite-element meshes used for pulse loadings: (top) mesh with absorbing boundary; (bottom) extended mesh with free boundary.

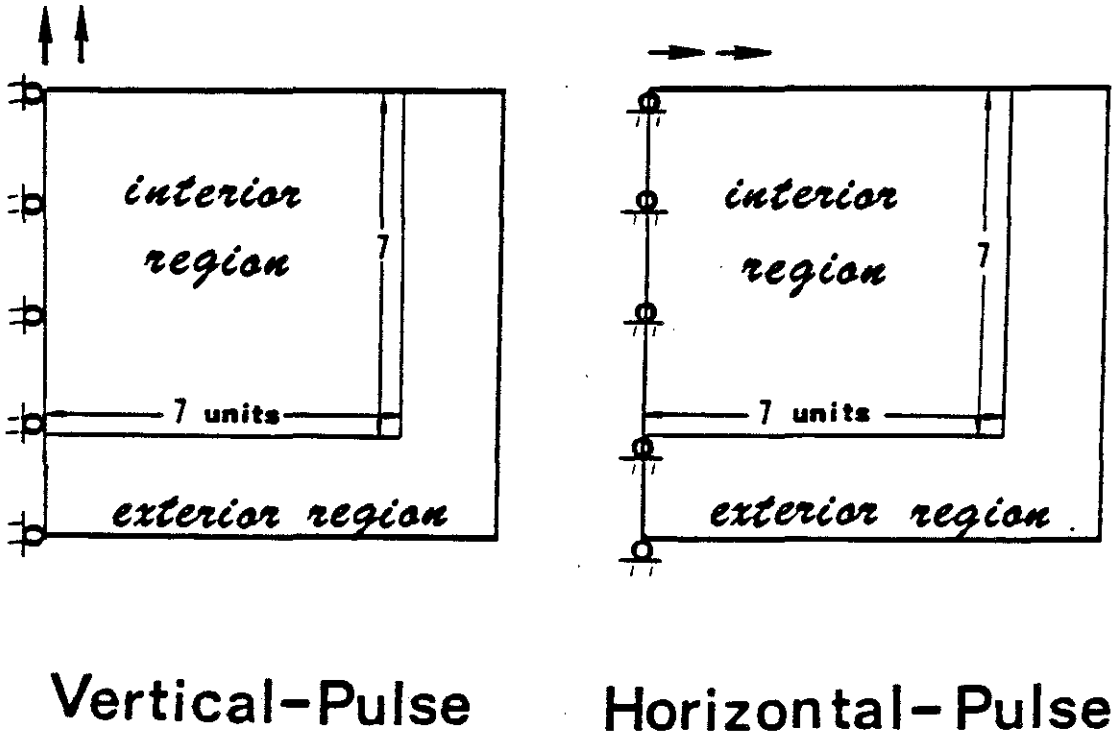

Figure 7. Schematic drawing of the horizontal- and vertical-pulse loadings.

are applied vertically over the first time step, and then they are abrogated.

Another group of numerical experiments falls under the heading of horizontal-pulse loading. Figure 7 illustrates their loading and boundary conditions. With this applied-traction problem, we are not analyzing a half space because it does not meet the requirements of symmetry. The conditions of Figure 7, however, ensure that shearing waves impinge upon the horizontal, silent boundary.

IV. HORIZONTAL-PULSE LOADING

IV.A. Comparisons Among the Boundary Methods

The first test problem shown is the horizontal-pulse loading in Figure 7. c_s = .5345 units/second, c_d = 1 unit/second, ρ = density = 1 (Poisson's ratio = 1/3), DT = .85 seconds, and 1 unit = the width of one of the square elements. With these values, the dilatational waves reach the boundary of the smaller mesh in 9 seconds; the shear waves arrive at the same point in 16 seconds. γ = .5, β = .25, and no material damping is present in the system. The interior region was solved using the explicit algorithm.

The horizontal displacements, the main components of the motion, are plotted in Figures 8 through 11. Figures 8 and 9 report those displacements recorded near the side boundary (point B in Figure 6); the arrival of the main pulse is evident in all of the figures. Wave reflections caused by a free boundary are clearly seen in Figure 8, while the paraxial and viscous boundaries largely succeed in eliminating this reflection. The extended-paraxial boundary is slightly more accurate

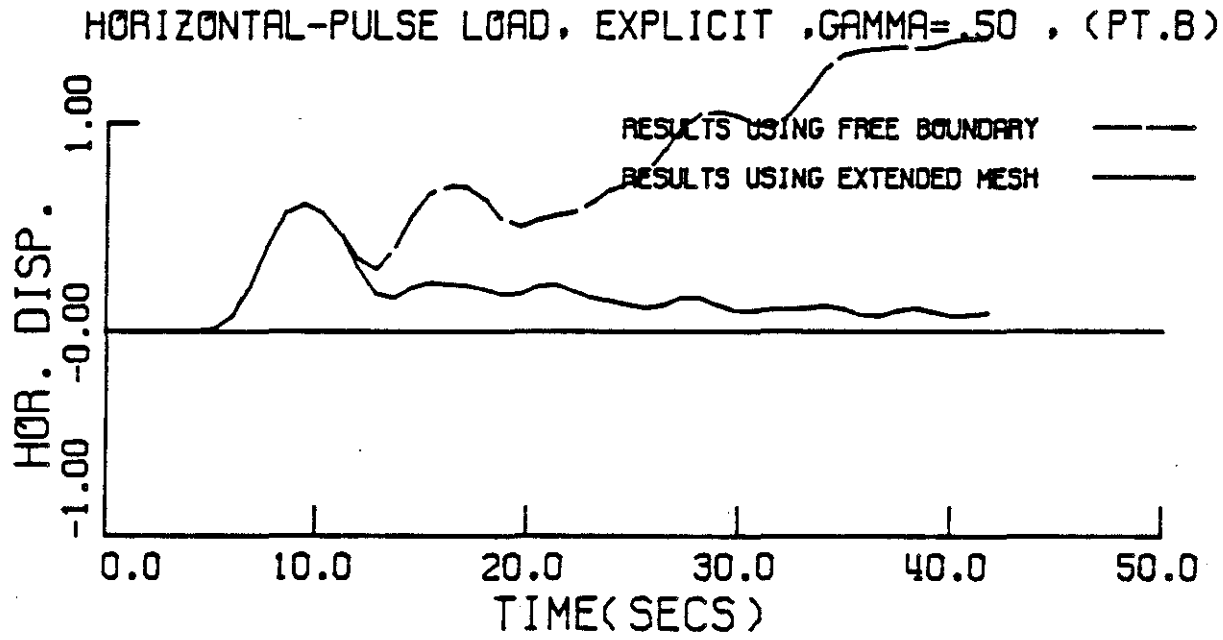

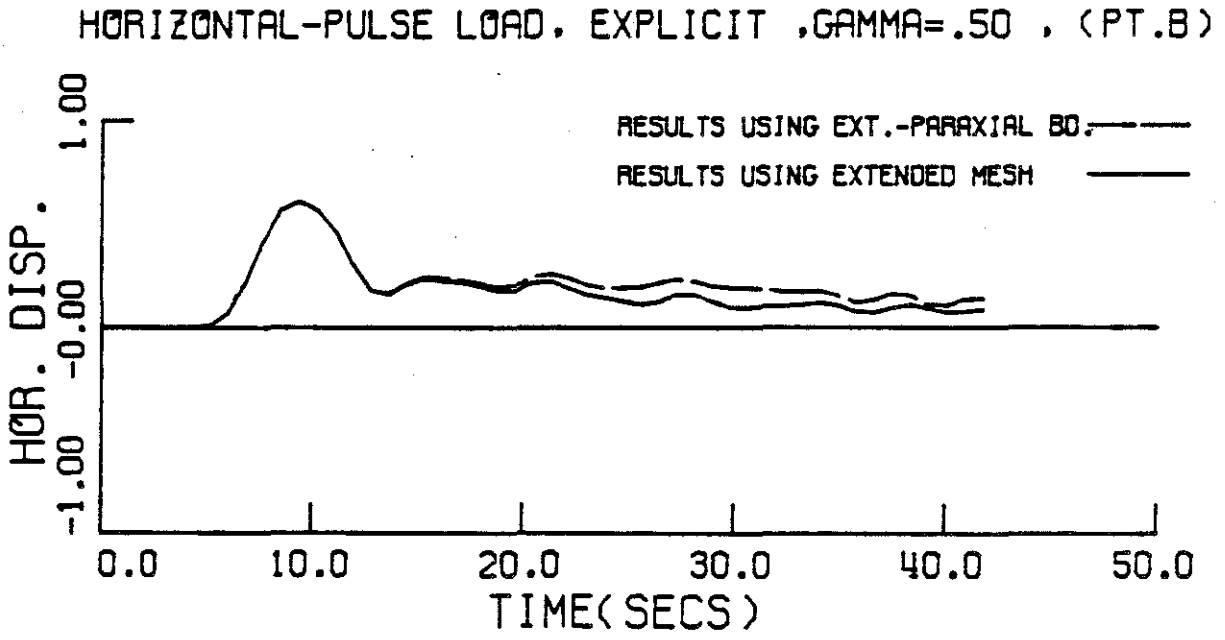

Figure 8. Horizontal displacement at point B as a function of time. (Horizontal-pulse loading, undamped case.)

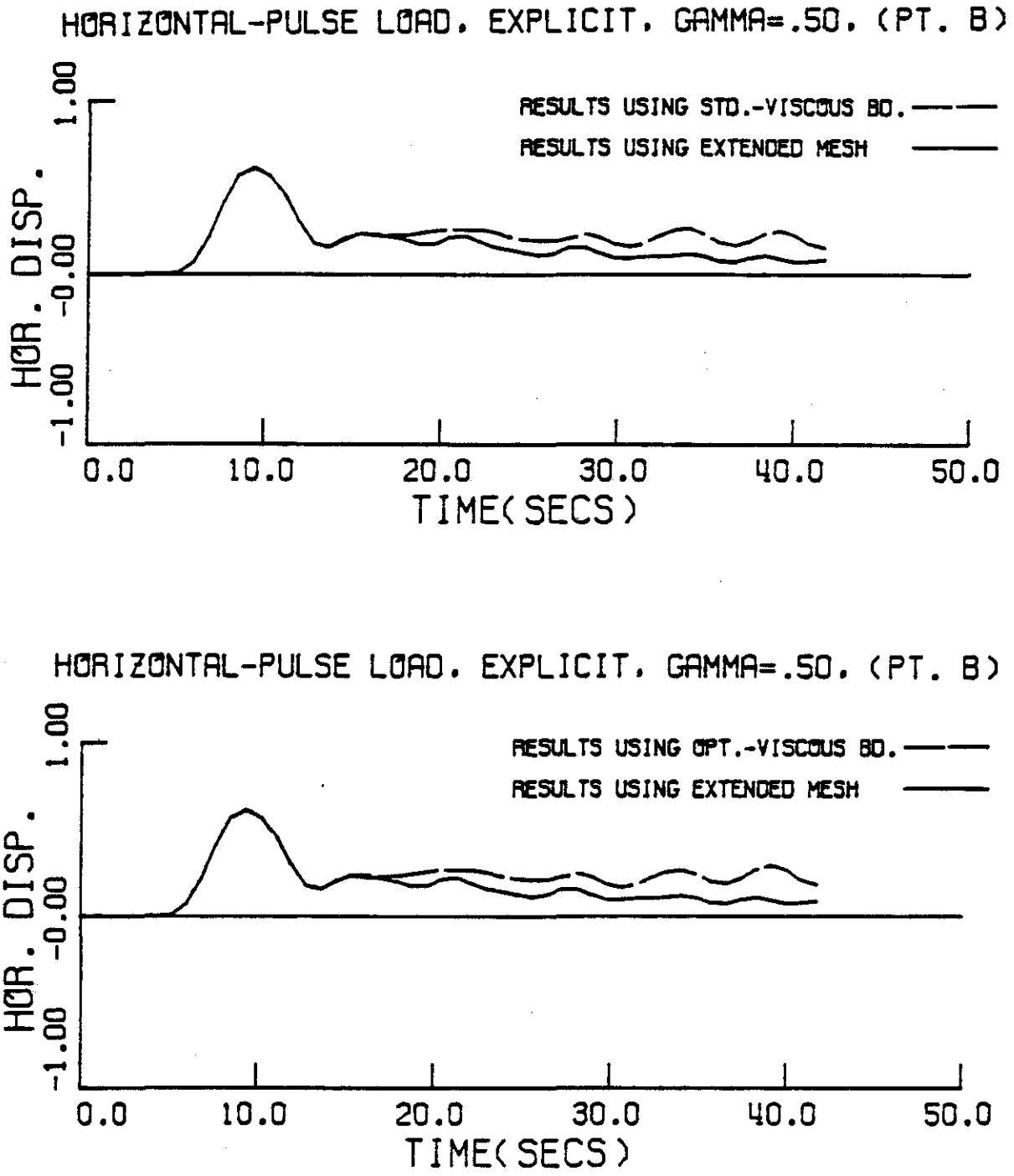

Figure 9. Horizontal displacements at point B as a function of time. (Horizontal-pulse loading, undamped case.)

than are the other transmitting boundaries. On the other hand, both the standard-, and the unified-viscous boundaries produce nearly the same response (see Figure 9).

Figures 10 and 11 demonstrate how well the silent boundaries simulate the infinite domain at point A in Figure 6. Figure 10 shows the results for the extended-paraxial boundary, and Figure 11 illustrates the behavior of the viscous boundaries. These figures corroborate the slight edge in the paraxial boundary's performance as seen earlier.

Oscillations of the horizontal displacement in Figures 10 and 11 arise in all of the calculations, including the extended mesh. Each of the transmitting boundaries preserves the period of these high frequency motions, which arise from the coarseness of the mesh and the character of the loading.

In the calculations of the displacements, as illustrated in Figures 9 and 11, the unified- (optimized-) viscous boundary almost duplicates those results produced by the standard-viscous boundary. The largest quantitative differences between the two methods appear in Figure 12. The vertical displacements that are recorded next to the side boundary (point B) indicate that the standard-viscous approach may be, to a small extent, the better alternative. The result for the paraxial boundary, corresponding to Figure 12, indicates a slightly better agreement with the extended mesh than does the viscous boundaries.

In Figure 12, it may also be noted that the vertical wave arrives later than does the horizontal pulse shown in Figure 8. This later arrival seems to be composed mainly of a shear wave, which travels more slowly than does the horizontal, dilatational pulse.

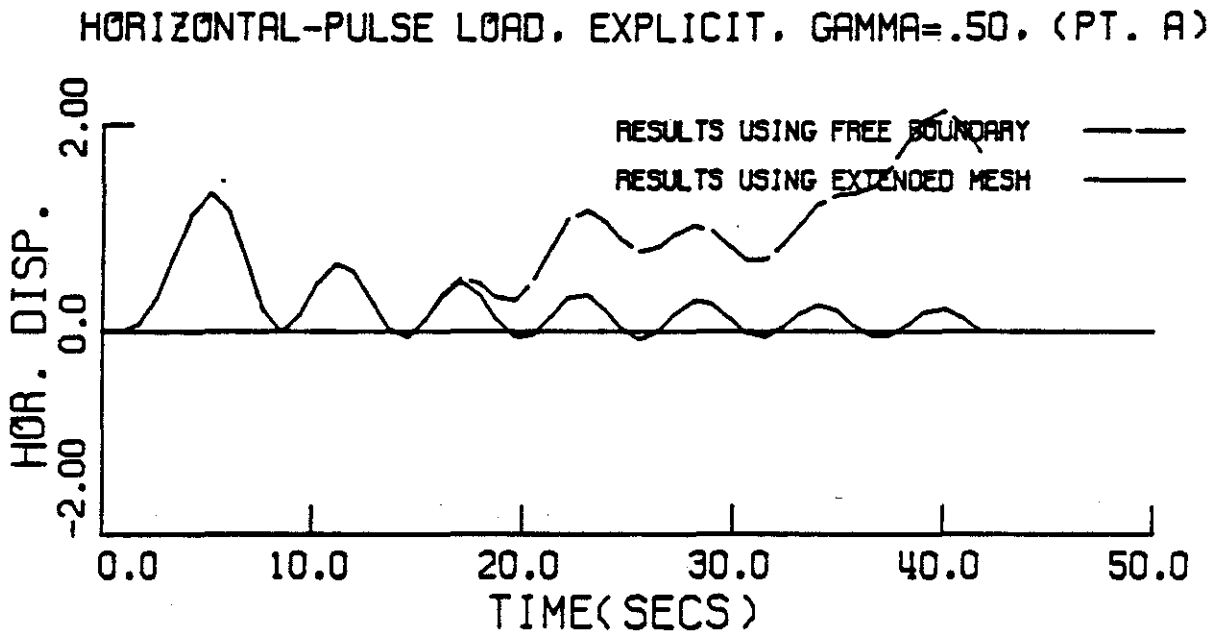

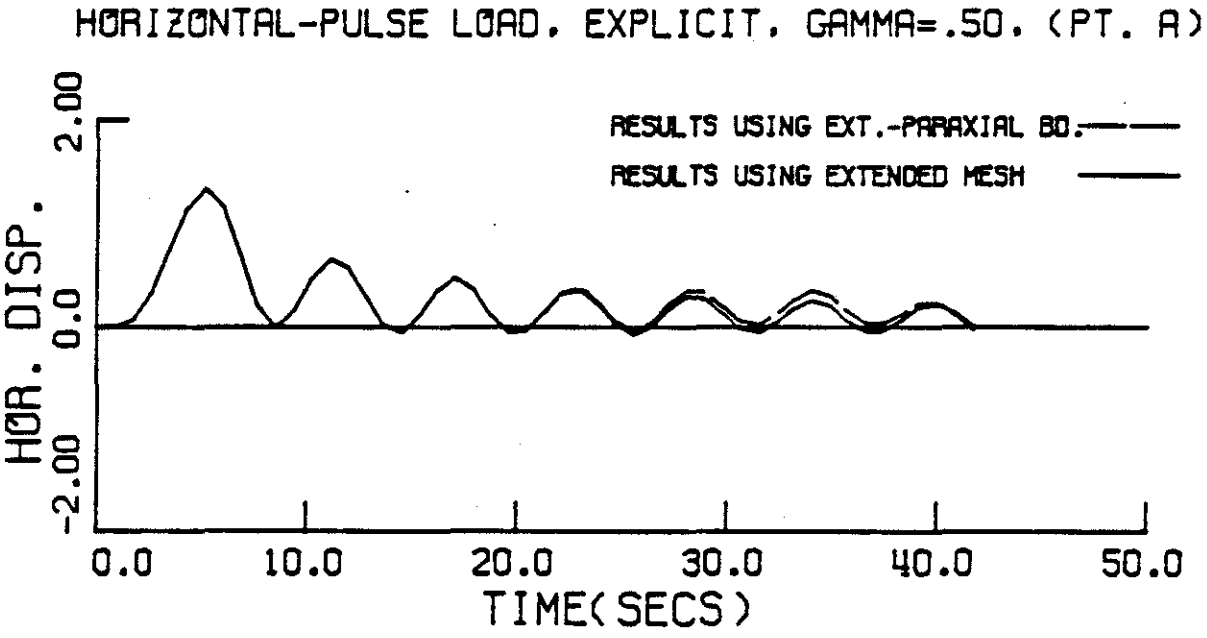

Figure 10. Horizontal displacements at point A as a function of time. (Horizontal-pulse loading, undamped case.)

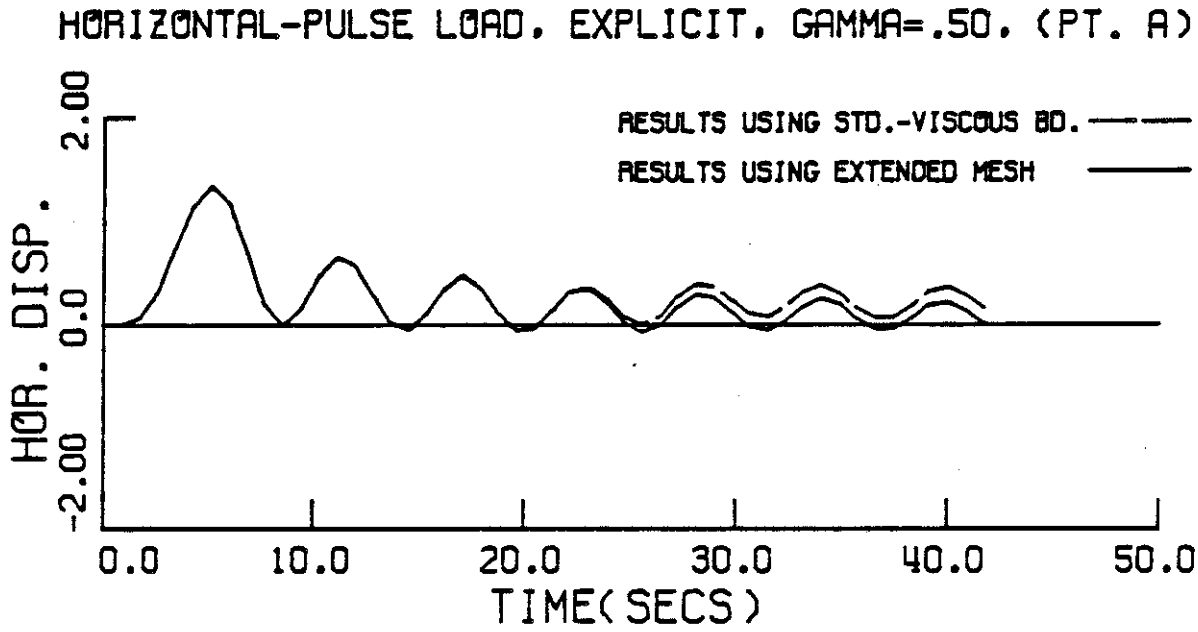

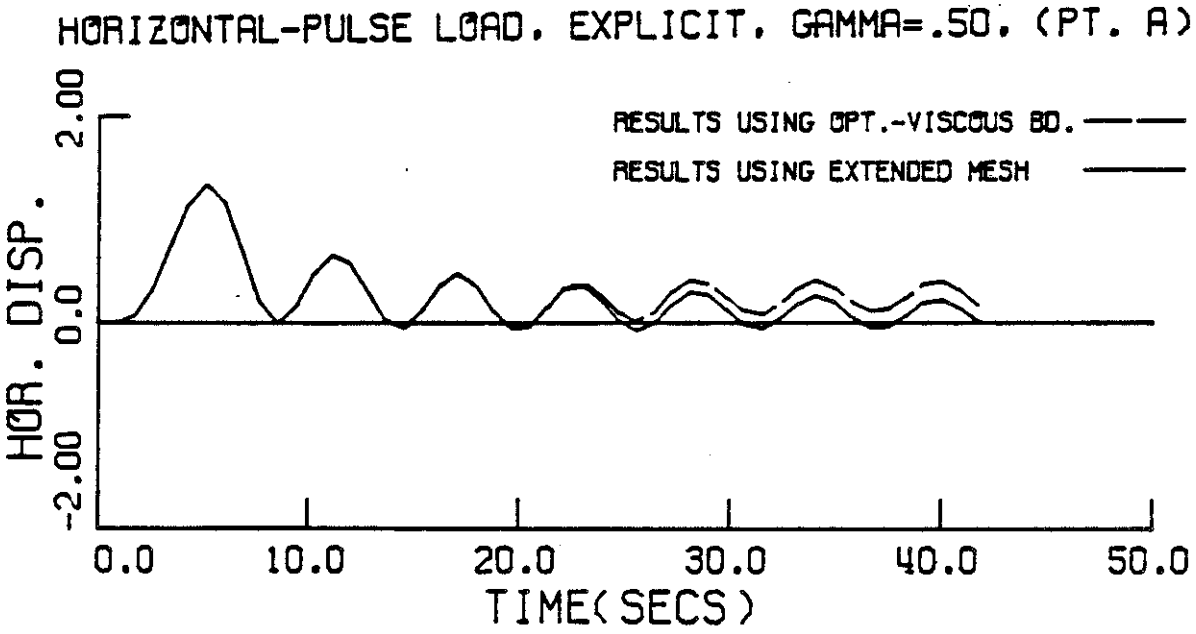

Figure 11. Horizontal displacements at point A as a function of time. (Horizontal-pulse loading, undamped case.)

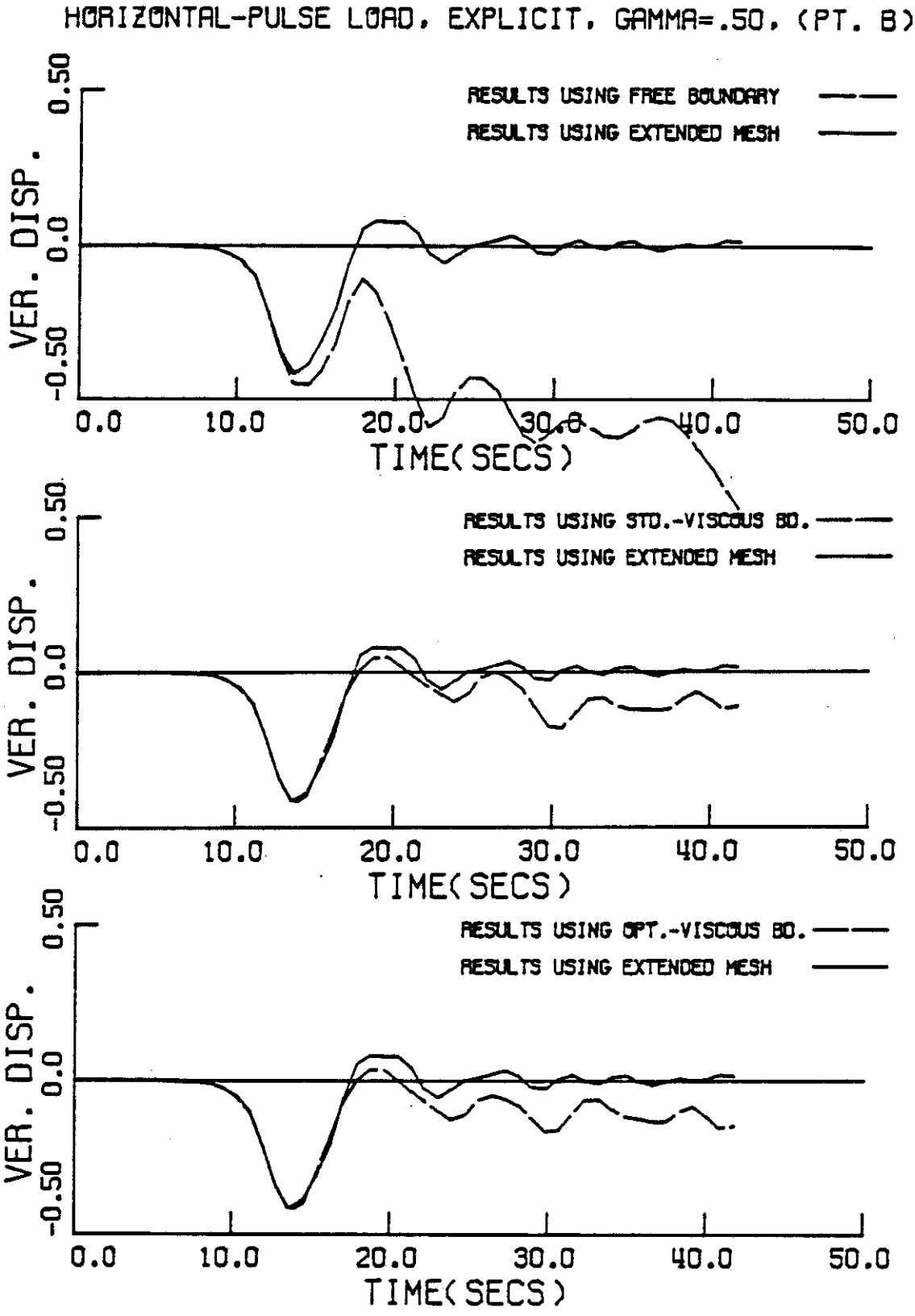

Figure 12. Vertical displacements at point B as a function of time. (Horizontal-pulse loading, undamped case.)

IV.B. High-Frequency Waves

One weakness of the silent boundaries is highlighted in Figures 13 and 14. The numerical noise following the arrival of the main stress pulses (between 9 and 14 seconds) is the predominant feature seen in these figures. Both the extended and the small meshes, which provide reasonable solutions to the high-frequency displacements, are too coarse to accurately determine the stresses; these latter quantities are evaluated from the derivatives of the displacements. It is, therefore, understandable that none of the boundary schemes produce the same high-frequency oscillations of the stress, σ_{22}, that the extended mesh does. The paraxial boundary actually magnifies this numerical noise, These errors propagate to the interior, where they arrive after t = 30 seconds. (See Figure 14.)

They are also evident in the energy plots of Figure 15. The total energy is the sum of the kinetic and strain energies, which are contained in the "interior" region of Figure 7. For each time step, we computed this value by integrating the energy terms over the region (using one-point Gaussian quadrature).[2] The effects of this reflected, high-frequency energy, for the case of the extended-paraxial boundary, become apparent after t = 30 seconds. The paraxial boundary is responsible for a slightly larger error than is the viscous mechanism.

---

[2]We should clarify why the energy level, even with the use of free boundary, declines in Figure 15. Some of the energy resides in a narrow band of elements, which is present outside of the "interior" zone. (This is the "exterior" zone shown in Figure 7.) Also, if numerical damping is present, then the high-frequency energy is reduced. In Figure 15, where no damping is used, the total energy in the free-boundary system is conserved after t = 20 seconds.

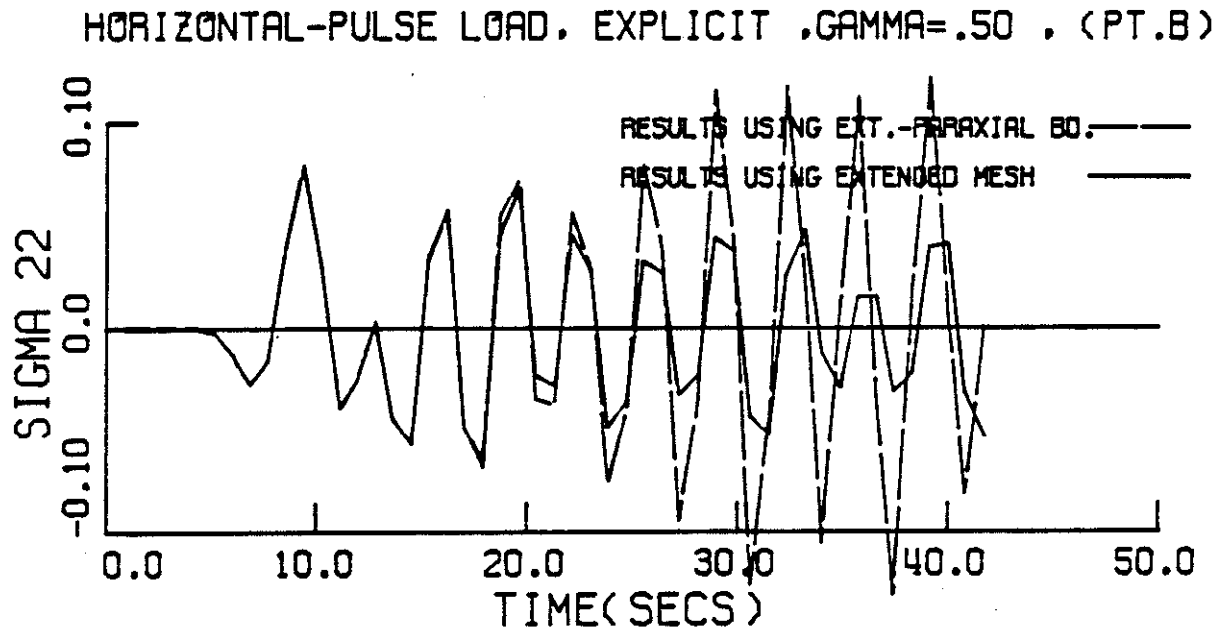

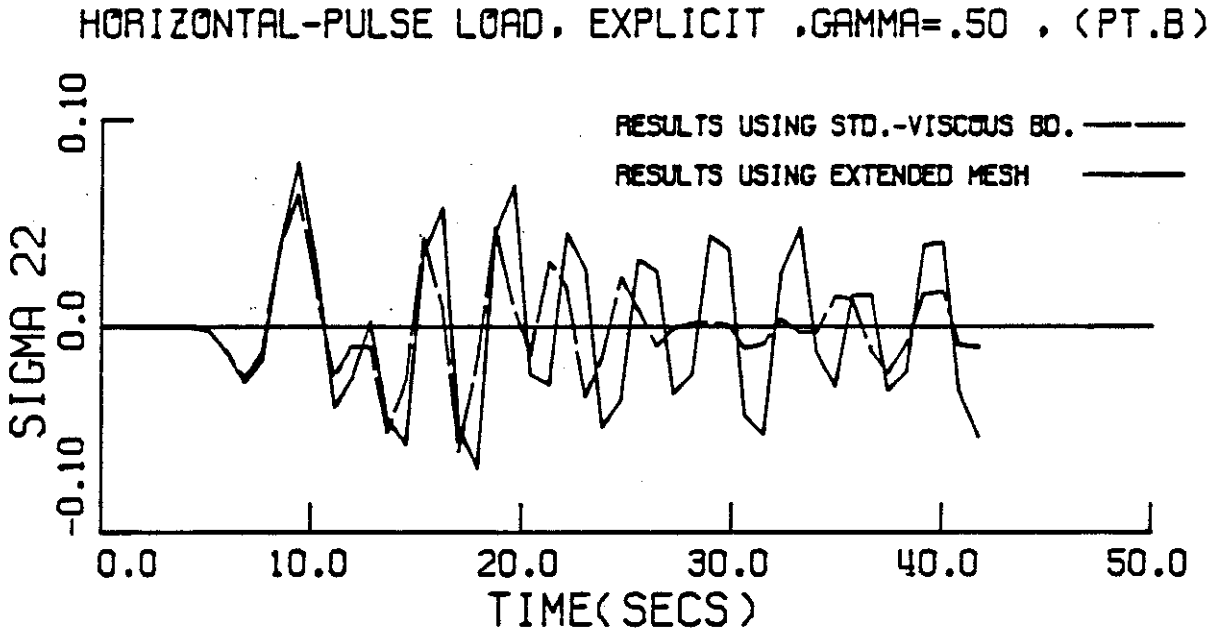

Figure 13. Stresses, σ_{22}, at point B as a function of time. (Horizontal-pulse loading, undamped case.)

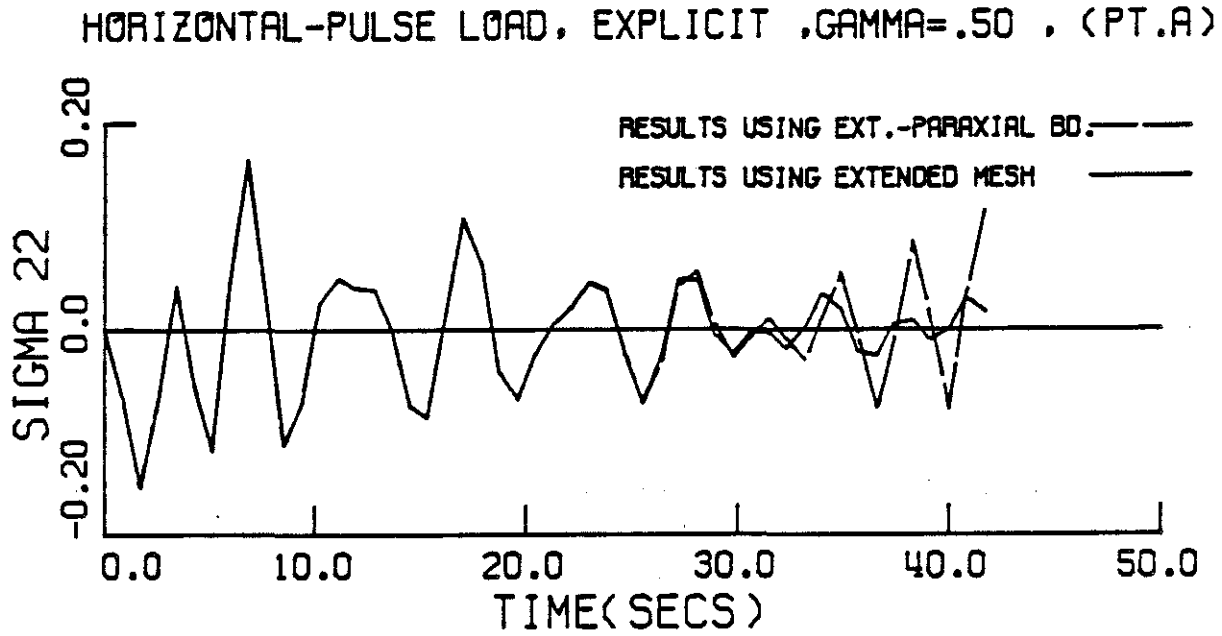

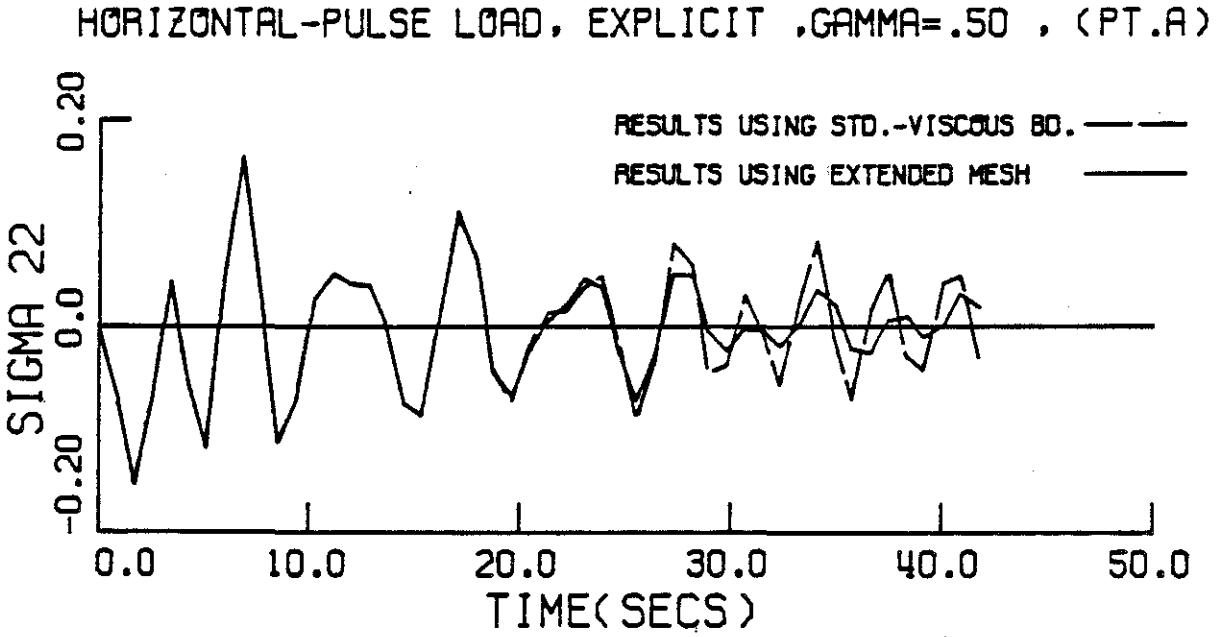

Figure 14. Stresses, σ_{22}, at point A as a function of time. (Horizontal-pulse loading, undamped case.)

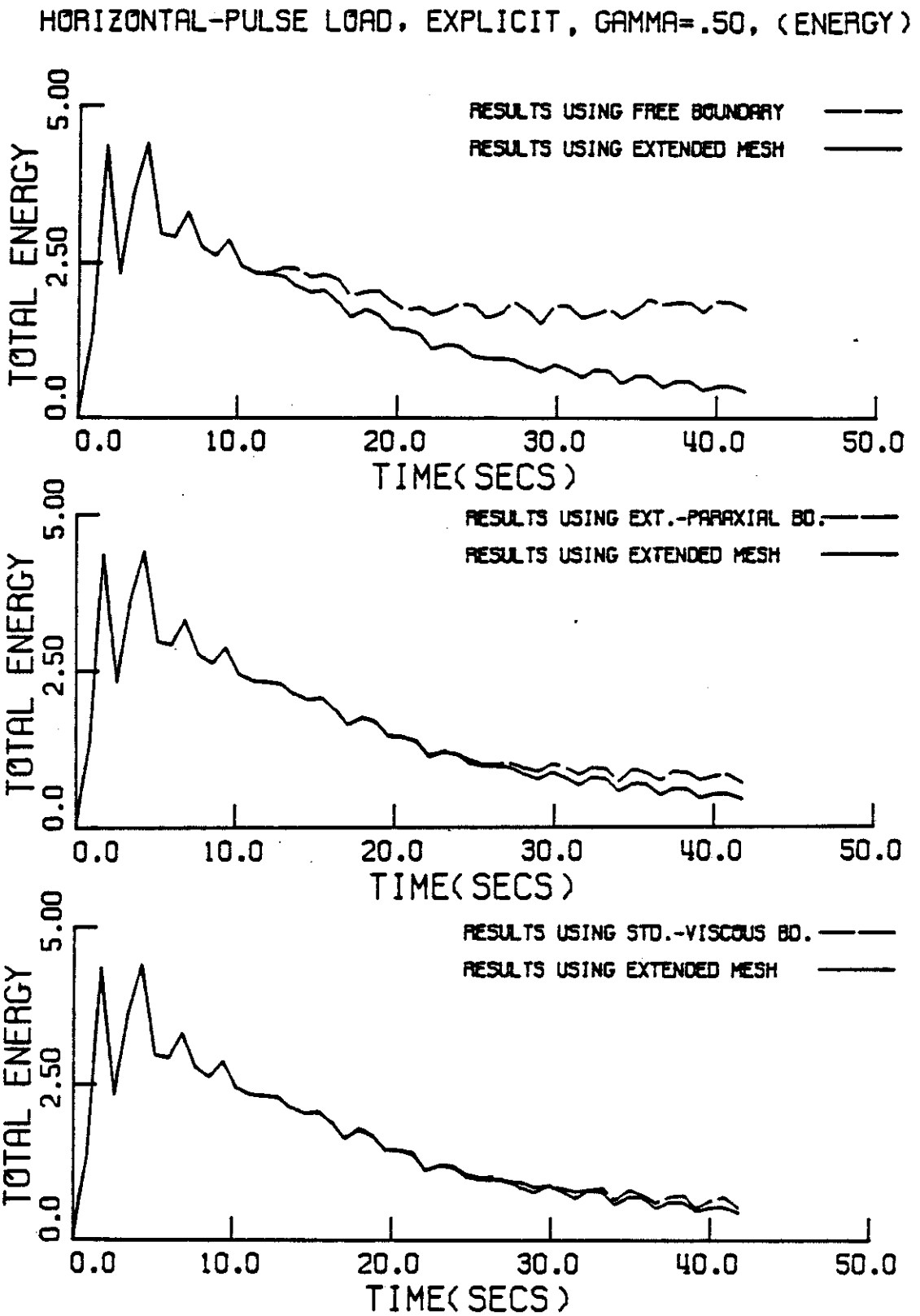

Figure 15. Total energy in the interior region as a function of time. (Horizontal-pulse loading, undamped case.)

One technique for filtering high-frequency noise is to apply some numerical damping, which selectively attenuates the high-frequency motion of the mesh. We implemented this idea in order to eliminate the noise introduced by the silent boundaries. In the next group of illustration, Figures 16 to 18, γ is set equal to .55, with β = .276. These parameters introduce some algorithm damping, which mainly affects the higher modes. Except for this change, Figure 16 depicts the same energy graphs as are in Figure 15. The damping's beneficial effect is clearly evident. It not only reduces the total energy for long times, it also annihilates the high-frequency errors in the total energy, including those associated with reflections from the silent boundaries.

On a local level, the effect of numerical damping is demonstrated in Figure 17. The spurious, high-frequency oscillations are significantly reduced compared to those of Figure 13. The numerical damping is especially effective in reducing the high-frequency reflections from the paraxial boundary.

For the lower modes, that is, the larger, wavelength components of the response, the algorithmic damping we applied has little effect, and the conclusions for the undamped case are also valid here. For example, in Figure 18, we plot the horizontal displacements near the side boundary (point B). As a function of time, the displacement curve appears to be a little smoother than does that for the undamped case in Figures 8 and 9, but the amplitudes are almost identical. The extended-paraxial boundary, again, enjoys a slight advantage over the viscous boundary.

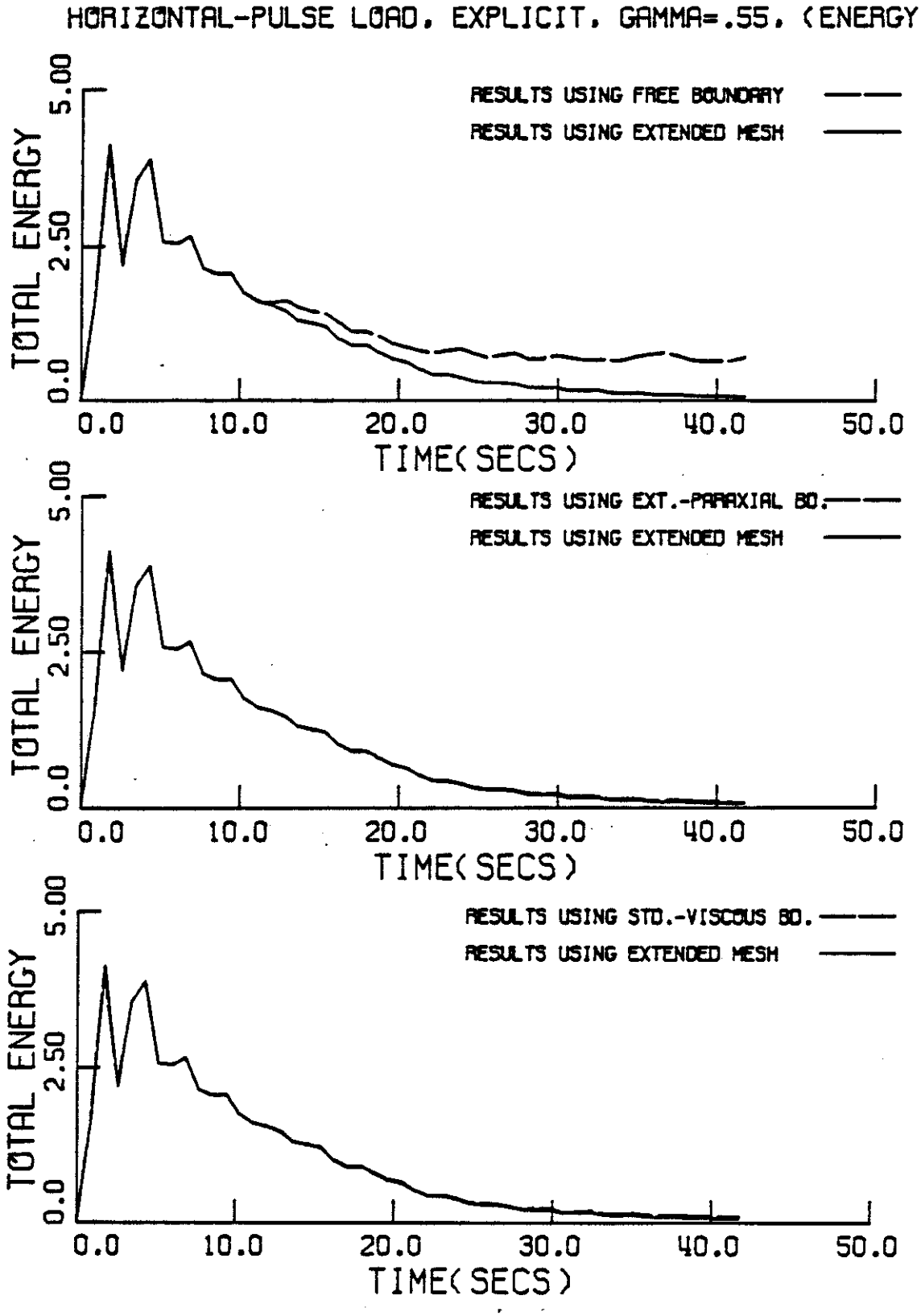

Figure 16. Total energy in the interior region as a function of time. (Horizontal-pulse loading, damped case.)

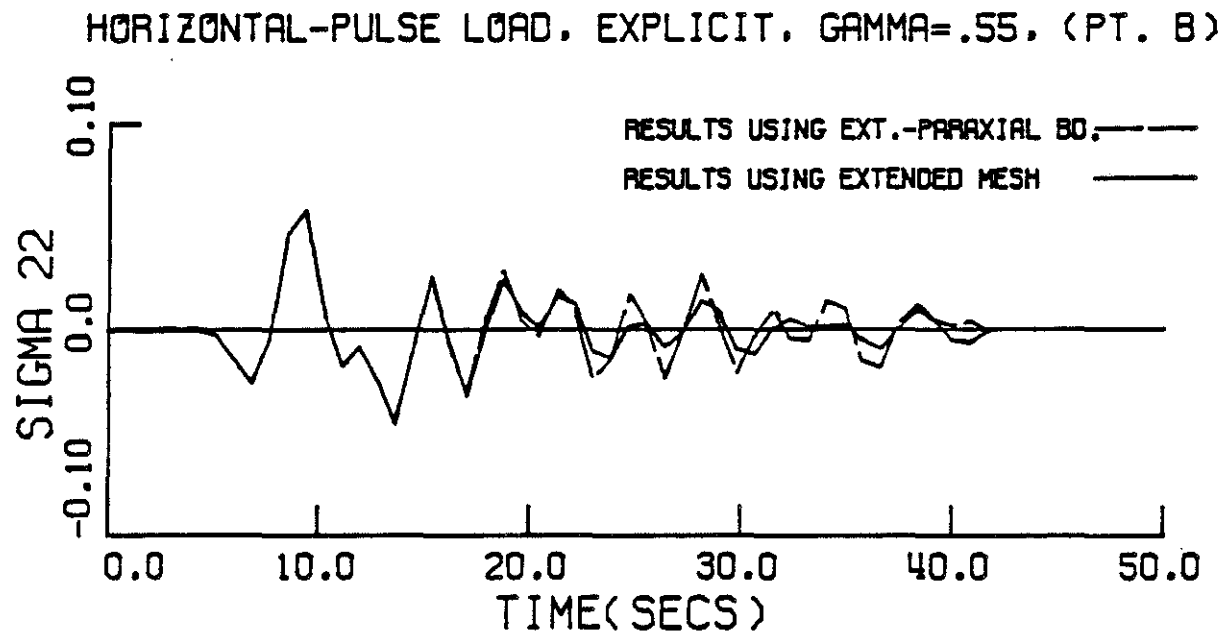

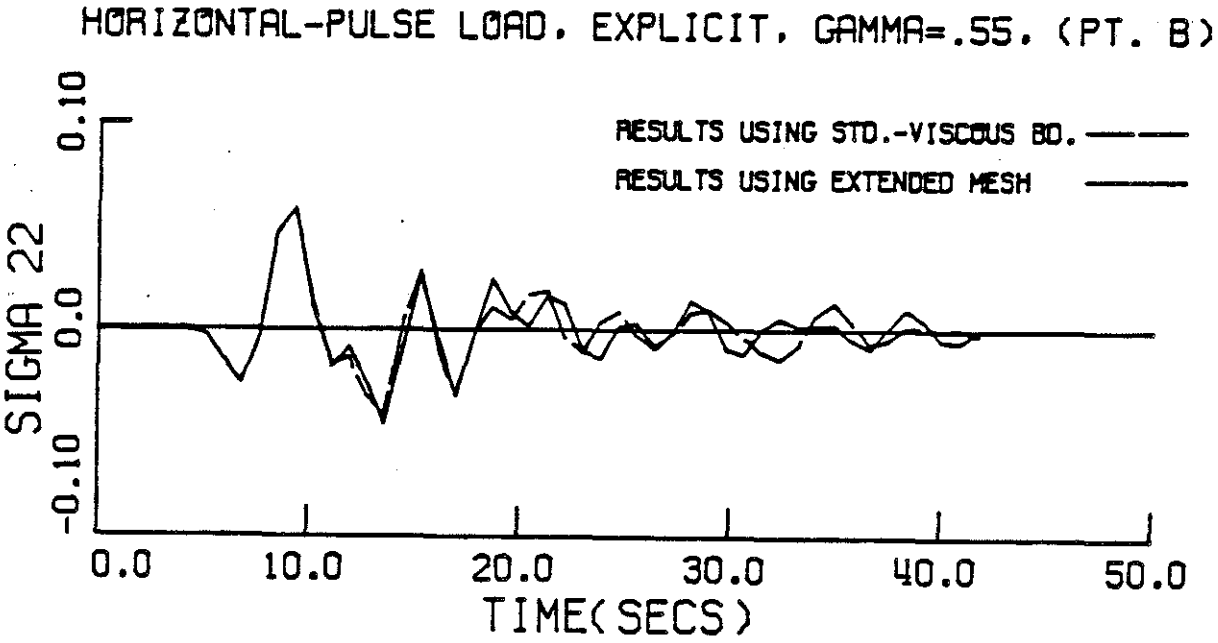

Figure 17. Stresses, σ_{22}, at point B as a function of time. (Horizontal-pulse loading, damped case.)

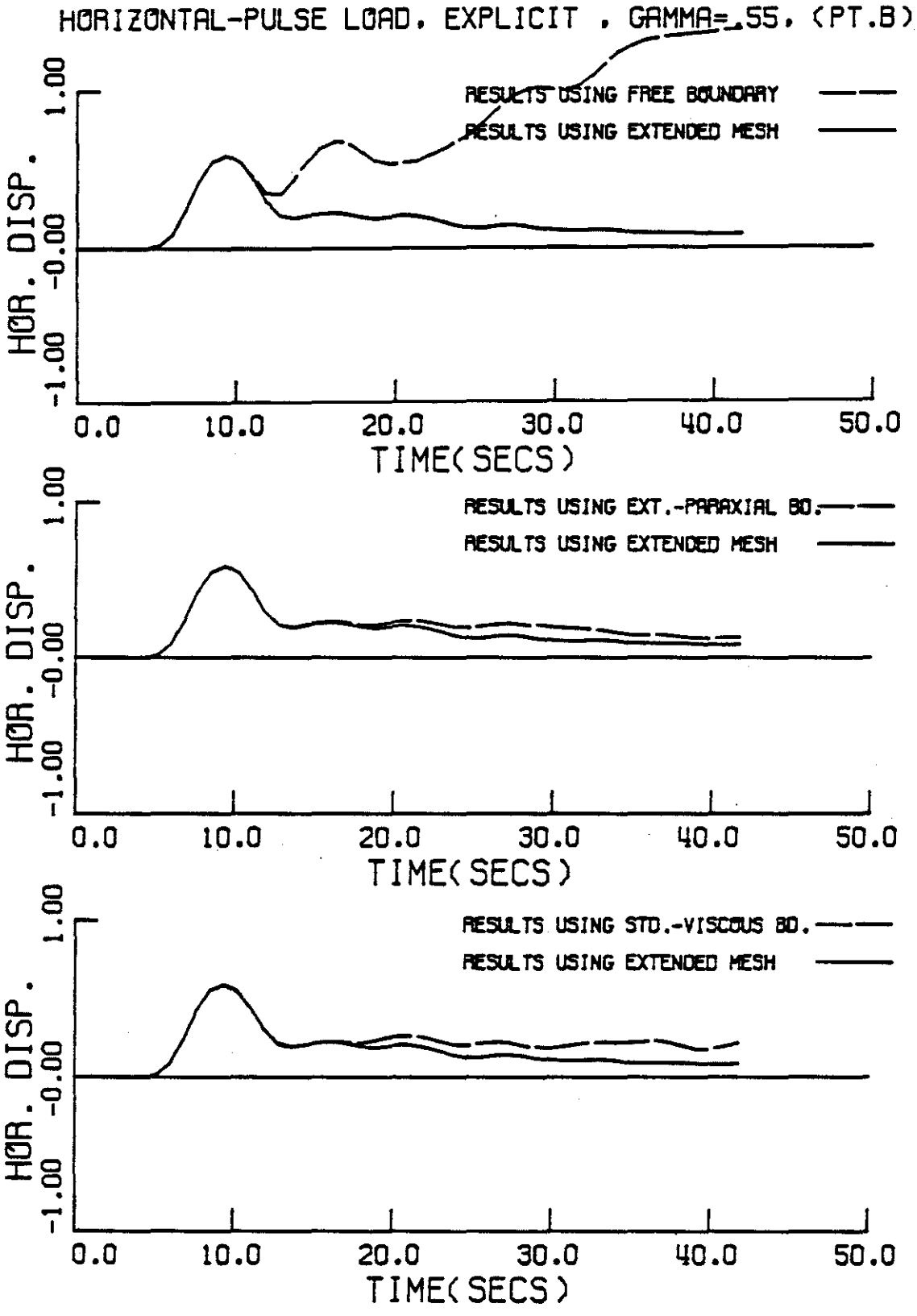

Figure 18. Horizontal displacements at point B as a function of time. (Horizontal-pulse loading, damped case.)

IV.C. Shear Waves

Shearing motion dominates the solution at point C, near the bottom of the mesh. Figures 19 and 20, respectively, present the undamped shearing stresses and horizontal displacements at the lower measuring point. Both figures indicate that the viscous boundary causes a greater reduction in the shearing amplitudes than is shown by the extended mesh. This could be due to some destructive interference by the reflected waves. These illustrations, however, do provide some evidence of the boundaries' ability to transmit shear waves, as well as dilatational waves.

V. VERTICAL-PULSE LOADING

The computations of the response to the vertical loading were conducted without using numerical or material damping. The interior equations were solved implicitly, and DT = .9 second. The material constants are the same as those above, and the load is applied for one time step. The loading and boundary conditions, as well as the locations of the points A, B, and C, are depicted in Figures 6 and 7.

In Figure 21, we illustrate the total energy (kinetic and strain) for the interior region. The reflections from the free boundary are evident, while both of the silent-boundary schemes remove the outgoing waves. The absorbing mechanisms perform better for the high-frequency stresses here than they do in the horizontal-loading case. This is illustrated in Figure 22 for σ_{11} near the side boundary (point B).

Vertical displacements constitute the largest part of the response, and they are recorded at point B in Figure 23. Although both of the dissipative mechanisms are effective, the paraxial boundary is slightly

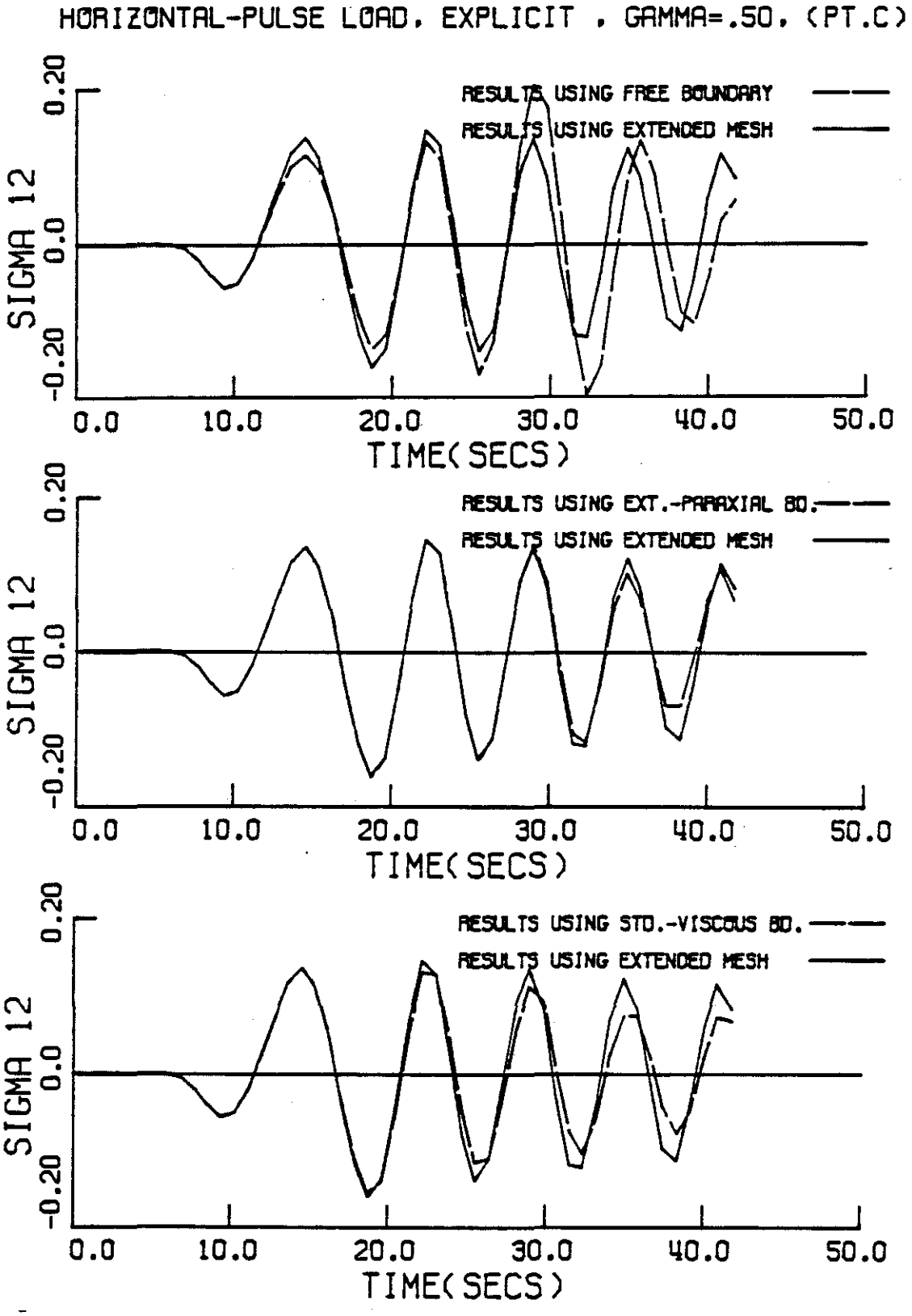

Figure 19. Stresses, σ_{21}, at point C as a function of time. (Horizontal-pulse loading, undamped case.)

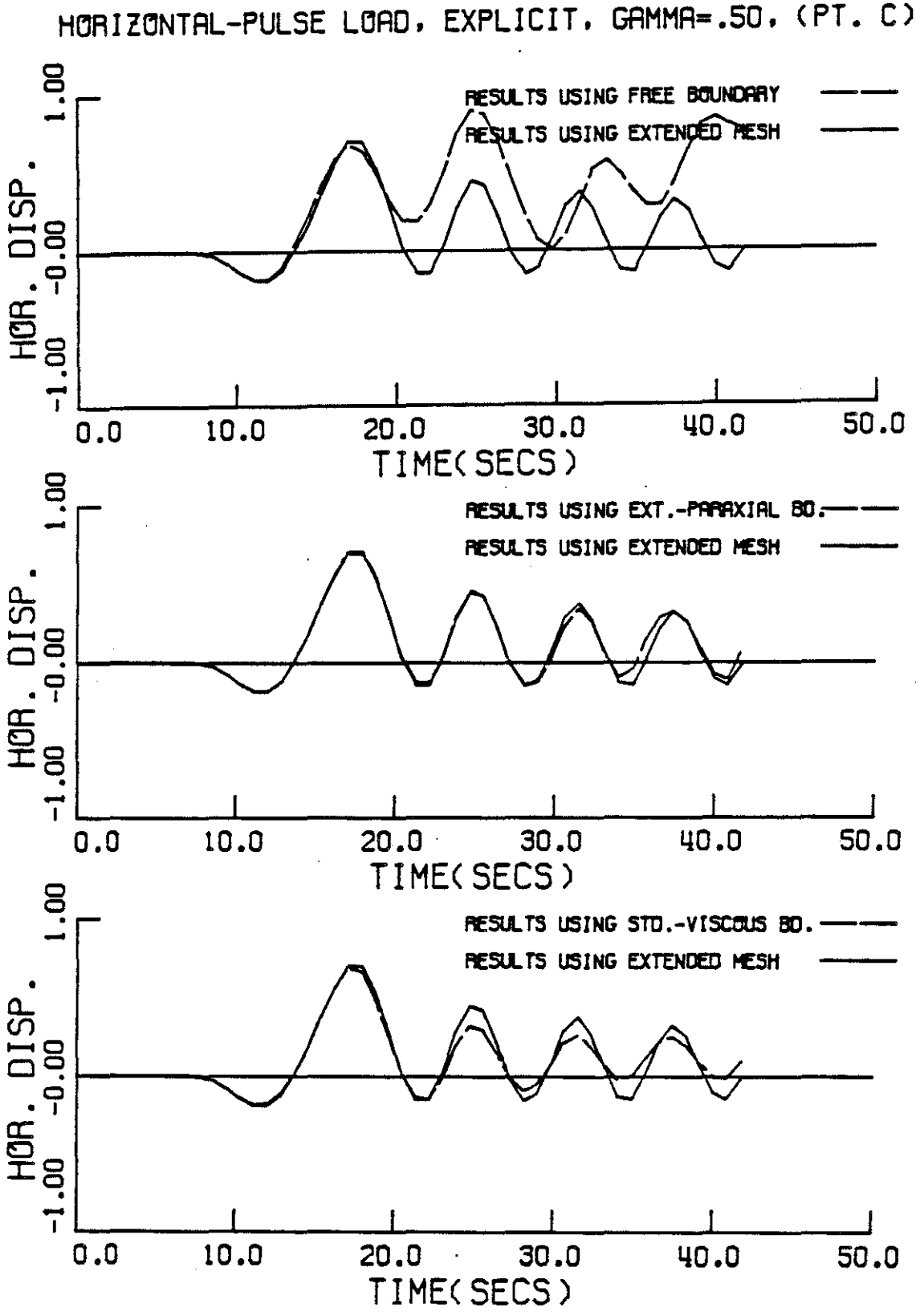

Figure 20. Horizontal displacements at point C as a function of time. (Horizontal-pulse loading, undamped case.)

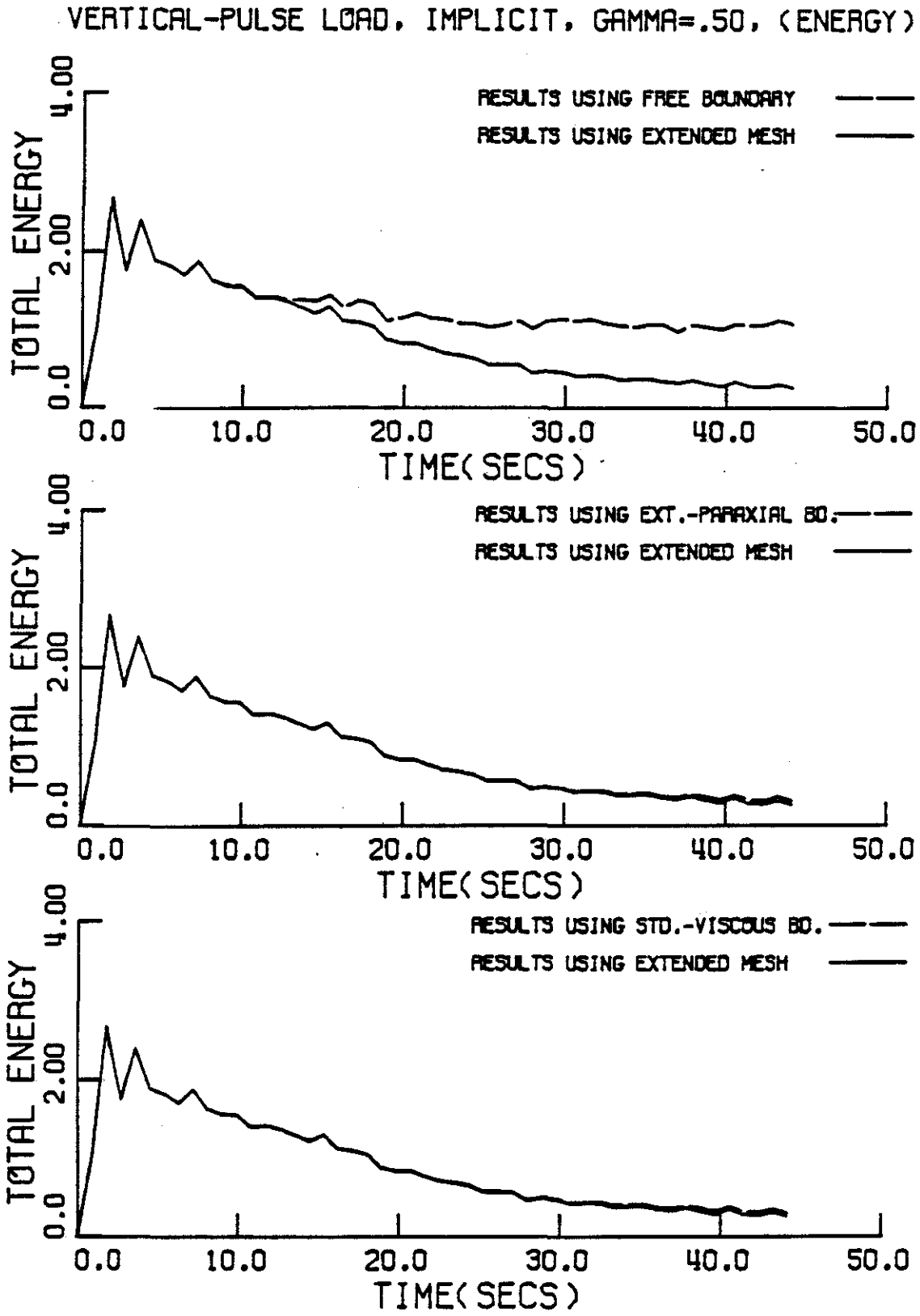

Figure 21. Total energy in the interior region as a function of time. (Vertical-pulse loading, undamped case.)

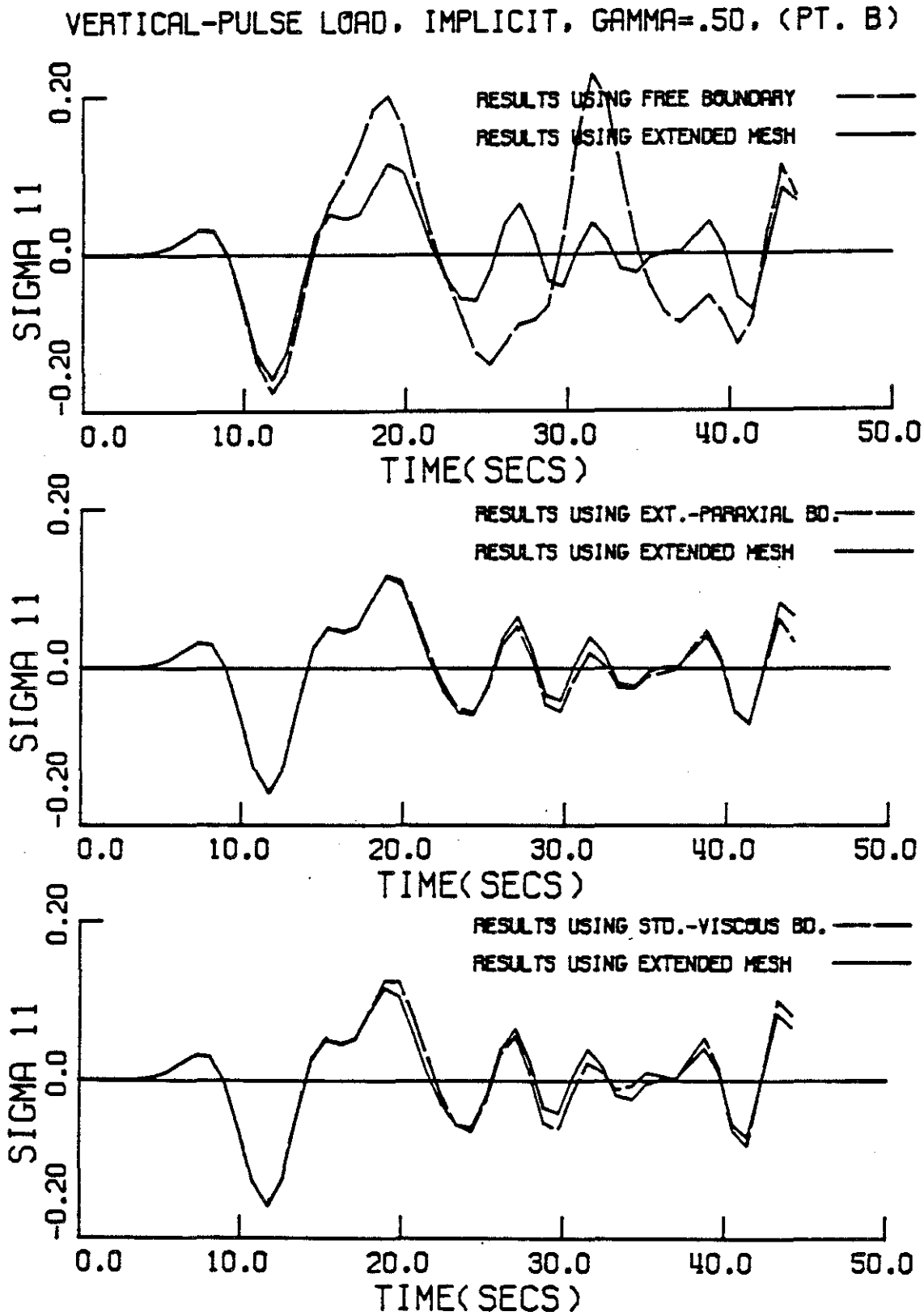

Figure 22. Stresses, σ_{11}, at point B as a function of time. (Vertical-pulse loading, undamped case.)

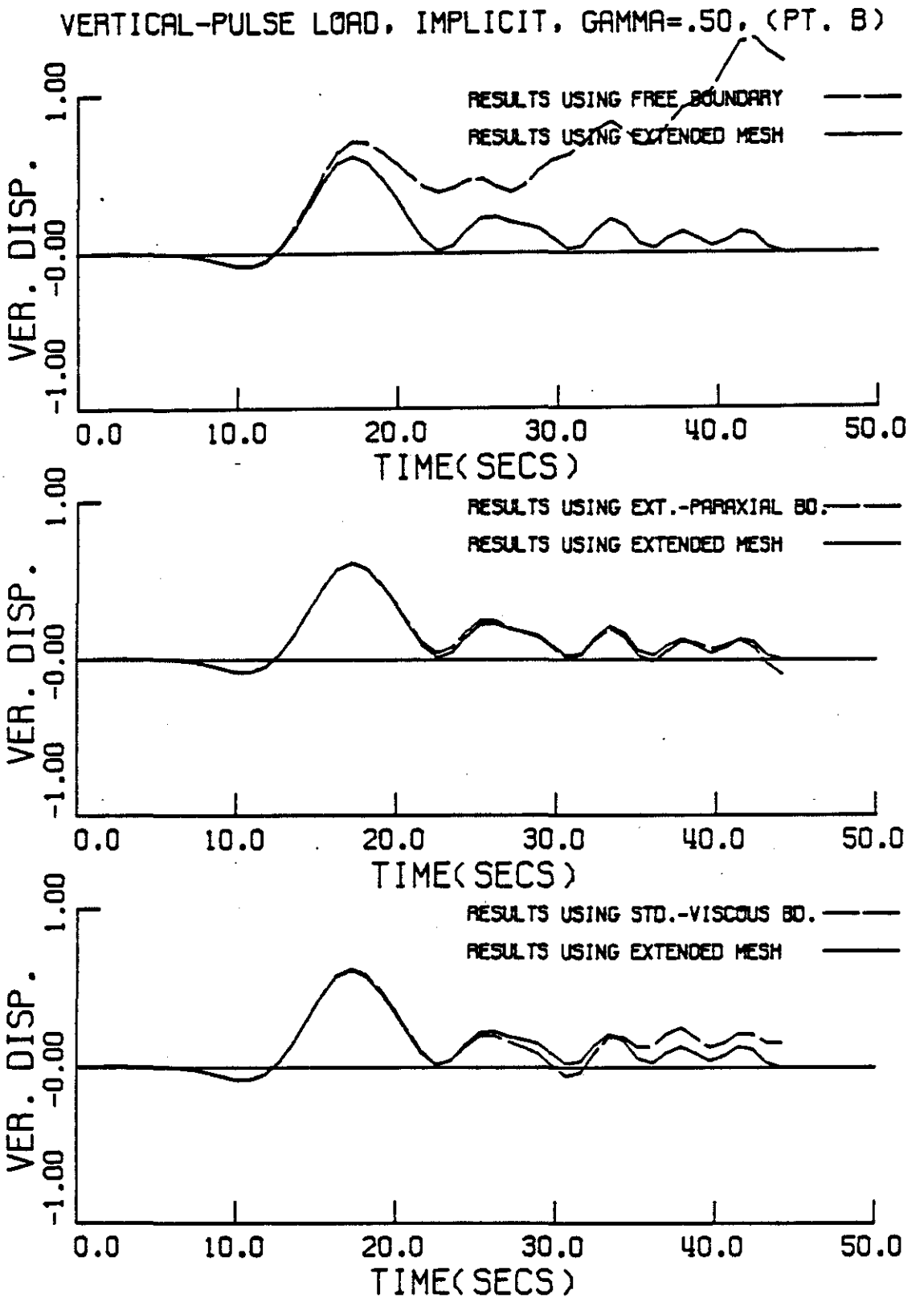

Figure 23. Vertical displacements at point B as a function of time. (Vertical-pulse loading, undamped case.)

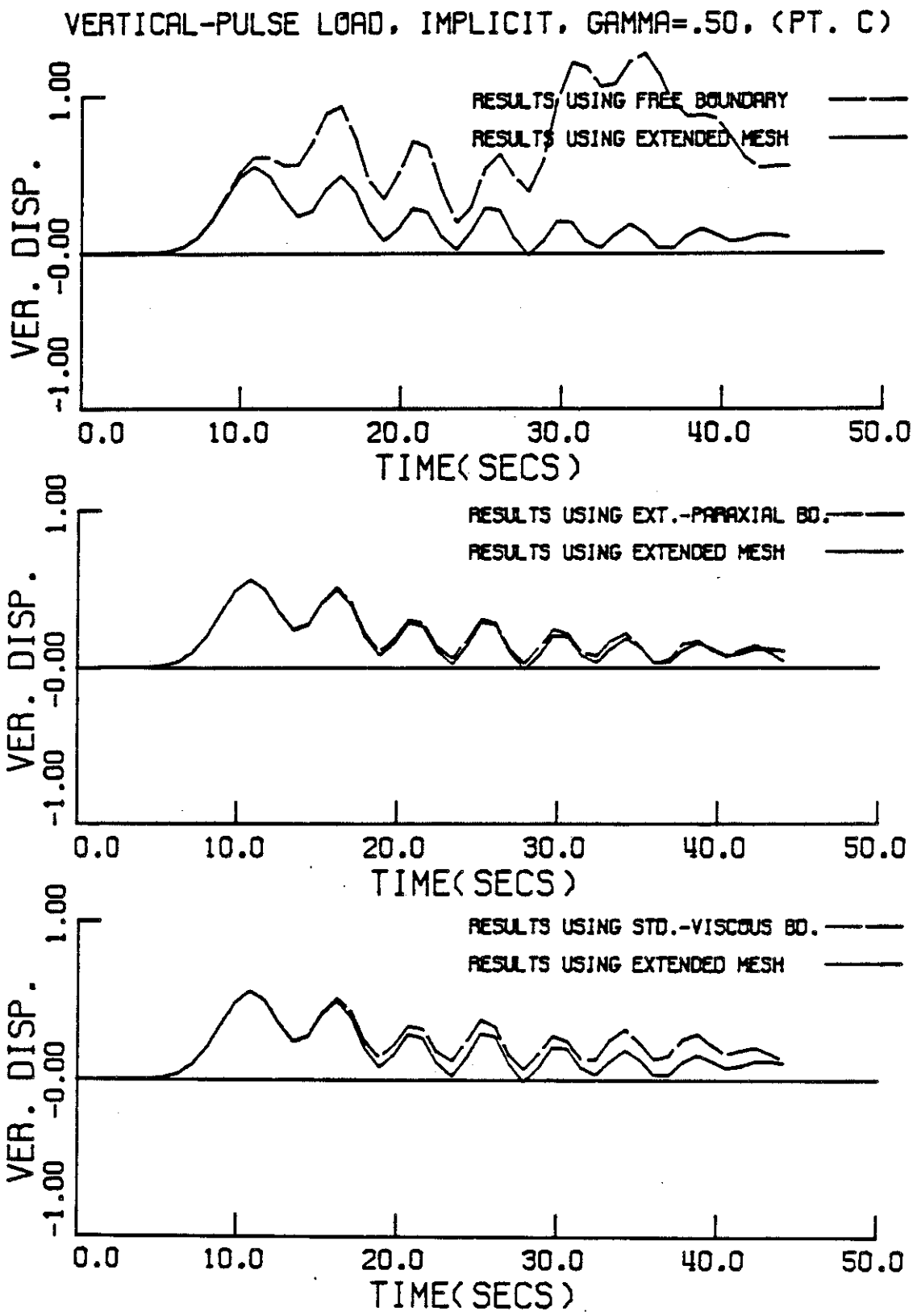

Figure 24. Vertical displacements at point C as a function of time. (Vertical-pulse loading, undamped case.)

more accurate than its counterpart. The same conclusion holds true for vertical displacements at the bottom of the mesh, point C, as is shown in Figure 24. The long-term displacement, which is observed in these figures, is similar to that which is found in Lamb's analytical solution.

Overall, for the undamped, vertical-loading problem, the absorbing boundaries remove the major part of the outgoing energy. The viscous and extended-paraxial boundaries perform almost equally well for the stresses, but the paraxial boundary has superior accuracy for the vertical displacements.

VI. VERTICAL HALF-SINE PULSE

Figures 25, 26, and 27 illustrate the progress of a half-sine pulse, applied over 5 elements, in the quarter mesh. The load is applied for one step, and is then removed. c_s = .5345 units/second, c_d = 1 unit/-second, DT = .9 second, γ = .55, and β = .276. The quarter mesh is drawn in Figure 6, and the boundary conditions are shown in Figure 7. This problem is identical to the previous, vertical-pulse examples, except for the half-sine loading. The purpose of this calculation is to show, qualitatively, the benefits of using the silent boundaries. These are used under conditions of relative mesh size which are more representative of practical applications. However, the pulse is "rapidly" applied, generating significant high frequency motion.

In Figures 25 and 26, the velocity amplitudes, v_a, are plotted as ordinates on the planar, two-dimensional mesh,

$$v_a = \sqrt{v_{1a}^2 + v_{2a}^2} \quad , \tag{1}$$

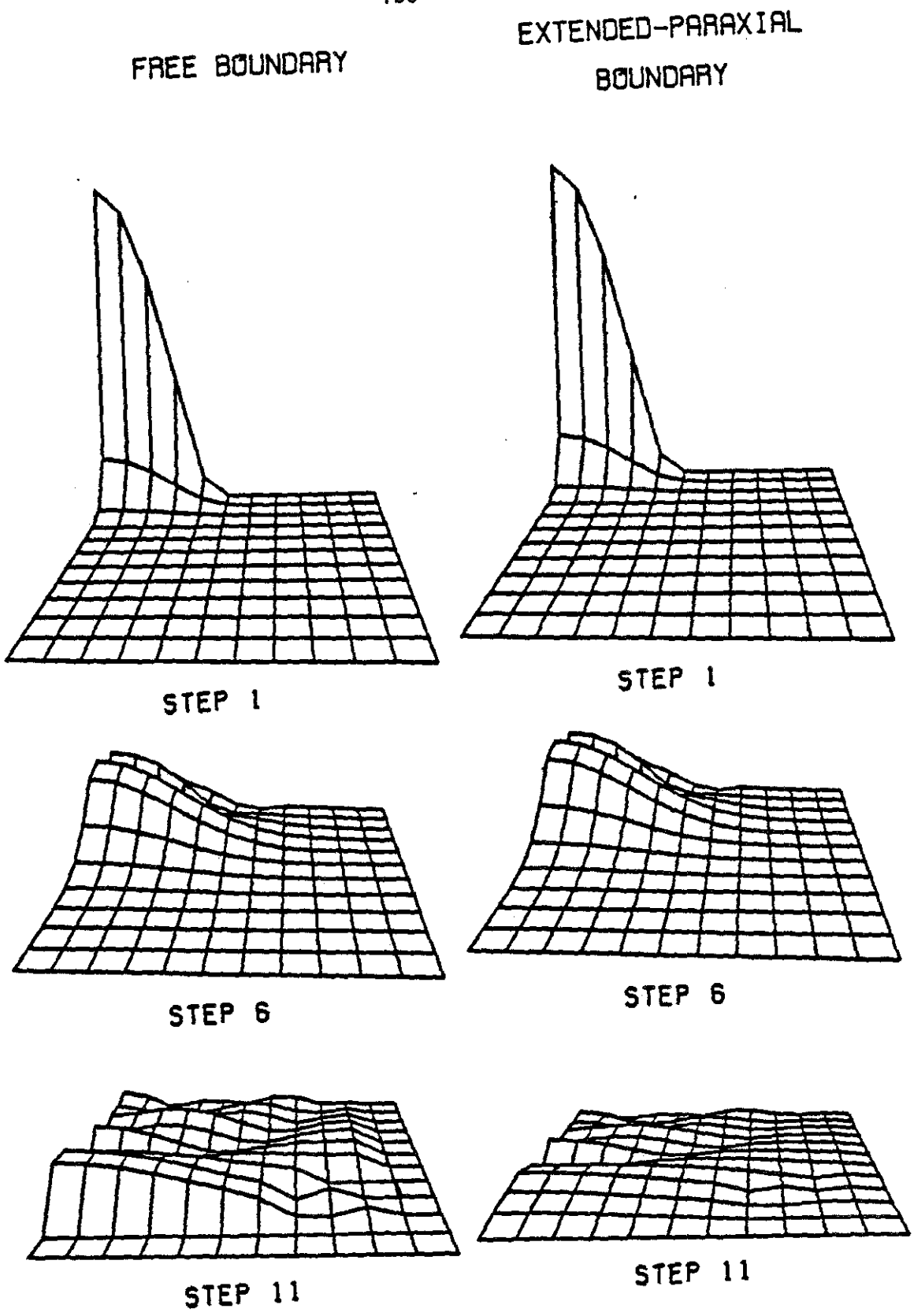

Figure 25. Absolute amplitudes of the velocities plotted as ordinates on a planar, two-dimensional mesh.

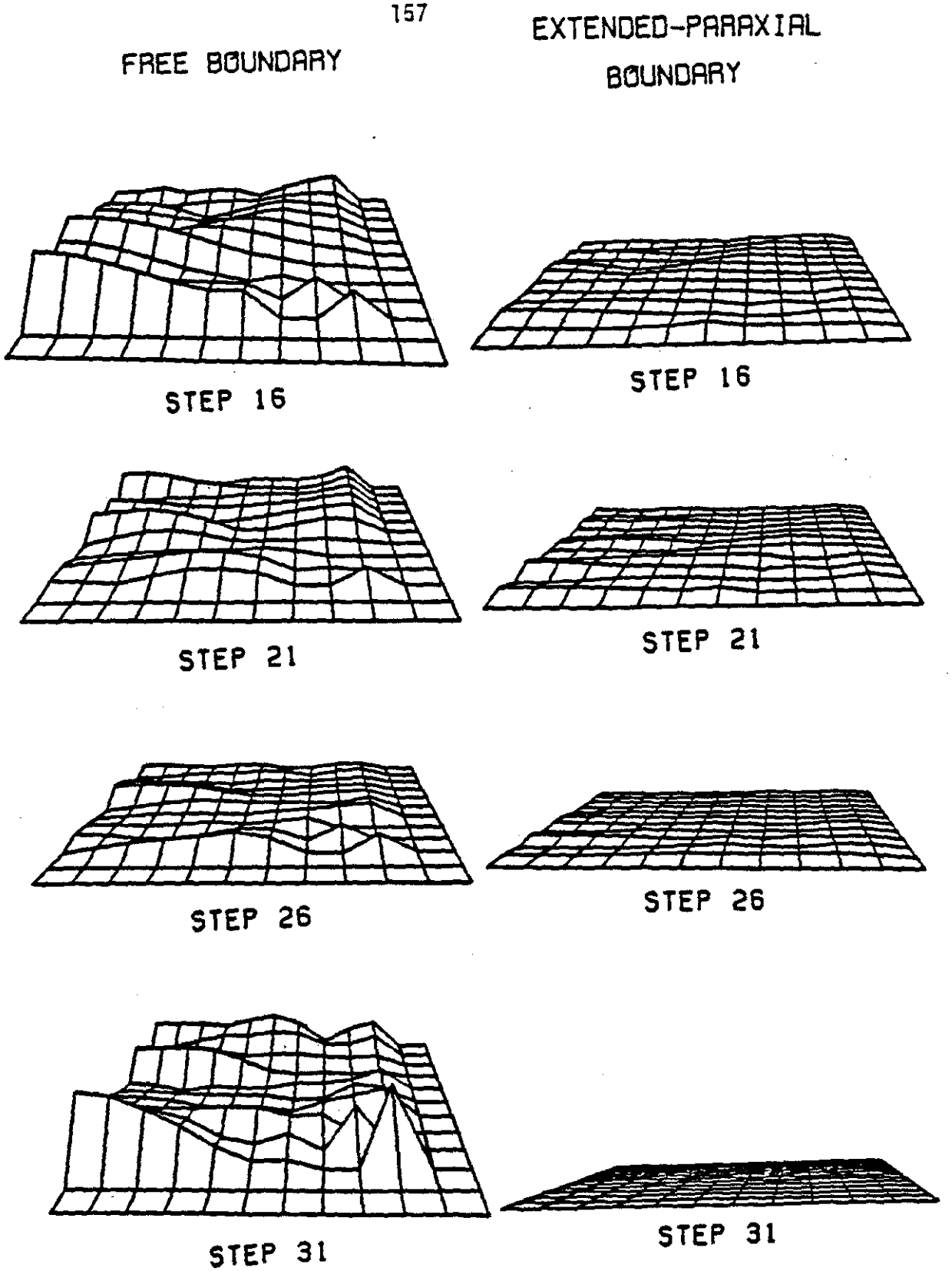

Figure 26. Absolute amplitudes of the velocities plotted as ordinates on a planar, two-dimensional mesh.

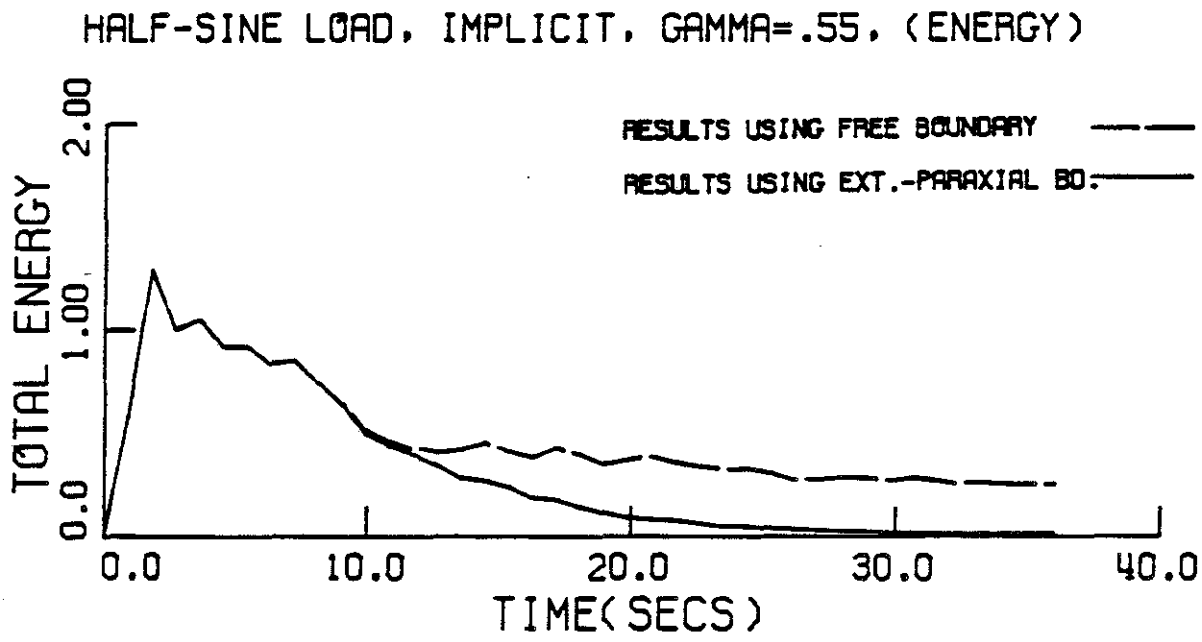

Figure 27. Total energy in the interior region as a function of time. (Half-sine, pulse loading, damped case.)

where v_{1a} and v_{2a} are the two velocity components of node a. For the free boundary, there is added an outer ring of undeformed elements, in order to provide a clearer picture of the velocity amplitudes.

The three-dimensional plots, in Figures 25 and 26, illuminate the qualitative behavior of the free and the extended-paraxial boundaries. The waves, generated by the loading, effectively propagate out of the system with the silent boundary, but energy is trapped within the mesh when it has only a free boundary. Figure 27 shows how much of the total energy remains in the interior region.

VII. DISCUSSION OF NONLINEAR WAVES

The analyses of Chapter 2, and the above results, are strictly valid only for waves in linear, elastic media. The interior of the mesh may be governed by nonlinear equations, but the region adjacent to the silent boundary must be linear. This assumption, that the governing equations are linear on the outer fringes of the computational mesh, is appropriate for many different problems. For example, in the soil-structure interaction analyses that were described in Chapter 1, the soil's strongly nonlinear behavior is mainly confined to an area near the structure. The wave motion which emanates from the interaction zone, and propagates to the outer boundaries, often can be represented adequately by linear models of the soil.

In some problems, however, the nonlinearity of the wave motion at locations "far" from the wave source, cannot be ignored. In these cases, a linear wave may be followed by slower-traveling, nonlinear waves. The silent boundaries, which are designed for only one set of wave speeds, may not effectively transmit the slower-moving waves.

The silent boundaries' ability to absorb waves depends on the parameters, ac_d and bc_s, in equation (45) of Chapter 2. The standard-viscous- and extended-paraxial boundaries set both a and b equal to one. (a and b were not explicitly defined for the paraxial equations, but the paraxial-viscous boundary comparison in Section VII, Chapter 2, shows that these parameters are equal to one.) The wave-reflection theory in Chapter 2, and the numerical examples in this chapter, both indicate that $a = b = 1$ is the foremost choice for linearly elastic waves.

For waves traveling at a slower speed, a or b should be somewhat less than 1. These parameters should be "tuned" to the wave speed.

Our experience with the unified- ("optimized-") viscous boundary indicates, however, that the viscous boundaries are relatively insensitive to the parameters, a and b. For the unified boundary, a ranges from .959 to 1.011, and b lies between .740 and .773. The numerical results, using either the standard- or the unified-viscous boundary, are nearly identical. (See Section IV.) This finding implies that the standard-viscous boundary might absorb waves traveling at different speeds.

In order to test this hypothesis more thoroughly, we repeated some of the above, horizontal-loading examples, with 'a' varying from .6 to 1.3. They were then compared to standard-viscous boundary results.

We found that the use of the modified-viscous boundaries, instead of the standard-viscous boundary, produces virtually no differences in the stresses and vertical displacements. In the case of the horizontal displacements, the differences are approximately 5-10% of the errors

created by the use of a free boundary. Thus, letting 'a' range from .6 to 1.3 has a generally minimal effect on the response.

The overall conclusion is that the linear boundaries may be useful for absorbing the slower-moving, nonlinear waves.[3] The parameters, a and b, would be chosen as shown in equation (2),

$$\left.\begin{aligned} \frac{c_{n1}}{c_d} < a < 1 \quad , \\ \\ \frac{c_{n2}}{c_s} < b < 1 \quad , \end{aligned}\right\} \tag{2}$$

where c_{n1} and c_{n2} are the speeds of waves which may be generated, for example, by plastic yielding.

VIII. RAYLEIGH-WAVE EXAMPLE

The previous calculations in this chapter shed light upon the boundary schemes' ability to transmit high-frequency, body-wave pulses. In this section, a Rayleigh wave is used to excite the system. The purpose of this test is twofold. We wish, first, to subject the boundary to a steady-state motion. A certain amount of reflection was observed for the pulse loadings, and this raises the question of whether the errors

---

[3] The efficiency of the extended-paraxial boundary is dependent on ah^e and bh^e, where h^e is the width of the paraxial element. It was pointed out in Chapter 1 that maintaining a uniform mesh size reduces reflections. Conversely, if large elements are placed adjacent to small elements, significant wave reflections will occur. After extensive testing, Day [12] found that when element sizes are kept within 90-110% of each other, minimal reflections will occur. Since the paraxial elements transmit waves in the same manner as elastic elements do, presumably this guideline would also hold for them.

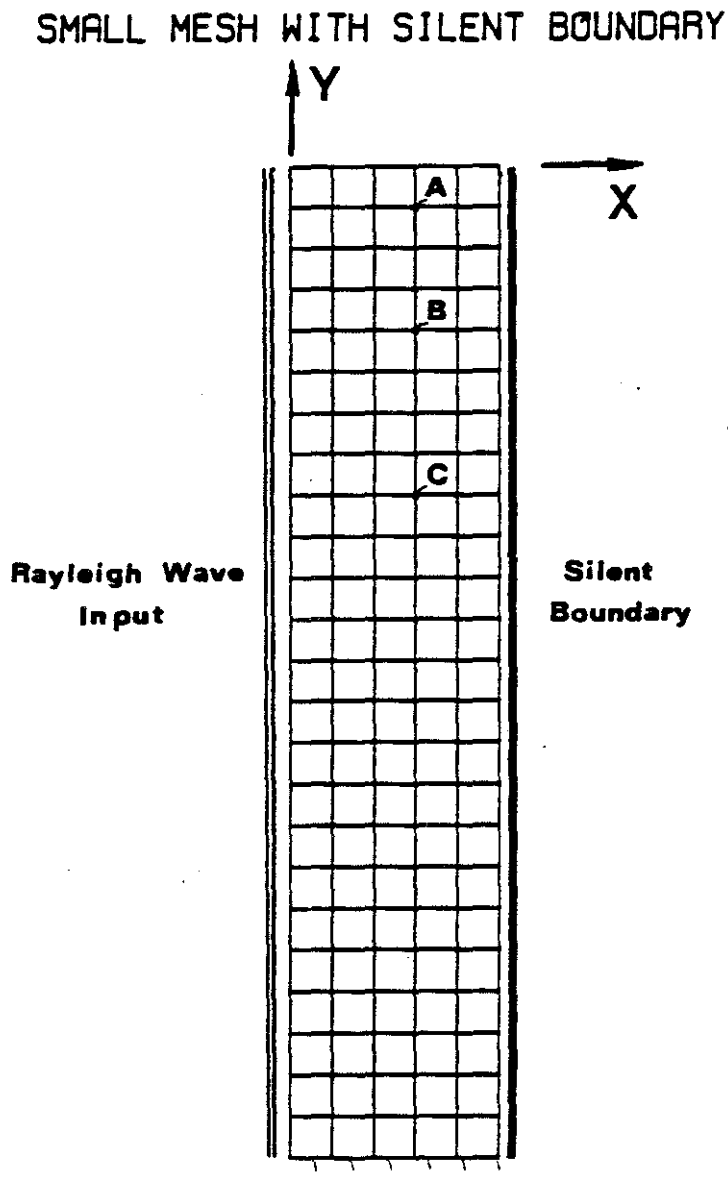

Figure 28. Finite-element mesh with absorbing boundary used for the Rayleigh-wave loading.

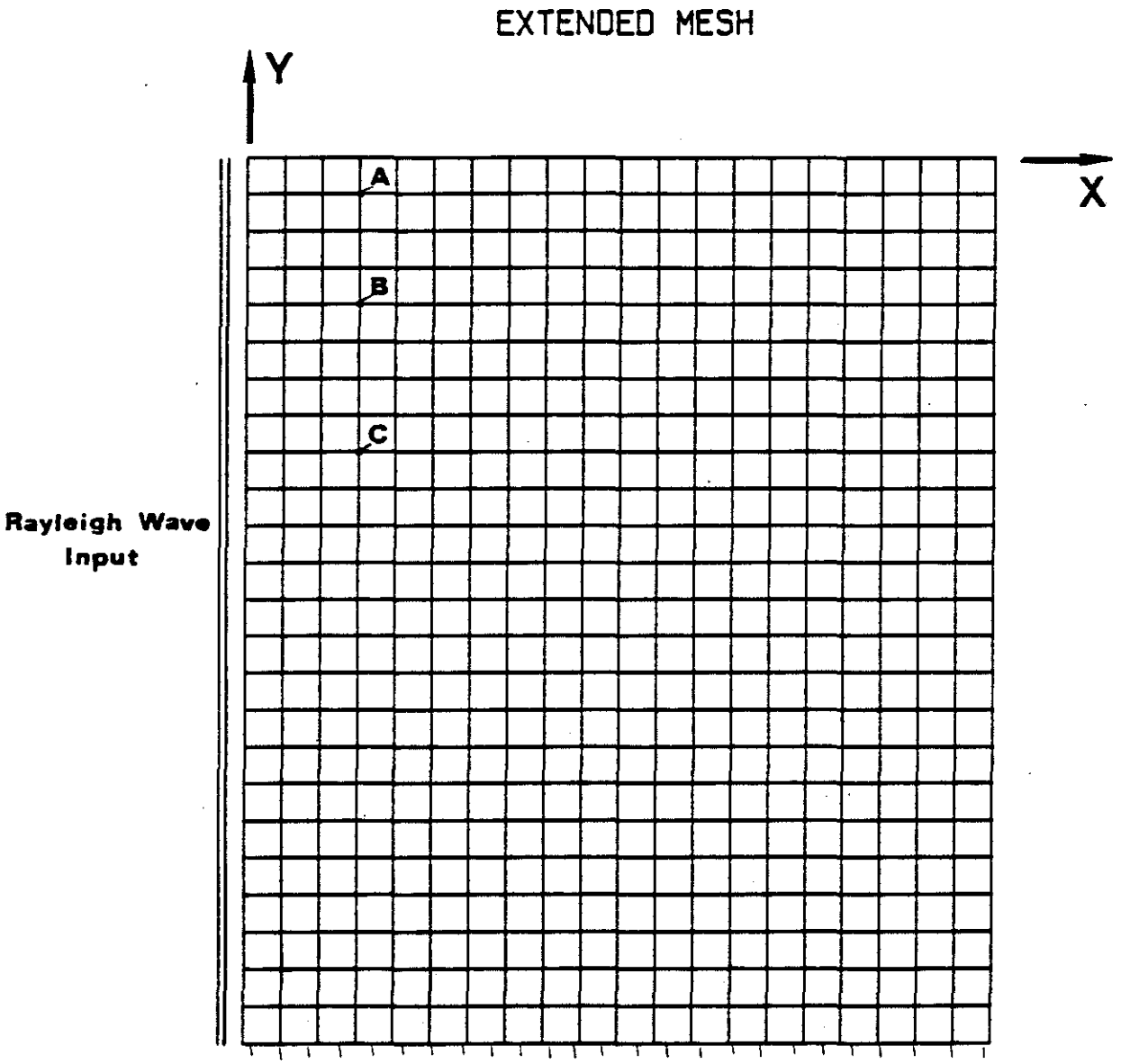

Figure 29. Extended, finite-element mesh with free boundary used for the Rayleigh-wave loading.

accumulate as the loading continues. Secondly, the ability of the silent boundaries to transmit Rayleigh waves needs to be evaluated. The analyses of Section VII, Chapter 2, indicate that the extended-paraxial, and a few other boundaries mentioned there, may be effective in this case. The efficiency of the standard-viscous boundary is uncertain.

It often turns out that, in soil-structure interaction analysis, some of the energy propagating from the interaction zone is in transition from body waves to Rayleigh waves. Several wave motions, including shear and dilatational components, are superimposed, but they gradually assume a Rayleigh-wave form along the surface. In practical instances, a computational mesh will not extend far enough for Rayleigh waves to form completely. Therefore, the measuring of the reflections of this transitory motion is of interest.[4]

Figures 28 and 29 illustrate the test problem, in which plane-strain elasticity is used. The mesh is initially at rest, at time t equal zero. The horizontal and vertical displacements along the left side of the mesh are prescribed, for all subsequent time, according to a known, Rayleigh-wave solution. The mesh is two wavelengths deep, and the bottom nodes are fixed. Due to reflections from the bottom boundary, it has been recommended(65) that the mesh depth extend to three or four wavelengths. In our case, these reflections will propagate to the outer areas of the extended mesh, so that the region adjacent to the input will not be significantly affected. For the small mesh in Figure 28,

---

[4]Similar comments apply to Love waves, where layered media are considered.

energy from the bottom can propagate to the surface, however, if it reflects from the mesh's right side.

The excitation on the left generates transient waves at first, and then the motion settles down and approaches steady state. There exists a period when waves, having not taken on their final, Rayleigh-wave form, will impinge on the various boundaries.

The displacements on the left are prescribed as:

$$\left.\begin{aligned} u &= D[\exp(.8475\,\kappa_R y) - .5773\exp(.3933\,\kappa_R y)]\sin(\kappa_R c_R t) \\ w &= D[-.8475\exp(.8475\,\kappa_R y) + 1.4678\exp(.3933\,\kappa_R y)]\cos(\kappa_R c_R t) \end{aligned}\right\} \quad (3)$$

Equations (3) represent the Rayleigh-wave solution for $\nu = .25$.[84] $\omega = .2781$ radians/second, L_R = the Rayleigh wavelength = 12 units, $\kappa_R = .5236$, c_R = the Rayleigh-wave speed = .5312 units/second, $c_s = .5774$ units/second, c_d = 1 unit/second, and 1 unit = the length of one element. $\gamma = .51$, and $\beta = .255$, so there is a negligible amount of numerical damping present in the system. The equations were solved explicitly, with DT = .9 second. Energy first strikes the right boundary at t = 6 seconds; Rayleigh-wave components follow shortly after.

We represent, in Figures 30 and 31, several comparisons among the various boundaries. Initial transient motion is evident in the first 10 seconds, and then the response becomes more nearly periodic. It has not quite settled to steady-state.

The silent boundaries generally prevent the reflection of energy. The vertical displacements in these figures exhibit a fairly close agreement between the extended-mesh results and those from using a silent

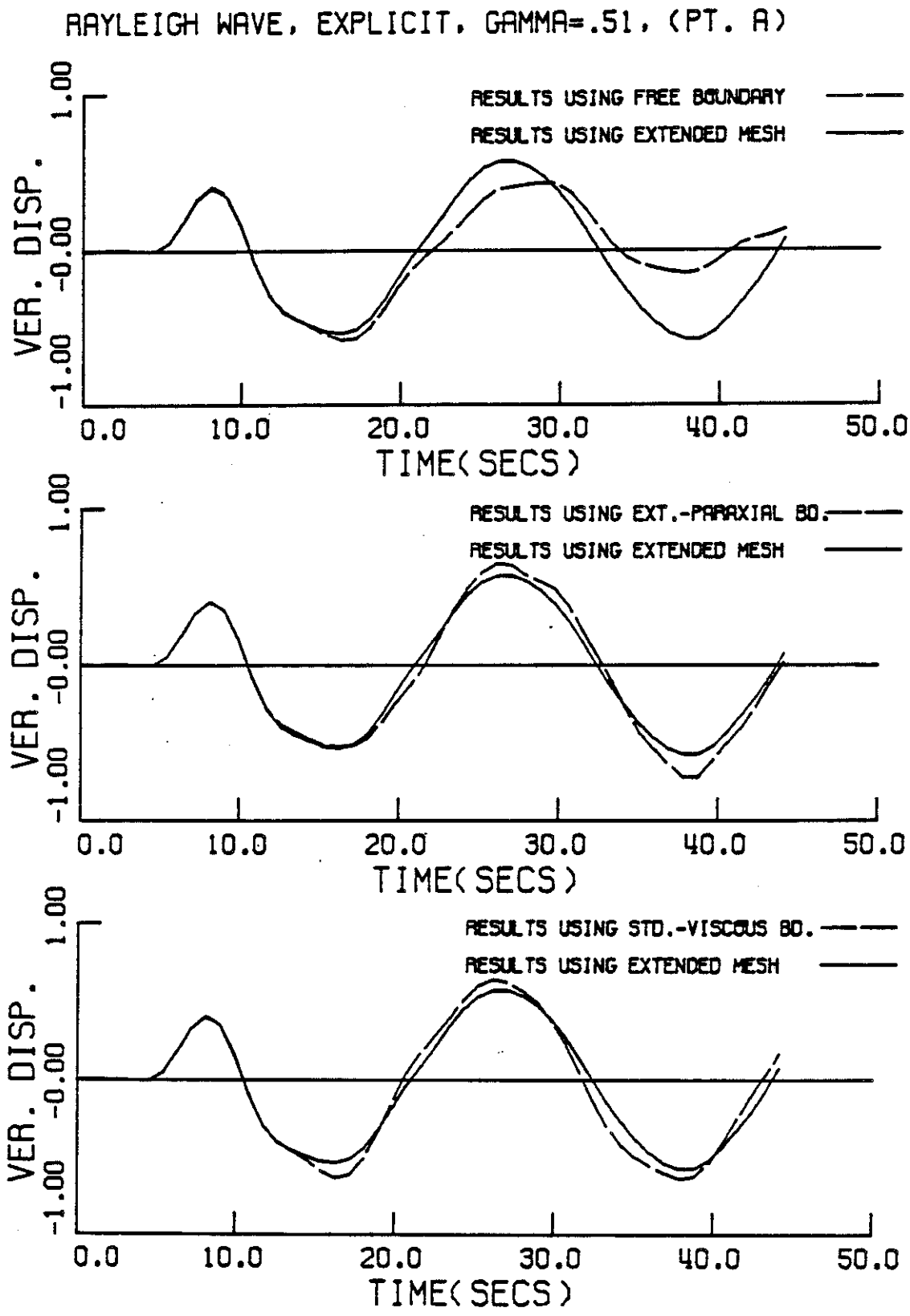

Figure 30. Vertical displacements at point A as a function of time. (Rayleigh-wave loading, slight damping.)

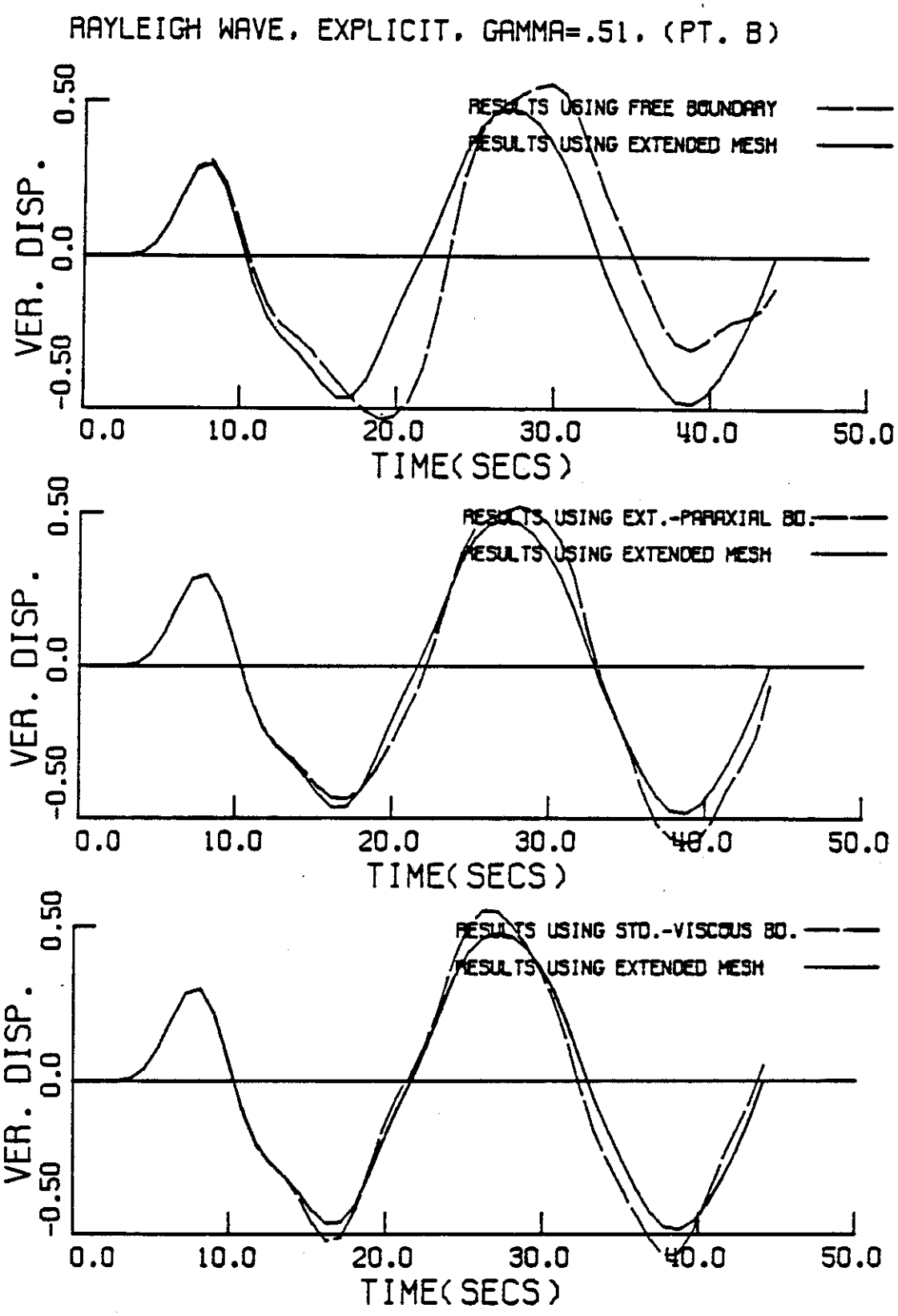

Figure 31. Vertical displacements at point B as a function of time. (Rayleigh-wave loading, slight damping.)

boundary. Other measurements of stresses and displacements, which were taken at points A, B, and C, but are not displayed here, suggest that the same, or better, agreement exists then that found in Figures 30 and 31. The distortions caused by a free boundary are most visible at point A, near the surface.

Figures 30 and 31 illustrate most of the poorest agreement between the extended-paraxial boundary and the extended mesh. The largest discrepancies caused by the standard-viscous boundary are shown in Figure 32, where the phase of the response appears to have been shifted.

Since virtually no numerical damping is utilized in this problem, we might expect numerical noise to be present in the stresses. (This was observed in Section 4.) In this case, the only component exhibiting significant noise is σ_{22}, which is pictured in Figure 33. The results of the extended-paraxial boundary contain spurious noise superimposed on the general wave form, while the viscous boundary alters the period of the motions. Again, one can eliminate the noise through slight numerical damping.

Figure 34 charts the total energy in the system. It is apparent that, when using the silent boundaries, the energy within the system remains at a fairly constant level. The boundary mechanisms eradicate energy at nearly the same rate as energy is generated on the mesh's left side. The small errors associated with the paraxial boundary are attributed to the numerical noise mentioned above.

The Rayleigh mode shapes can also be used to estimate the accuracy of the transmitting boundaries. In these graphs, presented in Figures 35 and 36, the solid-line curves represent the Rayleigh mode shape that

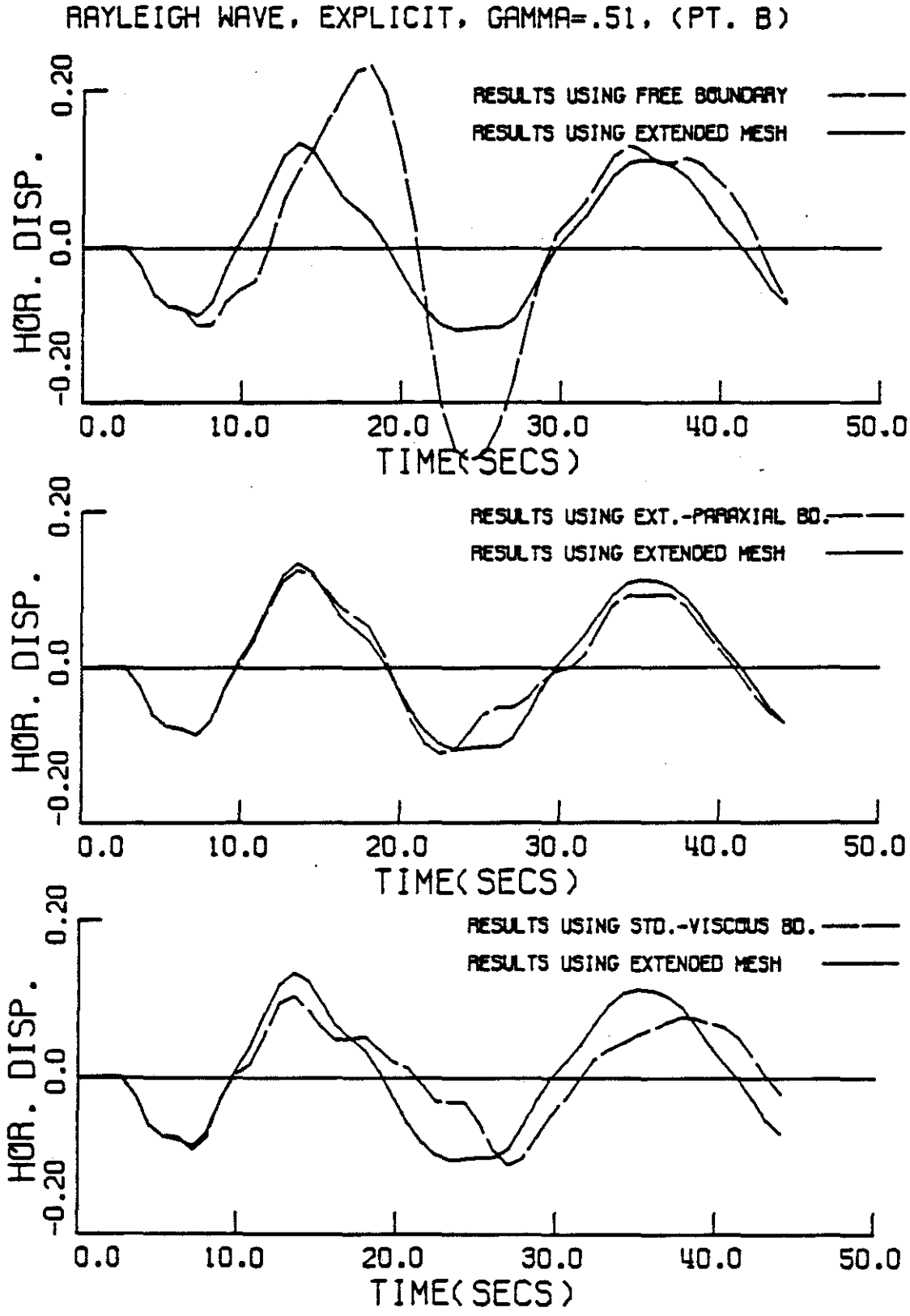

Figure 32. Horizontal displacements at point B as a function of time. (Rayleigh-wave loading, slight damping.)

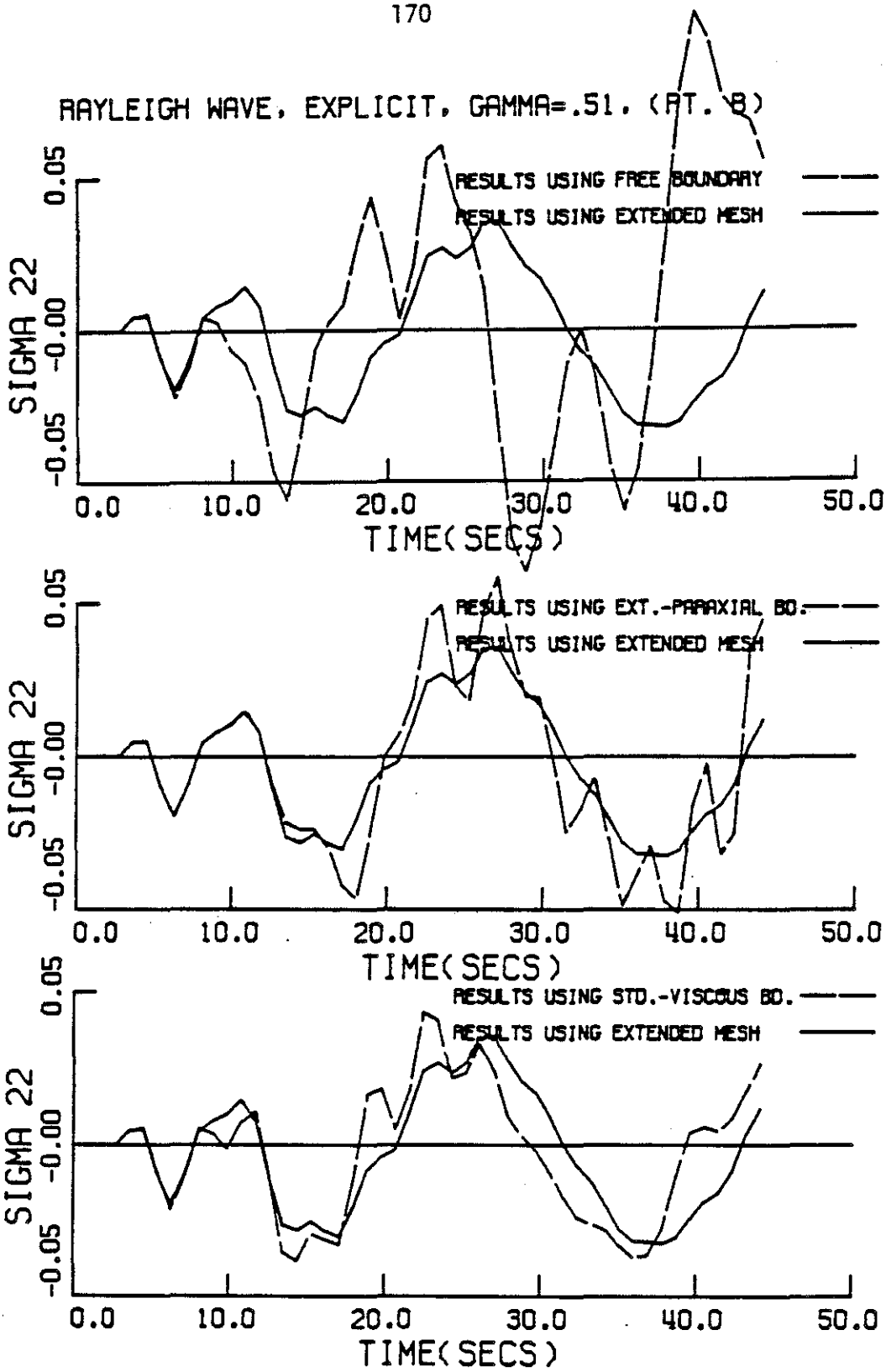

Figure 33. Stresses, σ_{22}, at point B as a function of time. (Rayleigh-wave loading, slight damping.)

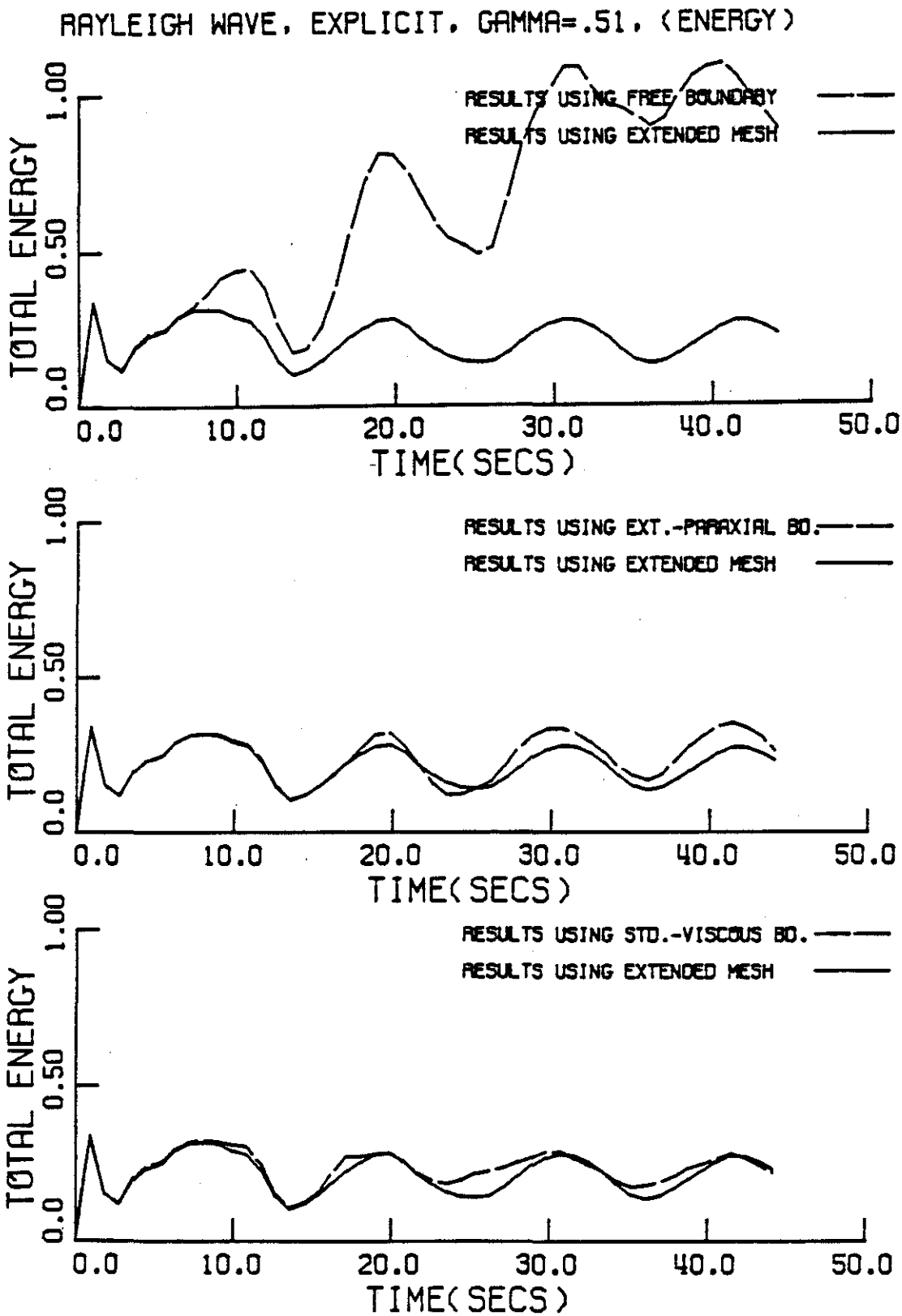

Figure 34. Total energy in the first five columns of elements adjacent to the Rayleigh-wave input.

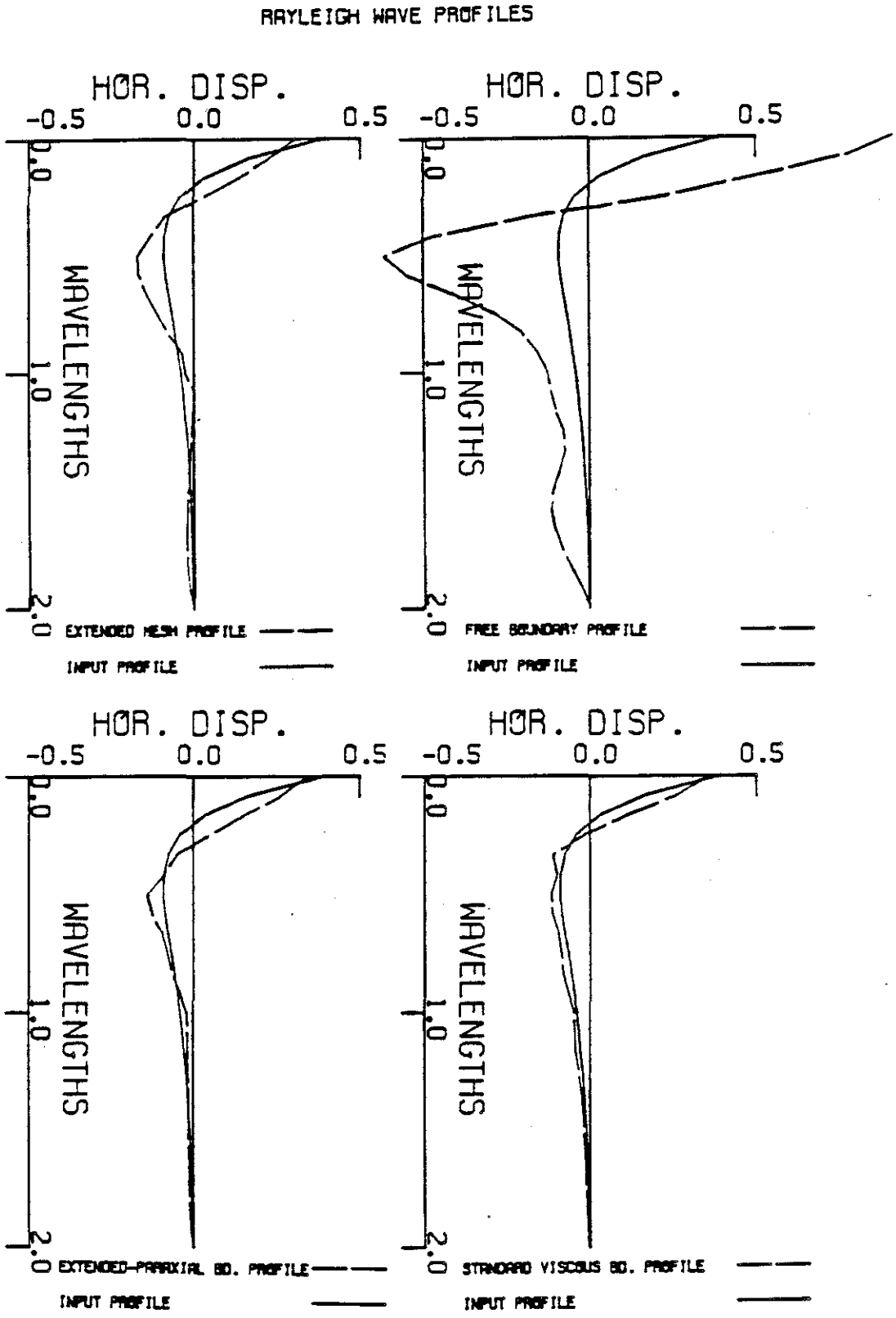

Figure 35. Horizontal displacements as a function of depth. (x = 3 units, t = 27 seconds, Rayleigh-wave input.)

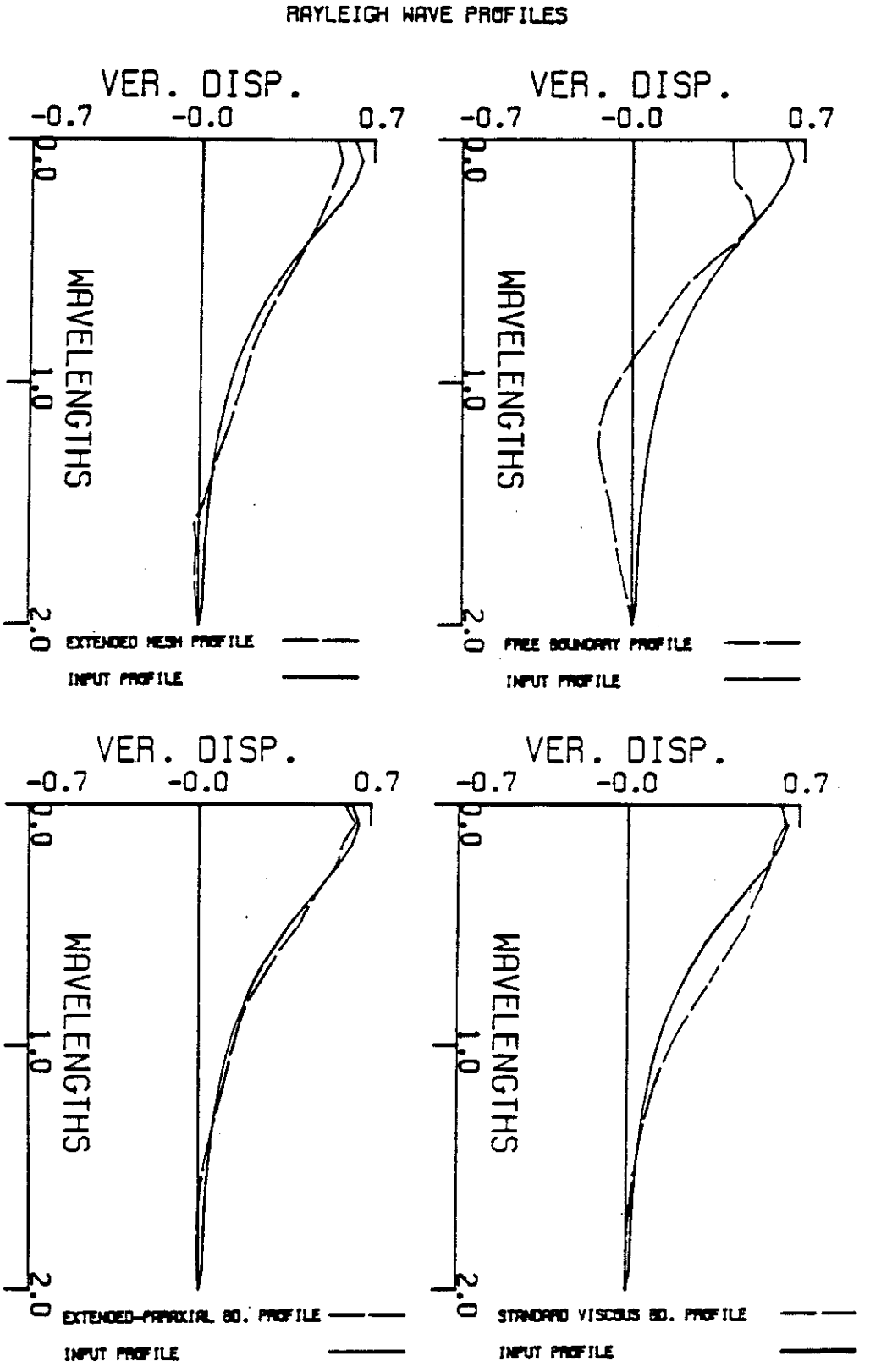

Figure 36. Vertical displacements as a function of depth. (x = 3 units, t = 27 seconds, Rayleigh-wave input.)

excites the system. The dashed-line curves are the resulting displacements at x = 3 when t = 27 seconds. (The displacements at x = 3, t = 36 seconds yielded similar results.) These profiles were calculated with the various conditions at the right side of the mesh: a) extended mesh, b) free boundary, c) extended-paraxial boundary, and d) standard-viscous boundary.

In the ideal case, the profile of the displacements at x = 3 will duplicate the input motion at x = 0. However, due to the presence of transient waves and discretization errors, the displacement profiles differ somewhat. As can be perceived in Figures 35 and 36, the extended mesh and the silent boundaries each generate displacement configurations that are similar to the input.

Overall, the boundary methods do not induce large distortions in the response, such as those that are observed in the free boundary case. The silent-boundary errors are of the same magnitude as are those introduced by the discretization and the transient motion. The two methods, extended-paraxial and standard-viscous, are again comparable in accuracy. If we consider all of the data accumulated in this problem, including deformed mesh plots not illustrated here, the paraxial results are slightly closer to those of the extended mesh.

As we mentioned in Chapter 1, several authors have pointed out that the viscous boundary may be ineffective in the case of Rayleigh waves. We determined that, at least in this one example, the viscous boundary appears to function in about the same manner as it does for body waves.

CHAPTER 5

In this thesis, the general topic of silent boundaries, as they are applied to the soil-structure interaction problem, was explored. First, we surveyed a wide range of ideas that had been suggested in the past. Most of these proposals were discussed only briefly, mainly because they are not applicable to the class of problems we wish to solve, or because they appear to be relatively cumbersome, or costly, to implement. Many of these transmitting boundary schemes, though not considered in detail, may be useful in other applications. We restricted this study to the more easily implemented, silent boundaries which can be directly employed in transient, time-domain analysis, and would be serviceable for many problems involving nonlinear materials. Two of the boundary methods, paraxial and viscous, which tender these qualities, were analyzed in detail in Chapters 2 and 3.

The major innovations in this thesis center upon the adaptation, development, and testing of the paraxial-boundary approach as it applies to finite element calculations. First, the paraxial equations were derived for the purpose of transmitting plane, harmonic waves. These considerations, in turn, led to questions of stability and to a modification of the equations' original form.

The revised paraxial equations were then compared to two viscous-boundary proposals. It was shown that the standard-viscous boundary apparently embodies the first-order terms of the paraxial equations. A wave-reflection analysis illustrates the distinct superiority of the paraxial approach, and indicates its potential as an energy absorber. This analysis also implies that the use of the "optimized"

parameters as suggested in [57] does not improve the efficiency of the boundary. From this theoretical standpoint, the modified-paraxial boundary reflects waves of the smallest amplitudes, but the standard- and unified-viscous boundaries are also fairly effective.

In Chapter 3, it was pointed out that a straightforward, finite-element implementation of the paraxial equations does not lead to a practicable transmitting boundary. Certain alterations in the numerical procedures are needed to upgrade the boundary's accuracy.

The test examples presented in Chapter 4 furnish most of the data for an evaluation and comparison of the various boundaries. In the problems we studied, all of the silent boundaries produced from adequate to exceptional results.

There are a number of features which should be emphasized. First, the viscous boundaries cause a permanent, "residual" displacement at almost all points in the mesh. This motion is, perhaps, 10% of that which results from the use of a free boundary. The extended-paraxial boundary largely eliminates this residual. On the other hand, the viscous boundaries do effectively absorb the correct amount of energy from the system. In most cases, the energy curves, which result from extended-mesh calculations, coincide exactly with those resulting from a viscous boundary. The extended-paraxial boundary is also competent in removing energy from the system, with the exception of eradicating noise from the solution.

A second feature of all the silent boundaries is their relative inability to remove high-frequency, node-to-node oscillations. The extended-paraxial boundary is worse in this capacity because it aggravates

this noise and sends it to the interior. One solution to this problem is to apply slight numerical damping to the algorithm. In the problems studied, it was found that the setting of γ = .55 eliminates most of the numerical oscillations, without distorting the solution of lower frequencies, and allows the silent boundaries to operate more effectively. Our experience indicates that the letting of γ = .51 does not induce enough damping into the system. (γ = .50 is the undamped case.)

A third conclusion is that the standard- and unified-viscous boundaries perform almost identically in all ways. Therefore, it would seem to be unnecessary to modify the parameters, a and b, in order to improve the boundary's behavior (the two boundaries differ only in the selected values of a and b). In fact, in one example we tested, the doubling of the parameter 'a' causes little change in the absorption character of the viscous boundary. This insensitivity of the viscous boundary suggests that it may be suitable for special cases of nonlinear waves. This was discussed in Section VII of Chapter 4.

Fourthly, the performance of the silent boundaries varies with the parameters being measured. By and large, the extended-paraxial boundary proffers a slight advantage in accuracy over the viscous schemes, although it does not achieve the superiority indicated by the wave-reflection theory of Chapter 2. The boundary adopted herein appears to be the best finite-element implementation of the paraxial idea, and we give some reasons for this, but it is possible that a different implementation may yield more accuracy.

Finally, the implementation of two silent boundaries, as considered, is inexpensive. Both the viscous and paraxial damping matrices

can be easily calculated by hand, in terms of the element dimensions, h^x and h^z. Hence, the generation of these expressions entails virtually no costs on the computer. A slight expense is incurred in the formation and assembly of the paraxial stiffness, and in the solution of the paraxial degrees of freedom. The cost of this latter computation, always being done explicitly, is not significant. Overall, the extended-paraxial scheme is slightly more expensive to use than is the viscous boundary.

In summary, the extended-paraxial boundary, as developed herein, possesses the following characteristics:

- It is founded upon a mathematical theory which indicates the method's capability to transmit wave energy.
- It is easily implemented and exacts a minimal computational expense.
- It sometimes projects numerical noise into the system, but this tendency is controlled by a slight amount of numerical damping.
- It enjoys some advantage in accuracy over other proposed silent boundaries (the standard-viscous and unified-viscous boundaries).
- It offers a broad scope in that it can be applied to Rayleigh waves and, presumably, to anisotropic materials.

- It can be applied to many problems in which nonlinear, material effects are important.

- It does not adversely affect the numerical stability properties of one family of algorithms that we tested.

In the course of our investigation, we also ascertained that the viscous boundary performed better than we had expected, and would be a suitable transmitting boundary in many applications. It is widely believed that this boundary acquits itself poorly when confronted by Rayleigh waves, but in the one example that we studied, the boundary seemed to absorb the waves to an acceptable degree, although it was somewhat less accurate than the extended-paraxial approach.

We believe that, when taking into account all of the factors mentioned above, such as cost, accuracy, ease of implementation, etc., the proposed extended-paraxial boundary technique is at least competitive with other transmitting boundary methods now available. More practical tests are needed to confirm this conclusion, and the next logical step would be to apply this boundary to the solution of soil-structure interaction problems.

APPENDIX A

DERIVATION OF A ONE-DIMENSIONAL, PARAXIAL ELEMENT

The basic finite element procedure, for a one-dimensional wave problem with a paraxial boundary, is sketched here. Two- and three-dimensional analyses ensue in an analogous fashion, except that all of the integrals are evaluated over an area, or a volume, instead of a line.

If we commence with the strong form of the initial-, and boundary-value problem,

$$u_{tt} - c^2 u_{xx} = f(x,t) \quad , \qquad x \in \Omega_i \quad , \tag{A1}$$

$$u_{tt} + c u_{tx} = 0 \quad , \qquad x \in \Omega_{by} \quad , \tag{A2}$$

where

u = the one-dimensional displacement,

Ω_i = the domain of the interior,

Ω_{by} = the domain of the boundary,

$$\Omega = \Omega_i + \Omega_{by} \quad , \tag{A3}$$

u = $q(t)$ on $\partial\Omega^u$ = the boundary where displacements are specified,

u_x = $p(t)$ on $\partial\Omega^t$ = the boundary where tractions are specified,

$$\begin{aligned} u(x,0) &= h(x) \qquad \text{for all } x \in \Omega \quad , \\ u_t(x,0) &= g(x) \qquad \text{for all } x \in \Omega \quad . \end{aligned} \tag{A4}$$

In order to derive the weak form of the problem, the following spaces are required:

$$\left.\begin{aligned} H_0^1(\Omega) &= \{v \mid v\colon \Omega \to \mathbf{R} \quad , \quad v(x) = 0 \ \forall\, x \in \partial\Omega^u\} \quad , \\ H_g^1(\Omega) &= \{u \mid u\colon \Omega \to \mathbf{R} \quad , \quad u(x) = g \ \forall\, x \in \partial\Omega^u\} \quad , \end{aligned}\right\} \tag{A5}$$

where $\mathbf{R}$ represents the set of continuous and uniformly bounded functions. The functions belonging in the space H^1 possess first derivatives which are square integrable. In other words, if $u \in H^1$, then

$$\int_\Omega u_x^2 dx < \infty \quad . \tag{A6}$$

If we multiply equations (A1) and (A2) by v, where $v \in H_0^1$, let $u \in H_g^1$, and integrate over Ω,

$$\int_{\Omega_i} u_{tt} v dx - c^2 \int_{\Omega_i} u_{xx} v dx + \int_{\Omega_{by}} u_{tt} v dx + c \int_{\Omega_{by}} u_{tx} v dx = \int_{\Omega_i} f v dx \quad . \tag{A7}$$

After the second term of equation (A6) is integrated by parts, the weak form can be distinguished. Given that q, p, h, and g are all sufficiently regular, one finds $u \in H_g^1$ such that for all $v \in H_0^1$,

$$\int_\Omega u_{tt} v dx + c^2 \int_{\Omega_i} u_x v_x dx + c \int_{\Omega_{by}} u_{tx} v dx = \int_{\Omega_i} f v dx + [c^2 p v]_{\partial\Omega^t} \quad . \tag{A8}$$

The matrix version of equation (A8) is formed by approximating u and v with u^h and v^h, respectively, where

$$u^h = \sum_{b=1}^{NN} N_b u_b{}^h \quad , \tag{A9}$$

$$v^h = \sum_{a=1}^{NN} N_a v_a{}^h \quad ; \tag{A10}$$

a,b = the node numbers; N_a,N_b = the shape functions associated with node a or node b; $u_b{}^h$,$v_a{}^h$ = the nodal values of u^h and v^h; and NN = the number of nodes. Next, one substitutes equations (A9) and (A10) into equation (A8):

$$\sum_{a=1}^{NEN}\left[\sum_{b=1}^{NEN}\int_{\Omega} N_a N_b dx\, u^h_{b,tt} + c\int_{\Omega_{by}} N_a N_{b,x} dx\, u^h_{b,t} + c^2\int_{\Omega_i} N_{a,x} N_{b,x} dx\, u_b{}^h\right.$$

$$\left. = \int_{\Omega_i} f N_a dx + [c^2 p N_a]_{\partial\Omega t}\right] v_a{}^h \quad , \tag{A11}$$

where NEN = the number of element nodes. Equation (A11) is rewritten:

$$m_{ab} u^h_{b,tt} + c_{ab} u^h_{b,t} + k_{ab} u_b{}^h = f_a \tag{A12}$$

The sum of the element contributions is described as:

$$\underset{\sim}{M}\, \underset{\sim}{u}^h_{tt} + \underset{\sim}{C}\, \underset{\sim}{u}^h_t + \underset{\sim}{K}\, \underset{\sim}{u}^h = \underset{\sim}{F} \quad ,$$

$$\underset{\sim}{M} = \sum^{NE} \underset{\sim}{m} \quad , \qquad \underset{\sim}{C} = \sum^{NE} \underset{\sim}{c} \quad , \qquad \underset{\sim}{K} = \sum^{NE} \underset{\sim}{k} \quad , \tag{A13}$$

in which NE = the total number of elements. $\underset{\sim}{M}$ and $\underset{\sim}{K}$ are evaluated in the standard fashion; the stiffness term is integrated analytically for this one-dimensional case. The matrices $\underset{\sim}{M}$ and $\underset{\sim}{C}$ can be determined for a paraxial element of length h. After transforming the integrals [in equation (A11)] into ξ-space, which is defined in Figure 2 of Chapter 3, we arrive at:

$$\underset{\sim}{m} = \frac{h}{2}\begin{bmatrix} 1 & 0 \\ 0 & 1 \end{bmatrix} , \tag{A14}$$

$$\underset{\sim}{c} = \frac{c}{2}\begin{bmatrix} -(1-\xi_\ell) & (1-\xi_\ell) \\ -(1+\xi_\ell) & (1+\xi_\ell) \end{bmatrix} , \tag{A15}$$

where ξ_ℓ is the integration point for the second term in equation (A11).

APPENDIX B

SUMMARY OF THE IMPLICIT-EXPLICIT ALGORITHM

Below is an outline of the Implicit-Explicit transient algorithm, as developed by Hughes and Liu.[77]

$$\underset{\sim}{M}\,\underset{\sim}{a}_{n+1} + \underset{\sim}{C}^{I}\,\underset{\sim}{v}_{n+1} + \underset{\sim}{C}^{E}\,\underset{\sim}{v}_{n+1} + \underset{\sim}{K}^{I}\,\underset{\sim}{d}_{n+1} + \underset{\sim}{K}^{E}\,\underset{\sim}{d}_{n+1} = \underset{\sim}{F}_{n+1} \tag{B1}$$

$$\tilde{\underset{\sim}{d}}_{n+1} = \underset{\sim}{d}_n + \Delta t \underset{\sim}{v}_n + \frac{\Delta t^2}{2}(1-2\beta)\underset{\sim}{a}_n \tag{B2}$$

$$\tilde{\underset{\sim}{v}}_{n+1} = \underset{\sim}{v}_n + t(1-\gamma)\underset{\sim}{a}_n \tag{B3}$$

$$\underset{\sim}{d}_{n+1} = \tilde{\underset{\sim}{d}}_{n+1} + \Delta t^2 \beta \underset{\sim}{a}_{n+1} \tag{B4}$$

$$\underset{\sim}{v}_{n+1} = \tilde{\underset{\sim}{v}}_{n+1} + \Delta t \gamma \underset{\sim}{a}_{n+1} \tag{B5}$$

$$\underset{\sim}{d}_0 = \underset{\sim}{D} \tag{B6}$$

$$\underset{\sim}{v}_0 = \underset{\sim}{V} \tag{B7}$$

$$\underset{\sim}{a}_0 = \underset{\sim}{M}^{-1}(\underset{\sim}{F}_0 - \underset{\sim}{C}\,\underset{\sim}{v}_0 - \underset{\sim}{K}\,\underset{\sim}{d}_0) \tag{B8}$$

$$\underset{\sim}{M} = \underset{\sim}{M}^{I} + \underset{\sim}{M}^{E} \tag{B9}$$

$$\underset{\sim}{C} = \underset{\sim}{C}^{I} + \underset{\sim}{C}^{E} \tag{B10}$$

$$\underset{\sim}{K} = \underset{\sim}{K}^{I} + \underset{\sim}{K}^{E} \tag{B11}$$

$$\underset{\sim}{F} = \underset{\sim}{F}^{I} + \underset{\sim}{F}^{E} \tag{B12}$$

Their notation is as follows: "Δt is the time step; $\underset{\sim}{d}_n$, $\underset{\sim}{v}_n$, and $\underset{\sim}{a}_n$ are the approximations to $\underset{\sim}{d}(t_n)$, $\dot{\underset{\sim}{d}}(t_n)$, and $\ddot{\underset{\sim}{d}}(t_n)$, respectively; $\underset{\sim}{F}_n = \underset{\sim}{F}(t_n)$; γ and β are free parameters which govern the accuracy and stability of the algorithm; and $\underset{\sim}{M}^I$, $\underset{\sim}{C}^I$, $\underset{\sim}{K}^I$, and $\underset{\sim}{F}^I$ (respectively, $\underset{\sim}{M}^E$, $\underset{\sim}{C}^E$, $\underset{\sim}{K}^E$ and $\underset{\sim}{F}^E$) are the assembled arrays for the implicit (respectively, explicit) groups. $\underset{\sim}{M}^E$ is assumed to be diagonal and $\underset{\sim}{M}$ is assumed positive definite."

REFERENCES

SOIL-STRUCTURE INTERACTION ANALYSIS - CONTINUUM APPROACH

1. Bycroft, G. N., "Forced Vibrations of a Rigid Circular Plate on a Semi-Infinite Elastic Space or on an Elastic Stratum," Philosophical Transactions of the Royal Society (London), Vol. 248, pp. 327-368, 1956.

2. Jennings, P. C., and Bielak, J., "Dynamics of Building-Soil Interaction," Bulletin of the Seismological Society of America, Vol. 63, No. 1, pp. 9-48, February, 1973.

3. Luco, J. E., and Westmann, R. A., "Dynamic Response of Circular Footings," Journal of the Engineering Mechanics Division, ASCE, Vol. 97, No. EM5, pp. 1381-1395, October, 1971.

4. Novak, M., "Effect of Soil on Structural Response to Wind and Earthquake," Earthquake Engineering and Structural Dynamics, Vol. 3, pp. 79-96, 1974.

5. Parmelee, R. A., "Building-Foundation Interaction Effects," Journal of the Engineering Mechanics Division, ASCE, Vol. 93, No. EM2, pp. 131-152, 1967.

6. Tajimi, H., "Dynamic Analysis of a Structure Embedded in an Elastic Stratum," Proceedings of the Fourth World Conference on Earthquake Engineering, Santiago, Chile, 1964.

7. Veletsos, A. S., and Wei, Y. T., "Lateral and Rocking Vibration of Footings," Journal of the Soil Mechanics and Foundation Division, ASCE, Vol. 97, pp. 1227-1248.

8. Wong, H. L., Dynamic Soil-Structure Interaction, Ph.D. Thesis, California Institute of Technology, 1975.

SOIL-STRUCTURE INTERACTION ANALYSIS - FINITE ELEMENT APPROACH

9. Anderson, J. C., "Seismic Response Effects on Embedded Structures," Bulletin of the Seismological Society of America, Vol. 62, No. 1, pp. 177-194, February, 1972.

10. Chen, W.W.H., and Chatterjee, M., "Response of Foundation Embedded in Layered Media," Seventh Conference on Electronic Computation, St. Louis, August 6-8, 1979.

11. Dasgupta, S. P., and Kameswara Rao, N.S.V., "Dynamic Response of Strip Footing on an Elastic Halfspace," International Journal for Numerical Methods in Engineering, Vol. 14, No. 11, pp. 1597-1612, 1979.

12. Day, S. M., Finite Element Analysis of Seismic Scattering Problems, Ph.D. Thesis, University of California, San Diego, 1977.

13. Gomez-Masso, A., Lysmer, J., Chen, J. C., and Seed, H. B., "Soil-Structure Interaction in Different Seismic Environments," Earthquake Engineering Research Center, University of California, Berkeley, Report No. UCB/EERC-79/18, August, 1979.

14. Hadjian, A. H., Luco, J., and Tsai, N. C., "Soil-Structure Interaction: Continuum or Finite Element," Nuclear Engineering and Design, Vol. 31, No. 2, pp. 151-167, January, 1975.

15. Haupt, W. A., "Surface-Waves in Nonhomogeneous Half-Space," Dynamical Methods in Soil and Rock Mechanics, Proceedings, Karlsruhe, Germany, September, 5-16, 1977.

16. Idriss, I. M., and Sadigh, K., "Seismic SSI of Nuclear Power Plant Structures," Journal of the Geotechnical Division, Proceedings, ASCE, Vol. 102, No. GT7, July, 1977.

17. Isenberg, J., "Interaction between Soil and Nuclear Reactor Foundations during Earthquakes," proposed for The Research Foundation of the University of Toledo, Contract No. AT(40-1)-3822, June 10, 1970.

18. Isenberg, J., and Adham, S. A., "Interaction of Soil and Power Plants in Earthquakes," Journal of the Power Division, ASCE, Vol. 98, pp. 273-291, October, 1972.

19. Isenberg, J., Vaughan, D. K., and Sandler, I., Nonlinear Soil-Structure Interaction, Report prepared by Weidlinger Associates for the Electric Power Research Institute, December, 1978.

20. Johnson, J. J., and Kennedy, R. P., "Earthquake Response of Nuclear Power Facilities," Journal of the Energy Division, ASCE, Vol. 105, No. EY1, pp. 15-32, January, 1979.

21. Joyner, W. B., "A Method for Calculating Nonlinear Seismic Response in Two Dimensions," Bulletin of the Seismological Society of America, Vol. 65, No. 5, pp. 1337-1357, October, 1975.

22. Joyner, W. B., and Chen, A.T.F., "Calculation of Nonlinear Ground Response in Earthquakes," Bulletin of the Seismological Society of America, Vol. 65, No. 5, pp. 1315-1336, October, 1975.

23. Kausel, E., Roesset, J. M., and Waas, G., "Dynamic Analysis of Footings on Layered Media," Journal of the Engineering Mechanics Division, ASCE, Vol. 101, No. EM5, pp. 679-693, October, 1975.

24. Liang, V. C., Dynamic Response of Structures in Layered Soils, Ph.D. Thesis, MIT, January, 1974.

25. Luco, J. E., Hadjian, A. H., Bos, H. D., "The Dynamic Modeling of the Half-Plane by Finite Elements," Nuclear Engineering and Design, Vol. 31, No. 2, pp. 184-194, January, 1975.

26. Lysmer, J., and Drake, L. A., "A Finite Element Method for Seismology," Methods of Computational Physics, Vol. 11, Chapter 6, Academic Press, 1972.

27. Lysmer, J., Udaka, T., Tsai, C-F., and Seed, H. B., "FLUSH - A Computer Program for Approximate 3-D Analysis of Soil-Structure Interaction Problems," Earthquake Engineering Research Center, University of California, Berkeley, Report No. EERC 75-30, November, 1975.

28. Lysmer, J., "Analytical Procedures in Soil Dynamics," Earthquake Engineering Research Center, University of California, Berkeley, Report No. EERC 78-29, December, 1978.

29. Nestor, G. A., Soil-Structure Interaction Analyses using the Finite Element Method, Prepared for the National Science Foundation, University of California, Los Angeles, June, 1977.

30. Tseng, W. S., and Tsai, N. C., "Soil-Structure Interaction for Transient Loads due to Safety Relief Valve Discharges," Nuclear Engineering and Design, Vol. 45, No. 1, January, 1978, pp. 251-259.

31. Seed, H. B., and Lysmer, J., "Soil-Structure Interaction Analysis by Finite Elements - State-of-Art," Nuclear Engineering and Design, Vol. 46, No. 2, pp. 349-365, 1978.

32. Ukaji, K., Analysis of Soil-Foundation-Structure Interaction During Earthquakes, Ph.D. Thesis, Stanford University, 1975.

33. Urlich, C. M., and Kuhlemeyer, R. L., "Coupled Rocking and Lateral Vibrations of Embedded Footings," Canadian Geotechnical Journal, Vol. 10, No. 2, pp. 145-160, 1973.

34. Valliappan, S., Favaloro, J. J., and White, W., "Dynamic Analysis of Embedded Footings," Journal of the Geotechnical Division, ASCE, Vol. 103, No. GT2, Technical Notes, pp. 129-133, February, 1977.

35. Waas, G. and Lysmer, J., "Vibrations of Footings Embedded in Layered Media," Proceedings of the Waterways Experimental Station, Symposium on the Applications of the Finite Element Method in Geotechnical Engineering, U.S. Army Engineers, Waterways Experimental Station, Vicksburg, Mississippi, 1972.

36. Weaver, W. J., Brandow, G. E., and Hoeg, K., "Three-Dimensional Soil-Structure Response to Earthquakes," Bulletin of the Seismological Society of America, Vol. 63, No. 3, pp. 1041-1056, June, 1973.

SILENT BOUNDARIES

37. Baladi, G. Y., "Ground Shock Calculation Parameter Study; Effect of Various Bottom Boundary Conditions," Technical Report S-71-4, Report 2, U.S. Army Engineer Waterways Experiment Station, CE, Vicksburg, Mississippi, 1972.

38. Castellani, A., "Boundary Conditions to Simulate an Infinite Space," Mechanicca, Vol. 9, No. 3, pp. 199-205, 1974.

39. Clayton, J., and Engquist, B., "Absorbing Boundary Conditions for Acoustic and Elastic Wave Equations," Bulletin of the Seismological Society of America, Vol. 67, No. 6, pp. 1529-1541, December, 1977.

40. Cundall, P. A., Kunar, R. R., Carpenter, P. C., and Marti, J., "Solution of Infinite Dynamic Problems by Finite Modelling in the Time Domain," Proceedings 2nd International Conference on Applied Numerical Modelling, Madrid, Spain, 1978.

41. Dominguez, J., "Dynamic Stiffness of Rectangular Foundations," MIT Report, Publication No. R78-20, Order No. 626, August, 1978.

42. Engquist, B., and Majda, A., "Absorbing Boundary Conditions for the Numerical Simulation of Waves," Mathematics of Computation, Vol. 31, pp. 629-651, July, 1977.

43. Engquist, B., and Majda, A., "Radiation Boundary Condition for Acoustic and Elastic Wave Calculations," Communications on Pure and Applied Mathematics, Vol. 32, No. 3, pp. 313-357, 1979.

44. Haupt, W. A., "Numerical Methods for the Computation of Steady-State Harmonic Wave Fields," Dynamical Methods in Soil and Rock Mechanics, Proceedings, Karlsruhe, Germany, September 5-16, 1977.

45. Isenberg, J., Weidlinger Associates, 3000 Sand Hill Rd., Bldg. 4, Suite 245, Menlo Park, CA, 94025 (personal communication).

46. Kunar, K. K., and Rodriguez-Ovejero, "Model with Non-Reflecting Boundaries for Use in Explicit Soil-Structure Interaction Analyses," Earthquake Engineering and Structural Dynamics, Vol. 8, No. 4, pp. 361-374, July-August, 1980.

47. Lysmer, J., and Kuhlemeyer, R. L., "Finite Dynamic Model for Infinite Media," Journal of the Engineering Mechanics Division, ASCE, pp. 859-877, August, 1969.

48. Lysmer, J., "Lumped Mass Method for Rayleigh Waves," Bulletin of the Seismological Society of America, Vol. 60, No. 1, pp. 89-104, February, 1970.

49. Lysmer, J., and Waas, G., "Shear Waves in Plane Infinite Structures," Journal of the Engineering Mechanics Division, ASCE, pp. 85-105, February, 1972.

50. Matthews, A. T., "Effects of Transmitting Boundaries in Ground Shock Computation," Technical Report S-71-8, U.S. Army Engineer Waterways Experiment Station, Vicksburg, Mississippi, September, 1971.

51. Robinson, A. R., "The Transmitting Boundary-Again," Structural and Geotechnical Mechanics, W. J. Hall, Ed., Prentice-Hall, Inc., 1976.

52. Roesset, J. M., and Ettouney, M., "Transmitting Boundaries: A Comparison," International Journal for Numerical and Analytical Methods in Geomechanics, Vol. 1, No. 2, April-June, 1977.

53. Roesset, J. M., and Scaletti, H., "Boundary Matrices for Semi-Infinite Problems," Third Engineering Mechanics Division Specialty Conference, University of Texas at Austin, September 17-19, 1979.

54. Tseng, M. N., and Robinson, A. R., "A Transmitting Boundary for Finite-Difference Analysis of Wave Propagation in Solids," Ph.D. Thesis, University of Illinois at Urbana-Champaign, November, 1975.

55. Smith, W. D., "A Nonreflecting Plane Boundary for Wave Propagation Problems," Journal of Computational Physics, Vol. 15, pp. 492-503, 1974.

56. Underwood, P. G., and Geers, T. L., "Doubly Asymptotic Boundary-Element Analysis of Dynamic Soil Structure Interaction," DNA Report 4512T, Defense Nuclear Agency (SPSS), Washington, D.C., 20305, March, 1978.

57. White, W., Valliappan, S., and Lee, I. K., "Unified Boundary for Finite Dynamic Models," Journal of the Engineering Mechanics Division, ASCE, pp. 949-964, October, 1977.

58. Zhen-peng, L., Pai-puo, Y., and Yi-fan, Y., "Feedback Effect of Low-Rise Buildings on Vertical Earthquake Ground Motion and Application of Transmitting Boundaries for Transient Wave Analysis," Institute of Engineering Mechanics, Academia Sinica, Harbin, China, October, 1978.

MATERIAL MODELING OF SOIL

59. Prevost, J. H., "Plasticity Theory for Soil Stress-Strain Behavior," Journal of the Engineering Mechanics Division, ASCE, Vol. 104, No. EM4, August, 1978.

60. Seed, H. B., and Idriss, I. M., "Influence of Soil Conditions on Ground Motions during Earthquakes," Journal of the Soil Mechanics and Foundations Division, ASCE, Vol. 95, January, 1969.

61. Seed, H. B., and Idriss, I. M., "Soil Moduli and Damping Factors for Dynamic Response Analysis," Earthquake Engineering Research Center, Report No. EERC 70-10, University of California, Berkeley, December, 1970.

OTHER FINITE-ELEMENT PROBLEMS IN MODELING SOIL-STRUCTURE INTERACTION

62. Luco, J. E., and Hadjian, A. H., "Two-Dimensional Approximations to the Three-Dimensional Soil-Structure Interaction Problem," Nuclear Engineering and Design, Vol. 31, No. 2, pp. 195-203, January, 1975.

63. Schnabel, P. B., Lysmer, J., and Seed, H. B., "SHAKE - A Computer Program for Earthquake Response Analysis of Horizontally Layered Sites," Earthquake Engineering Research Center, Report No. EERC 72-12, University of California, Berkeley, December, 1972.

64. Vaish, A. K., and Chopra, A. K., "Earthquake Finite Element Analysis of Structure-Foundation Systems," Journal of the Engineering Mechanics Division, ASCE, Vol. 100, No. EM6, pp. 1101-1116, 1974.

65. Wojcik, G. Weidlinger Associates, 3000 Sand Hill Rd., Bldg. 4, Suite 245, Menlo Park, CA, 94025 (personal communication).

FINITE ELEMENT TECHNOLOGY

66. Brooks, A., and Hughes, T.J.R., "Streamline-Upwind/Petrov-Galerkin Methods for Advection Dominated Flows," Proceedings of the Third International Conference on Finite Element Methods in Fluid Flow, Banff, Canada, June, 1980.

67. Christie, I., Griffiths, D. F., Mitchell, A. R., and Zienkiewicz, O. C., "Finite Element Methods for Second Order Differential Equations with Significant First Derivatives," International Journal of Numerical Methods in Engineering, Vol. 10, pp. 1389-1396, 1976.

68. Griffiths, D. F., and Lorenz, J., "An Analysis of the Petrov-Galerkin Finite Element Method," Computer Methods in Applied Mechanics and Engineering, Vol. 14, pp. 39-64, 1978.

69. Heinrich, J. C., Huyakorn, F. S., Zienkiewicz, O. C., and Mitchell, A. R., "An 'Upwind' Finite-Element Scheme for Two-Dimensional Convective Transport Equation," International Journal of Numerical Methods in Engineering, Vol. 11, pp. 131-143, 1977.

70. Hilber, H. M., Hughes, T.J.R., and Taylor, R. L., "Improved Numerical Dissipation for Time Integration Algorithms in Structural Dynamics," Earthquake Engineering and Structural Dynamics, Vol. 6, pp. 283-292, 1977.

71. Hughes, T.J.R., "Stability, Convergence, and Growth and Decay of Energy at the Average Acceleration Method in Nonlinear Structural Dynamics," Computers and Structures, Vol. 6, pp. 313-324, 1976.

72. Hughes, T.J.R., "Equivalence of Finite Elements for Nearly-Incompressible Elasticity," Journal of Applied Mechanics, Vol. 44, Series E, No. 1, p. 181, March, 1977.

73. Hughes, T.J.R., "A Simple Scheme for Developing 'Upwind' Finite Elements," International Journal for Numerical Methods in Engineering, Vol. 12, pp. 1359-1369, 1978.

74. Hughes, T.J.R., and Brooks, A., "A Multidimensional Upwind Scheme with no Crosswind Diffusion," in AMD, Vol. 34, Finite Element Methods for Convection Dominated Flows, T.J.R. Hughes (ed.), ASME, New York, 1979.

75. Hughes, T.J.R., Cohen, M., and Haroun, M., "Reduced and Selective Integration Techniques in the Finite Element Analysis of Plates," Nuclear Engineering and Design, Vol. 46, No. 1, pp. 203-222, March, 1978.

76. Hughes, T.J.R., and Liu, W. K., "Implicit-Explicit Finite Elements in Transient Analysis: Stability Theory," Journal of Applied Mechanics, Vol. 45, pp. 371-374, 1978.

77. Hughes, T.J.R., and Liu, W. K., "Implicit-Explicit Finite Elements in Transient Analysis: Implementation and Numerical Examples," Journal of Applied Mechanics, Vol. 45, pp. 375-378, 1978.

78. Hughes, T.J.R., Pister, K. S., and Taylor, R. L., "Implicit-Explicit Finite Elements in Nonlinear Transient Analysis," Computer Methods in Applied Mechanics and Engineering, Vol. 17-18, pp. 159-182, 1979.

79. Krieg, R. D., and Key, S. W., "Transient Shell Response by Numerical Time Integration," International Journal of Numerical Methods in Engineering, Vol. 7, No. 3, pp. 273-286, 1973.

80. Kuhlemeyer, R. L., and Lysmer, J., "Finite Element Method Accuracy for Wave Propagation Problems," Journal of the Soil Mechanics and Foundations Division, ASCE, pp. 421-426, May, 1973.

81. Mullen, R., and Belytschko, T., "Dispersion Analysis of Finite Element Semidiscretizations of the Two Dimensional Wave Equation," Department of Civil Engineering, The Technological Institute, Northwestern University, Evanston, Illinois, 60201 (preprint), 1980.

82. Zienkiewicz, O. C., The Finite Element Method, Third Edition, McGraw Hill Book Co. (UK), London, 1977.

WAVE PROPAGATION

83. Claerbout, J. F., Fundamentals of Geophysical Data Processing, McGraw-Hill, Inc., 1976.

84. Ewing, W. M., Jardetsky, W. S., Press, F., Elastic Waves in Layered Media, McGraw-Hill Book Co., New York, 1957.

85. Lamb, H., Philosophical Transactions of the Royal Society (London), Vol. 203, pp. 1-42, 1904.

86. Miklowitz, The Theory of Elastic Waves and Waveguides, North-Holland Publishing Co., Amsterdam, New York, Oxford, 1978.

87. Mow, C. C., and Pao, Y. H., "The Diffraction of Elastic Waves and Stress Concentrations," RAND Report, R-482-PR, 1971.

88. Viktorov, I. A., Rayleigh and Lamb Waves, Plenum Press, New York, 1967.

GENERAL REFERENCES

89. Housner, G. W., "Interaction of Buildings and Ground during an Earthquake," Bulletin of the Seismological Society of America, Vol. 47, No. 3, pp. 179-186, 1957.

90. Jennings, P. C., "Distant Motions from a Building Vibration Test," Bulletin of the Seismological Society of America, Vol. 60, No. 6, pp. 2037-2043, 1970.

91. Noble, B., Applied Linear Algebra, Prentice-Hall, Inc., Englewood Cliffs, N.J., 1969.

CALIFORNIA INSTITUTE OF TECHNOLOGY

Reports Published

by

Earthquake Engineering Research Laboratory
Dynamics Laboratory
Disaster Research Center

Note: Numbers in parenthesis are Accession Numbers assigned by the National Technical Information Service; these reports may be ordered from the National Technical Information Service, 5285 Port Royal Road, Springfield, Virginia, 22161. Accession numbers should be quoted on orders for reports (PB --- ---). Reports without this information either have not been submitted to NTIS or the information was not available at the time of printing. An N/A in parenthesis indicates that the report is no longer available at Caltech.

1. Alford, J.L., G.W. Housner and R.R. Martel, "Spectrum Analysis of Strong-Motion Earthquakes," 1951. (Revised August 1964). (N/A)

2. Housner, G.W., "Intensity of Ground Motion During Strong Earthquakes," 1952. (N/A)

3. Hudson, D.E., J.L. Alford and G.W. Housner, "Response of a Structure to an Explosive Generated Ground Shock," 1952. (N/A)

4. Housner, G.W., "Analysis of the Taft Accelerogram of the Earthquake of 21 July 1952." (N/A)

5. Housner, G.W., "A Dislocation Theory of Earthquakes," 1953. (N/A)

6. Caughey, T.K., and D.E. Hudson, "An Electric Analog Type Response Spectrum," 1954.(N/A)

7. Hudson, D.E., and G.W. Housner, "Vibration Tests of a Steel-Frame Building," 1954. (N/A)

8. Housner, G.W., "Earthquake Pressures on Fluid Containers," 1954. (N/A)

9. Hudson, D.E., "The Wilmot Survey Type Strong-Motion Earthquake Recorder," 1958. (N/A)

10. Hudson, D.E., and W.D. Iwan, "The Wilmot Survey Type Strong-Motion Earthquake Recorder, Part II," 1960. (N/A)

11. Caughey, T.K., D.E. Hudson, and R.V. Powell, "The CIT Mark II Electric Analog Type Response Spectrum Analyzer for Earthquake Excitation Studies," 1960. (N/A)

12. Keightley, W.O, G.W. Housner and D.E. Hudson, "Vibration Tests of the Encino Dam Intake Tower," 1961. (N/A)

13. Merchant, Howard Carl, "Mode Superposition Methods Applied to Linear Mechanical Systems Under Earthquake Type Excitation," 1961. (N/A)

14. Iwan, Wilfred D., "The Dynamic Response of Bilinear Hysteretic Systems," 1961. (N/A)

15. Hudson, D.E., "A New Vibration Exciter for Dynamic Test of Full-Scale Structures," 1961. (N/A)

16. Hudson, D.E., "Synchronized Vibration Generators for Dynamic Tests of Full-Scale Structures," 1962. (N/A)

17. Jennings, Paul C., "Velocity Spectra of the Mexican Earthquakes of 11 May and 19 May 1962," 1962. (N/A)

18. Jennings, Paul C., "Response of Simple Yielding Structures to Earthquake Excitation," 1963. (N/A)

19. Keightley, Willard O., "Vibration Tests of Structures," 1963. (N/A)

20. Caughey, T.K. and M.E.J. O'Kelly, "General Theory of Vibration of Damped Linear Dynamic Systems," 1963. (N/A)

21. O'Kelly, M.E.J., "Vibration of Viscously Damped Linear Dynamic Systems," 1964. (N/A)

22. Nielsen, N. Norby, "Dynamic Response of Multistory Buildings," 1964. (N/A)

23. Tso, Wai Keung, "Dynamics of Thin-Walled Beams of Open Section," 1964. (N/A)

24. Keightley, Willard O., "A Dynamic Investigation of Bouquet Canyon Dam," 1964. (N/A)

25. Malhotra, R.K., "Free and Forced Oscillations of a Class of Self-Excited Oscillators," 1964.

26. Hanson, Robert D., "Post-Elastic Response of Mild Steel Structures," 1965.

27. Masri, Sami F., "Analytical and Experimental Studies of Impact Dampers," 1965.

28. Hanson, Robert D., "Static and Dynamic Tests of a Full-Scale Steel-Frame Structure," 1965.

29. Cronin, Donald L., "Response of Linear, Viscous Damped Systems to Excitations Having Time-Varying Frequency," 1965.

30. Hu, Paul Yu-fei, "Analytical and Experimental Studies of Random Vibration," 1965.

31. Crede, Charles E., "Research on Failure of Equipment when Subject to Vibration," 1965.

32. Lutes, Loren D., "Numerical Response Characteristics of a Uniform Beam Carrying One Discrete Load," 1965. (N/A)

33. Rocke, Richard D., "Transmission Matrices and Lumped Parameter Models for Continuous Systems," 1966. (N/A)

34. Brady, Arthur Gerald, "Studies of Response to Earthquake Ground Motion," 1966. (N/A)

35. Atkinson, John D., "Spectral Density of First Order Piecewise Linear Systems Excited by White Noise," 1967. (N/A)

36. Dickerson, John R., "Stability of Parametrically Excited Differential Equations," 1967. (N/A)

37. Giberson, Melbourne F., "The Response of Nonlinear Multi-Story Structures Subjected to Earthquake Excitation," 1967. (N/A)

38. Hallanger, Lawrence W., "The Dynamic Stability of an Unbalanced Mass Exciter," 1967.

39. Husid, Raul, "Gravity Effects on the Earthquake Response of Yielding Structures," 1967. (N/A)

40. Kuroiwa, Julio H., "Vibration Test of a Multistory Building," 1967. (N/A)

41. Lutes, Loren Daniel, "Stationary Random Response of Bilinear Hysteretic Systems," 1967.

42. Nigam, Navin C., "Inelastic Interactions in the Dynamic Response of Structures," 1967.

43. Nigam, Navin C. and Paul C. Jennings, "Digital Calculation of Response Spectra from Strong-Motion Earthquake Records," 1968.

44. Spencer, Richard A., "The Nonlinear Response of Some Multistory Reinforced and Prestressed Concrete Structures Subjected to Earthquake Excitation," 1968. (N/A)

45. Jennings, P.C., G.W. Housner and N.C. Tsai, "Simulated Earthquake Motions," 1968.

46. "Strong-Motion Instrumental Data on the Borrego Mountain Earthquake of 9 April 1968," (USGS and EERL Joint Report), 1968.

47. Peters, Rex B., "Strong Motion Accelerograph Evaluation," 1969.

48. Heitner, Kenneth L., "A Mathematical Model for Calculation of the Run-Up of Tsunamis," 1969.

49. Trifunac, Mihailo D., "Investigation of Strong Earthquake Ground Motion," 1969. (N/A)

50. Tsai, Nien Chien, "Influence of Local Geology on Earthquake Ground Motion," 1969. (N/A)

51. Trifunac, Mihailo D., "Wind and Microtremor Induced Vibrations of a Twenty-Two Steel Frame Building," EERL 70-01, 1970.

52. Yang, I-Min, "Stationary Random Response of Multidegree-of-Freedom Systems," DYNL-100, June 1970. (N/A)

53. Patula, Edward John, "Equivalent Differential Equations for Nonlinear Dynamical Systems," DYNL-101, June 1970.

54. Prelewicz, Daniel Adam, "Range of Validity of the Method of Averaging," DYNL-102, 1970.

55. Trifunac, M.D., "On the Statistics and Possible Triggering Mechanism of Earthquakes in Southern California," EERL 70-03, July 1970.

56. Heitner, Kenneth Leon, "Additional Investigations on a Mathematical Model for Calculation of the Run-Up of Tsunamis," July 1970.

57. Trifunac, Mihailo D., "Ambient Vibration Tests of a Thirty-Nine Story Steel Frame Building," EERL 70-02, July 1970.

58. Trifunac, Mihailo and D.E. Hudson, "Laboratory Evaluations and Instrument Corrections of Strong-Motion Accelerographs," EERL 70-04, August 1970. (N/A)

59. Trifunac, Mihailo D., "Response Envelope Spectrum and Interpretation of Strong Earthquake Ground Motion," EERL 70-06, August 1970.

60. Keightley, W.O., "A Strong-Motion Accelerograph Array with Telephone Line Interconnections," EERL 70-05, September 1970.

61. Trifunac, Mihailo D., "Low Frequency Digitization Errors and a New Method for Zero Baseline Correction of Strong-Motion Accelerograms," EERL 70-07, September 1970.

62. Vijayaraghavan, A., "Free and Forced Oscillations in a Class of Piecewise-Linear Dynamic Systems," DYNL-103, January 1971.

63. Jennings, Paul C., R.B. Matthiesen and J. Brent Hoerner, "Forced Vibrations of a 22-Story Steel Frame Building," EERL 71-01, February 1971. (N/A) (PB 205 161)

64. Jennings, Paul C., "Engineering Features of the San Fernando Earthquake of February 9, 1971," EERL 71-02, June 1971. (PB 202 550)

65. Bielak, Jacobo, "Earthquake Response of Building-Foundation Systems," EERL 71-04, June 1971. (N/A) (PB 205 305)

66. Adu, Randolph Ademola, "Response and Failure of Structures under Stationary Random Excitation," EERL 71-03, June 1971. (N/A) (PB 205 304)

67. Skattum, Knut Sverre, "Dynamic Analysis of Coupled Shear Walls and Sandwich Beams," EERL 71-06, June 1971. (N/A) (PB 205 267)

68. Hoerner, John Brent, "Modal Coupling and Earthquake Response of Tall Buildings," EERL 71-07, June 1971. (N/A) (PB 207 635)

69. Stahl, Karl John, "Dynamic Response of Circular Plates Subjected to Moving Massive Loads," DYNL-104, June 1971. (N/A)

70. Trifunac, M.D., F.E. Udwadia and A.G. Brady, "High Frequency Errors and Instrument Corrections of Strong-Motion Accelerograms," EERL 71-05, 1971. (PB 205 369)

71. Furuike, D.M., "Dynamic Response of Hysteretic Systems with Application to a System Containing Limited Slip," DYNL-105, September 1971. (N/A)

72. Hudson, D.E. (Editor), "Strong-Motion Instrumental Data on the San Fernando Earthquake of February 9, 1971," (Seismological Field Survey, NOAA, C.I.T. Joint Report), September 1971. (PB 204 198)

73. Jennings, Paul C. and Jacobo Bielak, "Dynamics of Building-Soil Interaction," EERL 72-01, April 1972. (PB 209 666)

74. Kim, Byung-Koo, "Piecewise Linear Dynamic Systems with Time Delays," DYNL-106, April 1972.

75. Viano, David Charles, "Wave Propagation in a Symmetrically Layered Elastic Plate," DYNL-107, May 1972.

76. Whitney, Albert W., "On Insurance Settlements Incident to the 1906 San Francisco Fire," DRC 72-01, August 1972. (PB 213 256)

77. Udwadia, F.E., "Investigation of Earthquake and Microtremor Ground Motions," EERL 72-02, September 1972. (PB 212 853)

78. Wood, John H., "Analysis of the Earthquake Response of a Nine-Story Steel Frame Building During the San Fernando Earthquake," EERL 72-04, October 1972. (PB 215 823)

79. Jennings, Paul C., "Rapid Calculation of Selected Fourier Spectrum Ordinates," EERL 72-05, November 1972.

80. "Research Papers Submitted to Fifth World Conference on Earthquake Engineering, Rome, Italy, 25-29 June 1973," EERL 73-02, March 1973. (PB 220 431)

81. Udwadia, F.E. and M.D. Trifunac, "The Fourier Transform, Response Spectra and Their Relationship Through the Statistics of Oscillator Response," EERL 73-01, April 1973. (PB 220 458)

82. Housner, George W., "Earthquake-Resistant Design of High-Rise Buildings," DRC 73-01, July 1973. (N/A)

83. "Earthquakes and Insurance," Earthquake Research Affiliates Conference, 2-3 April, 1973, DRC 73-02, July 1973. (PB 223 033)

84. Wood, John H., "Earthquake-Induced Soil Pressures on Structures," EERL 73-05, August 1973. (N/A)

85. Crouse, Charles B., "Engineering Studies of the San Fernando Earthquake," EERL 73-04, March 1973. (N/A)

86. Irvine, H. Max, "The Veracruz Earthquake of 28 August 1973," EERL 73-06, October 1973.

87. Iemura, H. and P.C. Jennings, "Hysteretic Response of a Nine-Story Reinforced Concrete Building During the San Fernando Earthquake," EERL 73-07, October 1973.

88. Trifunac, M.D. and V. Lee, "Routine Computer Processing of Strong-Motion Accelerograms," EERL 73-03, October 1973. (N/A) (PB 226 047/AS)

89. Moeller, Thomas Lee, "The Dynamics of a Spinning Elastic Disk with Massive Load," DYNL 73-01, October 1973.

90. Blevins, Robert D., "Flow Induced Vibration of Bluff Structures," DYNL 74-01, February 1974.

91. Irvine, H. Max, "Studies in the Statics and Dynamics of Simple Cable Systems," DYNL-108, January 1974.

92. Jephcott, D.K. and D.E. Hudson, "The Performance of Public School Plants During the San Fernando Earthquake," EERL 74-01, September 1974. (PB 240 000/AS)

93. Wong, Hung Leung, "Dynamic Soil-Structure Interaction," EERL 75-01, May 1975. (N/A) (PB 247 233/AS)

94. Foutch, D.A., G.W. Housner, P.C. Jennings, "Dynamic Responses of Six Multistory Buildings During the San Fernando Earthquake," EERL 75-02, October 1975. (PB 248 144/AS)

95. Miller, Richard Keith, "The Steady-State Response of Multidegree-of-Freedom Systems with a Spatially Localized Nonlinearity," EERL 75-03, October 1975. (PB 252 459/AS)

96. Abdel-Ghaffar, Ahmed Mansour, "Dynamic Analyses of Suspension Bridge Structures," EERL 76-01, May 1976. (PB 258 744/AS)

97. Foutch, Douglas A., "A Study of the Vibrational Characteristics of Two Multistory Buildings," EERL 76-03, September 1976. (PB 260 874/AS)

98. "Strong Motion Earthquake Accelerograms Index Volume," Earthquake Engineering Research Laboratory, EERL 76-02, August 1976. (PB 260 929/AS)

99. Spanos, P-T.D., "Linearization Techniques for Non-Linear Dynamical Systems," EERL 76-04, September 1976. (PB 266 083/AS)

100. Edwards, Dean Barton, "Time Domain Analysis of Switching Regulators," DYNL 77-01, March 1977.

101. Abdel-Ghaffar, Ahmed Mansour, "Studies on the Effect of Differential Motions of Two Foundations upon the Response of the Superstructure of a Bridge," EERL 77-02, January 1977. (PB 271 095/AS)

102. Gates, Nathan C., "The Earthquake Response of Deteriorating Systems," EERL 77-03, March 1977. (PB 271 090/AS)

103. Daly, W., W. Judd and R. Meade, "Evaluation of Seismicity at U.S. Reservoirs," USCOLD, Committee on Earthquakes, May 1977. (PB 270 036/AS)

104. Abdel-Ghaffar, A.M. and G.W. Housner, "An Analysis of the Dynamic Characteristics of a Suspension Bridge by Ambient Vibration Measurements," EERL 77-01, January 1977. (PB 275 063/AS)

105. Housner, G.W. and P.C. Jennings, "Earthquake Design Criteria for Structures," EERL 77-06, November 1977. (PB 276 502/AS)

106. Morrison, P., R. Maley, G. Brady, R. Porcella, "Earthquake Recordings on or Near Dams," USCOLD, Committee on Earthquakes, November 1977. (PB 285 867/AS)

107. Abdel-Ghaffar, A.M., "Engineering Data and Analyses of the Whittier, California Earthquake of January 1, 1976," EERL 77-05, November 1977. (PB 283 750/AS)

108. Beck, James L., "Determining Models of Structures from Earthquake Records," EERL 78-01, June 1978. (PB 288 806/AS)

109. Psycharis, Ioannis, "The Salonica (Thessaloniki) Earthquake of June 20, 1978," EERL 78-03, October 1978. (PB 290 120/AS)

110. Abdel-Ghaffar, A.M. and R.F. Scott, "An Investigation of the Dynamic Characteristics of an Earth Dam," EERL 78-02, August 1978. (PB 288 878/AS)

111. Mason, Alfred B., Jr., "Some Observations on the Random Response of Linear and Nonlinear Dynamical Systems," EERL 79-01, January 1979. (PB 290 808/AS)

112. Helmberger, D.V. and P.C. Jennings (Organizers), "Strong Ground Motion: N.S.F. Seminar-Workshop," SL-EERL 79-02, February 1978.

113. Lee, David M., Paul C. Jennings and George W. Housner, "A Selection of Important Strong Motion Earthquake Records," EERL 80-01, January 1980. (PB 80 169196)

114. McVerry, Graeme H., "Frequency Domain Identification of Structural Models from Earthquake Records," EERL 79-02, October 1979.

115. Abdel-Ghaffar, A.M., R.F. Scott and M.J. Craig, "Full-Scale Experimental Investigation of a Modern Earth Dam," EERL 80-02, February 1980.

116. Rutenberg, Avigdor, Paul C. Jennings and George W. Housner, "The Response of Veterans Hospital Building 41 in the San Fernando Earthquake," EERL 80-03, May 1980.

117. Haroun, Medhat Ahmed, "Dynamic Analyses of Liquid Storage Tanks," EERL 80-04, February 1980.

Strong-Motion Earthquake Accelerograms
Digitized and Plotted Data

Uncorrected Accelerograms

Volume I

Part	Report No.	NTIS Accession No.
A	EERL 70-20	PB 287 847
B	EERL 70-21	PB 196 823
C	EERL 71-20	PB 204 364
D	EERL 71-21	PB 208 529
E	EERL 71-22	PB 209 749
F	EERL 71-23	PB 210 619
G	EERL 72-20	PB 211 357
H	EERL 72-21	PB 211 781
I	EERL 72-22	PB 213 422
J	EERL 72-23	PB 213 423
K	EERL 72-24	PB 213 424
L	EERL 72-25	PB 215 639
M	EERL 72-26	PB 220 554
N	EERL 72-27	PB 223 023
O	EERL 73-20	PB 222 417
P	EERL 73-21	PB 227 481/AS
Q	EERL 73-22	PB 232 315/AS
R	EERL 73-23	PB 239 585/AS
S	EERL 73-24	PB 241 551/AS
T	EERL 73-25	PB 241 943/AS
U	EERL 73-26	PB 242 262/AS
V	EERL 73-27	PB 243 483/AS
W	EERL 73-28	PB 243 497/AS
X	EERL 73-29	PB 243 594/AS
Y	EERL 73-30	PB 242 947/AS

Strong-Motion Earthquake Accelerograms
Digitized and Plotted Data

Corrected Accelerograms and Integrated
Ground Velocity and Displacement Curves

Volume II

Part	Report No.	NTIS Accession No.
A	EERL 71-50	PB 208 283
B	EERL 72-50	PB 220 161
C	EERL 72-51	PB 220 162
D	EERL 72-52	PB 220 836
E	EERL 73-50	PB 223 024
F	EERL 73-51	PB 224 977/9AS
G	EERL 73-52	PB 229 239/AS
H	EERL 74-50	PB 231 225/AS
I	EERL 74-51	PB 232 316/AS
J,K	EERL 74-52	PB 233 257/AS
L,M	EERL 74-53	PB 237 174/AS
N	EERL 74-54	PB 236 399/AS
O,P	EERL 74-55	PB 239 586/AS
Q,R	EERL 74-56	PB 239 587/AS
S	EERL 74-57	PB 241 552/AS
T	EERL 75-50	PB 242 433/AS
U	EERL 75-51	PB 242 949/AS
V	EERL 75-52	PB 242 948/AS
W,Y	EERL 75-53	PB 243 719

Analyses of Strong-Motion Earthquake Accelerograms
Response Spectra

Volume III

Part	Report No.	NTIS Accession No.
A	EERL 72-80	PB 212 602
B	EERL 73-80	PB 221 256
C	EERL 73-81	PB 223 025
D	EERL 73-82	PB 227 469/AS
E	EERL 73-83	PB 227 470/AS
F	EERL 73-84	PB 227 471/AS
G	EERL 73-85	PB 231 223/AS
H	EERL 74-80	PB 231 319/AS
I	EERL 74-81	PB 232 326/AS
J,K,L	EERL 74-82	PB 236 110/AS
M,N	EERL 74-83	PB 236 400/AS
O,P	EERL 74-84	PB 238 102/AS
Q,R	EERL 74-85	PB 240 688/AS
S	EERL 74-86	PB 241 553/AS
T	EERL 75-80	PB 243 698/AS
U	EERL 75-81	PB 242 950/AS
V	EERL 75-82	PB 242 951/AS
W,Y	EERL 75-83	PB 243 492/AS

Analyses of Strong-Motion Earthquake Accelerograms
Fourier Amplitude Spectra

Volume IV

Part	Report No.	NTIS Accession No.
A	EERL 72-100	PB 212 603
B	EERL 73-100	PB 220 837
C	EERL 73-101	PB 222 514
D	EERL 73-102	PB 222 969/AS
E	EERL 73-103	PB 229 240/AS
F	EERL 73-104	PB 229 241/AS
G	EERL 73-105	PB 231 224/AS
H	EERL 74-100	PB 232 327/AS
I	EERL 74-101	PB 232 328/AS
J,K,L,M	EERL 74-102	PB 236 111/AS
N,O,P	EERL 74-103	PB 238 447/AS
Q,R,S	EERL 74-104	PB 241 554/AS
T,U	EERL 75-100	PB 243 493/AS
V,W,Y	EERL 75-101	PB 243 494/AS

Index Volume	EERL 76-02	PB 260 929/AS